ABSTRACT

Title of Dissertation: HOW ARE NON-HERMITIAN SUPERFLUIDS SPECIAL?
THEORY AND EXPERIMENT

Junheng Tao
Doctor of Philosophy, 2024

Dissertation Directed by: Professor Ian Spielman
National Institute of Standards and Technology
and
Department of Physics, University of Maryland

Ultracold atoms emerge as a promising advanced platform for researching the principles of quantum mechanics. Its development of scientific understanding and technology enriches the toolbox for quantum simulations and quantum computations. In this dissertation work, we describe the methods we applied to build our new high-resolution $^{87}\mathrm{Rb}$ Bose-Einstein condensate (BEC) machine integrated with versatile quantum control and measurement tools. Then we describe the applications of these tools to the research of novel superfluidity and non-Hermitian physics.

Superfluids and normal fluids were often studied in the context of Landau's two-fluid model, where the normal fluid stemmed from thermally excited atoms in a superfluid background. But can there be normal fluids in the ground state of a pure BEC, at near zero temperature? Our work addressed the understanding of this scenario, and then measured the anisotropic superfluid density in a density-modulated BEC, where the result matched the prediction of the Leggett

formula proposed for supersolids. We further considered and measured this BEC in rotation and found a non-classocal moment of inertia that sometimes turns negative. We distinguished the roles of superfluid and normal fluid flows, and linked some features to the dipolar and spin-orbit coupled supersolids.

As a second direction, we describe our capability to create non-Hermiticity with Raman lasers, digital-micromirror device (DMD), and microwave, and present our work in engineering the real space non-Hermitian skin effect with a spin-orbit coupled BEC. By use of a spin-dependent dissipative channel, we realized an imaginary gauge potential which led to nonreciprocal transport in the flat box trap. We studied the system dynamics by quenching the dissipation, and further prepared stationary edge states. We link our discoveries to a non-Hermitian topological class characterized by a quantized winding number. Finally, we discuss the exciting promises of using these tools to study many-body physics open quantum systems.

How Non-Hermitian Superfluids are Special?
Theory and Experiments

by

Junheng Tao

Dissertation submitted to the Faculty of the Graduate School of the
University of Maryland, College Park in partial fulfillment
of the requirements for the degree of
Doctor of Philosophy
2024

Advisory Committee:
- Professor Mohammad Hafezi, Dean's representative
- Professor William D. Phillips
- Professor Steven Rolston, Chair
- Professor Trey Porto
- Professor Ian B. Spielman, Co-chair/Advisor

Dedication

To my dear parents.

Acknowledgments

I'm so grateful to the many nice people met during the path to my PhD. Prof. Ian Spielman was and still is a great and energetic advisor and my role model, who knows and learns as many great things as one could imagine learning. Every time I begin to lose faith in things, I think of his attitude and wisdom. I also owe amounts to the senior group members who guided me to the AMO lab life, Dr. Ana Valdes Curiel, Dr. (Paco) Francisco Salces Carcoba and Prof. Qi-yu Liang, who showed me different ways of spending my early academic career, as a doctoral student. I'm grateful to have excellent physicists on my dissertation committee: Prof. William Phillips, Trey Porto, Mohammad Hafezi, and Steven Rolston. Also, I'd like to thank my family and early friends who continuously supported me throughout this journey, and who are committed to continue doing so in the coming years.

The University of Maryland is a vibrant campus where different personalities can be encountered and appreciated. My peer Mingshu Zhao, my "only" lab mate, taught me important lessons both academic-wise and when facing life decisions. My greatest thanks go to his mental and technological support when I had hard times and to his open attitude to everything that happened in his life. My groupmates Graham Reid, Emine Altunas, Alina Escalera, Dina Genkina, Yuchen Yue, Michael Doris, Dario D'Amato, and Emmanuel Mercado, thank you for sharing interesting ideas at the group and private meetings, for making the group a friendly and fun environment. More thanks go to my JQI friends, basement life is a bit interesting only when chatting with you.

At last, I thank my “long-term” roommates, who kept my companions over the years, Yuxun Guo, Peihua Ma, and Zhi Zhang.

Table of Contents

List of Tables

List of Figures

List of Abbreviations

2D	Two-dimensional
3D	Three-dimensional
BEC	Bose-Einstein condensates
SF	Superfluid
SOC	Spin-orbit coupling
NH	Non-Hermitian
HWP	Half waveplate
QWP	Quarter waveplate
MOT	Magneto optical trap
NA	Numerical aperture
NIST	National Institute of Standards and Technology
PBS	Polarizing beam splitter
PGC	Polarization gradient cooling
PSF	Point spread function
cMOT	Compressed MOT
LIAD	Light-induced atomic desorption
RF	Radio frequency
TEC	Thermoelectric cooling
TOF	Time of flight
UHV	Ultra high vacuum
UV	Ultraviolet
JQI	Joint Quantum Institute
UMD	University of Maryland
µ-wave	Microwave
AOM	Acousto optic modulator
DMD	Digital micromirror device
SSH	Su–Schrieffer–Heeger
TTL	Transistor-Transistor Logic
GPE	Gross–Pitaevskii Equation

Chapter 1: Introduction

1.1 Quantum simulations with quantum gases

In the pioneering lecture in 1982 [5], Richard Feynman proposed to "*let the computer itself be built of quantum mechanical elements which obey quantum mechanical laws*". Many would not have expected that these words become the mainstream practice in the study of quantum mechanics in the early 21st century. This was due to the amount of previous efforts to experimentally harness the quantum dynamics using coherent approaches. Nowadays, people can already make mesoscopic quantum many-body systems in their labs. Among them, the playground of ultracold quantum gases has attracted broad attention and holds a large research community. Thanks to the decades of milestone research that brings us the versatile tools for cooling and controlling these atoms, making ultracold gases arguably the closest platform to Feynman's "quantum simulators". I would like to start my introduction by asking "why" we should still follow and lead the path of quantum simulation.

1.1.1 Why do we like quantum simulations?

One of the goals of quantum simulations is to solve quantum problems that are intractable via classical approaches [6]. A well-accepted instance is strongly correlated ultracold gases in optical lattices, could in principle, help understand and explore the phase diagram of the Fermi-Hubbrad model [7], which is expected to show signatures of high-temperature superconductivity in the extreme limit. Another direction of interest is building analogs of different quantum field theories by clever design. The inter-particle interaction in ultracold gases can be enhanced to allow for strong quantum fluctuations, such that the matter wave itself is described by a quantum field [8]. Proposals exist that one can use this fact to build analog models of quantum electrodynamics [8], dynamic gauge fields [9], and even those in curved space-time [10]. The ultimate goal of this line is to achieve the non-perturbative regime, where classical simulation and analysis are rarely useful.

Another aspect of quantum simulations is that they help people discover new science in new regimes. Often those regimes were less explored either because they are rare to find in nature, or people were misled by some “no-go” theorems. But with the right tools in hand, theorists and experimentalists could rethink together and sometimes have unexpected discoveries. The most recognizable example is the development of the booming field of quantum information, which would not attract so much attention without compatible experimental progress. Despite the applications, these new considerations also produced fruitful results in understanding quantum coding theory [11], topologically ordered matter [12] and open quantum systems [13], just to list a few.

1.2 Light-matter interaction

The main messenger through which we talk to the atoms is the photons. The photon field is a $U(1)$ gauge field often detonated by the vector potential $\mathbf{A}$ which couples to the electron in the atoms by Hamiltonian [14]

$$H_e = \frac{1}{2m_e}(\mathbf{p} - \frac{e}{c}\mathbf{A})^2 \tag{1.1}$$

in the free space. And the gauge field $\mathbf{A}$ is expanded to plane wave basis

$$\mathbf{A}(\mathbf{x}, t) = A\hat{\epsilon}(e^{i(\mathbf{k}\cdot\mathbf{x}-\omega t)} + \text{H.c.}) \tag{1.2}$$

where $\hat{\epsilon}$ is the polarization vector with $\mathbf{k}\cdot\hat{\epsilon} = 0$. One can make the so-called dipole approximation that the wavelength of the light $\lambda = 2\pi/k$ is much longer than the atomic size (the length scale of electron motion). This interaction is then modeled in the electromagnetic fields $\mathbf{E} = -\partial_t\mathbf{A}/c$.

$$H_e = \frac{p^2}{2m_e} - \hat{d}\cdot\mathbf{E} \tag{1.3}$$

where

$$\hat{d} = e\mathbf{x} \tag{1.4}$$

is the electric dipole of the electron. Similarly, one can make the magnetic dipole approximation which couples the magnetic field $\mathbf{B} = \nabla\cdot\mathbf{A}$ with the magnetic moments of the electron and the nucleus.

$$H_\mu = -\hat{\mu}\cdot\mathbf{B}. \tag{1.5}$$

Hence we usually write the total atomic Hamiltonian as

$$H_a = \frac{\mathbf{p}^2}{2m} - \hat{d}\cdot\mathbf{E} - \hat{\mu}\cdot\mathbf{B}. \tag{1.6}$$

In our experiments, we extensively used these couplings by EM fields such as optical lasers, magnetic coils, and radio frequency fields. The dipole approximations always hold for these scenarios.

For the coherent EM fields we generated in our lab, the photon occupation is large enough that one can ignore the fluctuations in the photon fields, making the so-called semi-classical approximation. This means we treat $\mathbf{E}$ and $\mathbf{B}$ as c-numbers instead of field operators, while in the meanwhile, we study the quantum evolution of the atomic or electron motion.

1.2.1 Atomic two-level system

We want to make a toy model out of the real atom (and this is often justified by energy scale separation). The simplest quantum system one can make is a two-level system (or pseudo-spin), with the Hamiltonian

$$H = \hbar\omega_0 \left|e\middle\rangle\!\middle\langle e\right| - (\hbar\Omega(t) \left|e\right\rangle \left\langle g\right| + \text{H.c.}). \tag{1.7}$$

This Hamiltonian is derived from the interaction term of (1.6) by defining $\Omega = \left\langle e\right| \hat{d} \cdot \mathbf{E} \left|g\right\rangle /\hbar$ and note that $\left\langle g\right| \hat{d} \left|g\right\rangle = \left\langle e\right| \hat{d} \left|e\right\rangle = 0$ (or similarly for $\mathbf{B}$) with only one field present at a time.

This is in general time-dependent Hamiltonian because of the coupling $\Omega(t)$. Consider a single tone coupling $\Omega(t) = \Omega\cos{(\omega t)} = \frac{1}{2}(e^{i\omega t} + e^{-i\omega t})$. We usually apply the rotating wave transformation by applying the unitary $\mathcal{U}(t) = e^{i\omega t|e\rangle\langle e|}$ so that H becomes

$$H = -\hbar\delta \left|e\middle\rangle\!\middle\langle e\right| - [\frac{\hbar\Omega}{2}(1 + e^{-i2\omega t}) \left|e\right\rangle \left\langle g\right| + \text{H.c.}] \tag{1.8}$$

where $\delta = \omega - \omega_0$. Because $\omega \gg \Omega, \delta$, we can use the rotating wave approximation (RWA) and

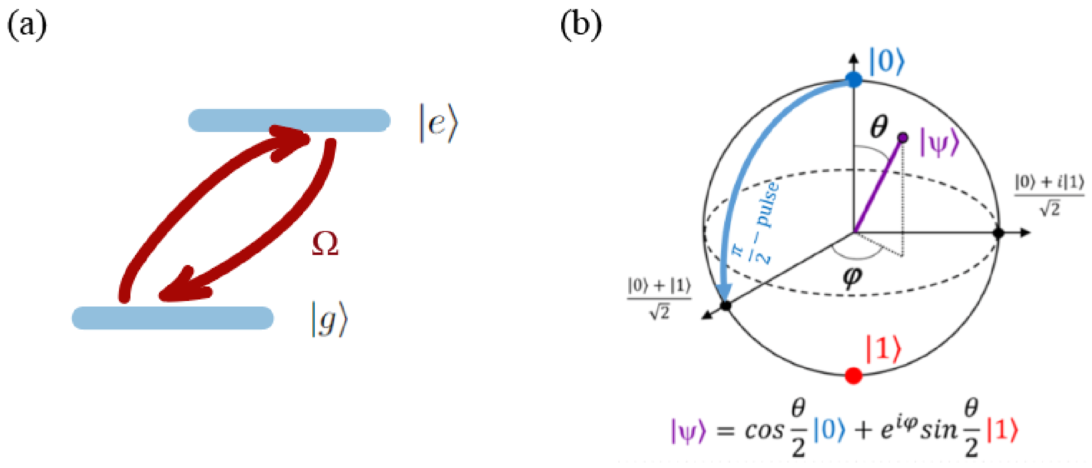

Figure 1.1: (a) An abstraction of two-level system coupled by Rabi frequency Ω. (b) Bloch sphere picture of the two-level system [1].

ignore the "fast rotating" coupling, and up to an offset

$$H = -\frac{\hbar\delta}{2}(|e\rangle\langle e| - |g\rangle\langle g|) - (\frac{\hbar\Omega}{2}\,|e\rangle\,\langle g| + \text{H.c.}). \tag{1.9}$$

This is a time-independent Hamiltonian that can be directly diagonalized. We get two energy eigenvalues

$$E_\pm = \hbar\omega_\pm = \pm\frac{\hbar}{2}\sqrt{\Omega^2 + \delta^2} \tag{1.10}$$

and as a function of δ, this is the typical picture of "avoided crossing" in a two-level system. Because the "real" eigenstates are superpositions of atom-photon dressed-states, the energy shifts from the bare atomic energy are termed the *AC Stark shifts*. In the limit of $\delta \gg \Omega$, we have a better known expression

$$E_\pm = \pm\frac{\hbar\delta}{2} \pm \frac{\hbar\Omega^2}{4\delta}. \tag{1.11}$$

Another useful consideration is to ask about the dynamics starting from an arbitrary state. This can be easily solved by projecting to the eigenstates, and the answer is population "flip flop" at the frequency of $\omega_+ - \omega_-$. For example, if at $t = 0$ the state vector is in $|g\rangle$, then

$$\langle e|\psi\rangle = -i\frac{\Omega}{\sqrt{\Omega^2 + \delta^2}} \sin\left(\frac{\sqrt{\Omega^2 + \delta^2}}{2} t\right). \tag{1.12}$$

Dynamics like such are named after I. I. Rabi and called the *Rabi oscillations*.

The Rabi oscillations can be visualized by the introduction of the "Bloch sphere" picture. It is because we can use the isomorphism mapping from SU(2) to SO(3) by defining the vector $\vec{r} = (\sin\theta\cos\phi, \sin\theta\sin\phi, \cos\theta)$ (where θ and ϕ are Euler angles). This corresponds to the state vector

$$|\psi\rangle = (\cos(\theta/2), \sin(\theta/2)e^{i\phi})^T \tag{1.13}$$

or if in a mixed state, the density matrix

$$\rho = \frac{1}{2}(\mathcal{I} + \vec{r}\cdot\vec{\sigma}). \tag{1.14}$$

We find that the equation of motion for the vector $\vec{r}$

$$\frac{\partial\vec{r}}{\partial t} = \vec{\tilde{\Omega}} \times \vec{r} \tag{1.15}$$

is a classical rotation driven by the "torque" *Rabi vector* $\vec{\tilde{\Omega}}$, which is defined as

$$\vec{\tilde{\Omega}} = -(\mathrm{Re}\,\Omega, \mathrm{Im}\,\Omega, \delta) \tag{1.16}$$

so that the rotation "frequency" is indeed $\sqrt{\Omega^2+\delta^2} = |\omega_+ - \omega_-|$ – recovers the result (1.12).

In a multilevel system (like with the energy levels of a real atom), we still mostly work with two of the many levels by deliberately isolating them in energy. This is often done in the ground state manifold by utilizing the linear or quadratic Zeeman shifts such that the other states are tuned far off resonance $\delta \gg \Omega$. The magnetic dipole transitions like RF or microwave were used to transfer atomic populations often in a two-level setting. In some optical transitions such as the cycling transition used for laser cooling, the two-level picture approximately applies, because of the well-designed photon polarization.

1.2.2 Optical Bloch equations

There are coherent processes and "incoherent" processes encountered in our typical experiments. Often the "incoherence" is induced by pumping into a continuous spectrum (with a high density of states), such as the degenerate photon states $|\mathbf{k}\rangle$ across the 4π spherical angle. This is encountered in the so-called "spontaneous emission" in which the excited atom scatters a photon into one of this degenerate sea of states.

To study such systems, people usually regard the whole physical system as an "open quantum system" plus "reservoir" setting. By tracing out the reservoir, they can derive the equations of motion for the system. We make two approximations [15]:

- The reservoir does not have a "memory" of its past evolution or its past interaction with the system;
- The reservoir state is stationary in the process of study, and is not affected by the interaction with the system.

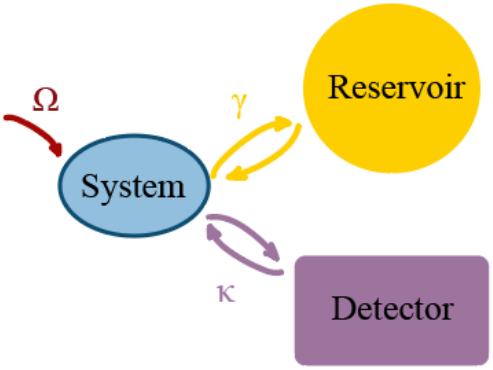

Figure 1.2: Illustration of an open quantum system. Typically there are coherent drives labeled by Ω, incoherent dissipations labeled by γ, and measurements labeled by κ.

It is realized that such processes can be effectively described by the *Markovian master equation*

$$\dot{\rho}(t) = -\frac{i}{\hbar}[H(t), \rho(t)] + \sum_n \frac{1}{2}\left[2C_n\rho(t)C_n^\dagger - \rho(t)C_n^\dagger C_n - C_n^\dagger C_n\rho(t)\right]. \tag{1.17}$$

Here all the operators are defined in the subsystem we are interested in. ρ is the density operator after tracing out the reservoir states. $C_n = \sqrt{\gamma_n}A_n$ are the “collapse operators”, where A_n describe the system-reservoir interaction, and γ_n are the coupling strengths.

Let’s look at the spontaneous emission in a two-level system, where on top of

$$H = -\frac{\hbar\delta}{2}(|e\rangle\langle e| - |g\rangle\langle g|) - (\frac{\hbar\Omega}{2}|e\rangle\langle g| + \text{H.c.}). \tag{1.18}$$

we also have the excited state $|e\rangle$ coupled to the reservoir photon modes with rate γ such that

$$C = \sqrt{\gamma}\,|g\rangle\langle e| \otimes a^\dagger. \tag{1.19}$$

We write out the matrix elements

$$
\begin{aligned}
\dot{\rho}_{ee} &= -\gamma(\bar{n}+1)\rho_{ee} + \gamma\bar{n}\rho_{11} + i\Omega^{*}\rho_{eg} - i\Omega\rho_{ge} \\
\dot{\rho}_{gg} &= \gamma(\bar{n}+1)\rho_{gg} - \gamma\bar{n}\rho_{11} - i\Omega^{*}\rho_{eg} + i\Omega\rho_{ge} \\
\dot{\rho}_{ge} &= -\frac{\gamma}{2}(2\bar{n}+1)\rho_{ge} - i\delta\rho_{ge} - i\Omega^{*}\left(\rho_{ee} - \rho_{gg}\right) \\
\dot{\rho}_{eg} &= -\frac{\gamma}{2}(2\bar{n}+1)\rho_{eg} + i\delta\rho_{eg} + i\Omega\left(\rho_{ee} - \rho_{gg}\right).
\end{aligned}
\tag{1.20}
$$

where $\bar{n}$ is the mode occupation number, and $\bar{n} = 0$ for vacuum. This set of equations describes the population and coherence evolution of the atom state and is named by *Optical Bloch equations* [14, 15].

There are steady-state solutions to the two-level system in a vacuum, namely $\dot{\rho} = 0$. We have then

$$\rho_{eg} = \frac{i\Omega\left(\rho_{ee} - \rho_{gg}\right)}{\gamma/2 - i\delta} \tag{1.21}$$

$$\rho_{ee} = \frac{R_{opt}}{\gamma + 2R_{opt}} \tag{1.22}$$

and

$$R_{opt} = \frac{\gamma|\Omega|^2}{(\gamma/2)^2 + \delta^2}. \tag{1.23}$$

There is rich physics in this solution. First, the photon scattering rate is $\rho_{ee}\gamma$; secondly, it predicts the nonlinear response of the two-level atom to the optical field – the single atom polarizability is $\alpha(\delta, \Omega) \propto \rho_{ge}/\Omega$. It has real and imaginary parts as shown in Fig. **??**; thirdly, it predicts "power broadening" as we ramp up the laser intensity – and in the extreme case $R_{opt} \gg \gamma$, $\rho_{ee} = 1/2$. This is crucial in the consideration of probing atoms as well as laser cooling, as will be elaborated.

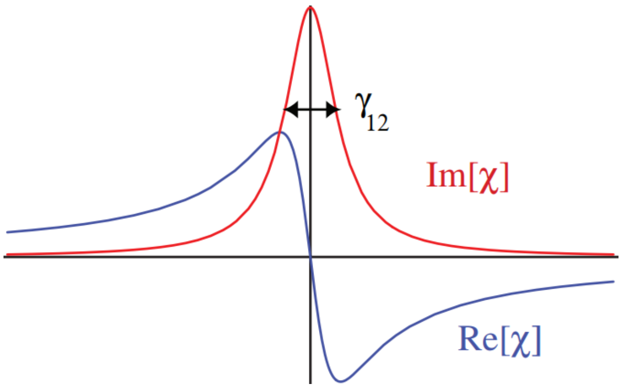

Figure 1.3: A two-level system is known for its nonlinear response to external drive Ω.

1.3 Atomic structure

The workforce is our lab is the rubidium 87 ($^{87}\mathrm{Rb}$) atoms, one of the simplest species in the alkali family. These atoms are simple because they are in the same family as hydrogen, and the eigenstates are labeled by the principal quantum number n, the angular momentum number l, and its projection m. For $^{87}\mathrm{Rb}$ atoms, the ground state has $n = 5$. Our lasers mainly address angular momentum l transitions between $l = 0$ and $l = 1$. So we label our ground state as $5S_{1/2}$.

But in general it is necessary to introduce the atomic structure for use of our experimental control. Almost all the information can be found in the Steck datasheet [16].

1.3.1 Fine structure

Because the Coulomb potential that restrains the electron is only function of $|r|$, the energy levels depend on n, but not l, m. So the different angular momentum states are degenerate. However, there are corrections to this which lift this degeneracy. These are:

1. The electron kinetic energy has relativistic correction (just by simply applying special

relativity)

$$\Delta E_{\text{rel}} = -\frac{E_n^2}{2mc^2}\left(\frac{4n}{l-1/2} - 3\right). \tag{1.24}$$

Here m is the electron mass.

2. There exists spin-orbit coupling. To understand it, one can calculate it in the electron's moving frame, where the nucleus orbits around it and generates a magnetic field. The interaction energy becomes

$$H_{\text{SO}} = \frac{Ze^2}{4\pi\epsilon_0}\frac{g_s}{4me^2c^2}\frac{\hat{\vec{L}}\cdot\hat{\vec{S}}}{r^3} \tag{1.25}$$

where Z is a correction factor. It follows that

$$\hat{S}\cdot\hat{L} = \frac{1}{2}\left(J^2 - L^2 - S^2\right). \tag{1.26}$$

3. The Darwin term is another correction from the Dirac equation. It only affects $l = 0$.

$$H_{\text{Darwin}} = \frac{\hbar^2}{8m^2c^2}4\pi\left(\frac{Ze^2}{4\pi\varepsilon_0}\right)\delta^3(\mathbf{r}) \tag{1.27}$$

Due to these corrections, the eigenstates are labeled by j through the angular momentum coupling rules, which is $\vec{J} = \vec{L} + \vec{S}$. Meanwhile, the coefficients of transformation are the *Clebsch–Gordan coefficients* defined through

$$|JM\rangle = \sum_{m_1=-j_1}^{j_1}\sum_{m_2=-j_2}^{j_2} |j_1 m_1 j_2 m_2\rangle \langle j_1 m_1 j_2 m_2 \mid JM\rangle \tag{1.28}$$

where $\vec{J} = \vec{J}_1 + \vec{J}_2$.

The fine structure lifts the degeneracy of our $5P$ state, and splits it into two $5P_{1/2}$ and $5P_{3/2}$ (the corresponding transitions are called $D1$ and $D2$). This splitting is $\sim$ 7.3 THz and is vital for our experiments. We generally address these two transitions in creating "spin"-dependent potentials and inducing the Raman dressed states.

1.3.2 Hyperfine structure

The nucleus also has a magnetic dipole moment $\mu_I = g_I I$ and can experience the magnetic field created by the orbiting valence electrons. In general this interaction is smaller than the fine strucutre by the factor of $g_I/g_s \sim m_e/m_p$, where m_p is the proton mass. On the other hand, there is electric quadrupole interaction because of the structure of the nuclei. But by accounting for that, we define

$$\hat{\vec{F}} = \hat{\vec{L}} + \hat{\vec{S}} + \hat{\vec{I}} \tag{1.29}$$

and such hyperfine interaction energy is

$$\Delta E_{\text{hfs}} = \frac{1}{2} A_{\text{hfs}} K + B_{\text{hfs}} \frac{\frac{3}{2}K(K+1) - 2I(I+1)J(J+1)}{2I(2I-1)2J(2J-1)} \tag{1.30}$$

where $K = F(F+1) - I(I+1) - J(J+1)$, A_{hfs} and B_{hfs} are the magnetic dipole constant and electric quadruple constant of the nuclei.

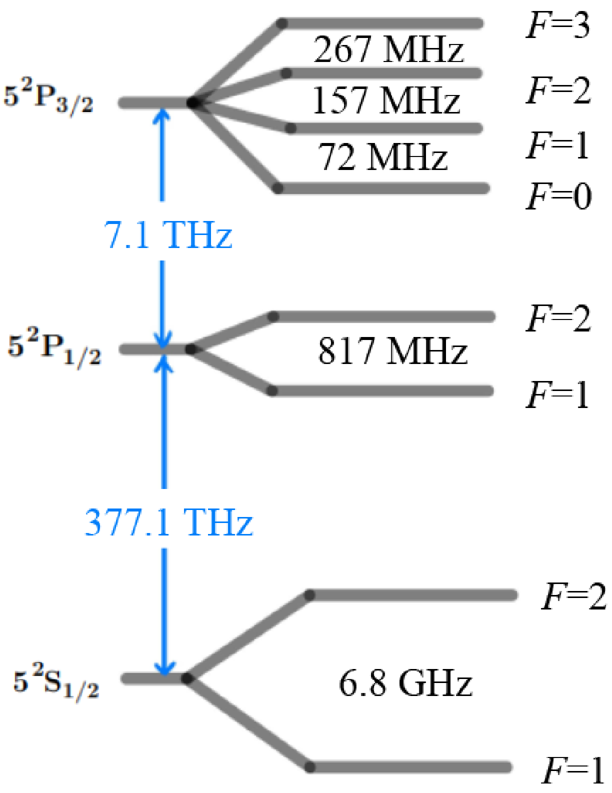

Figure 1.4: The low-lying level diagrams of a $^{87}\mathrm{Rb}$ atom. It includes both the D1 and D2 optical transitions.

1.3.3 Level diagram

After we introduced the principles of level splittings, we summarized the most used transitions in our experiment in the following chart (reproduced from [16]).

1.4 Multi-level simulation: internal states

The dynamics in a multi-level atom are complicated but are necessary to understand for conducting a variety of real experiments. On the primary level, we should at least model the

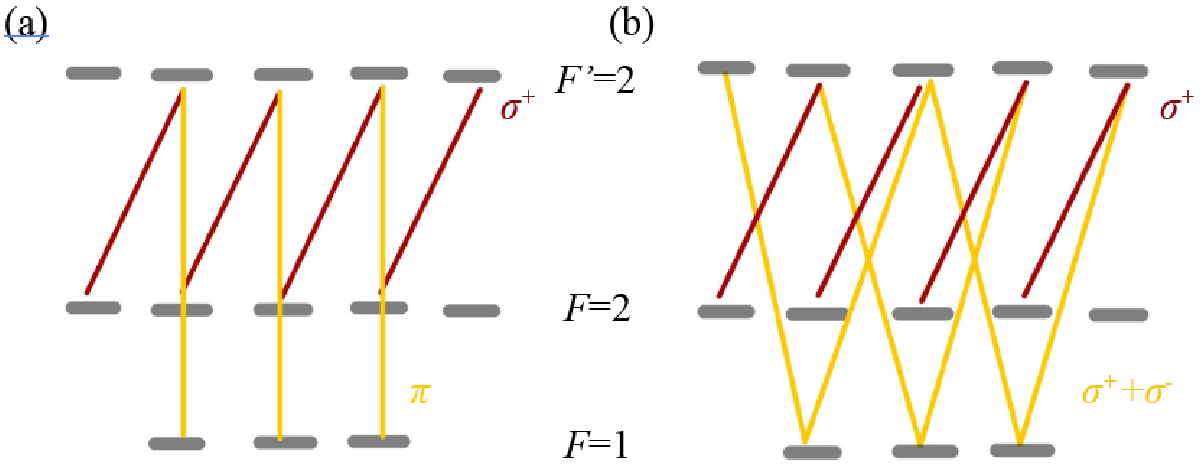

Figure 1.5: The two simulated optical pumping schemes. They both share a σ_+ polarized optical pumping beam. But their repump beams are of different polarizations, π versus $\sigma_+ + \sigma_-$ respectively.

internal dynamics with spontaneous emission. This can be done through the introduced master equation but generalized to many levels. Because our system dimension is large and involves a number of couplings either coherent or incoherent, it is preferable to lay a clear framework. For this purpose, I selected an open-source integrator *QuTiP2* [17, 18]. This simulation runs on the full $5S_{1/2}$ to $5P_{3/2}$ transitions.

1.4.1 E.g. optical pumping

Optical pumping is a widely used technique in cold atoms, as well as used daily in producing BECs. This puts a high standard on the efficiency and rate of optical pumping. We simulated this process to understand the parameters we should choose.

The optical pumping describes a population transfer, say, from an arbitrary m_F state of $|F = 2\rangle$ into a certain state $|2, 2\rangle$. This requires a "dissipative process" to remove the "entropy". This is usually done by shining a resonant σ_+ polarized light on the $F = 2$ to $F' = 2$ transition

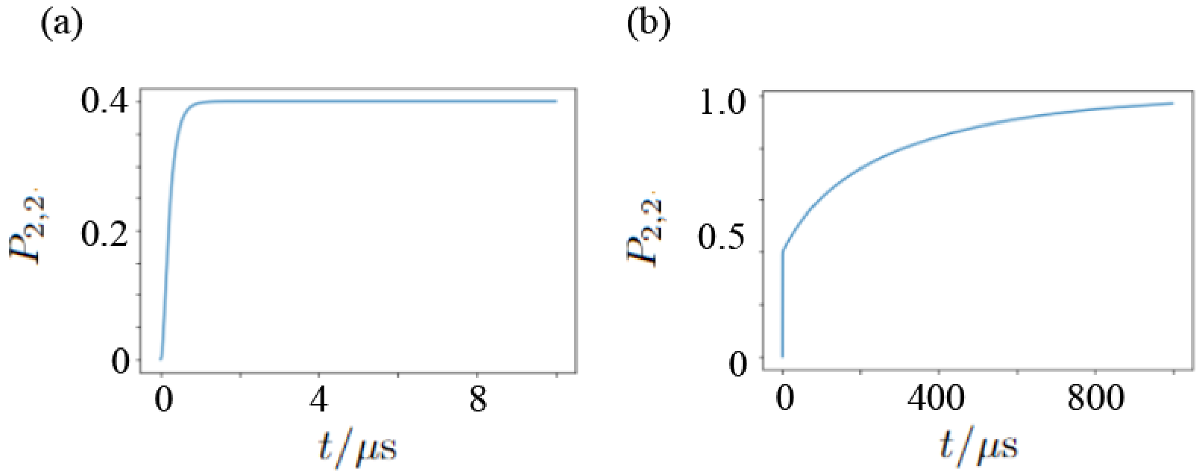

Figure 1.6: Real time evolution. (a) Optical pumping without the repumper; (b) Even when turning on a π polarized repumper (on resonance), it takes nearly 1 ms to pump 100% of population!

(D2). In Fig. 1.6(a) we initialized the atom in the $|2,1\rangle$, turned on the pumping light, and counted the probability in $|2,2\rangle$ as a function of time $P_{2,2}(t)$. However, the spontaneous decay channel from $F' = 2$ can also lead to residual population into $F = 1$. This calls for introducing a repumper laser, which brings the atoms back into the $F' = 2$ from $F = 1$.

It is “a reasonable guess” that this repumper detuning should be optimized to resonance for best efficiency. However, our simulation says that it is not the case. As shown in Fig. 1.6(b), with such a repumper on resonance, it takes almost “forever” to fully pump the atom (interestingly, a fast pump is followed by a very slow pump). A similar time scale is observed for both π and $\sigma_+ + \sigma_-$ polarized repump light.

Where does the atom probability go? With this question we examined the “meta-stable state” population, and found that it stays in some certain superposition of the $F = 1$ and $F = 2$. Ahh, this is simple *Coherent population trapping* (CPT) physics! Reconsidering the two schemes in Fig. 1.5, there are three (two) independent Λ three-level systems in the scheme a (b) – of course they support dark states. With spontaneous decay from $F' = 2$, the atom is also pumped to these states invisible to our lasers.

The resolution to this problem is also straightforward, and that is making these states "bright" again by tweaking the detuning δ. We scanned the detuning of the repumper beam and observed the *Electromagnetically induced transparency* (EIT) "dip" at the zero detuning (Fig. 1.7). We will need to park the repumper frequency a few MHz off the resonance to optimize efficiency. Even though this simulation was run at zero magnetic field, a small background field $\sim$1G like applied in our usual experimental runs is not helpful since the Zeeman shift isn't large enough.

Another "workaround" solution is to have stroboscopic lasers (which can be controlled by the AOMs). In Fig. 1.7(b) we simulated the scenario where we turned on the optical pumping light for 0.5 μs, and then switched to the repumper light for 0.5 μs, and thus went on. This sequence avoids dark states and allows for optical pumping on the 10μs time scale, slightly slower than the dettuning method.

1.4.2 E.g. spinor condensate imaging

In spinor BEC experiments, the spin projection along the quantization axis S_z is often measured by calculating from two sequential measurements $S_z = n_\uparrow - n_\downarrow$. The observables S_x, S_y can in principle be rotated to the e_z axis through an RF or microwave pulse. However, this approach is destructive because of the rotation. (One might consider applying a "reversed" pulse after the measurements, but this makes an interferometer which depends on the phase noises in

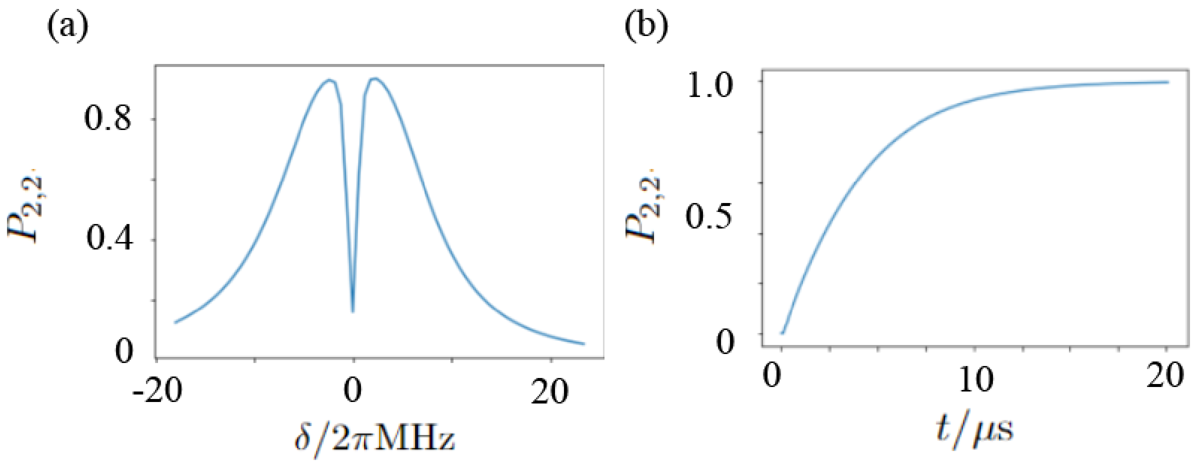

Figure 1.7: Two solutions to the CPT problem. (a) Scan the repumper detuning to locate the optimal pumping efficiency. Pump time is 5 μs. (b) Alternating the turning-on of the optical pumping laser and the repump laser at 0.5 μs time intervals.

the intermediate procedure.) We want to invent a "weak measurment" scheme for spin projection along arbitrary axes.

We consider $m_F = \pm 1$ states in the $F = 1$ as our psedo-spin space $|\uparrow\rangle, |\downarrow\rangle$. Then we couple the two spinors simultaneously to $|2, 0\rangle$ by microwaves as shown in Fig. 1.8. This coupling is off-resonant such that no real population is transferred to the $F = 2$. Meanwhile, we turn on a probe laser that is detuned to the $|2, 0\rangle$ to $|3', 1'\rangle$ transition, but compensate with the microwave detuning such that the two-photon (microwave+probe) coupling is resonant. We hope to build a scheme where we can simultaneously turn on a combined microwave plus probe pulse for several μs, and then read out the absorption signal on the probe.

We ran the master equation simulations, and indeed we were able to observe the absorption and diffraction of probe light as manifested by imaginary and real parts in the density matrix element ρ_{eg}. As we gave $\Omega_{\mu 1}$ and $\Omega_{\mu 2}$ the same phase, we found that ρ_{eg} is only function of $\langle S_x\rangle$ but a constant of $\langle S_y\rangle$. However, if we let $\arg(\Omega_{\mu 1}/\Omega_{\mu 2}) = \pi/2$, we could measure $\langle S_y\rangle$ instead

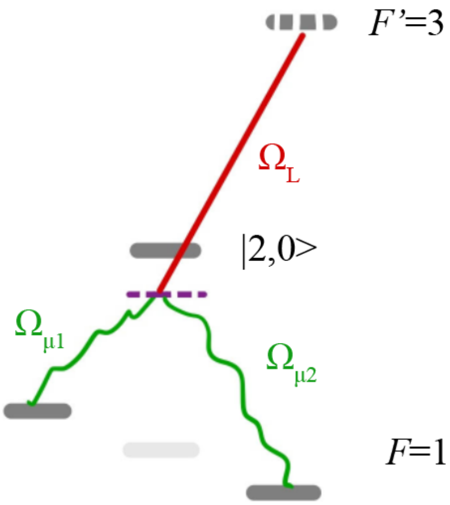

Figure 1.8: Microwave-assisted probe scheme. Two microwave couplings make a Λ system, and a probe laser is applied to read out the projected population.

of $\langle S_x\rangle$.

We have made such a nice tool, but how should we understand it? The intuition is that we made a Λ system by $|1,-1\rangle$, $|1,1\rangle$ and a "virtual state" detuned from $|2,0\rangle$ through the two microwave couplings $\Omega_{\mu 1}$ and $\Omega_{\mu 2}$ (see Fig. 1.8). The probe addresses the "population" of the virtual state, which is indeed Rabi coupled with the bright state of our Λ system. This bright state is made of $|B\rangle = (\Omega_{\mu 1}|1,1\rangle + \Omega_{\mu 2}|1,-1\rangle)/\sqrt{|\Omega_{\mu 1}|^2 + |\Omega_{\mu 2}|^2}$ and is clearly a function of the phase $\arg(\Omega_{\mu 1}/\Omega_{\mu 2})$.

1.5 Light forces: external states

We use lasers to apply forces to the atoms. To understand the origin of the forces [19], we go back to the two-level system Hamiltonian (1.9). We write out the Heisenberg equation for the atomic momentum $\hat{p}$

$$\hat{F} = \frac{d}{dt}\hat{p} = \frac{1}{i\hbar}[\hat{p}, \hat{H}] \tag{1.31}$$

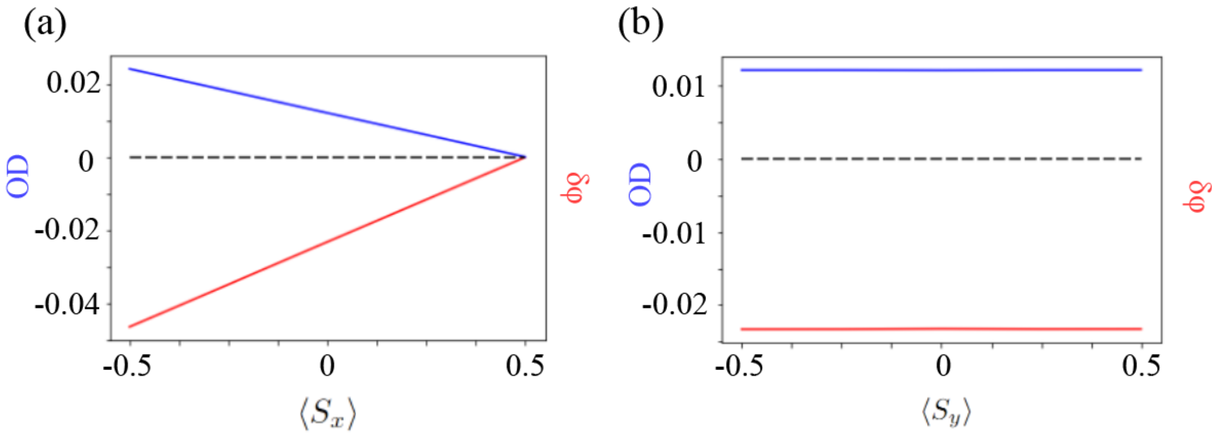

Figure 1.9: The optical depth and phase shift (arbitrary units) converted from ρ_{eg}, where $\rho_{eg} = \langle 2, 0| \rho |3', 1'\rangle$. Both signals measure the projection into the $|\rightarrow\rangle = (|\uparrow\rangle + |\downarrow\rangle)/\sqrt{2}$. Simulations are done with bias field $\mathbf{B} = B\mathbf{e}_z$ ($B = 10$G), detuning $\delta = 2\Gamma$ ($\Gamma = 2\pi \cdot 6.1$MHz), pulse time $\tau = 2\mu$s.

After plugging in (1.9) the expectation value of the force is

$$\begin{aligned} \langle \hat{F} \rangle =& \hbar \nabla \Omega \rho_{ge} + \hbar \nabla \Omega^* \rho_{eg} \\ =& \hbar \frac{1}{2} \nabla |\Omega|^2 \left(\frac{\rho_{ge}}{\Omega^*} + \frac{\rho_{eg}}{\Omega} \right) + i\hbar |\Omega|^2 \nabla \phi \left(\frac{\rho_{ge}}{\Omega^*} - \frac{\rho_{eg}}{\Omega} \right). \end{aligned} \tag{1.32}$$

We can separate it by the “dissipative force” and the “reactive force”

$$\langle \hat{F} \rangle = 2\hbar |\Omega|^2 \nabla \phi \, \mathrm{Im} \left(\frac{\rho_{eg}}{\Omega} \right) + \hbar \nabla |\Omega|^2 \, \mathrm{Re} \left(\frac{\rho_{eg}}{\Omega} \right). \tag{1.33}$$

Here $\phi = \arg \Omega$.

The dissipative force is related to the imaginary part of the coherence ρ_{eg}, which corresponds to the absorbed light. Consider a plane wave with $\vec{k}$ that illuminates our atom with velocity $\vec{v}$. In the weak light limit ($|\Omega| \ll \gamma$)

$$\operatorname{Im} \frac{\rho_{eg}}{\Omega} = \frac{2\gamma}{4\gamma^2 + (\delta - \vec{k} \cdot \vec{v})^2} \tag{1.34}$$

which leads to

$$\langle \hat{F} \rangle = \hbar k \frac{4\gamma |\Omega|^2}{4\gamma^2 + (\delta - \vec{k} \cdot \vec{v})^2} = \hbar k R_{opt}. \tag{1.35}$$

This expression has a clear explanation that the atom absorbs a photon from our laser and gets a momentum kick $\vec{k}$ from it, which multiplies the absorption rate is the force. The reason is that the spontaneous emission following this absorption randomly ejects the photon to the 4π solid angle, and hence is averaged out. Thus, an atom can be decelerated if it moves against our laser beam $\vec{k}$, or it can be accelerated if it moves away from the laser.

It is natural to ask if one can make something useful by counter-propagating two identical laser beams. Repeating the calculations and "naively" adding up the forces (in the weak intensity limit), we expand the expression to first-order in v ($\vec{k} \cdot \vec{v} \ll \delta, \gamma$)

$$\langle \hat{F} \rangle = \hbar k \frac{4\gamma |\Omega|^2}{4\gamma^2 + \delta^2} \left(1 + \frac{2\delta \vec{k} \cdot \vec{v}}{4\gamma^2 + \delta^2} \right). \tag{1.36}$$

This is such a great result that it allows us to laser-cool the atoms! When the detuning $\delta < 0$, the force always slows the atom down along the direction of the counter-propagated lasers. The technology was termed "*Doppler cooling*" when it was first discovered in the 1980s [20]. However, this nonlinear expression predicts a "turn-over" at large $\vec{k} \cdot \vec{v}$, which means there is a "capture range" $|v| < v_c$ of the frictional force. This parameter is vitally important when we design the laser cooling apparatus.

On the other side, the reactive force corresponds to the dispersive part of the atomic polarizability. We would take the large detuning limit $|\Omega| \ll \delta$ and have

$$\langle \hat{F} \rangle = -\hbar \nabla \left(\frac{|\Omega|^2}{\delta} \right). \tag{1.37}$$

We find this is the gradient of the AC Stark shift and hence is conservative. This force exists as the light-dressed state of the atoms can have ground state energies depending on the light intensity. For red-detuned laser, atoms would be attracted to the strong intensity; while for blue, the weak intensity. The force was termed the *Optical dipole foce* [21]. Thus, we can control in our experiment the external potential seen by the atoms easily through “sculpturing” the light intensities in space.

Chapter 2: Making and understanding your own Bose-Einstein condensates

2.1 Overview

The heroic move to make atomic Bose-Einstein condensates (BEC) was awarded the Nobel prize in 2001. 20 years passed and the task was completed and simplified by many groups around the world, and there have been standard techniques, although still challenging, to make degenerate gases step by step. In this chapter, I will review the path we've taken. Hopefully, this helps the readers build their apparatus as well.

Our approach to producing ultracold rubidium quantum gases borrows a lot of experience from the precursor experiments *RbChip* and *RbLi*. In summary, one needs an atom source to produce the atomic gas, laser cool them to mK$\sim$ μK temperature, trap them and then conduct evaporative cooling to reach nK temperature and a unity phase space density. In our new apparatus, we did these several steps with a "modular programming" spirit, in both space and time.

Our vacuum system has two glass cells connected by "differential pumping tubes" which allows vastly different vacuum pressures at the two ends. The alkali metal sources sit in the vacuum bellows that are joined via a tee and connected to one of the glass cells, named the "MOT cell". On the one hand, we need to quickly load the MOT from the alkali vapor at a relatively high density. But this high density of the background hot gases limits the lifetime (e.g. in a magnetic or dipole trap) at the "MOT cell" due to their collisions with the laser-cooled atoms; on the other hand, we want a low enough pressure at the "science cell", in order to run the scientific BEC experiments for at least a few seconds (including evaporation).

The structure of the first half of this chapter focuses on the scheme to make ultracold gases in BEC. The outline of the procedure is, we load a *magneto-optic trap* (MOT) at the "MOT cell", compress the MOT and conduct sub-Doppler cooling. We then recapture these atoms to a magnetic quadruple trap, and immediately transfer them to the "science cell" by *magnetic transport*. We run RF or microwave-forced evaporation there, and reload them to a hybrid trap made by an optical dipole beam with the quadruple trap. Finally, we lower the overall trap depth to allow dipole evaporation to reach quantum degeneracy.

2.2 Laser cooling and trapping

The first stage of laser cooling is done through the Doppler mechanism, as already described in the last chapter. For our rubidium atoms, the room-temperature vacuum pressure already provides too much background atomic density for loading a bright MOT. Thus, we put our rubidium source on a thermoelectric cooler (TEC) to maintain the source temperature at around 0°C. The role of our regular three-dimensional MOT is to slow down and capture the fast-flying atoms at $\sim$ 200m/s. It is made of six laser beams detuned slightly (by several natural line widths) to the red side of the $|F = 2, m_F = 2\rangle$ to $|F' = 3, m'_F = 3\rangle$ cycling transition, each of them is collimated, circularly polarized, and has a waist of $\sim$1 inch. Because it takes at least $\sim 3 \times 10^4$ photon recoils to slow down an atom from its initial momentum, repump laser beams are added to bring atoms back from $|F = 1\rangle$ to $|F' = 2\rangle$. (And to balance the radiation pressure, we added two of them in counterpropagation.)

The optical molasses provides a damping force $\vec{f} = -k\vec{v}$, which slows down the atoms within tens of microseconds. But these atoms would still be able to escape because there is little spatial trapping force. We then add a pair of anti-Helmholtz coils along the $\mathbf{e}_x$, making a local quadrupole magnetic field

$$\mathbf{B} = B_{xx}\mathbf{e}_x + B_{yy}\mathbf{e}_y + B_{zz}\mathbf{e}_z \tag{2.1}$$

where $B_{xx} = -2B_{yy} = -2B_{zz}$. The atoms are subjected to spatially varying linear Zeeman shift, and as our lasers are red-detuned to the cooling transition, those who are farther from the trap center experience a smaller detuning to the counter-propagating beam, which more likely pushes them back to the trap center. In a MOT simulation, it typically takes tens of milliseconds to trap atoms relatively close to the trap center.

To correctly address the cycling transition, we select our six cooling beams to be circularly polarized σ^+ with respect to the propagation axes. In our experiment, we typically turn on the cooling, repump lasers, and magnetic quadruple field at the same time, which makes a bright MOT that saturates in 3-5 seconds, limited by the background vapor pressure. Our typical magnetic gradient (B_{xx}) is 12 G/cm, and the cooling detunings are -20 MHz $\approx -3.3\Gamma$.

According to people's experience, loading a MOT with ultraviolet light (UV) could potentially help optimize the MOT loading rate and final atom number. This is because atoms tend to coat the glass cell's inner surface, and the UV makes them go off (*LIAD* process) so that they can be captured by the MOT. However, we were not able to observe such improvement, which needs further investigation.

A MOT should in principle be able to lower the captured cloud temperature to below the

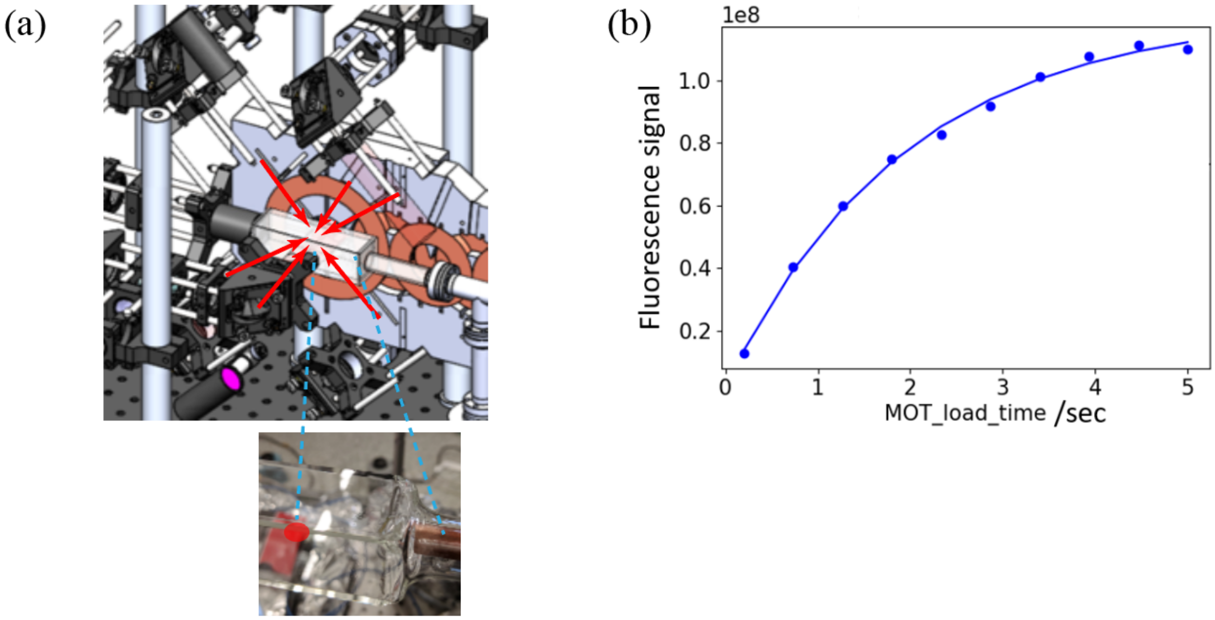

Figure 2.1: The laser cooling scheme at the MOT cell. (a) The six red detuned laser beams are delivered to intersect at the center of this glass cell. Together with the quadruple field generated by the two anti-Helmholtz coils, it can make a bright MOT cloud of $\sim 1\mathrm{mm}$ diameter. Its fluorescence makes it visible to the naked eye. (b) We load the MOT with 1.9 s 1/e saturation time.

Doppler limit, which is defined as

$$T_D = \frac{\hbar\Gamma}{2k_B} \approx 146\ \mu\text{K for } ^{87}\mathrm{Rb}\ \text{D}_2. \tag{2.2}$$

We applied the *release-and-recapture* method [22] with fluorescence imaging to measure the MOT temperature, and observed close to 1 mK. This can be due to the imperfect alignment and beam balances, as well as laser cooling efficiency. We moved on from it since we could run efficient *sub-Doppler cooling*.

Following the MOT stage, we make a *compressed MOT* by raising the quadrupole trap gradient and increasing the cooling laser detunings to match the gradient. The step is hoped to decrease briefly the cloud size (and increase the spatial density), in preparation for the sub-

Doppler cooling, where the atoms will not be spatially trapped. In our experiment, we ramped up the gradient (B_{xx}) from 12 up to 48 G/cm in 26 ms, and meanwhile, increased cooling laser detunings from -20 to -40 MHz.

Now here comes the sub-Doppler cooling, as we simply turn off the magnetic gradients, and ramp up the cooling detunings to -70 MHz in 15 ms. Because of the large detuning, there is rarely Doppler cooling going on, but instead, a well-known mechanism called *polarization gradient cooling* (PGC). This is explained by looking at the electric field made by say, our two counterpropagating **circularly polarized** cooling lasers

$$\begin{aligned}\tilde{\mathbf{E}}(z,t) &= E_0 e^{ikz-i\omega t}\left(\hat{e}_x + i\hat{e}_y\right) + E_0 e^{-ikz-i\omega t}\left(\hat{e}_x - i\hat{e}_y\right) \\ &= 2E_0 e^{-i\omega t}\left[\cos(kz)\hat{e}_x - \sin(kz)\hat{e}_y\right].\end{aligned} \tag{2.3}$$

This is a “polarization helix” standing wave in $\mathbf{e}_z$. It was often mistaken that such a field could lead to the *Sisyphus cooling* mechanism, where atoms undergo repetitive “climbing hill”$\rightarrow$ optical pumped into dark state process. It is worth noticing that can indeed be done in the field like

$$\tilde{\mathbf{E}}(z,t) = E_0 e^{-i\omega t}\left(e^{ikz}\hat{e}_x + e^{-ikz}\hat{e}_y\right) \tag{2.4}$$

which is made by two counterpropagating **linearly polarized** beams. Instead, the cooling mechanism in our case can be elaborated as the following.

Consider an atom moving along the $\mathbf{e}_z$ with velocity v. In the atom frame, the polarization rotates at a frequency $\omega = kv$. So we further choose a rotating frame to keep the polarization vector constant, but this introduces an additional Hamiltonian

$$\delta H = kvF_z. \tag{2.5}$$

This Hamiltonian breaks the degeneracy (at zero magnetic field) between different m_F states because it has the form of a Zeeman shift. Thus, the electric dipole coupling $H_\epsilon = -\mathbf{d} \cdot \tilde{\mathbf{E}}$ indeed creates an offset in F_z

$$\langle F_z \rangle = A\,\frac{\hbar k v}{\Delta_0} \tag{2.6}$$

where Δ_0 is the light shift for the $m_F = 0$ state, and A is a constant factor depending on the F, F'. In our molasses, the cooling lasers are red detuned to D_2, such that Δ_0 is also negative, meaning that there are more atoms in $m_F < 0$ when $v > 0$. These atoms turn out to be more likely to absorb a σ^- photon rather than σ^+ due to the asymmetry in Clebsch-Gordan coefficients, which carries a momentum opposite to v. Likewise, for $v < 0$, a σ^+ photon kicks the atom to backwards. This is a cooling force that theoretically could cool atoms to the *recoil limit*

$$T_r = \frac{\hbar^2 k_r^2}{m k_B} \approx 362 \text{ nK for } ^{87}\mathrm{Rb} \tag{2.7}$$

at zero field, but would be severely compromised at a finite magnetic bias field.

2.3 Magnetic transport

Magnetic traps are a classic way to trap neutral atoms with non-zero magnetic dipole moments. For $^{87}\mathrm{Rb}$ this is the case with the ground state of $5S_{1/2}\,|F=1\rangle$ or $|F=2\rangle$. Due to the sign of Laude g-factors, the trappable state in $F = 2$ are $m_F > 0$, and for $F = 1$ are

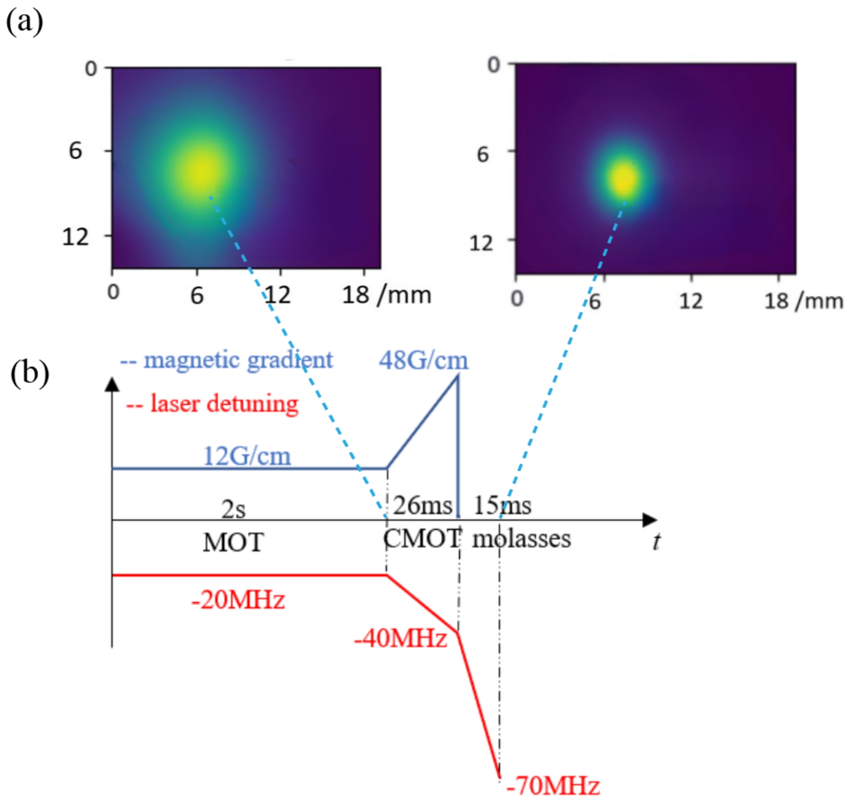

Figure 2.2: (a) In-situ fluorescence images of the atoms after the MOT stage and the molasses stage respectively. The cloud reaches a higher phase space density. (b) The commanded magnetic field gradients and the laser detunings throughout the three laser cooling stages.

$m_F < 0$. In order to achieve a deeper and tighter trap, we chose $|F = 2, m_F = 2\rangle$ state.

Magnetic transport is an idea to adiabatically transfer atoms in real space along a long distance. The atoms are always trapped in a magnetic quadrupole trap, but the trap center is quickly moved by turning on and off a series of pairs of coils. We implemented this technique in our apparatus, by using 11 pairs of transport coils, to transport atoms within 2 seconds over a 40 cm length between the two glass cells.

Before initializing the transport, we need to capture the atoms in a magnetic trap in the MOT cell. But the atoms' internal states are quite random after the PGC, because of the minimized bias field at that stage. To resolve this issue, we add an optical pumping stage to transfer all populations to the $|F = 2, m_F = 2\rangle$ state. This is done by addressing the $|F = 2\rangle$ to $|F' = 2'\rangle$ hyperfine transition with an additional circularly polarized σ^+ beam, in the presence of a small bias field which defines the quantization axis, and a weak repump as well. The transfer typically takes milliseconds.

Following this, we turn on the magnetic trap at 96 G/cm (B_{xx}), and to correct bias of the trap center, we ramp up a bias magnetic field at the same time. Due to the slow response time, the trap actually ramps on within 5-10 ms. With time of flight, we measured the magnetic trapped atom temperature to be $\sim 150\ \mu$K.

The most naive way of thinking of transport is by sequentially ramping off the first pair of coils and ramping on the second. Such a process will greatly change the magnetic trap aspect ratio, and is likely to excite the radial modes in such a trap. In fact, there is a clever way of designing a transporting quadruple trap whose aspect ratio is invariant over space. While the idea was summarized in the paper [23], it requires knowing the exact geometry of the setup and the coils. We tried out best to accommodate such prerequisites by designing two coil holders that hold the transport coils, which themselves are "anchored" via screws to the vacuum setup. For the coils, we ordered flattened ribbon coil foils and wound them in an "assembly line" with explored protocols. However, in practice, this is still not enough to match the pre-calculated geometric model, as it can only transport a tiny portion of atoms to the destination. But that tiny signal saved us, because we have then parameterized the transport geometry and dynamics, and used a feedback optimization algorithm to achieve maximum efficiency. The typical transport efficiency is 85% in terms of atom population, and the whole procedure takes 2 seconds.

2.4 Evaporative cooling

The laser cooling will get atoms down to typical phase space densities of $\sim 10^{-3}$, so all current techniques require an evaporative cooling stage to obtain BECs of large atom numbers (Tiny BECs were obtained, however, via Raman (sideband) cooling not long ago. And there are newer ideas, which are by themselves exciting). In terms of our magnetic trapped cloud after transport, the typical temperature of our Rb atoms is $\sim 100\mu$K, an order of magnitude hotter than laser-cooled atoms in the MOT cell. This is the price we paid for the transport, and is due to two reasons: 1. the "adiabatic heating" from the compressed trap, which is reversible if one decompresses the trap; 2. the non-adiabaticity in the transport process – this happens mostly during the acceleration/deceleration process at the beginning/end of the transport, where the cloud shape (aspect ratio) is forced to change rather quickly.

We follow a two-step evaporation sequence: first RF/microwave forced evaporation, and then dipole evaporation.

2.4.1 RF evaporation stage

Following the transport, we have a tight magnetic trap of 96 G/cm (B_{xx}) in the science glass cell. We make use of the high atom density in this trap for fast thermal equilibrium (with elastic collisions) while evaporating atoms out of the trap. We turn on our RF amplifier, which sends RF magnetic fields to atoms through circuit board antennas near the glass cell, and we chirp down the RF frequency slowly from 11 MHz to 3.5 MHz within 4-6 seconds. During this process, the atoms' internal states Zeeman splittings are spatially dependent, and the RF field resonantly flips the state at a certain radius of the trap. Because only half of the states are trappable, the flipped state would experience a magnetic force that expels it from the trap, which is called forced evaporation. Elastic collisions then help re-establishes a Boltzmann distribution with a lower temperature. We can reach below 2 μK in our experiment.

However, we soon found our RF antennas weren't powerful enough such that the RF Rabi frequency (smaller than $2\pi \times 2$ kHz) was slightly too small for efficient evaporation. This was further confirmed by switching to the microwave from RF. The working principle is the same, only that the microwave addresses more states between $F = 1$ and $F = 2$ manifolds, which complicates the picture. Fortunately, we didn't seem to hit unexpected resonances, and we can shorten the forced evaporation stage to 3 seconds due to the 2x larger Rabi couplings. However, the lowest achievable temperature is almost the same as using RF.

2.4.2 Dipole evaporation stage

The RF or microwave-forced evaporation can cool the atoms to around 2 μK in our setup. As we lowered the "knife edge" frequency, we experienced two obstacles – 1. the power delivered by our RF antenna dropped; 2. atoms in the magnetic trap are expected to find severe “Majorana spin-flip heating”. As such, we completed the final stage of evaporation in an optical dipole trap or a hybrid trap.

The dipole force originates from the conservative part of the light-matter interaction. The simplest two-level system atom would experience a potential when illuminated by a far from resonant laser light with frequency ω [24]

$$U(\vec{r}) = -\frac{3\pi c^2}{2\omega_0^3}\left(\frac{\Gamma}{\omega_0-\omega}+\frac{\Gamma}{\omega_0+\omega}\right)I(\vec{r}) \tag{2.8}$$

where ω_0 is the energy splitting between levels, Γ is the natural linewidth, and $I(\vec{r})$ is the light intensity at $\vec{r}$. Because $\omega_0 - \omega \ll \omega_0 + \omega$, the second term is often ignored and the sign of the potential is determined by the detuning $\Delta = \omega - \omega_0$. For red-detuned light, we have a negative potential (thus attractive), while for blue-detuned light we have a positive (repulsive).

For consideration of planned scientific experiments, we made an elongated dipole beam of 9 W 1064 nm laser incident from the $\mathbf{e}_x$, and provided tight confinement along the gravity $\mathbf{e}_z$ direction. While the dipole beam waist is much smaller than the magnetic trap length, we placed the dipole beam center just 30 μm below the magnetic trap center so as to capture fallen atoms upon evaporation and avoid Majorana losses. We first decompress the magnetic trap to just above the level against gravity (around 15 G/cm for B_{zz}) so that the cloud temperature is lower. The transfer process happens as we turn on the dipole beam to full intensity and further lower the magnetic trap depth. Although the magnetic trap cannot support atoms outside the dipole trap region, it also provides confinement in the $\mathbf{e}_x$ which increases the atom density. Finally, we ramp down the hybrid trap depth by lowering both the magnetic trap and dipole beam intensity, and observe the onset of the BEC transition in the harmonic trap.

2.5 Theory of Bose-Einstein condensates

The statistical mechanics of finite temperature systems made remarkable predictions regarding the statistics of quantum particles. For bosons whose wavefunctions are symmetric upon particle interchange, the condensation to a single quantum state is foreseeable at a finite temperature. This is made transparent by the onset of a singularity in the Bose-Einstein distribution.

2.5.1 Onset of condensation in trapped gas

For a realistic consideration, we look at the Bose gas trapped in a harmonic trap in 3D [25]. The potential is

$$V = \frac{1}{m}(\omega_x^2 x^2 + \omega_y^2 y^2 + \omega_z^2 z^2). \tag{2.9}$$

The single-particle Hamiltonian is exactly solvable and has an energy spectrum

$$\epsilon = (n_x + \frac{1}{2})\omega_x + (n_y + \frac{1}{2})\omega_y + (n_z + \frac{1}{2})\omega_z \tag{2.10}$$

where $n_x, n_y, n_z = 0, 1, 2, ...$ The ground state is marked by $n_x = n_y = n_z = 0$ with wavefunction

$$\psi_0 = (\frac{m\omega_{ho}}{\pi\hbar})^{3/4} \exp\Big\{-\frac{m}{2\hbar}(\omega_x^2 x^2 + \omega_y^2 y^2 + \omega_z^2 z^2)\Big\} \tag{2.11}$$

from which we define

$$\omega_{ho} = (\omega_x \omega_y \omega_z)^{1/3} \tag{2.12}$$

and the oscillator length

$$a_{ho} = (\frac{\hbar}{m\omega_{ho}})^{1/2} \tag{2.13}$$

With a grand canonical ensemble of atoms, at finite temperature T and chemical potential μ, the occupation number is

$$N = \Sigma_{n_x,n_y,n_z} \frac{1}{e^{\beta(\epsilon-\mu)} - 1}. \tag{2.14}$$

Here $\beta = 1/k_B T$ is the inverse temperature. The chemical potential μ is an increasing function of N and a decreasing function of T. Hence, upon increasing the atom number or lowering the temperature, we raise the chemical potential until

$$\mu = \epsilon_{000} = \frac{\hbar}{2}(\omega_x + \omega_y + \omega_z) \tag{2.15}$$

At this point, one finds that the occupation distribution becomes singular at the ground state. It turns out that this is when the bosons begin to condense. There is a macroscopic number of bosons in the ground state, as one further increases the N or lowers the T, but the $\mu = \epsilon_{000}$ does not change.

We define the occupation in the ground state as N_0, and calculate the sum

$$N - N_0 = \Sigma_{n_x,n_y,n_z>0} \frac{1}{e^{\beta(\epsilon-\mu)} - 1}. \tag{2.16}$$

Plug in the energies and replace the sum with an integral (in the thermodynamic limit):

$$N - N_0 = \int_0^\infty \frac{dn_x dn_y dn_z}{e^{\beta\hbar(n_x\omega_x + n_y\omega_y + n_z\omega_z)} - 1}. \tag{2.17}$$

By changing of variable, we derive

$$N - N_0 = \zeta(3)(\frac{k_B T}{\hbar\omega_{ho}})^3 \tag{2.18}$$

where $\zeta(n)$ is the Riemann ζ-function. When $N_0 = 0$,

$$k_B T_c = 0.94\hbar\omega_{ho} N^{1/3} \tag{2.19}$$

is the critical temperature. For $T < T_c$, we have the condensate fraction

$$\frac{N_0}{N} = 1 - (\frac{T}{T_c})^3. \tag{2.20}$$

This is the result for a non-interacting harmonically trapped Bose gas in the thermodynamic limit in 3D. There will be finite size correction, interaction correction, etc. otherwise [25]. With other trap shapes or different dimensions, the result will also be different. For example, for a homogeneous 3D gas (such as that trapped in a box potential), the exponent changes [26]

$$\frac{N_0}{N} = 1 - (\frac{T}{T_c})^{3/2} \tag{2.21}$$

as well as the critical temperature

$$k_B T_c = 0.527 n^{2/3} \frac{2\pi\hbar^2}{m} \tag{2.22}$$

One can rewrite the condensation condition to another form. Let us define the thermal de

Broglie wavelength

$$\lambda_{dB} = \hbar\sqrt{\frac{2\pi}{mk_BT}}. \tag{2.23}$$

Then we find that in the homogeneous case $\lambda_{dB}(T_c) \sim \sqrt{2}n^{-1/3}$ is slightly larger than the average inter-particle spacing. This is when interference dominates over kinetics, and suggests the coherent nature of the Bose-Einstein condensate.

2.5.2 Theory of a pure condensate

The real condensates created in the lab are interacting gases. Let us first consider the description of a pure condensate ($T \ll T_c$). The full many-body Hamiltonian is

$$\hat{H} = \int d\mathbf{r}\hat{\Psi}^{\dagger}(\mathbf{r})\left[-\frac{\hbar^2}{2m}\nabla^2 + V(\mathbf{r})\right]\hat{\Psi}(\mathbf{r}) + \frac{1}{2}\int d\mathbf{r}d\mathbf{r}'\hat{\Psi}^{\dagger}(\mathbf{r})\hat{\Psi}^{\dagger}\left(\mathbf{r}'\right)U\left(\mathbf{r}-\mathbf{r}'\right)\hat{\Psi}\left(\mathbf{r}'\right)\hat{\Psi}(\mathbf{r}). \tag{2.24}$$

where $\hat{\Psi}$ is the bosonic field. For a pure condensate, all the atoms are in the same quantum state, and then they move collectively. Thus we replace the field operator with a collective c-number wavefunction

$$\hat{\Psi}(\mathbf{r}) = \Phi(\mathbf{r}). \tag{2.25}$$

For weakly interacting alkali bosonic atoms at ultracold temperature, the magnetic dipole-dipole interaction is weak, and the three-body recombination process is slow. In this scenario, the collisions are mostly two-body and due to the symmetry, the interaction potential U is summarized in a pseudo-potential (according to the final phase shift) [26]

$$U\left(\mathbf{r}'-\mathbf{r}\right) = g\delta\left(\mathbf{r}'-\mathbf{r}\right). \tag{2.26}$$

This potential is characterized by a single parameter – the interaction strength

$$g = \frac{4\pi\hbar^2 a}{m} \tag{2.27}$$

or the scattering length a.

Finally, we arrive at the equation of motion for the state Φ

$$i\hbar\frac{\partial}{\partial t}\Phi(\mathbf{r},t) = \left(-\frac{\hbar^2\nabla^2}{2m} + V(\mathbf{r}) + g|\Phi(\mathbf{r},t)|^2\right)\Phi(\mathbf{r},t). \tag{2.28}$$

This is named the Gross-Pitaevskii equation (GPE), first written down by Gross [27] and Pitaevskii [28]. This GPE also defines an energy functional

$$E[\Phi] = \int d\mathbf{r}\left[\frac{\hbar^2}{2m}|\nabla\Phi|^2 + V_{\text{ext}}(\mathbf{r})|\Phi|^2 + \frac{g}{2}|\Phi|^4\right] \tag{2.29}$$

which is connected by

$$i\hbar\frac{\partial}{\partial t}\Phi = \frac{\delta E}{\delta\Phi^*}. \tag{2.30}$$

These equations very well approximate the low energy dynamics of the condensate [29]. They and their variants were used extensively to describe the experimental works with the BEC.

There is also a stationary version of GPE, which is derived by naming

$$\Phi(\mathbf{r}) = \psi(\mathbf{r})e^{-i\mu t/\hbar} \tag{2.31}$$

so that the GPE becomes

$$\left(-\frac{\hbar^2\nabla^2}{2m} + V(\mathbf{r}) + g|\psi(\mathbf{r})|^2\right)\psi(\mathbf{r}) = \mu\psi(\mathbf{r}). \tag{2.32}$$

This GPE is often used to find the ground state of the trapped BEC with a chemical potential μ. An analytically simple formula arises when we simply ignore the kinetic energy, which is termed the Thomas-Fermi approximation. On this we have

$$\left(V(\mathbf{r}) + g|\psi(\mathbf{r})|^2\right)\psi(\mathbf{r}) = \mu\psi(\mathbf{r}). \tag{2.33}$$

and the condensate density

$$n(\mathbf{r}) = |\psi(\mathbf{r})|^2 = \frac{\mu - V(\mathbf{r})}{g}. \tag{2.34}$$

2.5.3 Bogoliubov theory – excitations

The interacting BEC is an intrinsically many-body quantum system. But when the interaction is weak, we can apply the well-developed Bogoliubov theory in superconductors, which allows for analytical calculations of the elementary excitations. I'm going to explain the procedure in the language of second quantization.

We consider linearizing the problem [30]

$$\hat{\Psi} = \psi + \delta\hat{\psi} \tag{2.35}$$

and we use the contact interaction pseudo-potential in the original Hamiltonian $U\left(\mathbf{r} - \mathbf{r}'\right) =$

$g\delta(\mathbf{r}-\mathbf{r}')$

$$\hat{H}=\int d\mathbf{r}\hat{\Psi}^{\dagger}(\mathbf{r})\left[-\frac{\hbar^2}{2m}\nabla^2+V(\mathbf{r})\right]\hat{\Psi}(\mathbf{r})+\frac{g}{2}\int d\mathbf{r}\hat{\Psi}^{\dagger}(\mathbf{r})\hat{\Psi}^{\dagger}(\mathbf{r})\,\hat{\Psi}(\mathbf{r})\,\hat{\Psi}(\mathbf{r}). \tag{2.36}$$

We plug it in

$$\begin{aligned}\hat{H}-\mu\hat{N}=&E_0+\int d\mathbf{r}(-\delta\hat{\psi}(\mathbf{r})^{\dagger}\frac{\hbar^2}{2m}\nabla^2\delta\hat{\psi}(\mathbf{r})\\&+\left[V(\mathbf{r})+2g|\psi(\mathbf{r})|^2-\mu\right]\delta\hat{\psi}^{\dagger}(\mathbf{r})\delta\hat{\psi}(\mathbf{r})\\&+\frac{g}{2}\left\{\psi(\mathbf{r})^2\left[\delta\hat{\psi}^{\dagger}(\mathbf{r})\right]^2+\psi^*(\mathbf{r})^2[\delta\hat{\psi}(\mathbf{r})]^2\right\})\\=&\frac{1}{2}\delta\hat{\Psi}^{\dagger}\mathcal{M}\delta\hat{\Psi}\end{aligned} \tag{2.37}$$

where we define

$$\delta\hat{\Psi}=\begin{pmatrix}\delta\hat{\psi}\\ \delta\hat{\psi}^{\dagger}\end{pmatrix} \tag{2.38}$$

and

$$\mathcal{M}= \begin{pmatrix}-\left(\hbar^2/2m\right)\nabla^2+V+2g|\psi|^2-\mu & g\psi^2\\ g\psi^{*2} & -\left(\hbar^2/2m\right)\nabla^2+V+2g|\psi|^2-\mu.\end{pmatrix} \tag{2.39}$$

The eigenmodes can be found by diagonalizing $\mathcal{M}$

$$\mathcal{M}W_i=\epsilon_i\sigma_z W_i \tag{2.40}$$

and find eigenvectors

$$W_i = \begin{pmatrix} u_i \\ \\ -v_i \end{pmatrix}. \tag{2.41}$$

There are two obvious solutions to the linear problem

$$u_1 = v_1 = \psi \text{ and } u_2 = -v_2 = \frac{\partial \psi}{\partial N}. \tag{2.42}$$

We define operators related to these zero energy modes ($\epsilon_1 = \epsilon_2 = 0$)

$$\hat{Q} \equiv \int d\mathbf{r} \psi(\mathbf{r}) \left[\delta\hat{\psi}(\mathbf{r}) + \delta\hat{\psi}^\dagger(\mathbf{r}) \right] \tag{2.43}$$

and

$$\hat{P} \equiv \frac{1}{i} \int d\mathbf{r} \frac{d\psi(\mathbf{r})}{dN} \left[\delta\hat{\psi}(\mathbf{r}) - \delta\hat{\psi}^\dagger(\mathbf{r}) \right] \tag{2.44}$$

Besides those, for higher energies we write

$$\hat{\alpha}_i \equiv \int d\mathbf{r} \left[u_i^*(\mathbf{r}) \delta\hat{\psi}(\mathbf{r}) + v_i(\mathbf{r}) \delta\hat{\psi}^\dagger(\mathbf{r}) \right]. \tag{2.45}$$

Then the Hamiltonian is diagonalized

$$\hat{H} - \mu\hat{N} = \frac{1}{2}\frac{d\mu}{dN}\hat{Q}^2 + \sum_{\epsilon_i > 0} \epsilon_i \left(\hat{\alpha}_i^\dagger \hat{\alpha}_i + 1/2 \right) \tag{2.46}$$

and these are called *Bogoliubov modes* of the condensate.

2.6 Simulations of the condensates

Simulation (numeric experiment) is powerful when exploring the unknown territory of physics, which visualizes physics ideas and points the direction of understanding. We have done extensive simulations on BECs in our lab, both in use for directing new experiments and also for validating collected data and understanding.

2.6.1 GPE simulations: principles

The essence of the GPE simulation is numerically solving the nonlinear differential equation

$$i\hbar\frac{\partial}{\partial t}\Phi(\mathbf{r},t) = \left(-\frac{\hbar^2\nabla^2}{2m} + V(\mathbf{r}) + g|\Phi(\mathbf{r},t)|^2\right)\Phi(\mathbf{r},t). \tag{2.47}$$

It is indeed a well-studied field, and several methods are present differentiated by the way they handle the time and space derivatives. We hereby have applied the “pseudo-spectral” method to handle the spatial derivative, and used proper “time splitting” to handle the time derivative. This can be summarized in the following points (I’ll start with one dimension.)

- We first choose a proper time step and spatial grid which have intervals Δt and Δx, with total grid points N_t, N_x.
- We discretize and vectorize our wavefunction $\Phi(x,t)$ on our spacetime grid.
- In each step Δt of time evolution, we would like to apply the Hamiltonian

$$H = -\frac{\hbar^2\partial_x^2}{2m} + V(x) + g|\Phi(x,t)|^2 \tag{2.48}$$

- Instead of using "finite difference" to approximate the spatial derivative $\partial_x f \sim \Delta f/\Delta x$ (which needs $\sim N_x^2$ matrix elements of memory), we apply the "pseudo-spectral" method. That is

  $$\exp(-i\Delta t\mathcal{T})\Phi(x) = \exp\left(-i\Delta t\frac{\hbar\partial_x^2}{2m}\right)\Phi(x) = \mathcal{F}^{-1}\{\exp\left(-i\Delta t\frac{\hbar k^2}{2m}\right)\mathcal{F}[\Phi](k)\} \tag{2.49}$$

  which again allows vectorizing the kinetic energy matrix $\mathcal{T}$ to $\sim N_x$ elements. Here we note $\mathcal{F}$ as the Fourier transform from x to k, vice versa for $\mathcal{F}^{-1}$.

- However, because $[x, p] = i\hbar$,

  $$\exp(-i\Delta t\mathcal{T})\exp(-i\Delta t\mathcal{V})\Phi(x) \neq \exp(-i\Delta t H)\Phi(x). \tag{2.50}$$

  Here $\mathcal{V} = V(x) + g|\Phi(x,t)|^2$. We want to find proper "trotterization" of the time evolution Δt. There is a standard way to do this

  $$\exp(-i\Delta t\mathcal{V}/2)\exp(-i\Delta t\mathcal{T})\exp(-i\Delta t\mathcal{V}/2)\Phi(x) = \exp\big(-i\Delta t H + \mathcal{O}(\Delta t^2)\big)\Phi(x). \tag{2.51}$$

  We can also get to $\mathcal{O}(\Delta t^3)$ precision if time Δt is split into 5 intervals.

In the said procedure, the space complexity is $\mathcal{O}(N_x)$, and the step-wise time complexity is $\mathcal{O}(N_x \log N_x)$. Moreover, each evolution step that is matrix element-wise multiplication can be parallelized on a GPU. There is also a GPU-accelerated Fast Fourier Transform algorithm. We have implemented this with the Python framework CuPy on an NVIDIA GPU that supports CUDA. On a typical flagship GPU (e.g. GTX 3080) this shortened regular simulation hours by tens of times when running a 2D GPE of interest.

2.6.2 Dimensionless GPE

It is often more convenient to write the GPE in the units that is natural to the problem. In our simulations, we typically choose these:

- Reduced Planck constant $\hbar \to 1$. Atomic mass $m \to 1$.
- Frequencies are rescaled to the harmonic trap frequency $\omega \to \omega/\omega_x$; time is rescaled $t \to t\omega_x$. Energies are rescaled to $E \to E/\hbar/\omega_x$.
- Distances are rescaled to the harmonic trap characteristic length $x \to x/a_0$, where $a_0 = \sqrt{\hbar/m\omega_x}$; momentum is rescaled to $p \to pa_0$.
- Wavefunction is rescaled according to the dimension. In 1D, it is $\Phi \to \Phi a_0^{1/2}$; in 2D, $\Phi \to \Phi a_0$.
- The contact interaction strength g is rescaled according to the dimension. In a 2D trap, it becomes $g = \sqrt{8\pi} a_{3D}/a_z$, where $a_z = \sqrt{\hbar/m\omega_z}$.

This makes our GPE simple

$$i\frac{\partial}{\partial t}\Phi = \left(-\frac{\nabla^2}{2} + \frac{1}{2}x^2 + V_{others} + g|\Phi|^2\right)\Phi. \tag{2.52}$$

In the case where there is only a box trap (or something else), we either set a fictitious "ω_x" or can make a_{3D} our length unit instead. More caution needs to be paid to match the time and length scale of the problem.

2.6.3 Spinor GPE

The spinor GPE is a couple of equations describing a BEC with multiple internal states. Note that these states can be coupled via EM fields, different from real multi-species BECs (such as a Rb, K mixture). An important aspect of spinor BECs is the difference between interspin and intraspin scattering lengths.

We write out the equations for $F = 1$ manifold of ${}^{87}\mathrm{Rb}$,

$$\begin{aligned} \mathrm{i}\hbar\partial_t\Phi_1 =& \left\{-\frac{\hbar^2\nabla^2}{2m} + V + (c_0+c_2)\left[|\Phi_1|^2 + |\Phi_0|^2\right] + (c_0-c_2)\,|\Phi_{-1}|^2\right\}\Phi_1 \\ &+ c_2\Phi_{-1}^*\Phi_0^2, \\ \mathrm{i}\hbar\partial_t\Phi_{-1} =& \left\{-\frac{\hbar^2\nabla^2}{2m} + V + (c_0+c_2)\left[|\Phi_{-1}|^2 + |\Phi_0|^2\right] + (c_0-c_2)\,|\Phi_1|^2\right\}\Phi_{-1} \\ &+ c_2\Phi_1^*\Phi_0^2, \\ \mathrm{i}\hbar\partial_t\Phi_0 =& \left\{-\frac{\hbar^2\nabla^2}{2m} + V + (c_0+c_2)\left[|\Phi_1|^2 + |\Phi_{-1}|^2\right] + c_0\,|\Phi_0|^2\right\}\Phi_0 \\ &+ 2c_2\Phi_0^*\Phi_1\Phi_{-1}. \end{aligned} \tag{2.53}$$

For $m_F = \pm 1$ states the intraspin interaction strength is symmetric

$$g_{1,1} = g_{-1,-1} = c_0 + c_2, \tag{2.54}$$

while the interspin

$$g_{1,-1} = c_0 - c_2. \tag{2.55}$$

Those involve $m_F = 0$ are

$$g_{0,0} = c_0 \quad \text{and} \quad g_{0,1} = g_{0,-1} = c_0 + c_2. \tag{2.56}$$

In the absence of a magnetic field, this system is either in the ferromagnetic phase ($c_2 < 0$) or antiferromagnetic phase ($c_2 > 0$). Our $^{87}\mathrm{Rb}$ atom is the former case.

In many experiments, we can choose to make a "spin-1/2" system by only populating the $m_F = \pm 1$ states and ramping up a bias magnetic field to avoid spin-exchange collisions. We can also couple the two states

$$\begin{aligned} \mathrm{i}\hbar\partial_t\Phi_1 &= \left\{ -\frac{\hbar^2\nabla^2}{2m} + V + (c_0 + c_2)\left|\Phi_1\right|^2 + (c_0 - c_2)\left|\Phi_{-1}\right|^2 \right\} \Phi_1 \\ \mathrm{i}\hbar\partial_t\Phi_{-1} &= \left\{ -\frac{\hbar^2\nabla^2}{2m} + V + (c_0 + c_2)\left|\Phi_{-1}\right|^2 + (c_0 - c_2)\left|\Phi_1\right|^2 \right\} \Phi_{-1}. \end{aligned} \tag{2.57}$$

This pair of equations is symmetric, but depending on the sign of c_2, there are simply two phases: immiscible and miscible phases at zero temperature. For $^{87}\mathrm{Rb}$ condensate, $c_2 < 0$ so the ground state is a slightly immiscible phase, where the two spinors will spontaneously form a domain wall.

In some other experiments, we keep adjacent states $m_F = 1, 0$ which makes it convenient to coherently couple them,

$$\begin{aligned} \mathrm{i}\hbar\partial_t\Phi_1 &= \left\{ -\frac{\hbar^2\nabla^2}{2m} + V + (c_0 + c_2)\left[\left|\Phi_1\right|^2 + \left|\Phi_0\right|^2\right] \right\} \Phi_1 - \frac{\hbar\Omega}{2}\Phi_0^* \\ \mathrm{i}\hbar\partial_t\Phi_0 &= \left\{ -\frac{\hbar^2\nabla^2}{2m} + V + (c_0 + c_2)\left|\Phi_1\right|^2 + c_0\left|\Phi_0\right|^2 \right\} \Phi_0 - \frac{\hbar\Omega^*}{2}\Phi_1^*. \end{aligned} \tag{2.58}$$

These equations support plenty of interesting physics. If $\Omega = \Omega_0$ is induced by RF or microwave coupling and is hence homogeneous in space, it is called a *Rabi coupled condensate*. Otherwise if $\Omega = \Omega_0 \exp(i2\mathbf{k}_r \cdot \mathbf{r})$ induced by a pair of Raman lasers, it is often termed a *spin-orbit coupled condensate*.

2.6.4 Ground states

Ideally, the ground state of the condensate can be found by solving the stationary GPE

$$\left(-\frac{\hbar^2\nabla^2}{2m} + V(\mathbf{r}) + g|\psi(\mathbf{r})|^2\right)\psi(\mathbf{r}) = \mu\psi(\mathbf{r}). \tag{2.59}$$

We developed the *Newton's method* to directly solve this differential equation. But attention needs to be paid as one can easily run into the "higher energy" stable or metastable states, and hence the initial "guess" wavefunction needs to be wisely appointed. This method is more appreciated and robust when applied to finding the "metastable" states on purpose, e.g. the 1D and 2D soliton states, as well as magnetic solitons in the spinor case.

However, the simpler and often more efficient numeric method is called *imaginary time evolution*. In this method, one solves

$$\hbar\frac{\partial}{\partial\tau}\Phi(\mathbf{r},\tau) = \left(-\frac{\hbar^2\nabla^2}{2m} + V(\mathbf{r}) + g|\Phi(\mathbf{r},\tau)|^2\right)\Phi(\mathbf{r},\tau) \tag{2.60}$$

which just replaces $t \to i\tau$. Upon evolution in the imaginary time, the amplitude of each condensate mode j is suppressed by a factor $\propto \exp(-E_j\tau/\hbar)$, such that the ground state with smallest E_0 wins.

To accelerate the convergence, a small rotation is often used $t \to i\tau + t_\epsilon$ to introduce some real “dynamics” into the evolution. This is helpful to get out of “stubborn” steady states, such as states with (spinor) vortices or any other phase windings.

2.6.5 E.g. Interface instability in a spinor mixture

We consider the two-component spinor gas of a $^{87}\mathrm{Rb}$ BEC. As described in section 2.6.3, the ground state of such a binary mixture without any external coherent coupling is determined by the scattering lengths. More specifically, we look at the $|F = 1, m_F = \pm 1\rangle$ states, making an immiscible pair at zero temperature. This ground state is reached by the imaginary time evolution of the spinor GPEs with a tiny gradient force $\partial B_x/\partial x$, effectively acting like a perturbation that breaks the symmetry (Fig. 2.3a).

We are interested in the dynamics at $t > 0$, following a sudden quench of the gradient direction to the opposite. A famous hydrodynamics prediction is – the *Rayleigh-Taylor instability* [31], which says spontaneous patterns will form at the interface. This is reproduced in our dynamics simulations in Fig. 2.3b, where we selected different quench gradients and observed vastly different pattern sizes and growth rates. These scalings are summarized in Fig. 2.3c as a function of the $\partial B_x/\partial x$. These exotic behaviors can be understood within the Bogoliubov picture, which derives the “non-Hermitian” modes with imaginary energies. The length scale and growth rate of the patterns are determined by the “dispersion” of these modes.

Although this RT instability phenomenon was discovered to be universal in many hydrodynamic systems, especially with fluid mixtures of different densities subjected to gravity [31], our ultracold atom system can serve as a unique platform to study it due to our highly controllable tools. For example, we have controls over (effective) interactions, gradient forces, etc. We might even

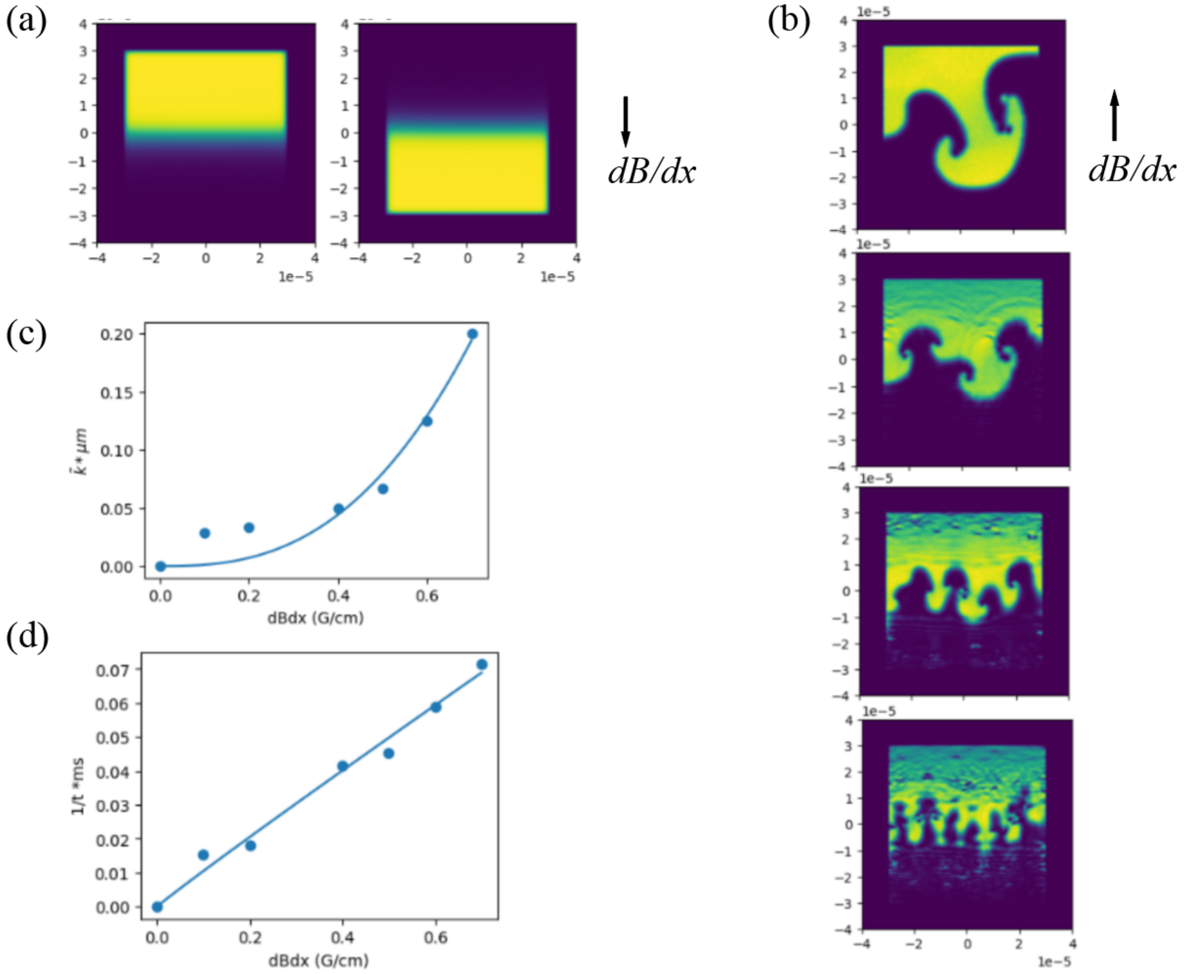

Figure 2.3: Illustration of the interface instability with spinor GPE simulations. (a) The ground state density profiles as are subjected to a tiny gradient of $1\mathrm{mG/cm}$. Shown are population densities of $|m_F = \pm 1\rangle$ states respectively. (b) The snapshots at different gradient forces where $dB/dx = 0.1,\ 0.4,\ 0.6,\ 0.7\ \mathrm{G/cm}$. (c) The scaling of the pattern inverse lengths with gradients. (d) The scaling of the pattern growth rates with gradients.

consider an oscillating gradient force, which alters the “dispersion” of the “instability modes”.

2.6.6 Bogoliubov theory: sound waves

To understand the dynamics on top of the BEC ground state, the natural thing to do is linearize the GPE to derive a perturbative description [30]

$$\Phi(\mathbf{r},t) = \Phi_g + \delta\Phi = \exp\left(-i\mu_g t\right)\left(\Phi_g(\mathbf{r}) + \sum_i u_i(\mathbf{r})\exp(-i\omega_i t) + v_i^*(\mathbf{r})\exp\left(i\omega_i t\right)\right). \quad (2.61)$$

ω_i is the oscillation frequency of each mode, and u_i, v_i the wavefunctions. Plugging it into the GPE and using the stationary GPE solution, we derive the *Bogoiubov-de Gennes equations*

$$\begin{aligned} \hbar\omega_i u_i(\mathbf{r}) &= \left(\hat{H}_0 - \mu + 2gn(\mathbf{r})\right)u_i(\mathbf{r}) + g\left(\Psi_0(\mathbf{r})\right)^2 v_i(\mathbf{r}) \\ -\hbar\omega_i v_i(\mathbf{r}) &= \left(\hat{H}_0 - \mu + 2gn(\mathbf{r})\right)v_i(\mathbf{r}) + g\left(\Psi_0^*(\mathbf{r})\right)^2 u_i(\mathbf{r}). \end{aligned} \quad (2.62)$$

where

$$\hat{H}_0 = -\frac{\hbar^2\nabla^2}{2m} + V(\mathbf{r}). \quad (2.63)$$

For a homogeneous condensate

$$\Phi_0 = \sqrt{n} \text{ and } \mu = gn \quad (2.64)$$

the solutions are

$$u(\mathbf{r}) = ue^{i\mathbf{k}\cdot\mathbf{r}} \text{ and } v(\mathbf{r}) = ve^{i\mathbf{k}\cdot\mathbf{r}} \quad (2.65)$$

with u, v satisfying

$$\begin{aligned} \hbar\omega u &= \frac{\hbar^2 k^2}{2m} u + gn(u+v) \\ -\hbar\omega v &= \frac{\hbar^2 k^2}{2m} v + gn(u+v) \end{aligned} \tag{2.66}$$

such that the dispersion is

$$\omega(\mathbf{k}) = \sqrt{\left(\frac{k^2}{2m}\right)^2 + \frac{k^2}{m} gn}. \tag{2.67}$$

It reduces to

$$\omega(\mathbf{k}) = \sqrt{\frac{gn}{m}} k = ck \tag{2.68}$$

in the long wavelength limit.

2.6.7 E.g. Excitation spectrum of a spinor mixture

As an application, we consider the problem set up in a population-balanced miscible binary mixture. Linking to the real laboratory setup, we consider an "interesting" scenario, we try to tune the miscibility of the pair $|F = 1, m_F = \pm 1\rangle$. The proposed way to engineer a tunable interspin interaction is by tuning the spatial overlap between the two wavepackets.

Suppose our trap geometry is tight in z but loose in xy, and we want to integrate out the z direction to derive a 2D "GPE". To build intuition, we consider the case where our trap in z is quasi-2D, meaning $\omega_z \gg \mu$. We can separate the wavefunction

$$\psi_a^{3D} = \psi_a \frac{e^{-\frac{z^2}{l_z^2}}}{\sqrt{\pi} l_z} \tag{2.69}$$

where l_z is the harmonic oscillator length and then

$$\begin{aligned} H_{\text{int}} &= \int d^2 r dz \frac{g_{3d}}{2} \left|\psi_a\right|^2 \left|\psi_b\right|^2 \frac{e^{-\frac{2z^2}{l_z^2}}}{\pi l_z^2} \\ &= \int d^2 r \frac{1}{\sqrt{2\pi} l_z} \frac{g_{3d}}{2} \left|\psi_a\right|^2 \left|\psi_b\right|^2 . \end{aligned} \tag{2.70}$$

We want

$$H_{\text{int}} \equiv \int d^2 r \frac{g_{2d,+1-1}}{2} \left|\psi_{+1}\right|^2 \left|\psi_{-1}\right|^2 . \tag{2.71}$$

Let us add a magnetic field gradient $B_{zz} = B'$, which pulls apart the two wavepackets in z such that (Fig. 2.4)

$$g_{2d,+1-1} = \frac{g_{3d}}{\sqrt{2\pi} l_z} e^{-\frac{2z_B^2}{l_z^2}} \tag{2.72}$$

is tunable by controlling

$$z_B = \frac{g_F B'}{m\omega^2}. \tag{2.73}$$

How does the change of the interaction strength affect the Bogoliubov modes in the system? The results are shown in Fig. 2.4c, d. In a miscible two-component BEC mixture, there exists two “sound” modes – the density sound and the spin sound. While the former reflects the ripples in the overall density oscillations, the latter has a lower energy cost, because it is made of out-of-phase oscillations of the two components (Fig. 2.4c). As we tune the interspecies interaction, we expect the density sound to not change its speed, but the spin sound is the opposite. As we almost fully minimize the spatial overlap (Fig. 2.4d), the spin sound speed becomes comparable to the density sound speed. Thus we create a new ”knob” for tuning the propagation speed of the spin ripples in our mixture.

This turns out to be useful for many of the experiments without introducing more complicated/nasty

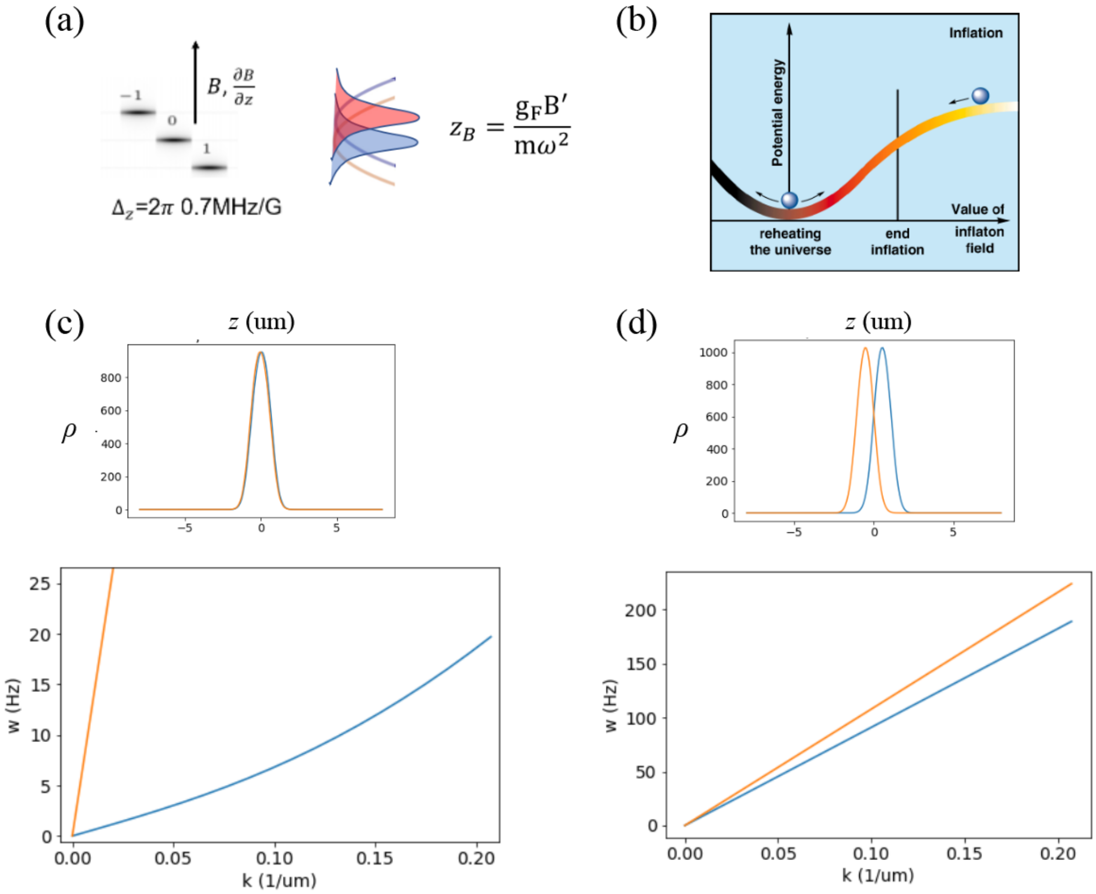

Figure 2.4: The proposed scheme to tune the interspecies interaction strength $g_{+1,-1}$. (a) By applying a magnetic field gradient $B_{zz} = B'$, the spatial distribution of $|m_F = \pm 1\rangle$ states are separated. (b) If one tunes the $g_{+1,-1}$ in real-time, it effectively simulates the dynamics of classical and quantum fields during the expansion/collapse of the universe [2]. (c, d) The numerically solved Bogoliubov modes when the gradient $B_{zz} = 0.5,\ 15\mathrm{G/cm}$. One can read the "spin sound" speed changes by 20x. Simulations were run with parameters $\omega_z = 2\pi \times 500\mathrm{Hz}$, $N = 10^5,\ L_x = L_y = 50\mu\mathrm{m}$ – a box trap in xy, and a harmonic trap in z.

ingredients such as the Feshbach resonance, which often induces loss. In analogy to cosmology/gravitational physics, the Bogoliubov modes (phonons) in the BEC see a effective metric locally

$$\eta_{\mu v}(t,\vec{x}) = \left(\frac{n_0}{mc}\right)^{2/(d-1)} \begin{bmatrix} c^2 - v^2 & \vec{v} \\ \vec{v} & -1 \end{bmatrix} \tag{2.74}$$

determined by the local speed of sound and atom velocity. If one makes a rapidly changing $c(t)$, there is hope that he can emulate the dynamics when the universe is expanding (e.g. Fig. 2.4b) [32, 33]. As another proposed example, the tunable miscibility stabilizes the stripe phase in a spin-orbit coupled BEC [34, 35].

2.7 Coherent manipulations

BECs are known for their simplicity in the ground state, but quantum simulations require ingredients that are not intrinsic in the natural Hamiltonian. To enrich the physics one can study, we often use laser light and RF fields to manipulate the atoms. This section sets the principles of these controls.

2.7.1 $^{87}\mathrm{Rb}$ atoms subjected to lasers

For completeness of the introduction, we lay out the framework that the real $^{87}\mathrm{Rb}$ atoms interact with applied laser fields. For our experimental consideration, we only address close to the transitions in the D_1 and D_2 lines and ignore all other electronic states.

The dipole approximated light atom interaction is [24]

$$\hat{H}(\omega) = -\hat{\alpha}_{\mu\nu}(\omega) E^*_\mu E_\nu \tag{2.75}$$

where Einstein-summation notation is assumed, in which we have defined the atomic polarizability tensor by $\hat{d}_\mu = \hat{\alpha}_{\mu\nu} E_\nu$. Such a second-rank tensor has its irreducible decomposition

$$\begin{aligned}\hat{\alpha}_{\mu\nu}(\omega) =& \hat{\alpha}^{(0)}(\omega)\delta_{\mu\nu} + \hat{\alpha}^{(1)}(\omega) \mathrm{i}\epsilon_{\sigma\mu\nu}\frac{F_\sigma}{F} \\ &+ \hat{\alpha}^{(2)}(\omega)\frac{3}{F(2F-1)}\left[\frac{1}{2}\left(F_\mu F_\nu + F_\nu F_\mu\right) - \frac{1}{3}\mathbf{F}^2\delta_{\mu\nu}\right].\end{aligned} \tag{2.76}$$

The $\hat{\alpha}^{(0)}(\omega), \hat{\alpha}^{(1)}(\omega), \hat{\alpha}^{(2)}(\omega)$ are named the “scalar”, “vector”, and “tensor” polarizibilities because their ways of coupling to the angular momentum $\mathbf{F}$.

In $^{87}\mathrm{Rb}$ atoms related to our experiments, we mainly consider manipulating atoms in the $F = 1$ ground hyperfine state. And thus we apply second-order perturbation theory treatment, for a “virtual process” that brings atoms to the $J' = 1/2$ and $J' = 3/2$ levels and returns to the ground state in $F = 1$, namely the AC Stark shifts (or light shifts) for the ground states. This simplifies our calculation for the scalar polarizability

$$\begin{aligned}\alpha^{(0)}(\omega) =& \sum_{J'} \frac{\left|\langle J\|\mathbf{d}\|J'\rangle\right|^2}{3\hbar}\left(\frac{1}{\omega+\omega_{J'J}} - \frac{1}{\omega-\omega_{J'J}}\right) \\ =& \frac{\left|\left\langle J=\frac{1}{2}\|\mathbf{d}\|\; J'=\frac{1}{2}\right\rangle\right|^2}{3\hbar\delta_1} + \frac{\left|\left\langle J=\frac{1}{2}\|\mathbf{d}\|J'=\frac{3}{2}\right\rangle\right|^2}{3\hbar\delta_2}\end{aligned} \tag{2.77}$$

where the detunings δ_1, δ_2 are defined with respect to the D1 and D2 transitions. Then the scalar light shift due to the Hamiltonian 2.75 is

$$\begin{aligned}\Delta E^{(0)}(\omega) =& -\alpha^{(0)}(F,\omega)|E|^2 \\ =& -\frac{\pi c^2 I}{2}\left[\frac{2\Gamma_{\mathrm{D2}}}{\omega_{\mathrm{D2}}^3}\left(\frac{1}{\omega+\omega_{\mathrm{D2}}}-\frac{1}{\omega-\omega_{\mathrm{D2}}}\right)+\frac{\Gamma_{\mathrm{D1}}}{\omega_{\mathrm{D1}}^3}\left(\frac{1}{\omega+\omega_{\mathrm{D1}}}-\frac{1}{\omega-\omega_{\mathrm{D1}}}\right)\right].\end{aligned} \tag{2.78}$$

This predicts that if we park the laser frequency in between the D1 and D2 transitions, we can "tune out" the scalar light shift. By noting that

$$\left\langle J=\frac{1}{2}\|\mathbf{d}\|J'=\frac{1}{2}\right\rangle = 2.992ea_0, \left\langle J=\frac{1}{2}\|\mathbf{d}\|J'=\frac{3}{2}\right\rangle = 4.227ea_0 \tag{2.79}$$

we derive the "tune out" wavelength to be $\lambda = 789.998$ nm. In our experiment, we frequently used this property by tuning the wavelength of our Raman Ti: sapphire laser.

Likewise, the vector part

$$\begin{aligned}\alpha^{(1)}(\omega) =& \sum_{J'}(-1)^{-2.J-J'-F-I+1}\sqrt{\frac{6F(2F+1)}{F+1}}(2J+1)\frac{\omega\left|\langle J\|\mathbf{d}\|J'\rangle\right|^2}{\hbar\left(\omega_{J'J}^2-\omega^2\right)} \\ & \begin{Bmatrix} 1 & 1 & 1 \\ J & J & J' \end{Bmatrix}\begin{Bmatrix} J & J & 1 \\ F & F & I \end{Bmatrix}\end{aligned} \tag{2.80}$$

with the *Wigner-6j* symbols and

$$\Delta E^{(1)}(\omega) = -\alpha^{(1)}(\omega)\left(iE^* \times E\right)_z \frac{m_F}{F}. \tag{2.81}$$

This part is linear to m_F, and can be used to create an "effective magnetic field" by lasers.

Finally, there is also the tensor part

$$\alpha^{(2)}(\omega) = \sum_{F'}(-1)^{F'+F}\sqrt{\frac{40F(2F+1)(2F-1)}{3(F+1)(2F+3)}} \left\{ \begin{matrix} 1 & 1 & 2 \\ F & F & F' \end{matrix} \right\} \frac{\omega_{F'F}\left|\langle F\|\mathbf{d}\|F'\rangle\right|^2}{\hbar\left(\omega_{F'F}^2 - \omega^2\right)} \tag{2.82}$$

with

$$\Delta E^{(2)}(\omega) = -\alpha^{(2)}(\omega)\frac{3\left|E_z\right|^2 - |E|^2}{2}\frac{3m_F^2 - F(F+1)}{F(2F-1)}. \tag{2.83}$$

This energy shift is only important when the laser is near resonant to either D1 or D2 where it can resolve the hyperfine splittings among Fs and F's. In addition, due to the opposite contributions of Wigner-6j's, the tensor polarizability exactly vanishes at the tune-out wavelength.

2.7.2 Potential engineering

The idea of "arbitrary" potential energy $V(\mathbf{r})$ engineering is one of the key motivations for building this apparatus. Typically, we can utilize atom response to the static magnetic and optical laser fields to "sculpture" the locally varying potentials within the scale of a BEC ($<\sim 100\ \mu$m).

This introduces the "new" tool of the digital-micromirror device (DMD) that can, in real time, change the optical potential engineering for our BEC experiments. Our DMDs have frame refresh rates of 11 KHz and 30 kHz for the *DLP 6500* and *DLP 9500* models. In contrast, our BEC has a chemical potential on the order of $h{\cdot}1$ kHz, which means the DMD patterns can change much faster than the "hydrodynamic" time scale of the BECs. This allows pretty interesting engineering ideas, including spectroscopy and even potential feed-forward. Spatial-wise, the

DMD patterns are projected to the atom plane through a pair of high-resolution microscopes (NA$\sim$0.55). Depending on the wavelengths, it permits micron-scale fine-tuning of the local potentials. This already is only several times the healing length (and almost equal to the spin-healing length of $^{87}\mathrm{Rb}$). In short, these devices allow us to "intervene" in the condensate's evolution.

Besides DMDs, we also use other laser light to make and change traps. For all these potential engineering, the lasers are detuned far from any transitions in the D_1 and D_2 lines, also in the sense that the detuning is much larger than the hyperfine splitting of any state.

2.7.2.1 Scalar potentials

The scalar potentials result from the AC Stark shift as discussed before. For the potential to be spin-independent, the laser detuning has to be much larger than the fine structure splitting between D_1 and D_2. For the DMD potential engineering, we tried a few light sources: a 532 nm fiber laser, a 670 nm lithium tapered amplifer (self-injected), and a 670 nm fiber-coupled diode laser with nm linewidth. According to other groups' experience (e.g. Greiner group theses), we also purchased an LED source but weren't able to collimate the beam due to poor beam quality M_2. In the end, we found that a finite nm scale linewidth helps minimize disorder due to coherent scattering/reflections.

We engineered potentials by uploading binary images to the DMD memory. Since the light source is blue-detuned, we are able to make box traps of homogeneous gas; we can also imprint lattice potentials, create local "dips" or make rotating harmonic traps.

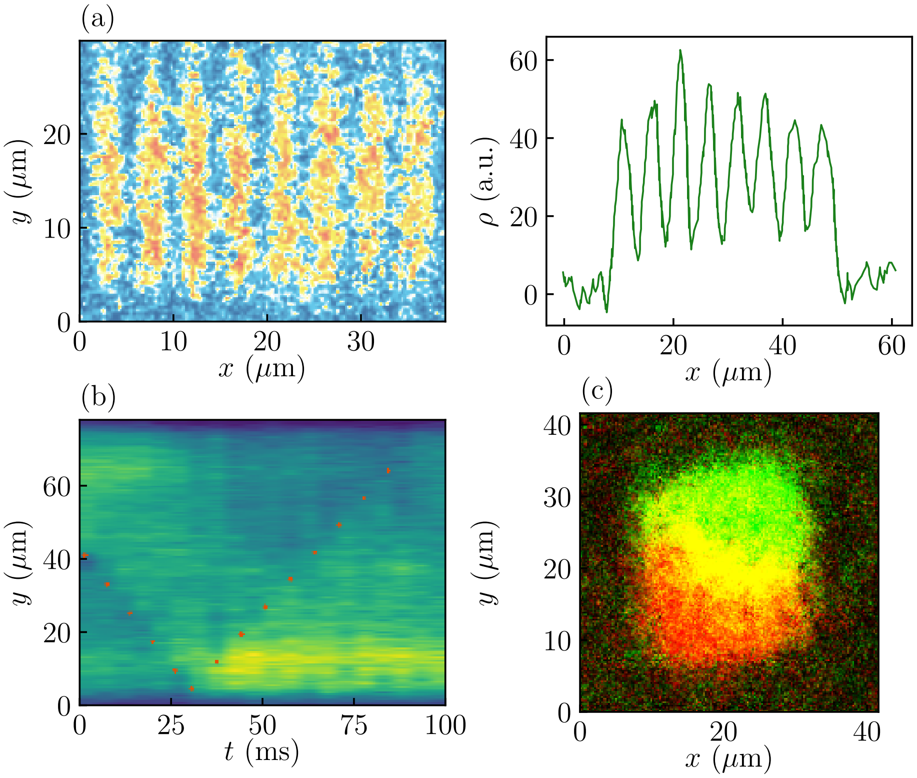

Figure 2.5: Examples of engineered experiments with our DMDs. (a) An optical lattice is directly projected by the DMD that creates density modulation. The single-shot image is captured with partial transfer absorption imaging (PTAI). The cross-section along $\mathbf{e}_y$ allows one to calibrate the lattice depth by reading out the density modulation. (b) A propagating and bouncing phonon wavepacket is created in a box trap. A series of cross-section of density images shows our ability to track the evolution in real-time. (c) An (overall) homogeneous spinor BEC mixture of $|1, \pm 1\rangle$ forms a single domain wall in a box trap. The false colors of red and green stand for the two components' densities.

2.7.2.2 Spin-dependent potentials

We consider two types of spin-dependent potentials – magnetic gradient and vector light shift.

In our apparatus, we can demand full control of magnetic bias fields and gradients, which allows us to apply uniform forces in any direction. This force is described by the Zeeman Hamiltonian

$$H_z = -\sum_s \mu_{Bs} \cdot (\mathbf{B}_0 + \nabla\mathbf{B} \cdot \mathbf{r}) \tag{2.84}$$

which is Taylor expanded at the condensate center of mass, s being the pseudo-spin. This is basically a spin-dependent linear tilt force for the BEC, and we used it to do several experiments.

- We used it to initialize and stabilize spinor BEC domains, such as for the $|F = 1, m_F = \pm 1\rangle$ mixture. A single domain wall is stabilized and perpendicular to the applied gradient force.
- We measured the lowest-order elementary excitation in both the homogeneous and harmonically trapped gas. For the former, we can extract the speed of sound; and for the latter, we measure the harmonic trap frequency along a certain direction.
- We used oscillatory linear potential to obtain spectroscopy of the low-lying modes.

We have also got a DMD which is illuminated by near-resonant light (with detuning comparable to the fine structure splitting), which can project to the atoms and create spin-dependent optical potential via vector light shift. We experimentally created a spin-dependent optical lattice and observed the periodic separation of the spinor wavepackets.

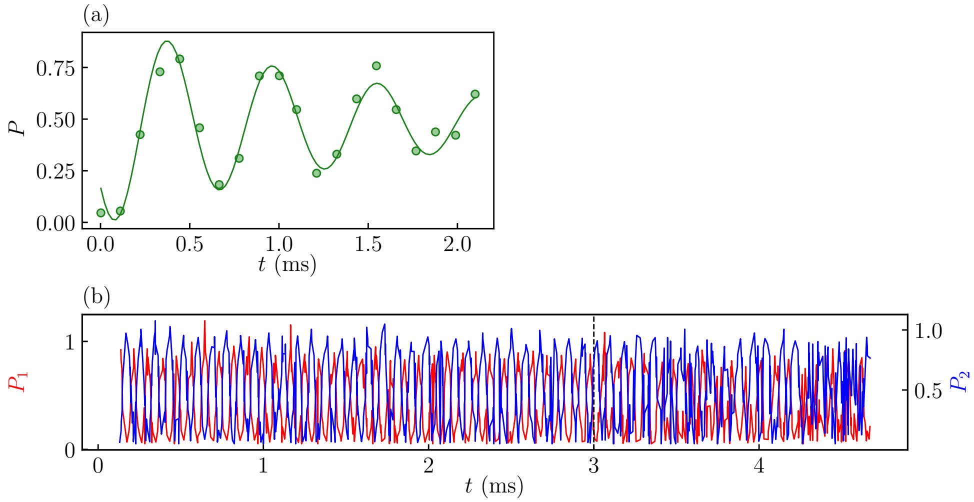

Figure 2.6: (a) RF Rabi oscillations between $|1, 1\rangle$ and $|1, 0\rangle$ at $B_y = 10$ G. (b) Microwave spin Rabi flops have a much longer coherence time, and eventually suffer from some phase noise after 3 ms. Transfer from $|1, 1\rangle$ to $|2, 0\rangle$.

2.7.3 Spinor population transfer

The $^{87}\mathrm{Rb}$ ground states have hyperfine levels $F = 1$ and $F = 2$, in a total of eight states, which we can call the "pseudo-spins states". The energy shifts between these states can be controlled simply via the Zeeman effect. To drive each of the allowed transitions between these states, there are typically three approaches: RF, microwave and Raman. For $^{87}\mathrm{Rb}$ atoms, because the spin exchange collision rates between and within the hyperfine levels are usually much slower compared to the driven coherent processes, we typically consider the latter in a single particle picture (ignoring the interaction). This also means we are lucky to avoid hyperfine relaxation which leads to decoherence and heating.

2.7.4 Raman and Bragg scattering

Raman process is another way of doing internal state transfer. This is made transparent by noticing the vector contribution from the light atom coupling

$$H^{(1)}(\omega) = -\alpha^{(1)}(\omega)\left(i\mathbf{E}^{*} \times \mathbf{E}\right) \cdot \frac{\mathbf{F}}{F}. \tag{2.85}$$

This is similar to a magnetic dipole coupling, and if there is more than one frequency of the laser, it will act like an AC magnetic field. This "field" can be put non-parallel to the quantization axis of $\mathbf{F}$, and thus have an orthogonal contribution that drives internal state transfer just like the RF or microwave fields. In the experiment, this can be done by illuminating the atom with two laser beams detuned against each other by the amount that approximately equals the internal state splitting. But since the atom will pick up a recoil momentum $\hbar(\mathbf{k}_1 - \mathbf{k}_2)$, the two-photon detuning needs to include a recoil energy that corresponds to

$$\Delta(\omega_1 - \omega_2) = E_r = \frac{\hbar(\mathbf{k}_1 - \mathbf{k}_2)^2}{2m}. \tag{2.86}$$

However, one can also put two frequencies into a single beam with any polarization that is not linear, by mixing two RF tones into what drives the AOM. In this way, there won't be any recoil energy and the Raman laser acts exactly like an AC magnetic field depending on its local intensity.

Bragg scattering can be considered as a "simpler" Raman process that only couples external momentum states but doesn't change the spin state. Due to this, the two Bragg beams have a much

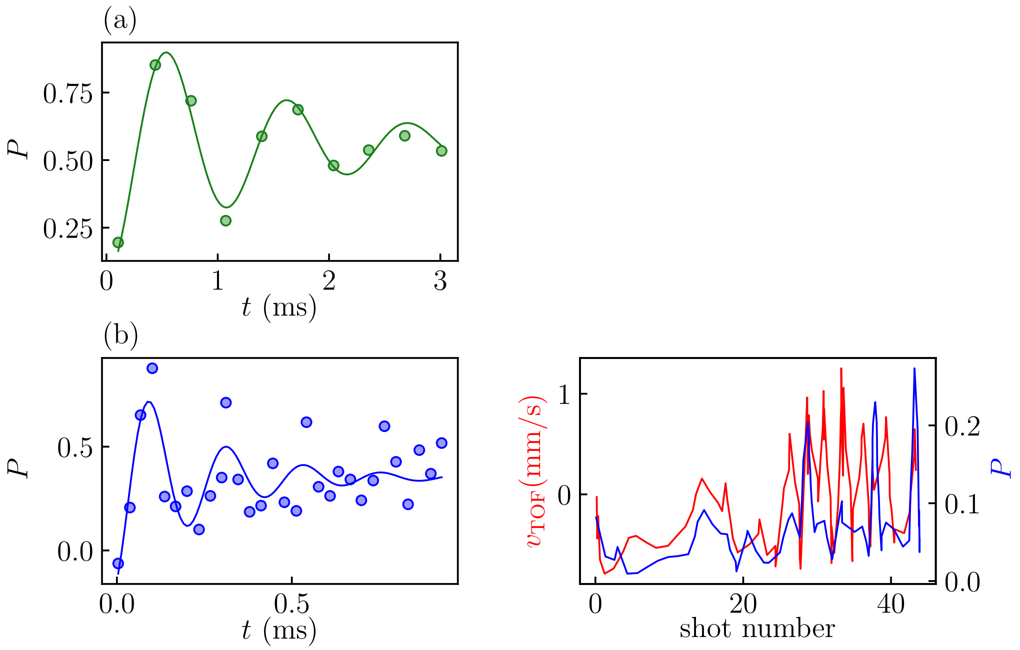

Figure 2.7: (a) Raman transition that simultaneously couples the spin and momentum states between $|F = 1, m_F = 1, p = 0\rangle$ and $|F = 1, m_F = 0, p = 2\hbar k_R\rangle$. (b) Bragg transition Rabi flops between momentum states $|F = 1, m_F = 1, p = 0\rangle$ and $|F = 1, m_F = 1, p = 2\hbar k_R\rangle$. (c) We used the Bragg spectroscopy to measure the velocity of our BEC, and found a strong correlation with the TOF-measured velocity.

smaller frequency difference

$$\omega_1 - \omega_2 = E_r \tag{2.87}$$

that couples momentum states $|p = 0\rangle$ and $|p = \hbar\mathbf{k}_1 - \hbar\mathbf{k}_2\rangle$. Typically the detuning is on the kHz level for Bragg instead of MHz for Raman.

We note that either the Bragg or Raman scattering picture mentioned above is in the single-particle picture. When running such considerations over BECs, and when the momentum transfer is comparable to the inverse healing length, interaction effects must be taken care of. This regime is theoretically and experimentally revisited in Chapter 4.

2.8 Optical lattices

The optical lattice acts as an external potential in the form

$$V(r) = U_0 \sin^2(k_{\mathrm{L}} x) \tag{2.88}$$

with

$$k_L = \pi/a \tag{2.89}$$

where a is the lattice period. These are made by two overlapping laser beams of the same frequency which form a stand-wave of light intensity, and thus dipole potential. First, they can easily address smaller spatial scales compared to the healing length and thus allow engineering single-particle band structures to first order. Second, they provide a platform for quantum simulations of “condensed matter physics”, namely, introducing the Brillouin zones, different geometry/symmetry of the lattice, and when deep enough, increasing the interplay of interaction with the former ingredients.

2.8.1 Single particle picture

The energy band structure can be solved by plugging in the potential in the Schrodinger equation

$$-\frac{\hbar^2}{2m}\frac{\mathrm{d}^2}{\mathrm{d}x^2}\Psi_n(x) + U_0 \sin^2(k_{\mathrm{L}} x)\,\Psi_n(x) = E_n \Psi_n(x). \tag{2.90}$$

This is a classic problem in solid-state physics, and one can prove the Bloch Theorem, which states that any eigenstate of the Hamiltonian has wavefunction

$$\Psi_{n,k} = e^{ikx} u_{n,k}(x) \tag{2.91}$$

where n labels the energy band index, and $\hbar k$ labels the quasi-momentum. It introduces the notion of the "Brillouin zone" since $k \in (-k_L, k_L)$ and the energies are periodic in k and $k + 2k_L$. The wavefunction u_n is a periodic function of x, i.e. $u_n(x + a) = u_n(x)$. To solve such a problem, one plugs it in and gets

$$-\frac{\hbar^2}{2m}\left(-k^2 + 2ik\frac{\mathrm{d}}{\mathrm{d}x} + \frac{\mathrm{d}^2}{\mathrm{d}x^2}\right) u_{n,k}(x) + U_0 \sin^2\left(k_{\mathrm{L}} x\right) u_{n,k}(x) = E_n u_{n,k}(x). \tag{2.92}$$

This differential equation can be numerically solved via finite difference methods. Analytically, perturbative solutions can also be derived via the Fourier method. The energy solutions are shown in Fig. 2.8. The lattice opens up an energy gap at the Brillouin zone boundary, called the *band gap*. Quasimomentum states that are not in the first Brillouin zone are then "folded" back, forming the higher energy bands. As for the eigenstates, the state labeled by quasimomentum k has the decomposition to free particle states

$$|n, k\rangle = \sum_i C_i(n, U_0, k_L) \left|k + 2ik_L\right\rangle \text{ where } k \in \mathcal{Z}. \tag{2.93}$$

We consider ramping on a lattice from zero depth while ignoring the atomic interaction. This involves considering how the states and energies adiabatically evolve into the known free particle case where $V = 0$ and $E = \hbar^2 k^2/2m$. By looking at (2.93), we know we can load

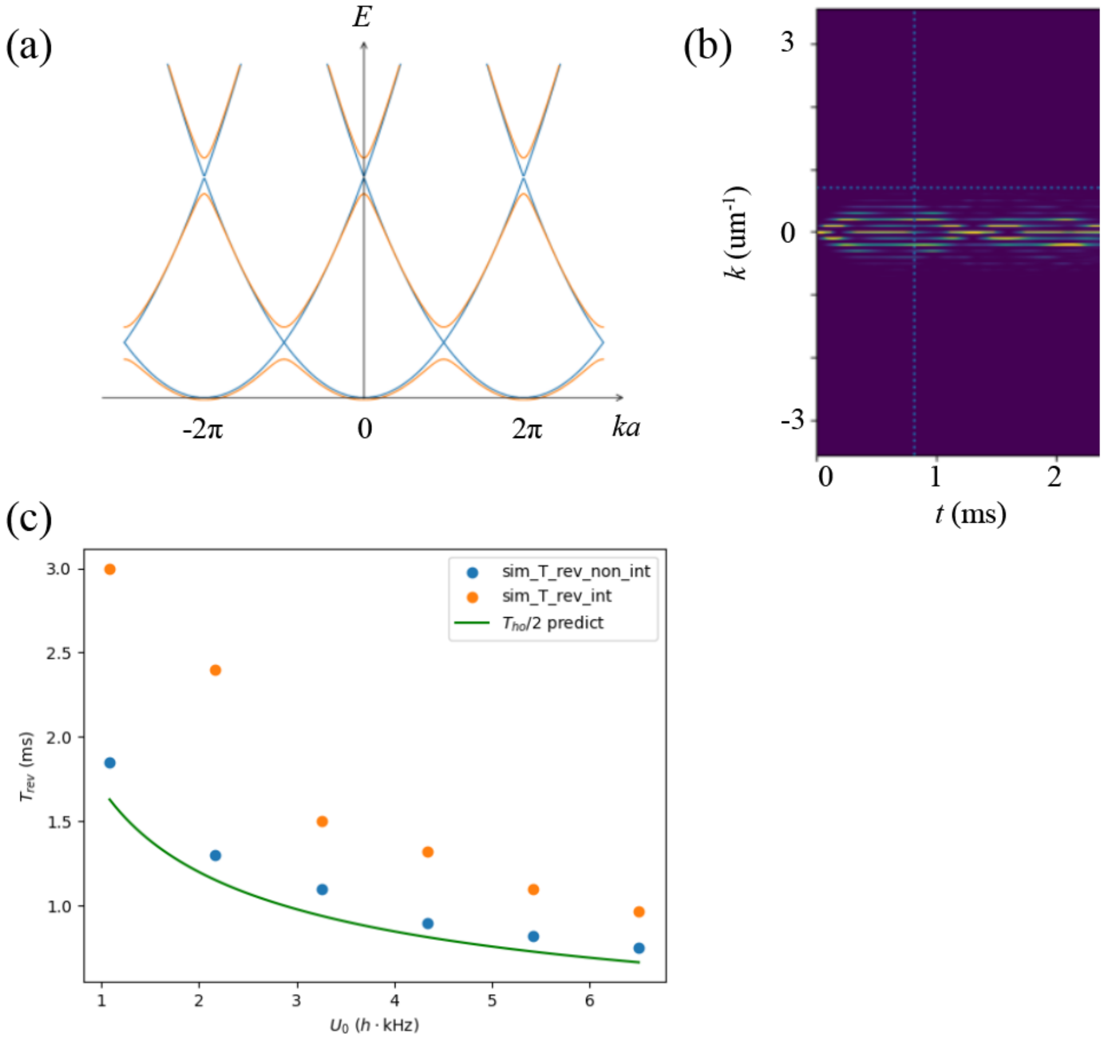

Figure 2.8: Some optical lattice physics. (a) Illustration of the energy dispersion in the extended Brillouin zone picture. (b) The simulated TOF image when one pulses the optical lattice for variable time. One observes two oscillation periods: the shorter oscillation time corresponds to energy scale of lattice depth U_0, whereas the longer revival time T_{rev} corresponds to $\sqrt{U_0 E_R}$. (c) If the lattice depth is comparable to the chemical potential, the prediction of the interacting GPE simulation gives vastly different results from the non-interacting prediction [3].

the BEC state into $|k=0, n=0\rangle$ quasimomentum state from a static free particle state $|p=0\rangle$. With p starting in the first BZ, we can reach a finite quasimomentum state with $|k=p, n=0\rangle$ in the ground band. However, starting from higher BZ, we will likely load atoms to higher bands with $n > 0$. Loading finite momentum states can be easily done with changing the counter-propagating laser beams' relative detuning, which makes a moving lattice respective to the atoms.

Another relevant experiment is by pulsing the lattice, we can also couple atoms to higher momentum states. This is the same principle as introduced in the last section, but perhaps requires a more specific calculation. Since the lattice is static, all the couplings in the "Bragg scattering" sense are off-resonant, i.e. $\epsilon(p=\hbar k_L) \neq \epsilon(p=0)$.

Near the ground band bottom $k=0, n=0$, one can always Taylor expand the dispersion to be

$$E_0 = \frac{\hbar^2 k^2}{2m^*} \tag{2.94}$$

which defines the *effective mass* m^*. Or equivalently

$$\frac{1}{m^*} = \frac{\partial^2 E_0}{\partial k^2}. \tag{2.95}$$

With this, the semi-classical dynamics is captured by

$$\frac{\partial k}{\partial t} = \frac{F}{\hbar} \tag{2.96}$$

with the force F. This force induces periodic motion of atoms in a lattice, named *Bloch oscillations* with frequency

$$\omega_B = \frac{Fa}{\hbar}. \tag{2.97}$$

One also asks what the elementary excitations are like on top of the ground state of a lattice trapped BEC. For a weakly interacting BEC, if the interaction energy is much smaller than the lattice potential energy or the kinetic energy increase led by the lattice density modulation, we regard the interaction as a perturbation. And thus, we run Bogoliubov formalism on the lowest band of the lattice, which is near $k = 0$ free particle-like with $H_0 = \hbar^2 k^2/2m^*$. Hence we simply replace m with m^* everywhere

$$\omega(\mathbf{k}) = \sqrt{\left(\frac{k^2}{2m^*}\right)^2 + \frac{k^2}{m^*} gn}. \tag{2.98}$$

2.8.2 Long period lattice

The characteristic length scale of our BECs is the healing length ξ determined by the mean-field interaction. We can imagine increasing the optical lattice period a such that $a \geq \xi$ while keeping the lattice depth constant, the role of interaction would surpass that of the lattice potential. In the ultimate limit $a \gg \xi$, the system is similar to separately trapped condensates which are “disconnected”, because the tunneling between wells is no longer fast enough to secure long-range coherence.

While that limit is by itself interesting, we first look at the intermediate case where $a \sim \xi$. It is known that such a system might be described by a “tight-binding” model with on-site interaction – the Josephson model. Here we consider GPE

$$i\hbar\partial_t \phi = -\frac{\hbar^2}{2m}\nabla^2\phi + \left(V_{\text{ext}} + g_0|\phi|^2\right)\phi \tag{2.99}$$

where

$$V_{\text{ext}} = U_L \sin^2 k_L z. \tag{2.100}$$

We expand

$$\phi = \sqrt{N} \sum_n \psi_n(t) \phi\left(r - r_n\right) \tag{2.101}$$

and assuming

$$\int dr \phi_n \phi_m^* = \delta_{mn} \tag{2.102}$$

ϕ_ns are the orthonormal basis that is localized at each lattice site, the so-called *Wannier functions*. Plug it in

$$i\hbar \sum_n \partial_t \psi_n(t) \phi\left(r - r_n\right) = -\frac{\hbar^2}{2m} \sum_n \psi_n(t) \nabla^2 \phi\left(r - r_n\right) + +V_{\text{ext}}\, \phi + g_0 |\phi|^2 \phi \tag{2.103}$$

We make use of the orthonormal condition by multiplying both sides by $\phi^*\left(r - r_m\right)$ and integrate over r

$$i\hbar \partial_t \psi_m(t) = -\frac{\hbar^2}{2m} \sum_n \psi_n \int dr \phi_m^* \nabla^2 \phi_n + \int d_r V_{\text{ext}} \sum_n \phi_m^* \phi_n \psi_n + N g_0 \left|\psi_m\right|^2 \psi_m \int dr \left|\phi_m\right|^4 . \tag{2.104}$$

Sorting the terms out

$$\begin{aligned} i\hbar \partial_t \psi_m = & \frac{\hbar^2}{2m} \psi_{m\pm1} \int \nabla \phi_m^* \cdot \nabla \phi_{m\pm1} dr + \frac{\hbar^2}{2m} \psi_m \int dr \left|\nabla \phi_m\right|^2 \\ & + \psi_{m\pm1} \int dr V_{ext} \phi_m^* \phi_{m\pm1} + \psi_m \int dr V_{\text{ext}} \left|\phi_m\right|^2 \\ & + N g_0 \int dr \left|\phi_m\right|^4 \left|\psi_m\right|^2 \psi_m . \end{aligned} \tag{2.105}$$

We can finally define

$$
\begin{aligned}
K &= -\frac{\hbar^2}{2m}\int \nabla\phi_m^* \cdot \nabla\phi_{m+1} dr - \int \phi_m^*\phi_{m+1}V_{\text{ext}}\, dr \\
\mu_m &= \frac{\hbar^2}{2m}\int \left|\nabla\phi_m\right|^2 + V_{\text{ext}}\,\left|\phi_m\right|^2 dr \\
\Lambda &= N g_0 \int \left|\phi_m\right|^4 dr
\end{aligned}
\tag{2.106}
$$

respectively the local tunneling energy, chemical potential, and self-interaction. Our Josephson equation becomes

$$
i\hbar\partial_t\psi_m = -K\left(\psi_{m-1} + \psi_{m+1}\right) + \left(\mu_m + \Lambda\left|\psi_m\right|^2\right)\psi_m. \tag{2.107}
$$

It turns out the on-site interaction term Λ can greatly affect the dynamics of such a system. The most famous example is “self-trapping”, where an initially localized wavepacket cannot fully spread in the lattice even in the absence of any disorder, as the interaction leads to density-dependent “energy splittings” between the otherwise degenerate sites. Within our interest, the term also has an impact when considering a non-Hermitian loss at the boundaries of the lattice. It was found that the atom density would instead localize to the center lattice site as in analogy to the “quantum Zeno effect”.

The superfluid transport in such a long wavelength lattice can still define an effective mass m^* (e.g. using the sound mode dispersion), but it is noticeably different from what is found in eq. (2.95). Instead, one has to resort to the *Leggett formula* to calculate the m^*, which is relabeled by “superfluid density”, as is to be elaborated in Chapter 4.

2.9 Spin-orbit coupling

The spin-orbit coupling (SOC) is ubiquitous in condensed matter physics, which is defined as the interaction between the electron spin and the electron momentum. The origin of that in solids is inversion symmetry breaking, e.g. the ionic electric field coupling to the moving electron's spin (because in the electron moving frame, it is understood as magnetic dipole coupling). Typically the Hamiltonian takes the form of

$$H_{SOC} = \sum_{ij} \alpha_{ij} \sigma_i p_j. \tag{2.108}$$

The usual experimentally relevant cases in 2D are the *Rashba* and *Dresselhaus* SOCs

$$H_{Rashba} = \alpha(\sigma_x p_y - \sigma_y p_x) \tag{2.109}$$

and

$$H_{Dresselhaus} = \alpha(\sigma_x p_x - \sigma_y p_y). \tag{2.110}$$

We should note that it is not to be confused with the atomic SOC which typically refers to the coupling between the outer shell electron's orbital and spin angular momenta $H' = L \cdot S$. However, in an atomic system, there is no intrinsic coupling between an atom's linear momentum p and its internal states. The approach to introducing this coupling is by laser fields.

The technique that was invented in Ian's group is *Raman dressed states*. Two counter-propagating Raman lasers in $\mathbf{e}_x$ of wavelengths λ_R illuminate the atoms, which leads to the interaction Hamiltonian in the rotating wave approximation

$$H_{lab} = \frac{p^2}{2m} + \frac{\hbar}{2}\left(\Omega e^{i2k_r x} \left|\downarrow\right\rangle \left\langle\uparrow\right| + \text{H.c.}\right) + \frac{\hbar\delta}{2}\sigma_z. \tag{2.111}$$

These Raman fields coherently couple two internal states of the atom $|\downarrow\rangle$ and $|\uparrow\rangle$ with Rabi frequency $\Omega_R = \Omega\exp(i2k_r x)$ with a detuning $\delta = \omega_1 - \omega_2 - \omega_{\downarrow\uparrow}$, where $\omega_{\downarrow\uparrow}$ is the energy splitting between the states. We call the Hilbert subspace made by these internal states a pseudo-spin half system.

To see how it relates to the spin-orbit coupling, we run a gauge transformation that is spin-dependent

$$\mathcal{U} = e^{ik_r x\sigma_z} \tag{2.112}$$

so that the rotated Hamiltonian (we call H) becomes (up to a constant offset)

$$H = \mathcal{U}^\dagger H \mathcal{U} = \frac{(p - \hbar k_r\sigma_z)^2}{2m} + \frac{\hbar\Omega}{2}\sigma_x + \frac{\hbar\delta}{2}\sigma_z. \tag{2.113}$$

This is a linear combination of the Rashba and Dresselhaus Hamiltonians (upon rotation), but with a non-commutating σ_x term. This σ_x term is important because otherwise, the Hamiltonian can be gauge transformed back to a trivial $p^2/2m$ Hamiltonian. It is interesting to point out that the gauge transformation is not a physical observable, e.g. the real velocity field will be

$$v = \frac{\langle p\rangle}{m} - \frac{\hbar k_r}{m}\langle\sigma_z\rangle. \tag{2.114}$$

However, the change of the quasi-momentum p (over space and time) is observable. By loading the BEC to the lower band, this Hamiltonian can create artificial gauge fields for nonzero detuning δ, or quantum phases that interplay with the spin-dependent interaction at near zero δ. These will be discussed in detail in Chapter 5.

Chapter 3: High-Resolution Quantum Gas Apparatus

3.1 Introduction

Ultracold quantum gas experiments were great platforms for quantum simulations. But quantum simulations require accurate control of the quantum state, with advancing complexity of the problem of interest. In the context of quantum gases, it means local measurement and manipulation of the quantum state. For Bose-Einstein condensates, the relevant length scale is often defined by the healing length ξ, which is typically sub-micron depending on the interaction strength. In the meanwhile, the relevant time scale is determined by the chemical potential, often on the order of sub-millisecond. It would be preferable to be able to detect the physics process that happens around these scales. Furthermore, it would introduce an interesting interplay with physics if one can change the control parameter of the experiment on the time scale of the dynamics.

This is the big picture why we were building the high-resolution capability into this apparatus. It is the first high numeric aperture (high-NA) attempt in our lab. We used microscope objectives to probe the atoms in situ at high resolution, and also manipulated atom density and spin locally in real time with two digital micromirror devices (DMDs). Nearly all our physics experiments were based on these capabilities, which we spent lots of effort setting up and debugging. In this chapter, I will summarize the experience.

But before that, we spent nearly two years getting our degenerate rubidium gases in the glass cell. Because the two of us built every setup in the experiment, I reckon that I am the suitable person to detail a description of our apparatus just for a memorial purpose and future reference. The narrative would be in the chronological order of the building process.

3.2 Overview

The design of the new basement lab and our new apparatus began before we joined the group. I should acknowledge all the people who contributed to the design. Here is an incomplete list: Ian Spielman, Francisco Salces Carcoba, Ana Valdés Curiel and Chris Billington. Thank you!

The design is shown in Fig. 3.1. We have a very compact vacuum system, which is composed of three major parts – the MOT glass cell (left), the stainless-steel transport section, and the science glass cell (right). The vacuum system is designed to have two stages of differential pumping, with the two ion pumps, and each stage achieves an order of magnitude drop in the vacuum pressure. Thus the vacuum-limited atomic lifetime in the science cell can be as long as a few minutes.

Attached to the first vacuum tee is our source part, where the Rb and K ampules (Fig. 3.2) are sitting and temperature controlled so that the MOT cell has a pressure below 10^{-9} torr. A typical experiment starts with a vapor-fed MOT. The atoms are then further compressed and laser-cooled to below the Doppler limit in a small volume, and transported via turning on and off a series of quadrupole fields in 2 seconds all the way down to the other vapor cell – the science cell. The science glass cell is specially chosen to be anti-reflective at wideband, so will allow

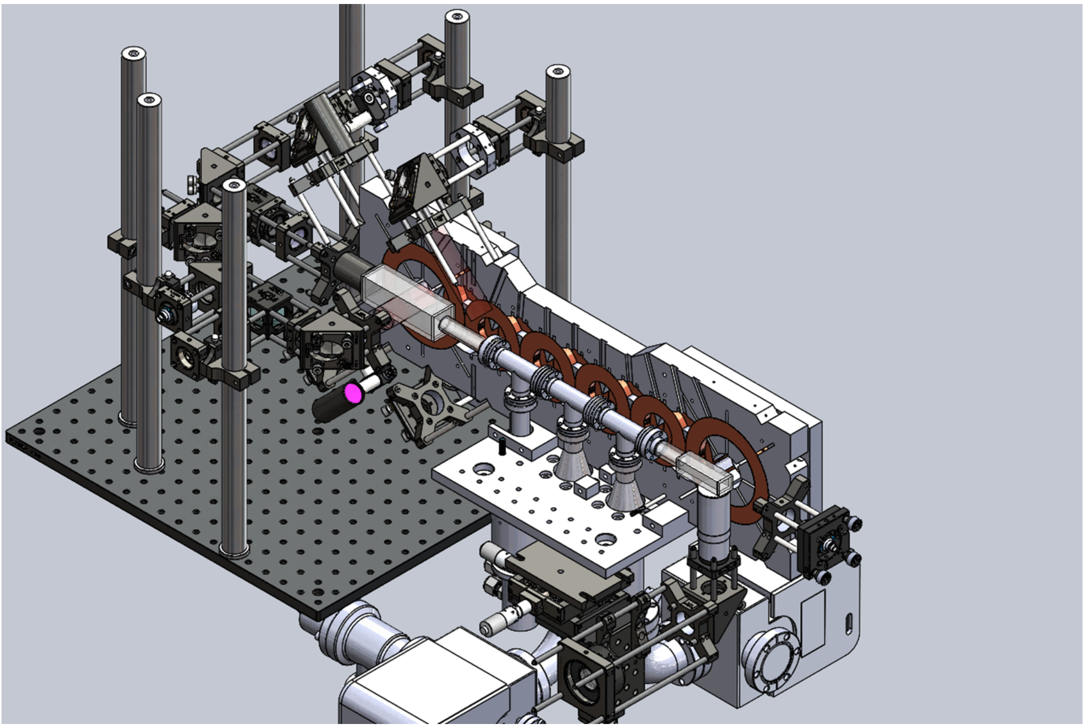

Figure 3.1: The Solidworks sketch of our apparatus design. (Noticeably, I hide the coil holder sketch closer to the reader, to let expose the vacuum design. Also, the microscope setups on the science cell side are partially hidden here. We also made modifications to the mounting design.) Credits to Paco and Ian.

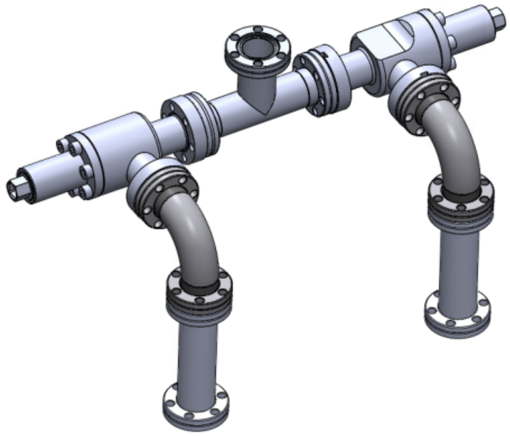

Figure 3.2: The Solidworks assembly of the dual-species sources parts. Credits to Paco, Chris and Ian.

multiple optical trapping and controls, and this is where the real science experiment is taking place.

The whole apparatus should sit on the optical table. But in our design, because we have such a compact vacuum system, all the weight is supported by the stainless-steel holder plate (brown plate in Fig. 3.4). The vacuum system is connected to this plate via the screws on the conical expanders from 1.33in to 2.75in, which further connect to the two ion pumps. We slide the stainless-steel plate in the C-slot on the second layer breadboard (Fig. 3.4 and 3.3)), and there are designed screws to anchor it to the breadboard. We designed three layers for all the optics needed in the future, and the top two layers are supported by the 80/20s. In our final setup, the first (ground) layer is used for the high-NA imaging path and far-off-resonant beam shaping with a DMD. The middle layer is for laser cooling optics, dipole trap, optical lattice, and Raman lasers. The top layer is for sending in the resonant probe light and near-resonant laser beam shaping by another DMD.

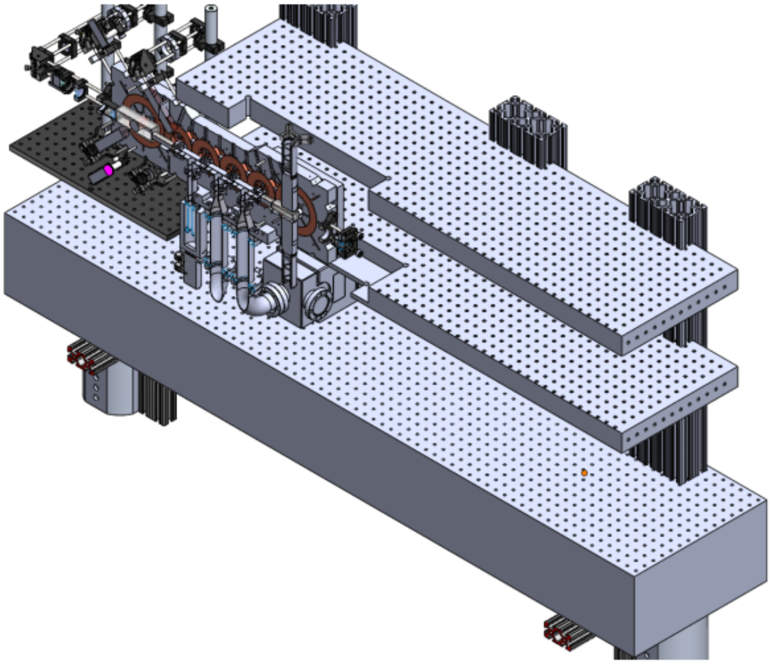

Figure 3.3: The three-layer breadboard design for the vacuum assembly and the accompanying optics. Credits to Paco.

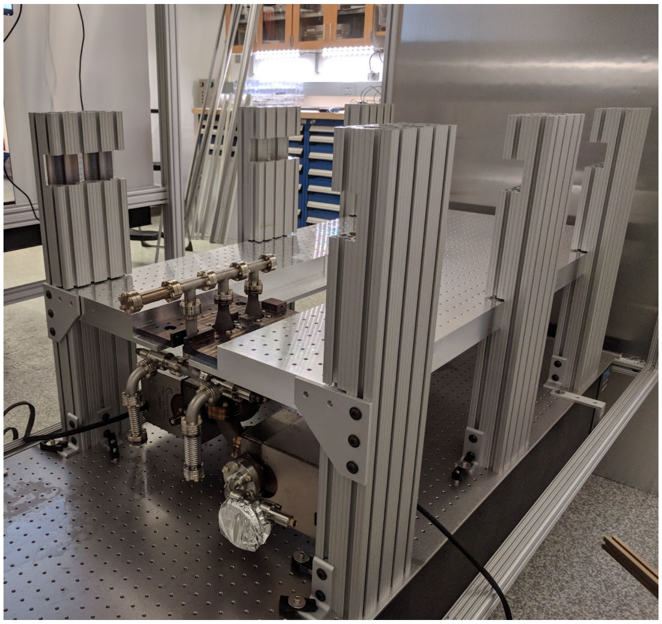

Figure 3.4: The preliminary vacuum assembly sitting on the breadboard.

3.3 Preparation: lab space, coil winding

When we started working in the basement lab B0134 of the Physical Science Complex, we already had three empty optical tables sitting in the lab space. The first few things we did in 2019 were:

1. We designed and built the enclosure for the apparatus optical table. This was for isolation from the environment as good as possible. Basically, we did not want stray laser light to affect our apparatus from the other optical tables. More importantly, we wanted the temperature and humidity stable at where the experiment was happening.

2. We set up the electric cables in the lab to connect the reference voltages (+15, 0, -15V) to the power buses in the lab. These voltages were defined by an external "lab ground" and two Agilent power supplies sitting in the corridor outside the lab.

3. We installed several BNC panels for each of the optical tables and connected them with one another. This was to provide enough signal connectivity for the control and readout signals across the lab.

4. We set up the lab control computer and the Labscript software.

5. We installed the plumbing system in the lab to allow for cooling water flowing to different devices, including the main magnetic transport coils, high power lasers, and atomic sources' temperature controllers.

6. We prepared and pre-baked the vacuum stainless-steel parts separately at high temperature (~ 400 °C) to degas the hydrogen.

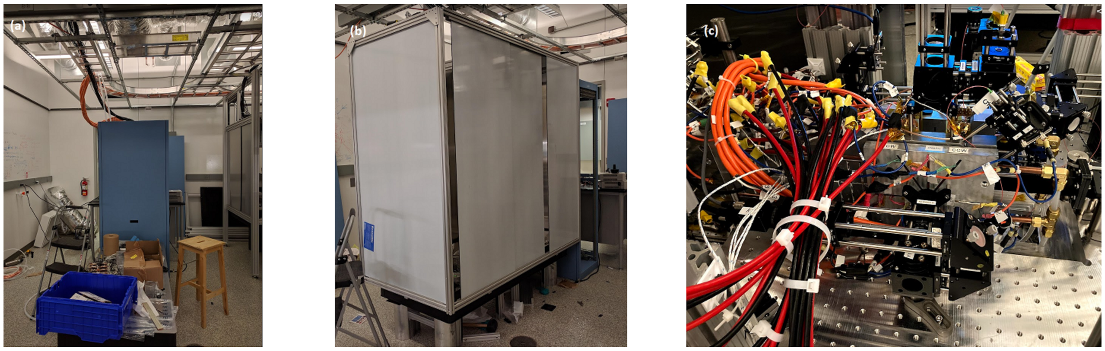

Figure 3.5: The time evolution of the main lab space. (a) 2018-2019: we had the apparatus optical table sitting in the center of the room. Next to it was the supporting electrical bench: holding the transistor banks and power buses. Also, plumbing was set up down there. (b) 2019-2020: we designed and made the enclosure from 80/20 aluminum parts. (c) 2021: we put on the middle layer breadboard and set up the laser cooling and magnetic transport. We also obtained a BEC in the hybrid dipole-magnetic trap.

Since we decided to use magnetic transport between the two glass cells, we had to prepare the magnetic coils to produce the moving fields.

The first step was to count to number of coils needed. We designed the transport with 11 pairs of quadrupole transport coils (including the large quadrupole coils to make static quadrupole traps at both glass cells). Besides those, we needed to control the magnetic bias fields. For the MOT cell we designed eight triangular bias coils to control the B_y and B_z. We had another pair of round coils to provide the B_x. We followed the usual approach to controlling them with three current channels, each of them proportional to B_{y+z}, B_{y-z} and B_z respectively. The wiring scheme will be detailed later.

For the science cell, we aimed for more controls over all the bias fields and gradient fields (first-order derivatives) with high precision and careful calibration. So we designed this ”complex” scheme. We had eight triangular coils, each controlled by a separate current channel, in order to generate all the bias fields and gradients except B_{xx}. B_{xx} is controlled by another eight coils of the racetrack shape with a single current channel.

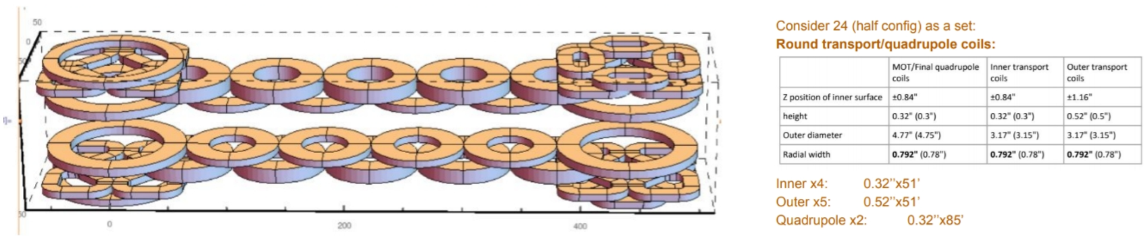

Consider 24 (half config) as a set:

Round transport/quadrupole coils:

	MOT/Final quadrupole coils	Inner transport coils	Outer transport coils
Z position of inner surface	±0.84"	±0.84"	±1.16"
height	0.32" (0.3")	0.32" (0.3")	0.52" (0.5")
Outer diameter	4.77" (4.75")	3.17" (3.15")	3.17" (3.15")
Radial width	**0.792"** (0.78")	**0.792"** (0.78")	**0.792"** (0.78")

Inner x4:	0.32''x51'
Outer x5:	0.52''x51'
Quadrupole x2:	0.32''x85'

Figure 3.6: All the magnetic coils that we needed and wound. The coil configuration design is done by calculating the fields and gradients using the *Radia* plugin in *Mathematica*.

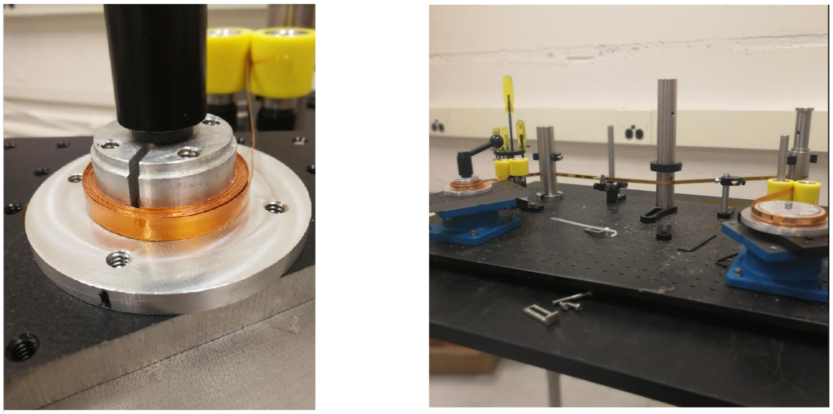

Figure 3.7: The setup in the IPST lab space was designated for coil winding.

The coil winding party started in 2019. The wires we used were quite special – we chose the “Laminax” copper ribbon foils (from Bridgeport) that came in with “Kapton” insulation. These were good for their compactness, and since they were eventually water-cooled via close contact with the aluminum coil holder, the Joule heating was acceptable by design. We cleared a lab space in the IPST building and made this setup for manufacturing these coils (Fig. 3.7). The coil-winding aluminum forms were manufactured at the NIST machine shop for different shapes of coils (round, triangle, and racetrack).

We first wound the ribbon wire by rotating the winding form (shown in Fig. 3.7) up to around 60 turns. Next, we kept the winded wires on the form and added the *Epoxy* glue that fills in the gaps between layers of ribbon wires. We put the form into a vacuum bell, and pumped out

Figure 3.8: Right: Epoxy was used to fill in the gap between layers of the winded coils, which fixed their form as well. They typically took several hours to cure. So before that, we put them in a vacuum bell and extracted any bubbles that were inside the glue. Left: we tried fitting the coils into the aluminum coil holder. Before finally putting them in, we added a layer of thermal paste on the holder to fill in the gaps and allow for better heat conduction.

the air for ~ 1 hour, which allowed the bubbles in the epoxy to be also pumped out. We took the coil out and let it cure at room temperature for half a day. Then we separated the coil from the form (so it was easier if the form was pre-waxed), and added epoxy to the back surface. After the whole process, the coil was taller than the coil holder, and hence was taken to the machine shop and lathed to the correct height. We then cleaned the surfaces, checked any shorts, and insulated the coil with Kapton tapes again.

3.4 Vacuum

The vacuum system of this apparatus is very compact. It is mainly made of stain-steel parts, two glass cells, two ion pumps, and a titanium sublimation (Ti: sub) pump.

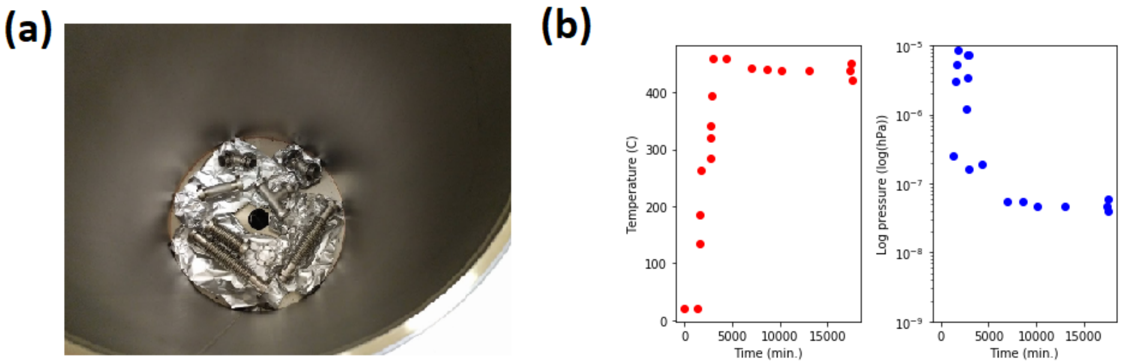

Figure 3.9: The stainless steel parts were pre-baked to over 400°C. In the figure, we have the source parts. We baked twice in 2/2019 and 6/2019.

3.4.1 Vacuum bakeout

The first step to prepare the vacuum was the bakeout. The step is vital to eliminate the gas molecules in the vacuum parts, which can slowly be released into the vacuum from the inner surfaces if we don't do the bakeout. To maximize the efficiency of the breakout, we did it in three steps. First, we baked all stainless steel parts to around 450°C in a separate big cylindrical container connected to a turbo pump. We had the bakeout logged in real-time via an interface with the turbo pump and a bunch of temperature sensors attached to the system. The data was then read by a Python program. This pre-bake process typically took about 12-15 days, after which we didn't observe a significant pressure change (Fig. 3.9b). We did it for the transport and connecting parts to the ion pumps as well.

The second step is the assembly of the vacuum parts except the glass cells. The second bakeout would follow it and include the ion pumps, so the bake temperature would only be slightly above 200°C. We built an aluminum foil tent over the whole vacuum system and wrapped the bulky parts including the ion pumps. We then attached the electric heater tapes around this tent and started baking. Because we had the ion pumps turned on, the aimed pressure could be

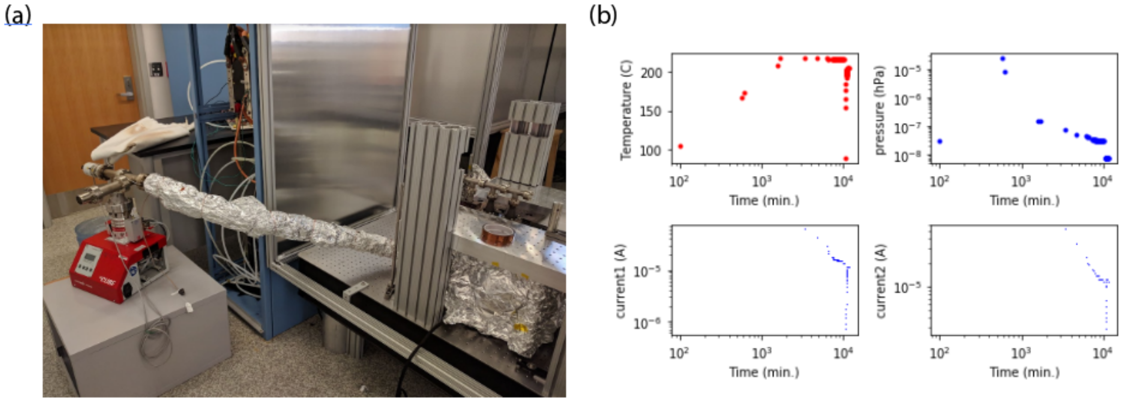

Figure 3.10: We were wrapping the assembled vacuum system with aluminum foils to prepare for the bakeout. We could get three pressure readings at the turbo pump and both ion pumps. The bakeout happened in Oct. 2019.

an orders of magnitude lower.

However, an incident happened after the second bakeout. As we lowered the temperature, we found at some point the pressure reading rose. This was an indication of leakage due to an abrupt change in thermal stress and was severed because our system had two heavy “big nipples” connecting to the ion pumps – the weight was not even. We used the helium leak detection method and identified the leakage spot was indeed the conical part. (We basically tried injecting helium gas into the leakage spot and observed small pressure spikes at the pressure gauge after a short delay. Fig. 3.12.)

After fixing the leak, we moved on to a third bakeout after getting the glass cells assembled. This time the temperature could only go to 150°C because of the glass. And it was our final bakeout, and we aimed at ion gauge currents as low as $\sim 10^{-10}$ A ($\sim 10^{-11}$ mbar) after we adiabatically cooled the system down. Eventually after a long bakeout, we were able to reach it and the ion gauges couldn’t read the low pressure anymore. We then fired the titanium sublimation pump (*Gamma Vacuum* TSP) twice. By running high voltages over the titanium filaments, they

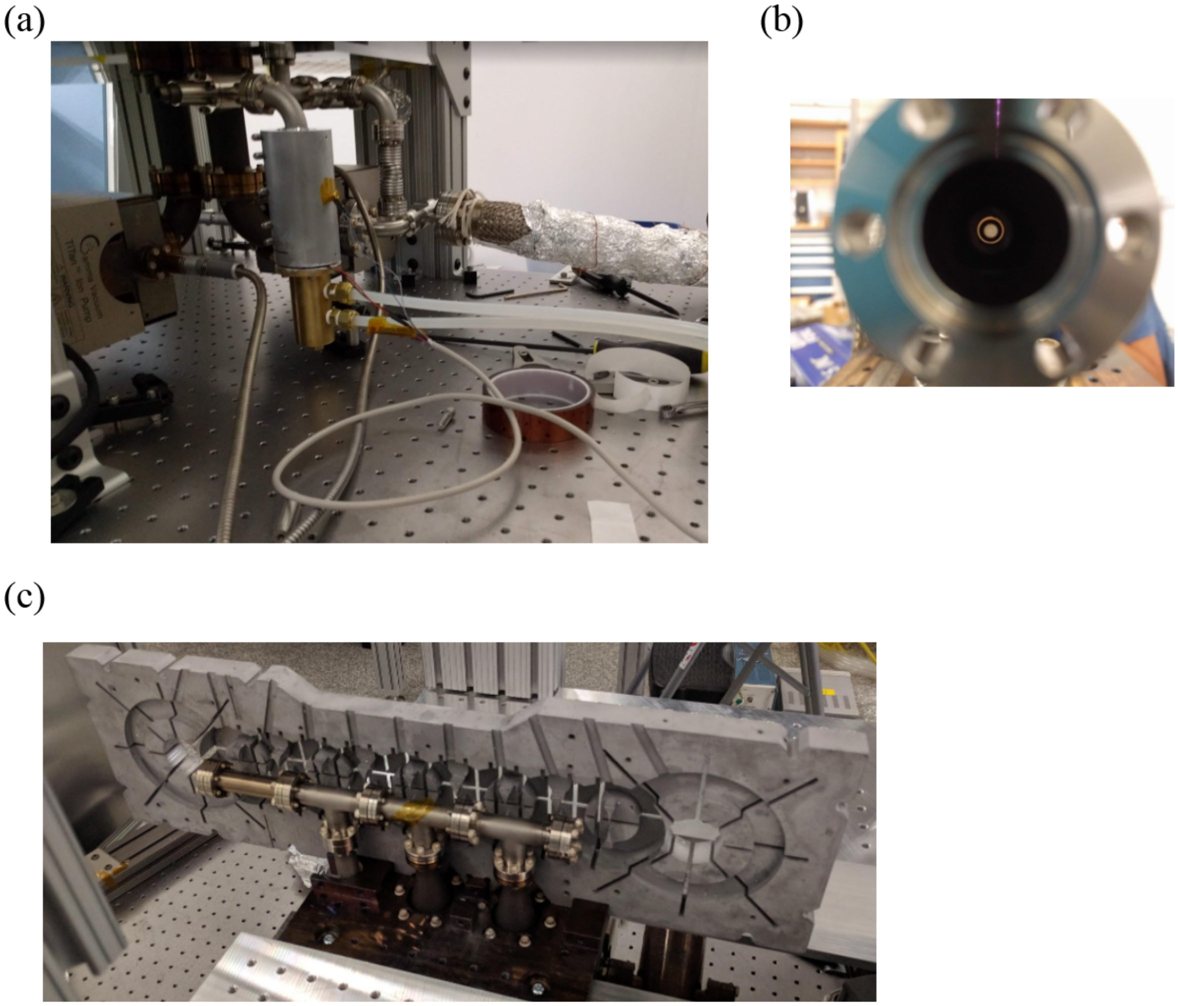

Figure 3.11: (a) The source part. We machined an enclosure that holds the vacuum bellow with an atomic source. The whole enclosure is placed on a TEC with water cooling. We would wrap the whole thing with space blanket. (b) We made sure that we could see light from the other side. (c) The first assembly photo, taken with the coil holder.

were heated to sublimate titanium atoms which are chemically active with remaining hydrogen and water molecules as well as deposit on the stainless steel surface to form an active layer. After these steps, we assured an ultrahigh vacuum (UHV) in our system.

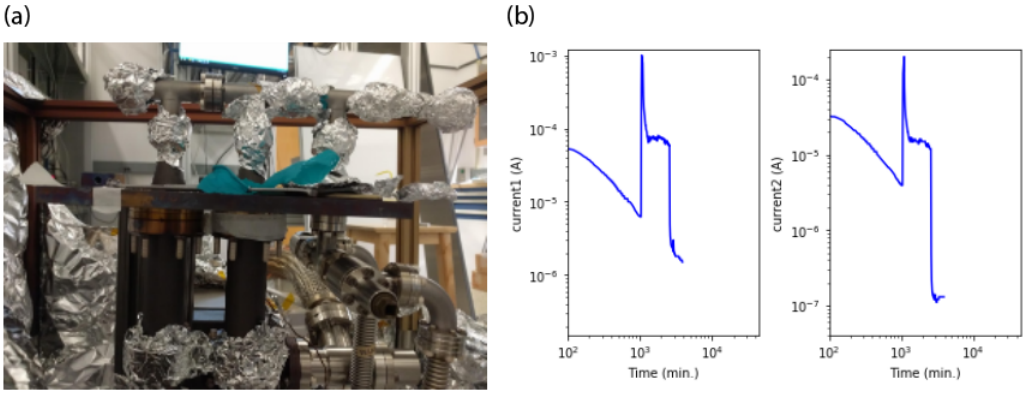

Figure 3.12: (a) Leakage detection as we only exposed one flange at a time, where helium gas flow was produced from a nozzle and injected to vacuum through the leaked flange. (b) Pressure readings from the ion gauge during the third bakeout. The bakeout happened in Jan. 2020.

3.4.2 Vacuum assembly

We assembled the whole vacuum system during and between all the bakeouts. The first part that was assembled (which was done at NIST) was the two ion pumps and Ti:sub pump, which are connected using 2.75" flanges and via the two conical adapters to the upper "transport section" which uses 1.33" flanges. Then we assembled the source part: Rb and K ampules in the vacuum bellows, vacuum tees, elbows, all-metal valves, etc. Next we worked on the transport part: three vacuum tees with two copper differential pumping tubes. We were extra careful about it because we wanted to keep the transport axis in a straight line to not clip the atomic cloud during transport, which is indeed hard because of the small inner diameter of the differential pumping tubes (Fig. 3.11b). In the last step, we mounted the two glass cells.

3.5 MOT cell configuration

We make a 3D MOT directly loaded from the vapor, with six cooling laser beams and two repump beams. We use a 10 meter long fiber multiplexer (*Evanscent Optics*) with two input ports

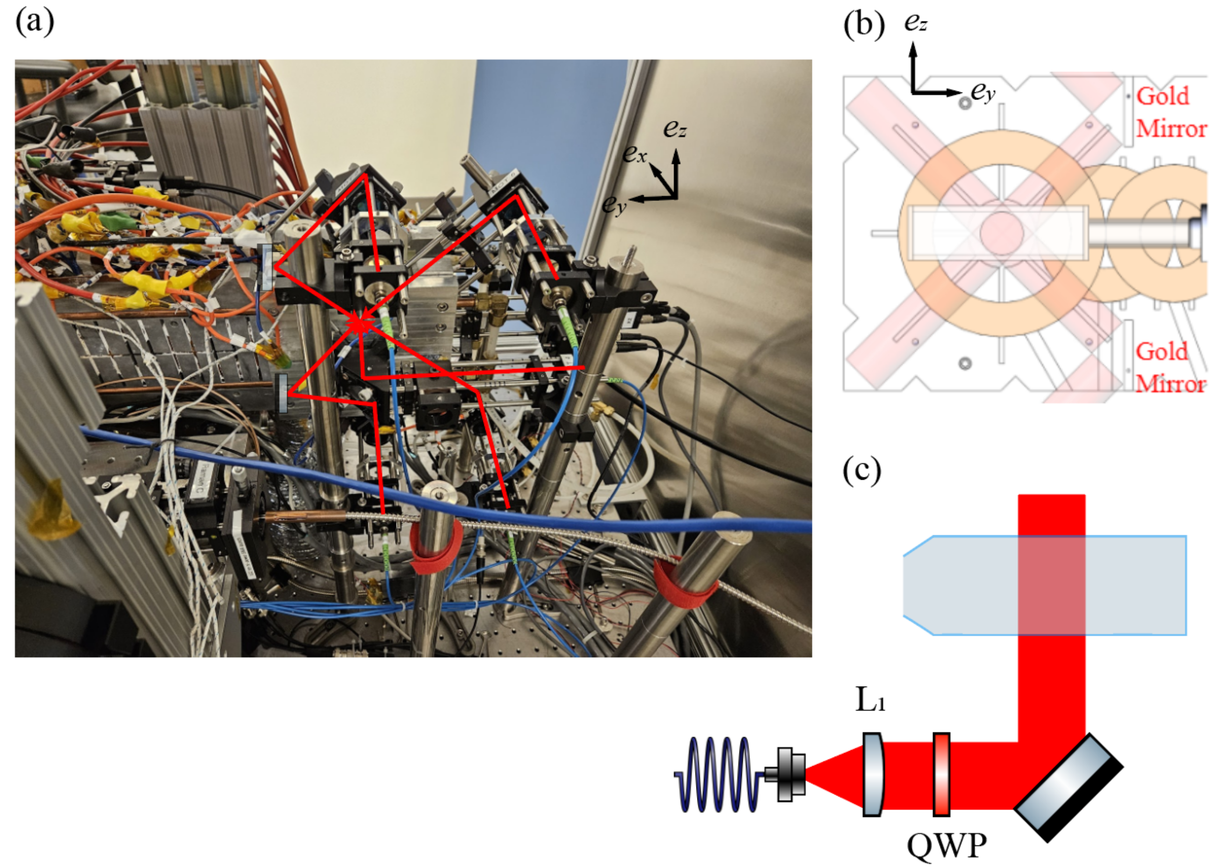

Figure 3.13: MOT optics scheme. (a) Lab image of the MOT optics. Red lines/arrows mark the cooling laser propagation direction. (b) Drawing of the MOT cell and related optics in $\mathbf{e}_y - \mathbf{e}_z$. (c) Beam shaping of each single MOT beam which generates a 1 in circularly polarized collimated beam. $f_{L1} = 50$ mm.

and six output ports. The cooling light is coupled to input 1 and equally distributed into the six fiber outputs. The repump light is coupled to input 2 and distributed into two output ports, which counter-propagate by design. Each of the outputs is engineered to generate a 1 in MOT beam at the glass cell center. Because this fiber multiplexer has a built-in polarizer, we don't worry about the MOT beam polarization drift, which only translates to power drift. These beams illuminate the glass cell from $\mathbf{e}_x$, $\mathbf{e}_y + \mathbf{e}_z$, and $\mathbf{e}_y - \mathbf{e}_z$. There is another optical pumping beam that goes in from $-\mathbf{e}_x$.

For laser cooling, our experimental sequence has five stages: MOT, compressed MOT, molasses, optical pumping and magnetic trap. We lock our cooling laser (Toptica DL Pro) to another master laser ~ 1 GHz away (to the red) using a fast photodiode (EOT GaAs ET-4000AF) and phase-locked loop circuit (ADF4007) that compares the beatnote frequency with an external local oscillator (Novatech 409B). Since we need different frequencies for the cooling beams at different stages, we jump or ramp the local oscillator frequency to tune the cooling laser frequency which has a ~ 1 ms response time for jumps within ~ 300 MHz. Similarly, the repump laser is ~ 5.5 GHz away (to the blue) beat-note-locked to the master laser.

The magnetic quadruple field needed for the MOT is generated by a pair of anti-Helmholtz coils. These coils are driven by "home built" transistor banks for large currents up to 150 A (but the MOT coils are limited by the coil resistance so the maximum is around 50 A for a 15 V supply). These transistors are further controlled by a gate voltage generated from a PI servo board, which uses an op-amp circuit to compare and feedback to the current running through the coil (measured by Hall sensors), with an external voltage setpoint (set by an NI analog channel). By tuning the PIs of the feedback loop we achieve a 20 kHz bandwidth, well above that determined by the magnetic inductance of the coils.

3.6 Magnetic transport

We have 11 pairs of magnetic transport coils, which are used to generate continuous deformation and translation of a magnetic quadruple trap from the MOT cell to the science cell [36, 37]. We start by asking a mathematical question: at a certain time t, given the requirement of magnetic field gradient $B_{xx} = -(B_{zz} + B_{yy})$, the quadruple center position x, and the trap aspect ratio $\beta = B_{zz}/B_{yy}$, can we solve the "inverse problem" to calculate the electric currents flowing in nearby transport coils? The answer is certainly a yes, and we only need to calculate three adjacent coils that run currents (I_{j-1}, I_j, I_{j+1}). Next, we parameterize the atom trajectory $x(t)$ as a function of time. We define the trajectory into several piecewise functions, each one having a given (dt, dv), where dt and dv are the time interval and constant coast velocity during this interval. This is because we expect the adiabaticity conditions to vary in space, e.g. due to differences in the coils/environment, and at the beginning and end of the transport. In this way, however, the velocity is discontinuous between the pieces which might also contribute to nonadiabaticity. To resolve that, we insert an "acceleration" period at the beginning of each piece, which connects the velocity between the previous and the current pieces. This acceleration is chosen to be a quintic polynomial of time, as we solve the coefficients under constraints of given $(x_0, x_1, v_0, v_1, a_0 = 0, a_1 = 0)$. Besides all that, at the beginning and end of the transport, we have to decrease the number of active pairs of coils from three to one, which will include more parameters on, e.g., when to switch between these stages.

Finally, we have a well-parameterized transport trajectory, but question is whether we trust that the physical geometry reflects the magnetic field calculation from the design. Hence, we add more parameters based on errors in the numbers of turns, geometric sizes and spacings of these coils. For our setup, it gives us 35-45 parameters in total, but many of them are correlated. It is generally a hard problem for humans to optimize over correlated parameters, but machines are good at that. We use the open-source Python package *MLOOP*, which relies on built-in kernels such as the gaussian process or neural network of *sklearn*. The feedback results are summarized in Fig., which the optimizer found after ~ 1500 experimental shots in two days, and it transports the atoms from cell to cell with an $> 80\%$ number efficiency in 2 s.

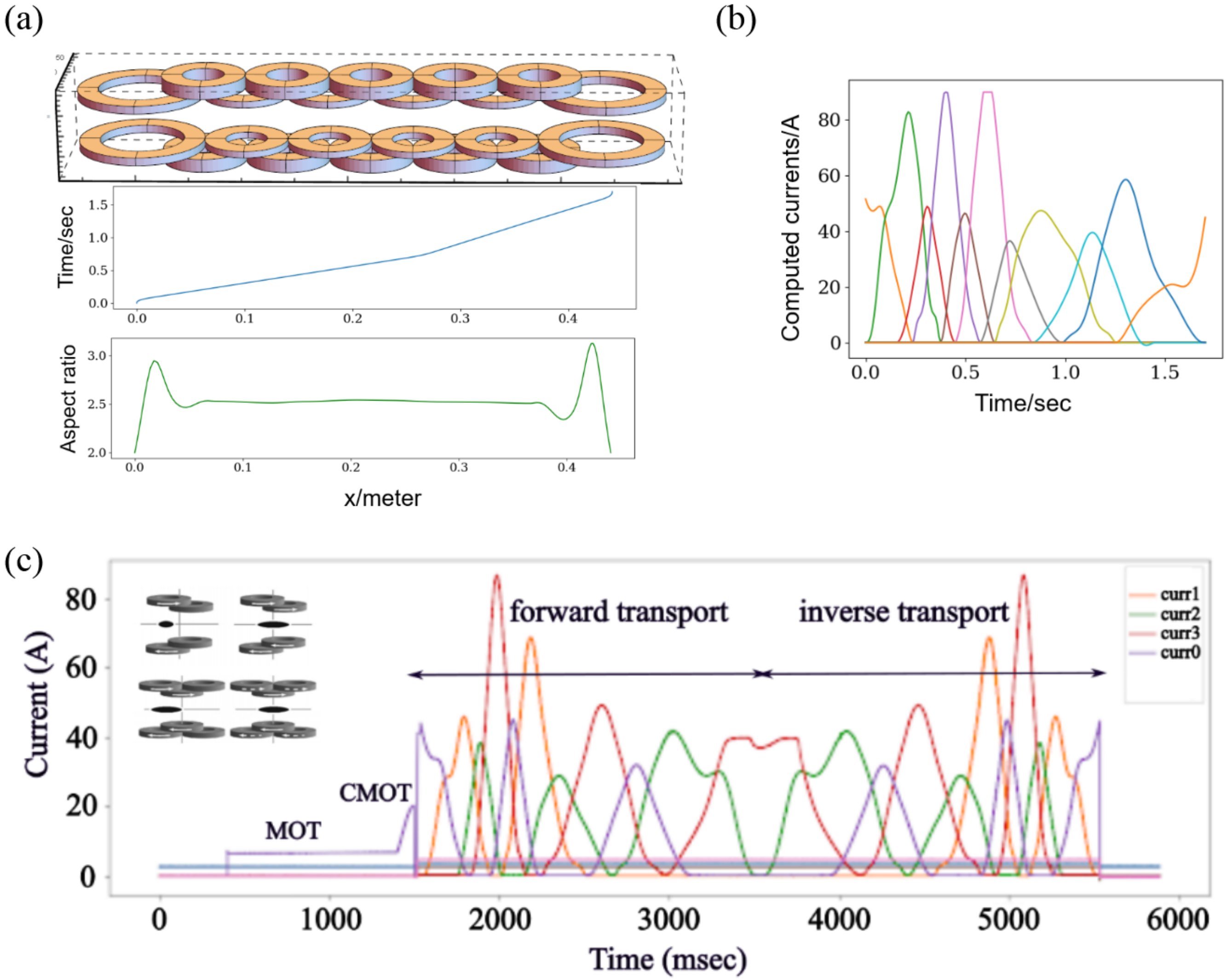

Figure 3.14: (a) The geometry of the transport coils. The optimized atom trajectory and the aspect ratio variation. (b) The corresponding electric currents on different pairs of coils as a function of transport time. (c) The experimentally measured currents during the laser cooling and transport stages. To measure the transport efficiency, we made a round trip.

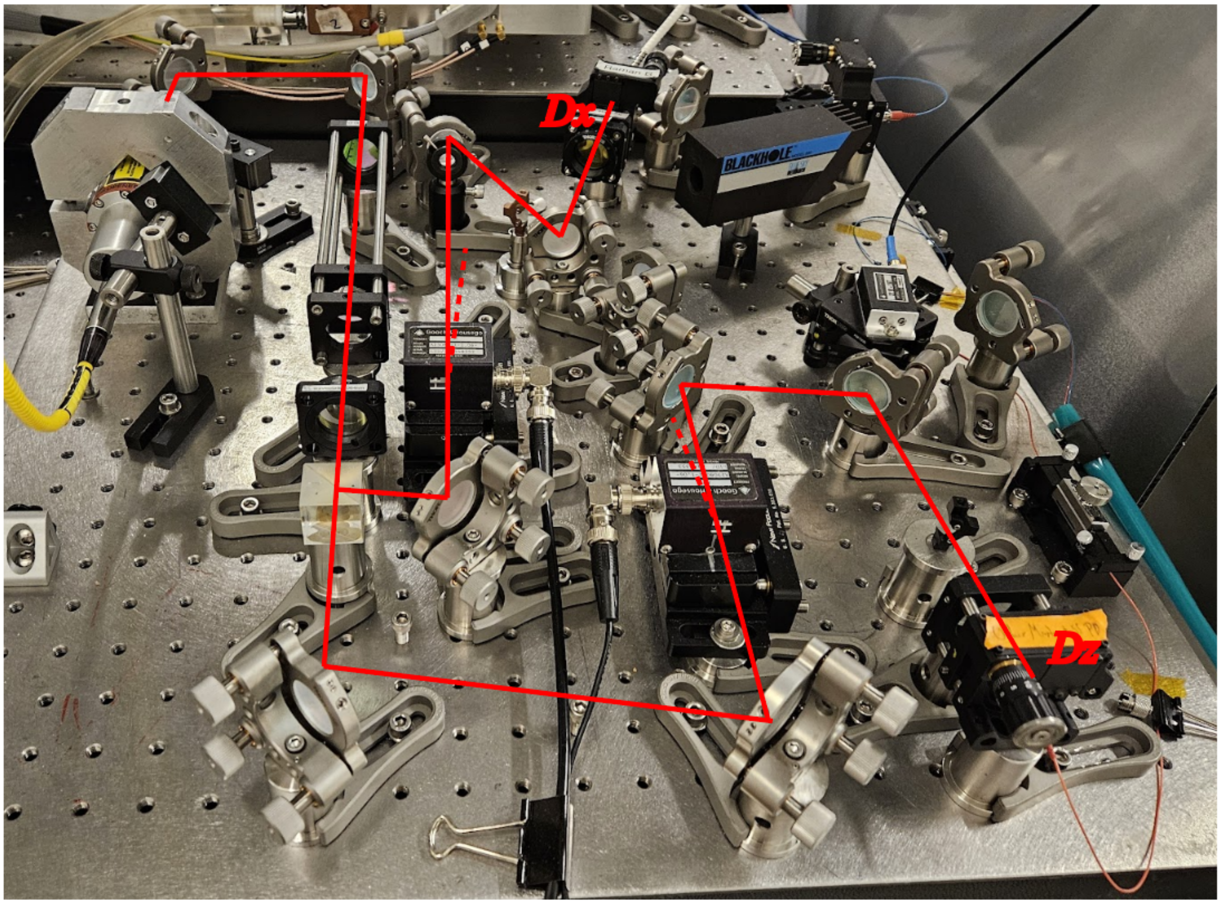

Figure 3.15: The breadboard that produced the two IR dipole beams. The beams D_x, D_z are sent to the horizontal and vertical dipole beams to make a crossed dipole trap.

3.7 Evaporative cooling

3.7.1 Dipole evaporation

We sent in a dipole beam from the lab e_x direction, with a largely elongated aspect ratio. The atoms will be attracted to the dipole beam region when transferred from a magnetic trap. The dipole beam is an IR beam ($\lambda = 1064$ nm, up to 10 W) delivered by a photonic crystal fiber (which is designed to deliver high powers). The beam is measured to have a beam waist of (w_x, w_z)=(120,17)μm, and is engineered by a telescope system shown in Fig. 3.16. Due to power loss at the optics along the beam path, the final delivered power is $\lesssim 8$ W.

The beam comes from a 50 W IPG YLR-50-1064-LP single-mode laser with 1 nm spectrum bandwidth, which was deliberately chosen to avoid unwanted optical lattices led by reflections from the glass cell window. (A 1% power reflection from an 8 W beam can create $\sim E_r$ depth of lattice, partly due to the small glass cell size! We used to have a single-frequency IR laser that created lattices along $\mathbf{e}_z$ and $\mathbf{e}_x$. The $\mathbf{e}_z$ lattice was even able to hold atoms against gravity for several Bloch oscillation periods, whereas the $\mathbf{e}_x$ lattice leads to severe damping when trying transport experiments.) The laser output is magnified in size from a telescope, and then distributed via the PBS to two paths for two dipole beams which can create a crossed dipole trap. The two beams are generated from opposite orders of two AOMs, and thus differ by $80 \times 2 = 160$ MHz in frequency (Fig. 3.15).

Both dipole beams have optical power servos after the fibers, which can reach ~ 10 μs rising time. We snap on the dipole beam power and slowly ramp down to get to the final trap depth for dipole evaporation.

3.8 Bose-Einstein condensates

3.8.1 Time of flight

The time of flight (TOF) technique was the first measurement performed on BECs once they were generated in the labs. It is done by snapping off any trapping potential and letting the atomic cloud freely expand while it falls due to gravity. An absorption image is then taken to calculate the optical depth. For uncondensed thermal atoms, free expansion is ballistic, so the

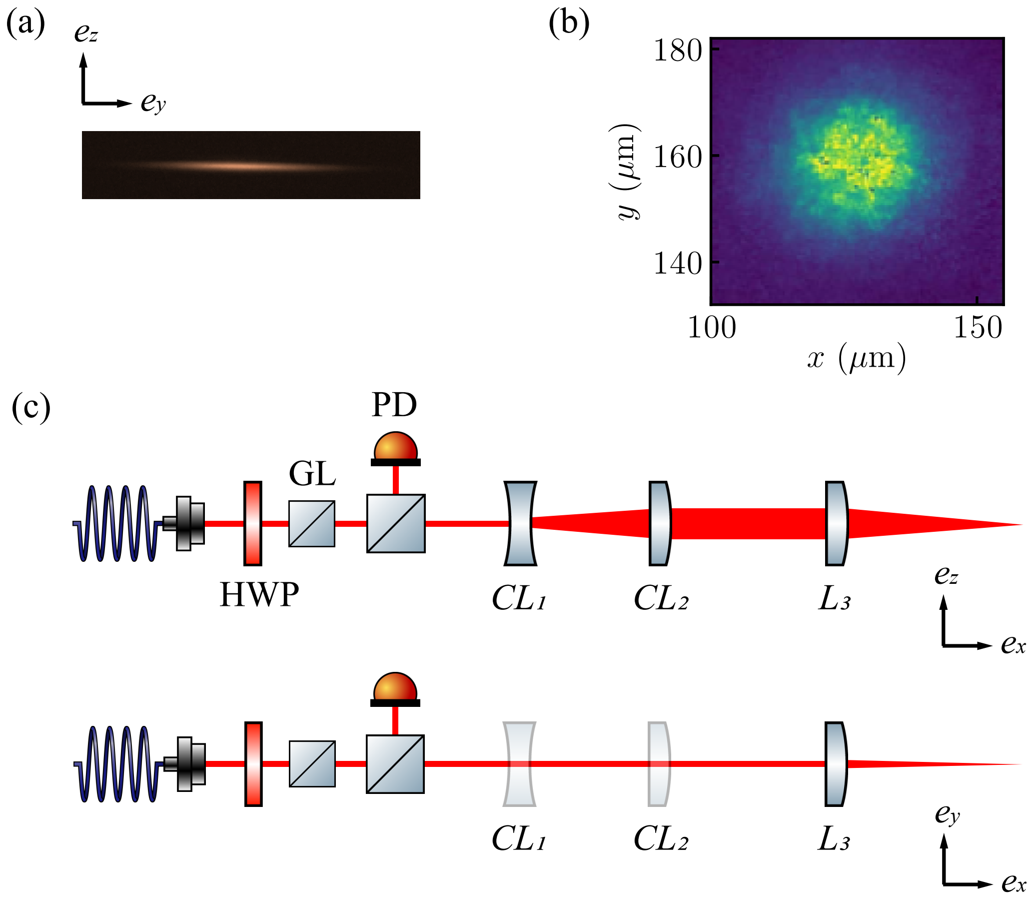

Figure 3.16: (a) The horizontal $\mathbf{e}_x$ dipole beam profile imaged on the side camera. The measured widths are (w_x, w_z)=(120,17)μm at the atom plane. (b) The BEC of atoms trapped in a crossed dipole trap. In-situ image. The trap frequencies are $2\pi \times (51, 50, 220)$Hz. The chemical potential is $2\pi \times 2.1$ kHz. (c) The beam path to generate the $\mathbf{e}_x$ dipole beam. CL_1 and CL_2 are cylindrical lenses of focal lengths $f_{CL1} = -50$ mm, $f_{CL2} = 400$ mm. L_3 is a plano-convex with $f_{L3} = 150$ mm that focuses the beam at the atoms. The GL (Glen-laser polarizer), HWP, pick-off PBS, and PD work together to make an intensity servo for the beam, insensitive to polarization drifts before the fiber.

final cloud width after time τ

$$\sigma_i(\tau) = \sqrt{\sigma_{i0}^2 + (v_T\tau)^2} \text{ where } v_T^2 = \frac{k_B T}{m}. \tag{3.1}$$

And this is how we extract the temperature of a thermal cloud. But after the atoms condense, their time evolution is strongly impacted by the interaction strength g, so one has to resort to the GPE solution. Unless with a super long τ where the atomic density is low enough to ignore g, the expansion is very different from the superposition of independent evolution of the Fourier modes. However, if the goal of measurement is the modes with length scales smaller than the healing length (e.g. optical lattice diffraction), the TOF is still satisfactory.

BECs usually are high optical depth objects (OD$\gtrsim 10$) such that absorption imaging fails to extract atomic density. Long TOF is often used to reduce the density which allows for a more accurate determination of atomic density. For a harmonically trapped cloud, the TOF evolution with GPE has simplified approximate solutions which we use to determine the trap frequencies. By applying the known equation of state in the trap, it provides us a good estimation of the chemical potential.

For a partially condensed cloud, because of the very different expansion rates between the condensed and uncondensed atoms, we can fit the density profile to a Gaussian plus bimodal distribution and extract the condensate fraction.

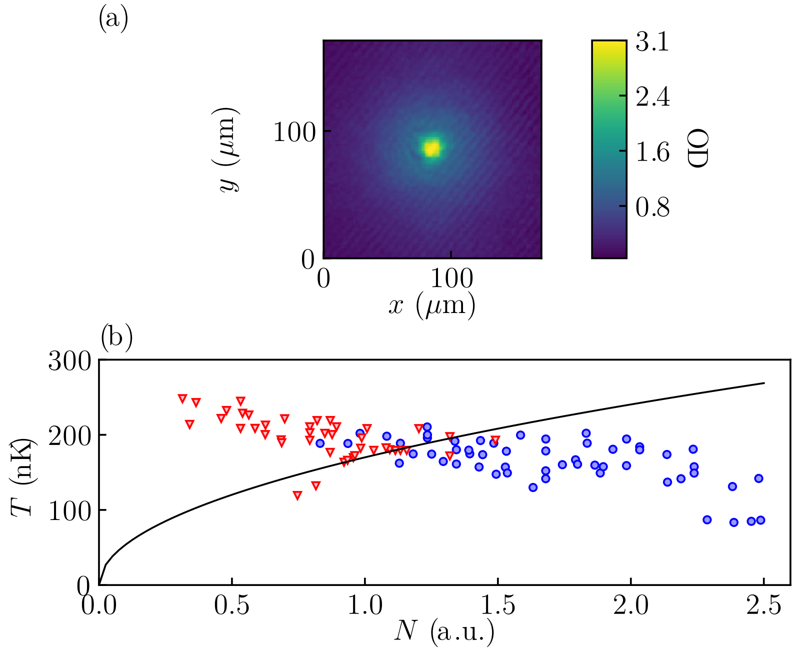

Figure 3.17: (a) TOF=20 ms image of a partially condensed cloud. A gaussian fit to the thermal cloud is done by spatially masking out the BEC, and then a bimodal fit is applied to the residue. (b) Measurement of the BEC transition N (atom number) vs T (temperature) in a quasi-2D box trap. The e$_z$ dimension is still a harmonic trap of $\omega_z = 220$ Hz.

3.8.2 Collective modes – calibrating the trap

We put the BECs in a harmonic trap

$$V(\mathbf{r}) = \frac{1}{2}m(\omega_x^2 x^2 + \omega_y^2 y^2 + \omega_z^2 z^2) \tag{3.2}$$

The lowest-lying excitations of such a trapped cloud are the dipole and quadruple modes. The dipole modes feature variations in $\langle x\rangle$, $\langle y\rangle$, and $\langle x\rangle$. The quadruple modes are $\langle x^2\rangle$, $\langle y^2\rangle$, $\langle z^2\rangle$, $\langle xy\rangle$, $\langle yz\rangle$, $\langle zx\rangle$.

From the formalism in the last chapter, by plugging in the Thomas-Fermi approximated ground state, the mode frequencies can be derived. The dipole mode frequencies are $\omega_x, \omega_y, \omega_z$, exactly the same as the trap frequency. The correction due to interaction effects is negligible for our $^{87}\mathrm{Rb}$ cloud. It is also noticeable such modes also exist for gases above the BEC transition temperature T_c, which can be derived by solving the Boltzmann equation. For a perfectly harmonic trap, such a dipole mode will not be damped. However, in reality, any anharmonicity will lead to damping of the dipole mode, which can be classically understood as "dephasing" due to the variance of oscillation periods starting from different initial displacements. Besides that, external potentials such as disorder can also dampen the oscillation. In the presence of uncondensed atoms, the collisions between them and the condensate lead to *Landau damping* of the condensate oscillation.

We can straightforwardly create an initial state in overlap with the mode wavefunction by ramping on $\delta\hat{H} = f\hat{x}$ perturbation (with controlling a magnetic gradient), and snap it off at $t = 0$. We then track the center of mass oscillation using TOF measurements. Similarly, we can ramp

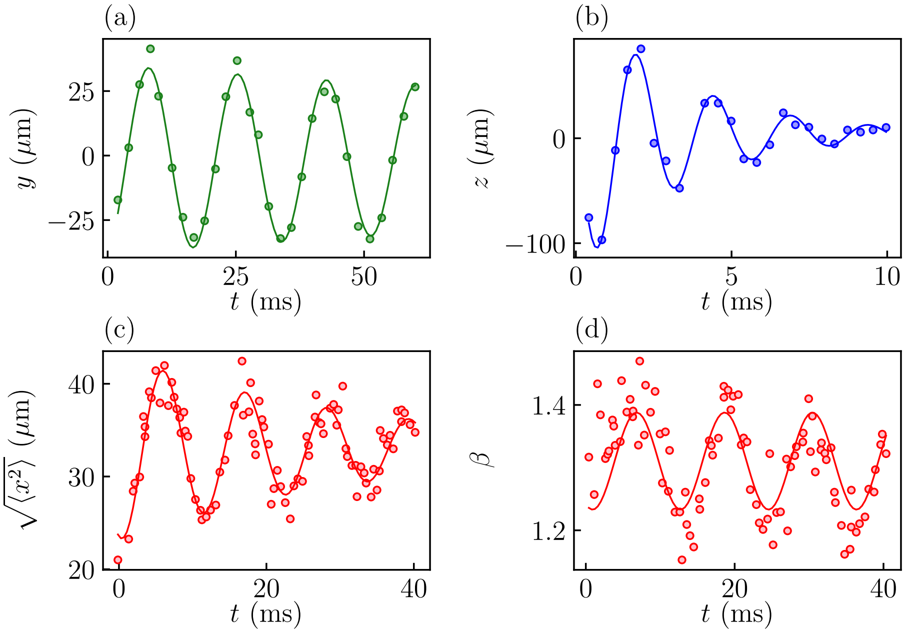

Figure 3.18: Real-time evolution of collective modes in a harmonic trap (crossed dipole trap), from TOF measurements. (a) Dipole moment $\langle y \rangle$; (b) Dipole moment $\langle z \rangle$; (c) Quadruple moment $\sqrt{\langle x^2 \rangle}$; (d) Aspect ratio $\beta = \sqrt{\langle x^2/y^2 \rangle}$.

up the dipole beam intensity to create $\delta\psi$ in overlap with the quadruple modes $x_i x_j$, and then measure the oscillation of the radii of the cloud.

3.8.3 Sheet trap – lower dimension

The plan was to trap the cloud in a quasi-2D setup such that the vertical trap frequency was higher than the chemical potential. Therefore, we engineered a "sheet beam" sent in from the $\mathbf{e}_x$, which reflects over a dichroic mirror and combines with the IR dipole beam. The key idea is adding a phase plate at the Fourier plane, which flips the optical phase by π at the upper half plane ($z > 0$). This discontinuity of phase turns into an approximate Hermite Gauss 10 mode which can hold the atoms in the middle (intensity minimum) against gravity.

The alignment of atoms into the sheet trap relies on a pico-motor-driven mirror. By tuning

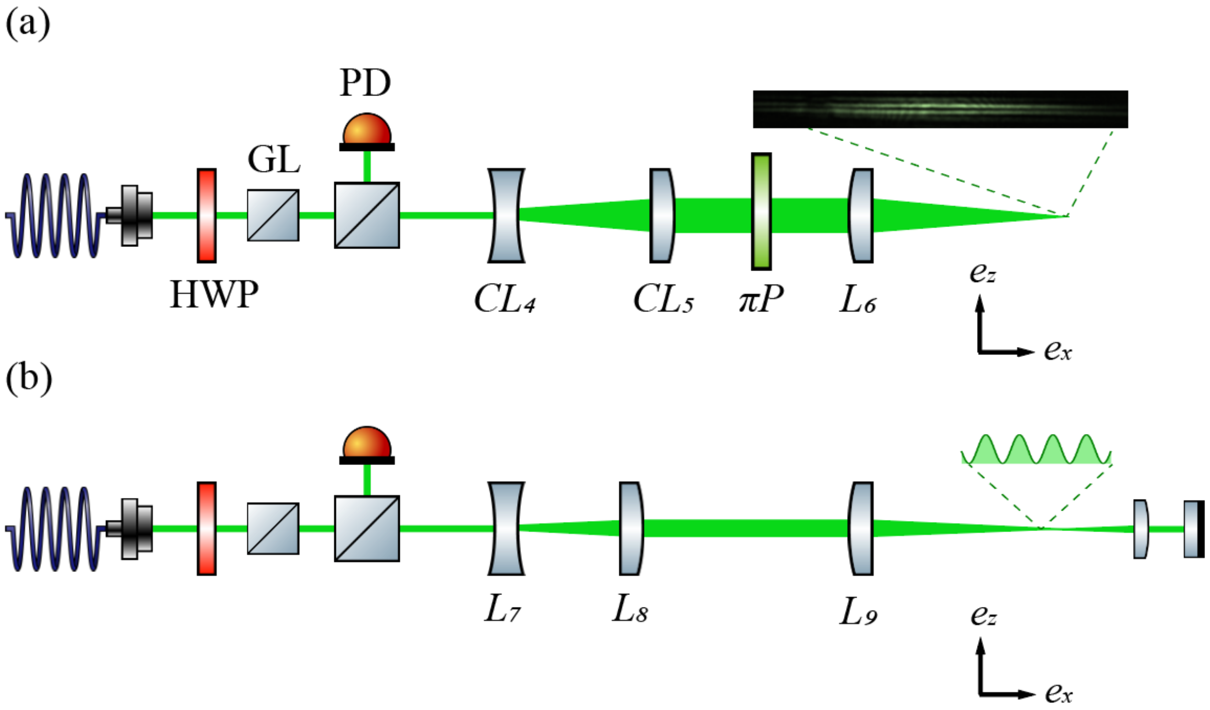

Figure 3.19: Green beam path. We reuse the same beam path to create either the sheet trap or the 1D optical lattice.

the z position of the sheet beam, we can load the atoms either to the gap or the top of the beam, clearly observed from the side camera. To measure the trap frequency ω_z in the sheet trap, we implemented a *parametric driving* method, namely

$$V(\mathbf{r},t) = \frac{1}{2}m(\omega_x^2x^2 + \omega_y^2y^2 + \omega_z(t)^2z^2) \tag{3.3}$$

and

$$\omega_z(t) = \omega_{z0} + \delta\omega\sin(\Omega t). \tag{3.4}$$

This will lead to a parametric resonance at $\Omega = 2\omega_z$ where maximized response or heating can be observed.

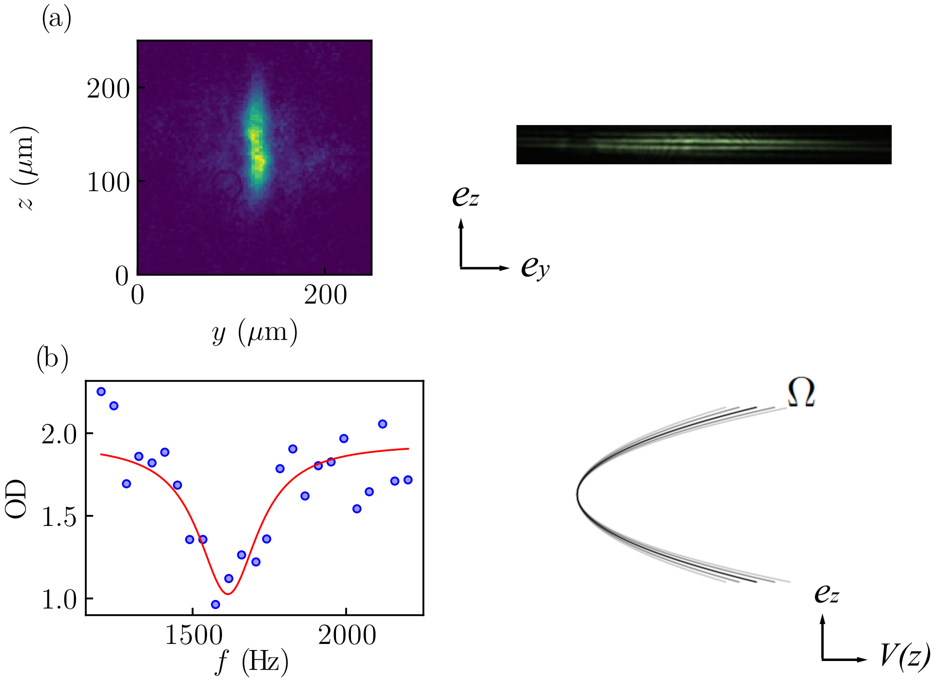

Figure 3.20: Sheet trap. (a) The sheet beam and trapped atom in TOF. We observed a large aspect ratio inversion. (b) The design of the beam waist along $\mathbf{e}_x, \mathbf{e}_y$ tries to balance the anti-trap effects. (c) Parametrically exciting the $\mathbf{e}_z$ dipole mode. Watch the remaining number of atoms after the drive.

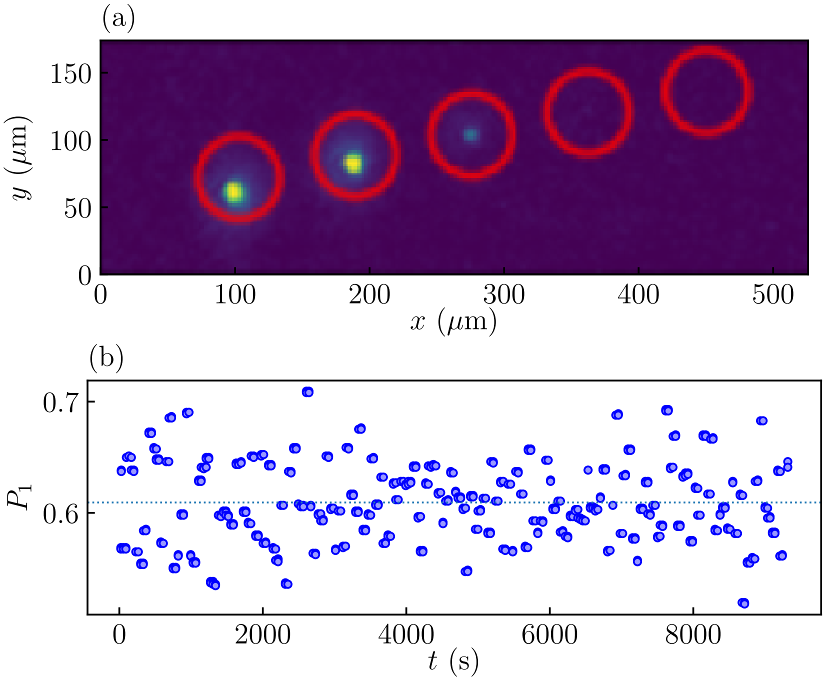

Figure 3.21: (a) Showcase of the Stern-Gerlach imaging. The five m_F states in $F = 2$ are separated into wavepackets in space. (b) Use of microwave ARP spectroscopy to test the magnetic field stability. The y-axis is the transferred fraction.

3.9 Coherent transfers in ground state

After we reached the BEC stage, the first thing we did was using the RF and microwave to calibrate the magnetic fields in the science cell.

3.9.1 Stern-Gerlach imaging

We apply a large magnetic gradient by adding a bias field on top of the quadruple magnetic trap. This exerts a spin-dependent force on our atoms during the TOF, and separates the wavepackets into different orders. We can then count the population in different spin states at once, and calculate the spin fraction which gets rid of total number fluctuation.

3.9.2 Magnetic field stability

Because the intention of this apparatus is partly to create Raman-dressed states, we care about the stability of the magnetic field without feedback or shielding. To the first order, this is determined by the electric current stability that drives the bias coils. (For the real BEC experiment, we turn off the quadruple coils.) We prepared the BEC in $|1,0\rangle$ state and made microwave Rabi spectroscopy of the $|1,0\rangle \rightarrow |2,1\rangle$ transition, which is the least sensitive to bias field noise other than the $|1,0\rangle \rightarrow |2,0\rangle$ clock transition.

3.9.3 Spin exchange collisions

At a low enough bias field, it is harder to use RF/microwave to calibrate the field due to the degeneracy of different m_F states. The data becomes difficult to interpret. In contrast, at low fields, the spin-dependent interaction takes over and drives transitions between the Zeeman sublevels. We observed these oscillations as a function of the bias field, and were able to identify the zero point of the bias fields using this method.

3.10 Microscope system

We use an identical pair of microscope objectives *Mitutoyo G Plan APO 50*x ULWD Objective Lens with NA=0.50. This gives the diffraction limit $\lambda/2\mathrm{NA} = \lambda$. The microscope objectives are corrected for the 3.5 mm glass thickness of our glass cell (ColdQuanta high NA imaging cell, inner coated for 532, 1064, and 780 nm, photo shown in Fig. 3.23b). They have a working distance of 15.08 mm (as shown in Fig. 3.23c), and thus are very close to the cell window. The focal length is 4 mm on the image side, and when accompanied with a $f_{L1} = 200\mathrm{mm}$ tube

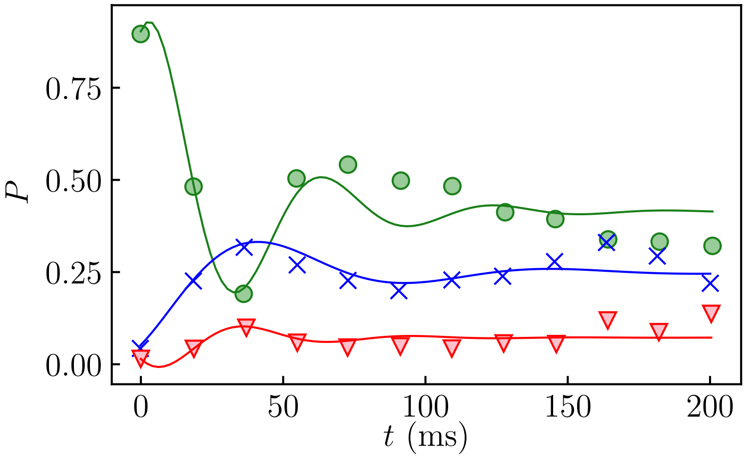

Figure 3.22: Coherent spin exchanges collisions starting in $|2,0\rangle$. Population fraction in $|2,0\rangle$ (green dots), $|2,1\rangle$ (blue crosses), $|2,2\rangle$ (red triangles). Hyperfine relaxation is approximately ignored in this model.

lens, gives 50x times magnification for our imaging system. The depth of field in this case is only 1.10 μm.

The idea of the apparatus is to use these microscope objectives for high resolution imaging and projecting potentials. This is illustrated in Fig. 3.23a. The two objectives are symmetrically looking at the atom and each other from the above and below. A resonant probe laser is sent from the top through the objective, absorbed/scattered by atoms, of which light is collected by the bottom objective and sent to the CCD after reflected from the dichroic D_1. Absorption image is then processed from two sequential images with and without the presence of atoms. The lower DMD$_1$ is responsible for projecting spin-independent potentials (with laser detuning far from fine structure splitting between D1 and D2). It is placed in the imaging plane of the telescope made by the objective and L_2 ($f_{L2} = 500$ mm), and thus is de-magnified by 125x. Similarly, the upper DMD$_1$ is used to project spin-dependent potentials, whose pattern is de-magnified by 75x with L_3 ($f_{L3} = 300$mm).

We mounted both objectives on cage systems with five axes tuning capability (displacements in $\mathbf{e}_x - \mathbf{e}_y$, focal length $\mathbf{e}_z$, tilt axes $\mathbf{e}_x, \mathbf{e}_y$). Because of the smallest of the depth of field, we used the translation stages for $\mathbf{e}_x, \mathbf{e}_y, \mathbf{e}_z$ (*Thorlabs Z-Axis Translation Mount* with 50 μm/rev and *Newport Standard 70 mm* with $2\ \mu\mathrm{m}$ accuracy). The upper objective is mounted on the upper breadboard, while the lower objective is supported by another added breadboard (between the optical table and the middle layer breadboard) which holds the whole imaging system. For imaging, we inserted a "flipped mirror" that can switch between the a 50x magnification (in-situ) and a 10x magnification (TOF).

3.10.1 Bench test of the imaging system

To understand the imaging system, we replicate the design offline and test it using artificial objects. We mainly test it upon two objects: a commercial USAF target and a pinhole array.

The USAF target has pre-calibrated fringe patterns on a transparent window. We used it to test the tuning accuracy of our micrometer stages. We deliberately misaligned the probe beam as well as the tilt angle of the target to observe the image aberration. We also looked at the modulation transfer function of the smallest fringe pattern, which has a spacing $\sim 2\ \mu\mathrm{m}$, well above our imaging resolution.

We did more quantitative test on the pinhole array (manufactured at NIST). This is a piece of opaque glass with a transparent pinhole array, where the array grid size is $10\ \mu\mathrm{m}$, and the single pinhole radius ranges from $0.5 - 1.5\ \mu\mathrm{m}$. It is a "pity" that the size is still above the diffraction limit, which convolves with the point spread function (PSF) in understanding the measurement. However, simple simulation suggests that this doesn't affect the PSD by very much. We calibrated

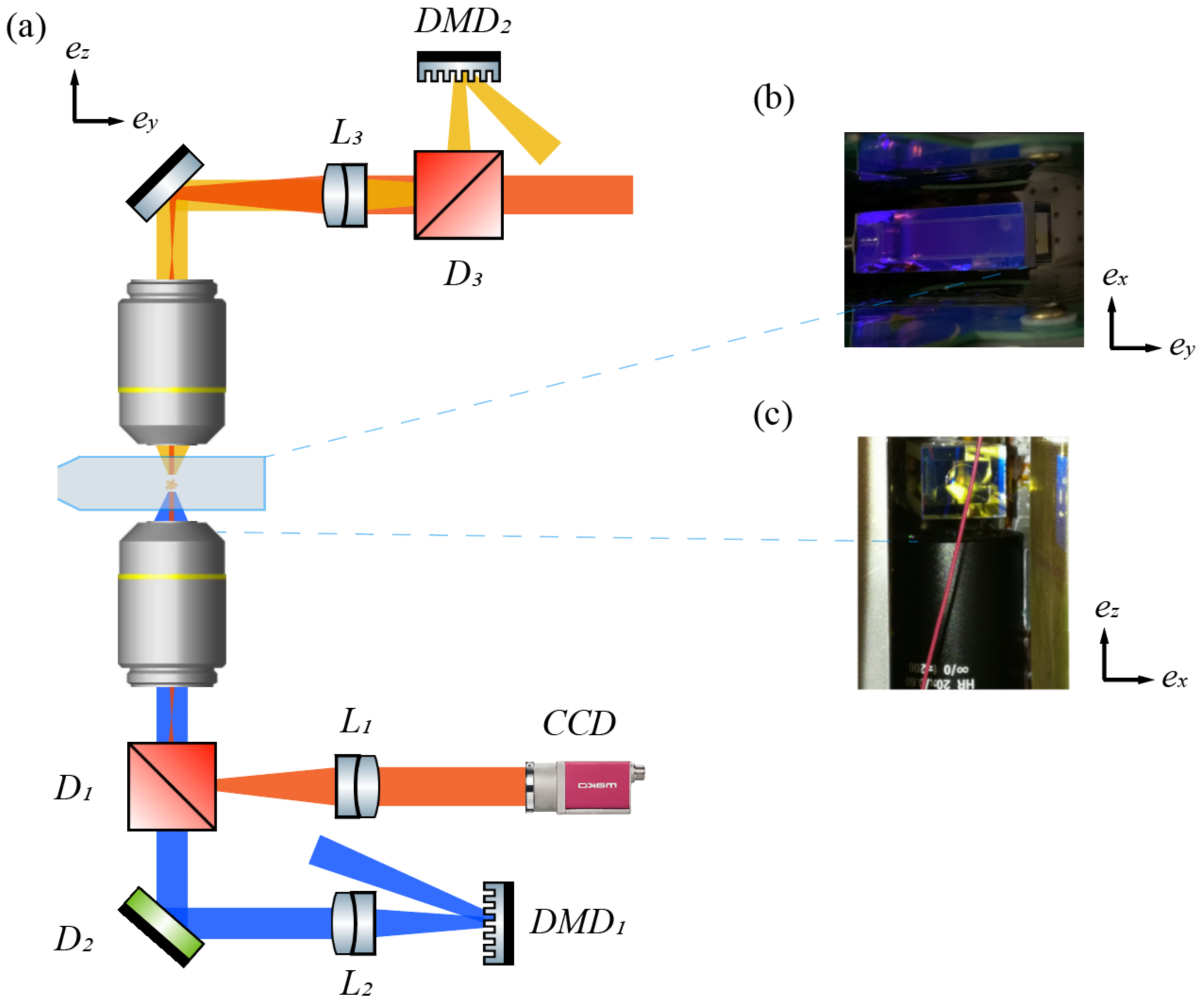

Figure 3.23: Crossection overview of the whole microscope setup. L_1, L_2, L_3 are achromat doublet lenses. L_1 is the tube lens for imaging. D_1, D_2, D_3 are three dichroic beam splitters. (b, c) are views from the top and side of the glass cell.

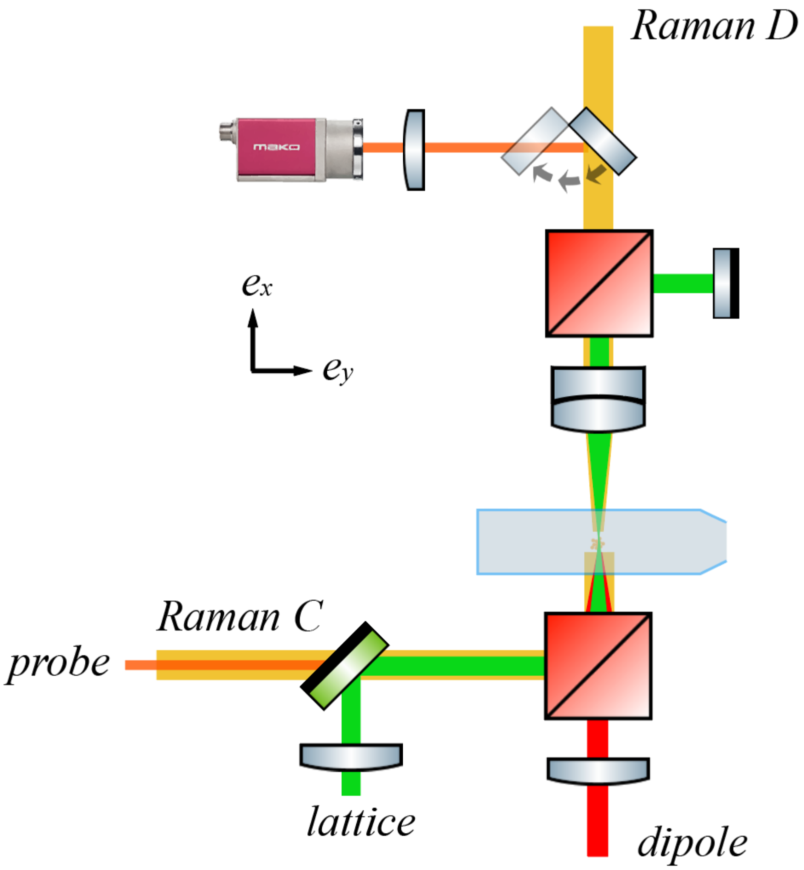

Figure 3.24: The scheme in $\mathbf{e}_x - \mathbf{e}_y$ plane near the glass cell, and the way different colors of lasers are combined on the second layer breadboard. We used three dichroic beam splitters to combine the 532, 780/790, 1064 nm lasers. Additionally, we insert a “flipper mirror” to switch between the Raman and side imaging paths.

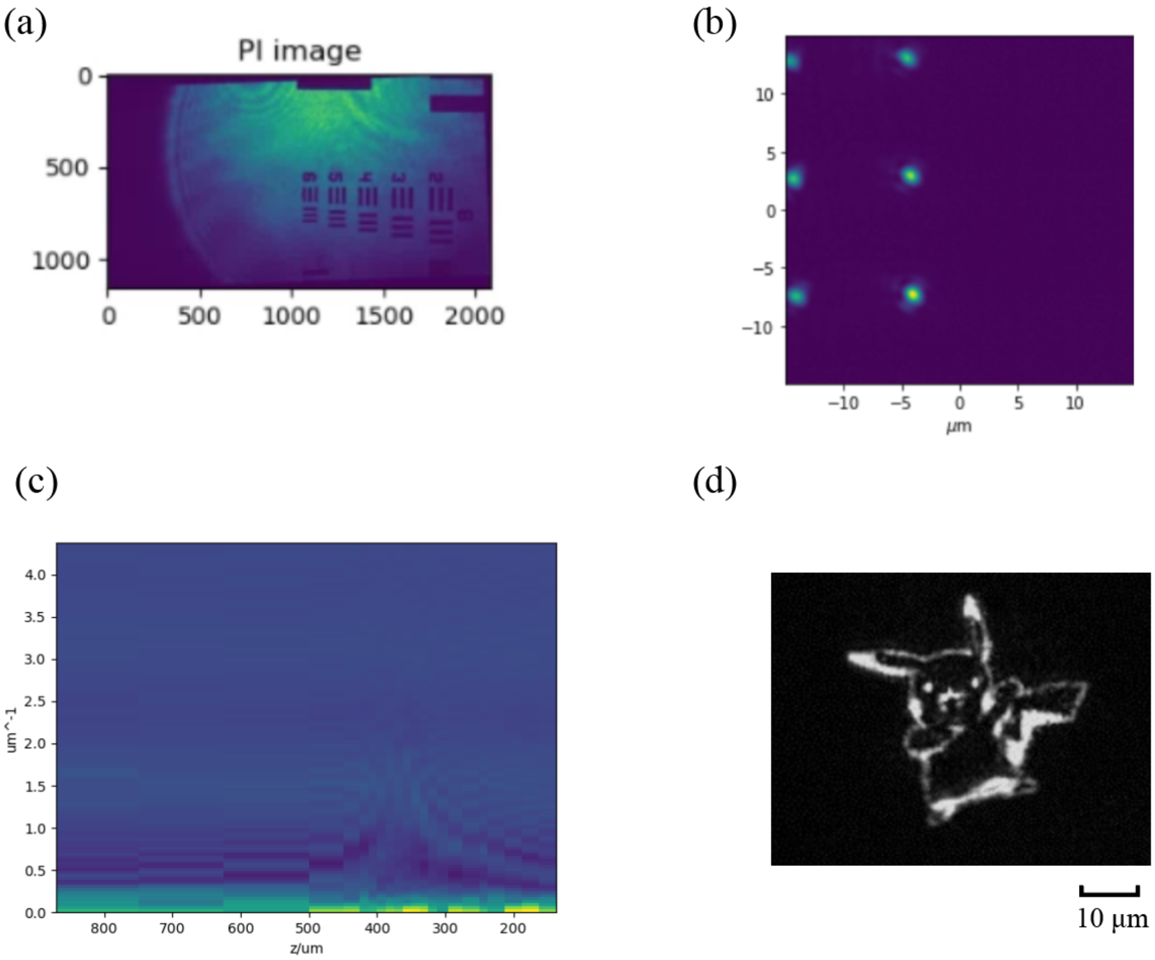

Figure 3.25: Preliminary test of microscope system. (a) USAF image. (b) Pinhole array image. (c) Atom density power spectrum (normalized to 1D) as a function of defocused distance. (d) In the experimental system, one microscope image of the other one's projected pattern.

the imaging system by measuring the averaged PSF of several individual pinholes, and proved that we are able to reach $\mathrm{NA} \approx 0.5$.

3.10.2 In-situ imaging of atoms

Due to the smallness of the depth of field, we cannot image a thick cloud such as atoms in the magnetic trap. The best candidate is the quasi-2D atoms in the sheet trap. However, because the horizontal confinement (in $\mathbf{e}_x - \mathbf{e}_y$) is either provided by the vertical dipole beam or DMD projection that both go through the objective, it is hard to "disentangle" the alignment of the imaging focus and the trap itself. We noticed that we could make use of the hybrid trapped cloud (no need for BECs), since the confinement comes from an $\mathbf{e}_x$ dipole beam and the quadruple trap, neither is correlated with the microscope. (Moreover, this trap makes tightly confined cloud in $\mathbf{e}_z$.)

We have used two approaches to aligning the microscopes' focus in reference to the hybrid trap. For the first method, we project test patterns from the upper DMD_1 on the trapped atoms, and tune the lower objective focus for a most clear image of the patterns on the atoms. Next, we image the laser pattern itself rather than atoms, and tune the upper objective focus looking for the sharpest pattern. We repeat the two steps above and tune the upper and lower objective iteratively. This approach usually converges with 5-6 iterations in terms of regular maintenance correction for the focal drifts.

A second approach is useful for a more defocused case, like when one completely realigns the imaging system. That is by noticing that the high density of BECs contribute to large refractive index when the probe is detuned, but the refraction effects are "minimal" when atoms are close to the focal plane. We detune the probe by ±50-150 MHz $\approx$ 10-30Γ, and minimize the lensing effect by tuning the imaging focus. We typically observe the local OD distribution flips sign when we tune it across the focal plane. But this approach is not as sensitive as the first one, which can bring the focus to within several μm.

Ultimately, we calibrated the imaging system performance by measuring the density-density correlation function of the quasi-2D atomic cloud. This method was elaborated in [38, 39]. We collected 50 absorption images as a set of data, and calculated the 2D density variation $\delta n(x, y) = n - \langle n \rangle$. It is shown that the power spectrum density of the density variation contains information about all the imaging aberrations

$$\mathrm{PSD}(\delta\mathrm{n})(\mathbf{k}) = |\mathcal{FT}(\delta\mathrm{n})|^2 = \mathcal{FT}[\langle\delta\mathrm{n}(\mathbf{r})\delta\mathrm{n}(\mathbf{r}')\rangle] \tag{3.5}$$

assuming transnational invariance. The first order effect such as defocusing would show up as "ring" like pattern in the 2D PSD, and is expected to vanish near the focal plane. Ideally one can fit the aberrations to Zernike polynomials to extract information for redesigning improvement of imaging quality.

3.11 Digital micromirror devices

We mainly used two DMDs for our experiments. The DMD_2 is a Luxbeam 4600 1080p VIS from Visitech. It carries the *DLP 9500* DMD chip, which features a fast $\sim$30 kHz refresh rate, 1080p resolution, and 10.8 μm pitch size. The mirror coating is optimized for visible light. The other DMD_1 is a bbs 6500 from a German company bbs. It carries the *DLP 6500* DMD chip, which features an $\sim$11 kHz refresh rate, 1080p resolution, and 7.6 μm pitch size. We illuminate the DMD_1 with our Ti: sapphire output that is practically tunable in the range of $750 - 830$ nm. Meanwhile, we use our DMD_2 with a broadband ($\sim$ several nm wide) fiber-coupled laser source, which might minimize the disorder in the projected potential that comes from the interference with different light paths ($\Delta l < \Delta\lambda^2/\lambda$).

Because the mirror spacing on a DMD is comparable to the laser wavelength, it effectively acts as a reflective grating for our single-frequency laser beam. This leads to many diffraction orders whose intensity distribution varies with the incident angle. For projecting the DMD pattern faithfully on the atom plane, we need to align the DMD normal to the optical axis. Within a

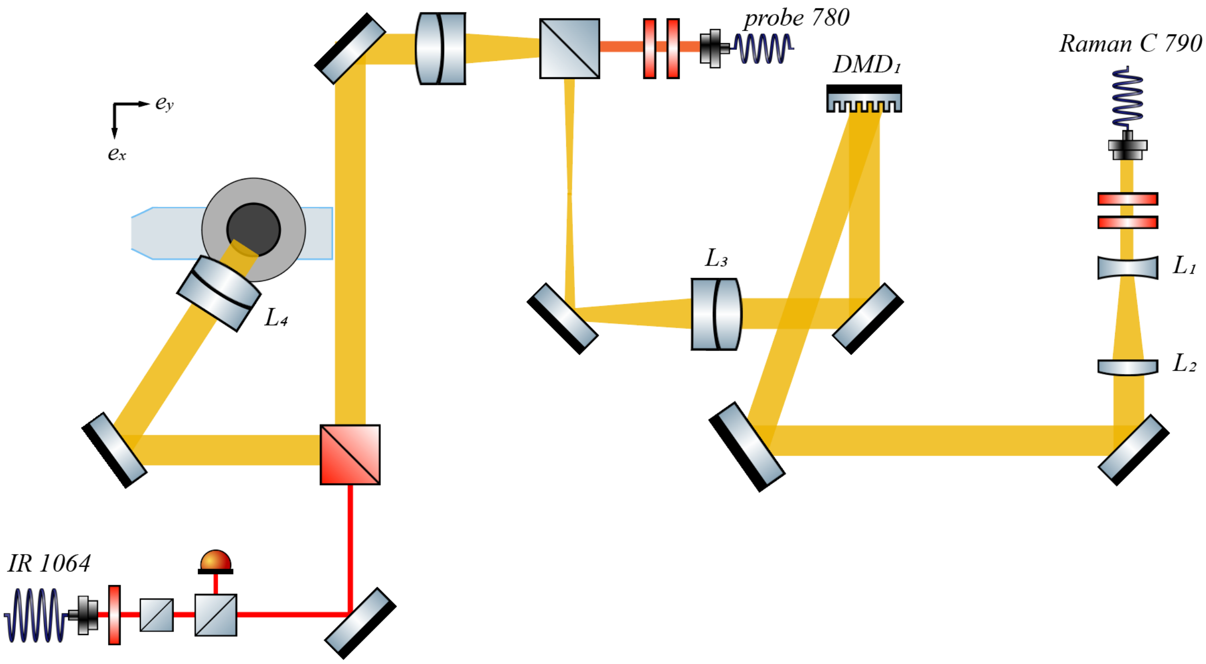

Figure 3.26: Configuration of the upper breadboard: a Ti: sapphire beam (modulated by a DMD), probe beam, and an IR beam are combined here and sent to the microscope.

limited tuning range of incident angle, we optimized the diffraction efficiency into the central order. Unfortunately, commercial DMDs are not specially designed for the use of a laser (of a certain wavelength), and hence, the waste of optical power is basically out of control (it's difficult to optimize it for e.g. the blaze condition). For our DMD$_1$, we get a diffraction efficiency of $\sim 25\%$, and for DMD$_2$ $\sim 30\%$.

We placed the DMD$_1$ on the upper layer breadboard. The optical paths for the DMD as shown in Fig. 3.26 include a beam telescope, a relay system, and a final projecting lens. A pair of lenses ($f_{L1} = -75$ mm, $\mathrm{f}_{\mathrm{L2}} = 150$ mm) prodcues a magnified collimated beam of ~1 in, which is incident on the DMD. Next an optical relay of about 1:1 extends the path length, during which we combine using a PBS with our probe beam. The relay system also allows us to add masks in the Fourier plane (e.g. block the zeroth order). The beams are then combined at the dichroic BS with the IR 1064 nm beam that makes the vertical dipole beam. Finally, all these copropagating

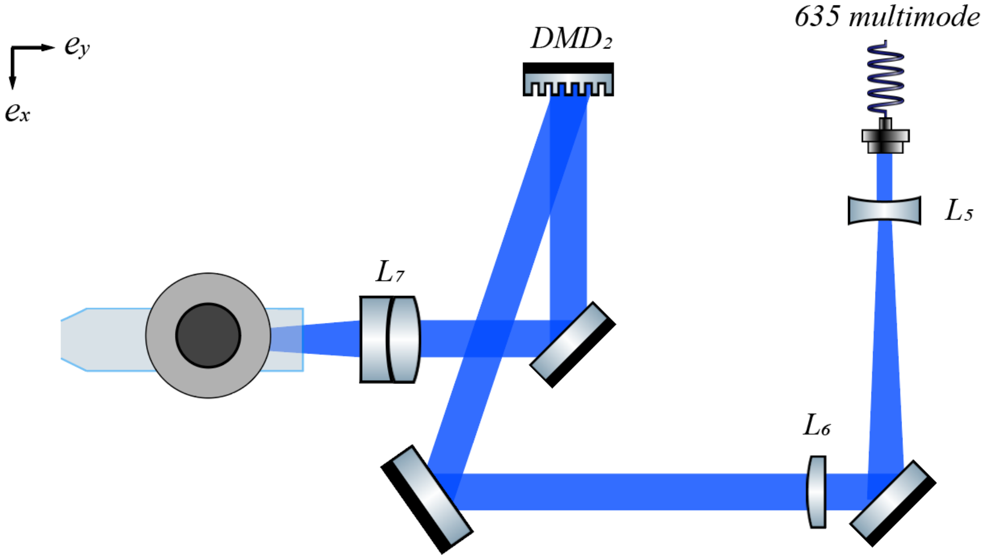

Figure 3.27: Setup on the optical table (lower layer): it is only used for DMD spatial engineering of a blue-detuned laser. The beam is expanded and illuminates the DMD, then imaged to the atom plane through a microscope.

beams are collected by the achromat tube lens $f_{L4} = 300\ \mathrm{mm}$ and sent through the microscope objective.

The DMD_2 is placed on the bottom layer optical table. The output of the 635 nm broadband laser is collected by the 1:3 telescope $f_{L5} = 50\ \mathrm{mm}, \mathrm{f}_{\mathrm{L6}} = 150\ \mathrm{mm}$. Next it is sent to reflect over and imprint the pattern on the DMD. Then it passes through the achromat tube lens $f_{L7} = 500\ \mathrm{mm}$ and is sent to the microscope objective.

Because we sometimes need to imprint dynamic patterns changing on the timescale of ∼ms, we set up the triggers for both DMDs. A series of patterns are formatted into an array and pre-uploaded to the RAM of the DMD before the experimental sequence starts. These DMDs support external triggering in the way they flash the pattern at the rising/lowering edge of a TTL voltage. Besides that, they also have internal clocks and allow for simple loop and "goto" commands. The typical use of the APIs are summarized in the Appendix.

3.12 Optical lattices

We have in general two ways of creating optical lattices: counterpropagating laser beams or direct projection.

Due to the optical access, it is most straightforward to counter-propagate beams in the $\mathbf{e}_x$. We choose $\lambda = 532$ nm produced by the IPG GLR-030 green single-mode fiber laser, which creates a 266 nm period lattice. The incident lattice beam is first combined with a side probe beam, and then the IR dipole beam at two dichroic mirrors. After it passes through the science cell, it is reflected by another dichroic mirror and focused onto a retro-reflecting mirror. Both the incident and the reflected beams are picomotor steered. Because we used a photonic crystal fiber to deliver the lattice beam, the power is limited to $\lesssim 2$ W. We need to compromise with the beam homogeneity to reach a deeper lattice depth.

For direct projection, we simply print a pattern on our DMD. In some cases, we opted to block the zeroth order of the lattice beams in the Fourier plane, which can make a shorter period lattice (by twice), and also help reduce some disorder in the beam.

3.13 Raman lasers

The Raman beams that we use in the experiments are produced by a Ti:sapphire laser (M-Squeared SolsTiS system with an external cavity). This laser needs to be pumped by a single-mode 532 nm pump laser. During our use, we swapped the pump laser with a new IPG GLR-30 (the same as that generates the optical lattice or sheet trap, the power distribution controlled by a

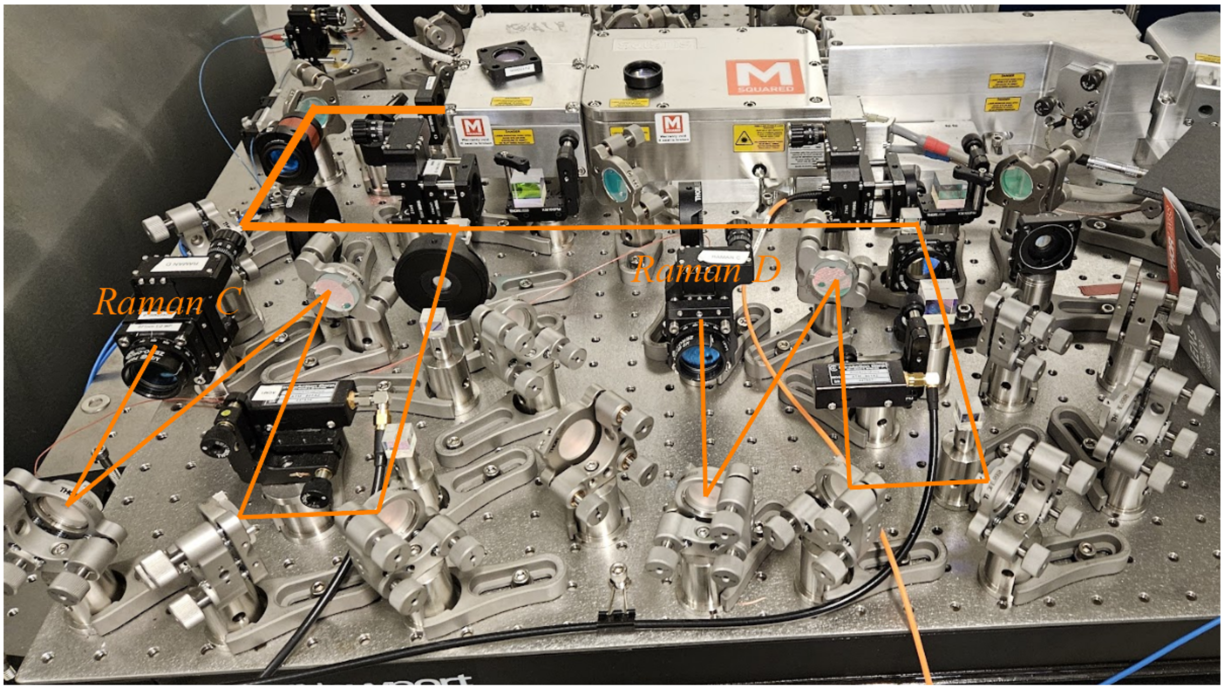

Figure 3.28: The Ti:sapphire laser breadboard. Shown in orange beam paths are Raman C and D which we used for most experiments.

PBS), from where we re-aligned the pump beam to the Ti: sapphire crystal using the two built-in mirrors and a lens. We typically set the pump power to 10 W, which delivers 1.5-2 W at the wavelength of around 790 nm. Both the Ti:sapphire laser and the pump laser need external water cooling.

The light paths on the laser breadboard (Fig. 3.28) can produce 3-4 beams delivered by the fibers to the apparatus table, while we usually use two among them and label them *Raman C* and *D*. These two beams are generated by the same order of separate AOMs, whose frequencies are controlled by two DDS channels (*Novatech*).

We used these beams for driving Raman or Bragg transitions, making optical lattices, and creating spin-dependent potentials. In Fig. 3.24, the two beams are sent in counterpropagation in $\mathbf{e}_x$. We used such a setup to carry out experiments such as spin-orbit coupling with large recoil momentum, Bragg spectroscopy in $\mathbf{e}_x$, and creating an incommensurate optical lattice with the green lattice. In Fig. 3.23 and 3.26, we illuminate *Raman C* on the upper DMD$_1$, which allows us to create arbitrary patterns. For the experiment described in Chapter 5, we commanded an optical lattice with the DMD and blocked the 0th and -1st order in the Fourier plane. With a copropagating *Raman D* beam combined at a PBS, this can create a small recoil spin-orbit coupling, which is beneficial for the observation of the non-reciprocal transport due to the non-Hermitian gauge potential. For another superfluid turbulence project, we added two RF tones to drive the AOM of the *Raman C* beam, which is again sent to the DMD and microscope. This can create spatially varying "effective RF" Rabi frequency. We used this feature to locally introduce spin impurity for local velocity measurements.

braket

Chapter 4: Measurement of superfluid density

4.1 Introduction

The study of superfluidity was one of the beginning marks of the laboratory study of quantum physics. It is macroscopic phenomenon, where the liquid helium atoms flow without feeling any frictional force by its container, yet has its deep roots in the matter wave coherence. It is widely believed today that the superfluidity has close connection to the phenomenon of Bose-Einstein condensation (BEC). The theory is well formulated for the low energy Bose liquids, marking one of the simplest many-body systems. Yet there are always surprises and new discoveries with the lately matured tools of understanding and manipulating these Bose systems at ultralow temperature.

One of these surprises lies in that some people (Like Anthony Leggett) realized that the superfluid is not a usual state of matter that parallels the division of solid, liquid, or gas. Actually it is widely found phenomenon in all of the three states. Heliums (^{3}He and ^{4}He) are both liquids when they are superfluids, and the 1995 discovery of BEC in alkali gases like Rb and Na (with following hydrodynamic experiments) showed to us that the weakly interacting gases state can be a superfluid. However, it seems counter-intuitive that a solid, which usually has small response to compression and shear forces, can be a superfluid.

Leggett believes that any bosonic matter at low enough temperature (i.e. near its ground state), should show similar superfluid behavior as an argument of quantum mechanics. Although it was debated at the time, many soon realized that nothing fundamental could prevent such a state from forming. In an early seminal paper, Leggett introduced the simple way of defining superfluid density from the non-classical rotational inertia (NCRI), and derives an upper bound of superfluid density regardless of the microscopic wavefunction, called the ”Leggett formula”[40]. The bound elegantly links the atomic density modulation to the superfluid transport behavior.

Despite the idea being early born, the sought for supersolids was arduous journey. People tried to find the onset of superfluid density in solid Helium in terms of NCRI, measured by the oscillation frequency in a called torsion experiment. Early signatures almost had them convince themselves the discovery of the supersolids, marking a sudden change of oscillation period upon lowering the temperature. However, later experiments have found similar drop in the shear modulus of the solid helium at the same temperature, which was measured by a different approach. It was argued and then verified by the same group that the drop of frequency was most likely due to the change of shear modulus.

On the opposite side of the same coin, another group of people tried to tackle this by engineering a crystalline order starting from a simple gases BEC. Proposals were many but the main idea was to engineer a ”roton” minimum in the dispersion relation of momentum space which a Bose cloud could condense into. The successful example is by using the dipolar interaction, which naturally dresses the simple Bogoliubov dispersion into that feature. Experiments were carried out with different atomic species, and the predicted crystalline structure has been verified using simple imaging techniques[41, 42]. To this end, people again tried to measure transport properties, like superfluid density, via a torsion-like setting but in an optical dipole potential. However, it is recently found that this is obscured by the internal degrees of freedom of the spontaneously formed crystal (which features both a Goldtone and a Higgs mode). The theme of research is hence still going on.

In this work, we take a methodology of investigating the origin of (reduced) superfluid density in the simple model of supersolidity (i.e. by Leggett), in a hybrid experimental and theoretical approach. Our experimental system of Rb BEC gas in a 1D optical lattice, although not featuring any dipolar interaction, captures the key physics of supersolidity and verifies the Leggett formula. The results we derive from this, including experimental probes of the superfluid properties, can help construct the different perspectives of understanding, and also is directly valuable to the similar experiments in the real supersolids.

This paper is structured as the following: in section 4.2 we introduce the formalism of linear response to calculate transport properties of a superfluid system. In section 4.3 we apply the formalism to the lattice gas. In the next section 4.4 we derive the principle of the measurement tool – the sum rules. In section 4.5 we introduce our experimental apparatus and display the measurement of anisotropic speed of sound via Bragg scattering. In the next section 4.6 we alternatively formulate the same problem via the effective mass approach, which is both technically simple and helps understand the coarse-grained problem. In section 4.7 and 4.8 we again show our data and numerical simulation of the rotational properties: the NCRI, and discuss the emergent normal fluid in our system. In the last section 4.11 we draw connections to other systems which share similar physics, and future experimentally realisable schemes.

4.2 Generalized formalism: Superfluid density

The superfluid density remarks an important transport property in a bosonic superfluid system. It describes the response of the system to the superfluid phase twist, i.e. $\delta\theta$ when we define the complex superfluid order parameter as

$$\psi(\mathbf{r}) = |\psi(\mathbf{r})| e^{i\theta(\mathbf{r})}. \tag{4.1}$$

Lies in the center of superfluid density is the current-current correlation function. Gordon Baym [43] gave a physical example which lets us see how it is the case. Consider a long cylinder container with superfluid flowing in the $\mathbf{e}_z$ direction. The container is at rest, while the normal component is in equilibrium with the wall, such that the momentum is only carried by the superfluid component. To employ thermodynamics, we need to relate it to the reference frame moving with the superfluid, where the walls move at velocity u. Define the momentum density (or current) $g(r)$, and the current in the wall/lab frame is

$$\langle g(r)\rangle_u = \frac{\operatorname{tr} e^{-\beta\left[H - P\cdot u + \frac{1}{2}Mu^2 - \mu N\right]} g(r)}{\operatorname{tr} e^{-\beta\left[H - P\cdot u + \frac{1}{2}Mu^2 - \mu N\right]}} \tag{4.2}$$

Expand it $\langle g_z(\boldsymbol{r})\rangle_u = \langle g_z(\boldsymbol{r})\rangle + \beta\left[\langle g_z(\boldsymbol{r}) P_z\rangle - \langle g_z(\boldsymbol{r})\rangle \langle P_z\rangle\right] u$ where $\boldsymbol{P} = \int d\boldsymbol{r} g(\boldsymbol{r})$. Play with the Green function for a bit,

$$\begin{aligned} \langle g_z(\boldsymbol{r})\rangle_u &= i \int_0^{-i\beta} d\left(-t'\right) \left[\langle g_z(\boldsymbol{r}0) P_z\left(t'\right)\rangle - \langle g_z(\boldsymbol{r})\rangle \langle P_z\rangle\right] u \\ &= i \int d\boldsymbol{r}' \int_0^{-i\beta} d\left(-t'\right) \left[\langle g_z(\boldsymbol{r}0) g_z\left(\boldsymbol{r}'t'\right)\rangle - \langle g_z(\boldsymbol{r})\rangle \langle g_z\left(\boldsymbol{r}'\right)\rangle\right] u \end{aligned} \tag{4.3}$$

One can get

$$\langle g_z(\boldsymbol{r})\rangle_u = \int d\boldsymbol{r}' \int_{-\infty}^{\infty} \frac{d\omega}{2\pi} \frac{\Upsilon_{zz}\left(\boldsymbol{r}, \boldsymbol{r}', \omega\right)}{\omega} u \tag{4.4}$$

where

$$\Upsilon_{ij}\left(\boldsymbol{r}, \boldsymbol{r}', \omega\right) = \int_{-\infty}^{\infty} dt e^{i\omega(t-t')} \left\langle [g_i(\boldsymbol{r}t), g_j\left(\boldsymbol{r}'t'\right)]\right\rangle . \tag{4.5}$$

Assuming translation invariance,

$$\langle g_z(\boldsymbol{r})\rangle = \int \frac{d\boldsymbol{k}}{(2\pi)^3} \int d\boldsymbol{r}' e^{i\boldsymbol{k}\cdot(\boldsymbol{r}-\boldsymbol{r}')} \int_{-\infty}^{\infty} \frac{d\omega}{2\pi} \frac{\Upsilon_{zz}(\boldsymbol{k}\omega)}{\omega}. \tag{4.6}$$

As a tensor, the current-current correlation can be decomposed

$$\Upsilon_{ij}(k\omega) = \frac{k_i k_j}{k^2} \Upsilon^L(k, \omega) + \left(\delta_{ij} - \frac{k_i k_j}{k^2}\right) \Upsilon^T(k, \omega). \tag{4.7}$$

One can verify that

$$\Upsilon^L(k, \omega) = \int_{-\infty}^{\infty} dt e^{i\omega(t-t')} \int dr e^{-ik\cdot(r-r')} \left\langle \left[g_z^L(rt), g_z^L\left(r't'\right)\right]\right\rangle . \tag{4.8}$$

So is the transverse $\Upsilon^T(k, \omega)$. Here the transverse and longitudinal current operators are first introduced.

How does one identify the superfluid and normal components from this? Gordon argued that for the situation we considered (where the cylinder is infinitely long without boundaries), we first take the limit $k_z = 0$ when integrating out r', and then $k_x = k_y = 0$

$$\langle g_z(\boldsymbol{r})\rangle_u = \lim_{k_x, k_y \to 0} \lim_{k_x \to 0} \int_{-\infty}^{\infty} \frac{d\omega}{2\pi} \frac{\Upsilon_{zz}(k\omega)}{\omega} u. \tag{4.9}$$

But because

$$\lim_{k_x,k_y\to 0}\lim_{k_z\to 0}\frac{k_z k_z}{k^2}=0, \tag{4.10}$$

the longitudinal $\Upsilon^L(k,\omega)$ does not contribute. Hence we have the normal component $\langle g_z(r)\rangle = \rho_n u$

$$\rho_n=\lim_{k\to 0}\int_{-\infty}^{\infty}\frac{d\omega\Upsilon^T(k,\omega)}{2\pi\omega},$$

which is the most important relation we are after. Interestingly, if we reverse the order of integration,

$$\lim_{k_z\to 0}\lim_{k_x,k_y\to 0}\frac{k_z k_z}{k^2}=1,$$

we get the f-sum rule instead

$$\rho=\rho_n+\rho_s=\lim_{k\to 0}\int_{-\infty}^{\infty}\frac{d\omega}{2\pi}\frac{\Upsilon^L(k,\omega)}{\omega}.$$

This sum-rule can also be rigorously derived from the continuity equation of total density. The reason why we get the total density is that this order of integration indicates the situation where there are in addition two walls which are (infinitely far away from each other) along z. So no matter the fluid is superfluid or normal it must move together with the container.

The form of the Hamiltoninan after frame translation, $H' = -\int p\cdot u$ reminds one of the classical gauge coupling. Actually, by introducing an artificial charge to the system, the problem is reminiscent of the simple BCS superconductor model. There, the gauge dependent moment operator

$$P=p-A$$

where p is the canonical momentum, introduces another diamagnetic current so that the total current becomes

$$J = j - \rho A$$

made of the canonical and gauge part.

In the same approach, one can fix a gauge

$$\nabla \cdot \mathbf{A} = 0$$

and find that the canonical current is proportional to $\mathbf{A}$:

$$j = \rho_n A$$

This makes a total diamagnetic current

$$J = -\rho_s A$$

proportional to the superfluid density.

4.2.1 Rotational property

The last section considered the most classic situation of superfluid in translation. But another important experiment is the rotating bucket. In this section I will derive the moment of inertia's relation to the normal density.

The moment of inertia tensor is

$$I_{ij} = \left[\frac{\partial \left\langle L_i \right\rangle_\omega}{\partial \omega_j} \right]_{\omega=0} = \beta \left[\left\langle L_i L_j \right\rangle - \left\langle L_i \right\rangle \left\langle L_j \right\rangle \right].$$

Plug in $L = \int d\boldsymbol{r}\, \boldsymbol{r} \times \boldsymbol{g}(r)$,

$$I_{ij} = \int \frac{d\boldsymbol{k}}{(2\pi)^3} \int d\boldsymbol{r} \int d\boldsymbol{r'} e^{i\boldsymbol{k}\cdot(\boldsymbol{r}-\boldsymbol{r'})} \varepsilon_{isl} \varepsilon_{jmn} r_s r'_m \int_{-\infty}^{\infty} \frac{d\omega}{2\pi} \frac{\Upsilon_{ln}(k\omega)}{\omega}.$$

And as before, decompose $\Upsilon_{ij}(k\omega) = \frac{k_i k_j}{k^2} \Upsilon^L(k,\omega) + \left(\delta_{ij} - \frac{k_i k_j}{k^2} \right) \Upsilon^T(k,\omega)$.

Now in a rotating bucket, we calculate Υ_{zz}. Note that

$$\int dr e^{i\boldsymbol{k}\cdot\boldsymbol{r}} \varepsilon_{zsl} r_s k_l = \int dr e^{i\boldsymbol{k}\cdot\boldsymbol{r}} (\boldsymbol{r} \times \boldsymbol{k})_z = 0$$

if the rotation center axis is at $\boldsymbol{r} = 0$. So we are again left with only the transverse current. The rest is just algebra.

$$I_{zz} = \int \frac{d\boldsymbol{k}}{(2\pi)^3} \int d\boldsymbol{r} \int d\boldsymbol{r'} e^{i\boldsymbol{k}\cdot(\boldsymbol{r}-\boldsymbol{r'})} \varepsilon_{zsl}^2 r_s r'_s \int_{-\infty}^{\infty} \frac{d\omega}{2\pi} \frac{\Upsilon_{ll}^T(k\omega)}{\omega}.$$

The integration trick is to write

$$\int dr' e^{-ik\cdot r'} r'_s = i \left(\nabla_k \right)_s \int dr' e^{ik\cdot r'} = i \left(\nabla_k \right)_s (2\pi)^3 \delta(k)$$

and integrate by parts

$$
\begin{aligned}
I_{zz} =& - i \int d\boldsymbol{r} \varepsilon_{zsl}^2 r_s \int \frac{d\boldsymbol{k}}{(2\pi)^3} (2\pi)^3 \delta(k) \left(\nabla_k\right)_s (e^{i\boldsymbol{k}\cdot\boldsymbol{r}} \int_{-\infty}^{\infty} \frac{d\omega}{2\pi} \frac{\Upsilon_{ll}^T(k\omega)}{\omega}) \\
=& \int d\boldsymbol{r} \varepsilon_{zsl}^2 r_s^2 \int \frac{d\boldsymbol{k}}{(2\pi)^3} (2\pi)^3 \delta(k) e^{i\boldsymbol{k}\cdot\boldsymbol{r}} \int_{-\infty}^{\infty} \frac{d\omega}{2\pi} \frac{\Upsilon_{ll}^T(k\omega)}{\omega} \\
=& \int d\boldsymbol{r} \varepsilon_{zsl}^2 r_s^2 \rho_n \\
=& \rho_n \int d\boldsymbol{r} (x^2 + y^2)
\end{aligned}
$$

In the second line we used $\nabla_k \Upsilon_{ll}^T(k, \omega) = 0$ as $k \to 0$. So we arrived at the conclusion that the moment of inertia is only contributed by the normal component as defined by the transverse current.

4.3 Periodic modulation of density

Optical lattice has been used to quantum simulate the solid state crystalline structure for a long time. By shining two counterpropagating laser beams which coherently generates a standing-wave intensity pattern, the atoms cooled to ultracold temperature can be efficiently trapped in the lobes of the induced dipole force potential. Because the standing wave pattern is periodic in space, the density modulation of atoms mimics that of electrons in a normal crystal. However, the cold atoms we used are bosons, which is fundamentally different from electrons and form a BEC that displays macroscopic matter wave coherence.

When the lattice is shallow and the depth is lower than the chemical potential, it is known that the atoms can freely flow despite the varying lattice potential, thus one knows that the matter wave coherence still remains. When one ramps up the lattice depth above the chemical potential, classical hydrodynamics are forbidden, but quantum tunneling process can kick in, which again helps maintain the whole cloud as a coherent state. It is predicted and later realized in the lab that in a particularly deep lattice, a quantum phase transition can happen at zero temperature, to a tensor product of atomic number Fock state reminiscent of the Mott insulator discovered in solid state physics. The transition is usually called the superfluid to Mott insulator transition, marking the change to a qualitatively different transport properties and complete loss of atomic coherence across many lattice sites. The cold atom variant of this transition was discovered in the Bose-Hubbard model realized with a quantum simulator.

However, there hasn't been much attention to whether the superfluid is still pure before the transition happens. Indeed we will find that the superfluid fraction is suppressed to close to 0 long before the atomic coherence is lost, meaning that a superfluid transport experiment will find little superfluid current. This paper develops different ways of understanding this fact. We start with the simplest pictorial approach in a similar spirit to the famous Leggett formula.

It can be formally proved that the definition of the superfluid density in section 4.2 is equivalent to the following definition: A superfluid is manifested by an order parameter $\varphi(\mathbf{r}) = \sqrt{\rho^{\mathrm{sf}}}\exp[i\theta(\mathbf{r})]$. We consider a superfluid subjected to a "printed" phase pattern, and define the superfluid density ρ^{sf} in terms of the induced current

$$J_i = \rho_{ij}^{\mathrm{sf}}\left[\hbar\partial_j\theta/m\right]$$

This definition clearly shows the tensor nature of this quantity.

Now let's consider a periodically modulated BEC. A BEC has its own order parameter $\psi(\mathbf{r}) = |\psi(\mathbf{r})|\exp[i\phi(\mathbf{r})]$, and we will only consider the problem in a setting where the system is well described by the mean field Gross-Pitaevskii equation (GPE). As in Fig. 4.1 we apply a phase winding a 2π across the whole BEC, and assume periodic boundary condition over the dimension length of the system L. We solve for the BEC wavefunction in such as setup. Because of the continuity equation which ensures there isn't a time dependence in the solution, the current $J(x) = \rho(x) \left[\hbar \partial_x \phi(x)/m\right]$ has to be a constant of x. The only way to do that is to introduce a periodically modulated phase and velocity as well $v(x) = \hbar \partial_x \phi(x)/m$.

Now we consider the superfluid parameter to be a coarse-grained version of the condensate parameter, but in a subtle way. We should be able to directly equalize the phase winding of both over L. From macroscopic considerations the current is $J = \rho^{\text{sf}} \left[\hbar \partial_x \theta(x)/m\right] = 2\pi\hbar\rho^{\text{sf}}/(mL)$. Equating the currents obtained from considering the condensate mode and the SF order parameter and integrating over the whole system yields Leggett's equation

$$\rho^{\text{sf}} = L \left[\int \rho(x)^{-1} dx \right]^{-1} = a \left[\int_{\text{UC}} \rho(x)^{-1} dx \right]^{-1}. \tag{4.11}$$

This implies that $\rho^{\text{sf}} \leq \bar{\rho}$, where $\bar{\rho}$ is the spatial average of the condensate density and as we discuss below the remaining density $\bar{\rho} - \rho^{\text{sf}}$ behaves as a pseudo-normal fluid. In the more general context which does respect the time reversal symmetry, the Leggett expression for ρ^{sf} is an upper bound for the SF density in systems with crystalline order [40].

The pictorial explanation captures the essence of the superfluid transport in a periodic system. Now we can actually calculate the ρ_n in another approach, by using the definition of the normal fluid density in section 4.2. We note that this definition is applicable to any system, and generalizes to the cases where GPE is inapplicable due to the onset of fluctuations.

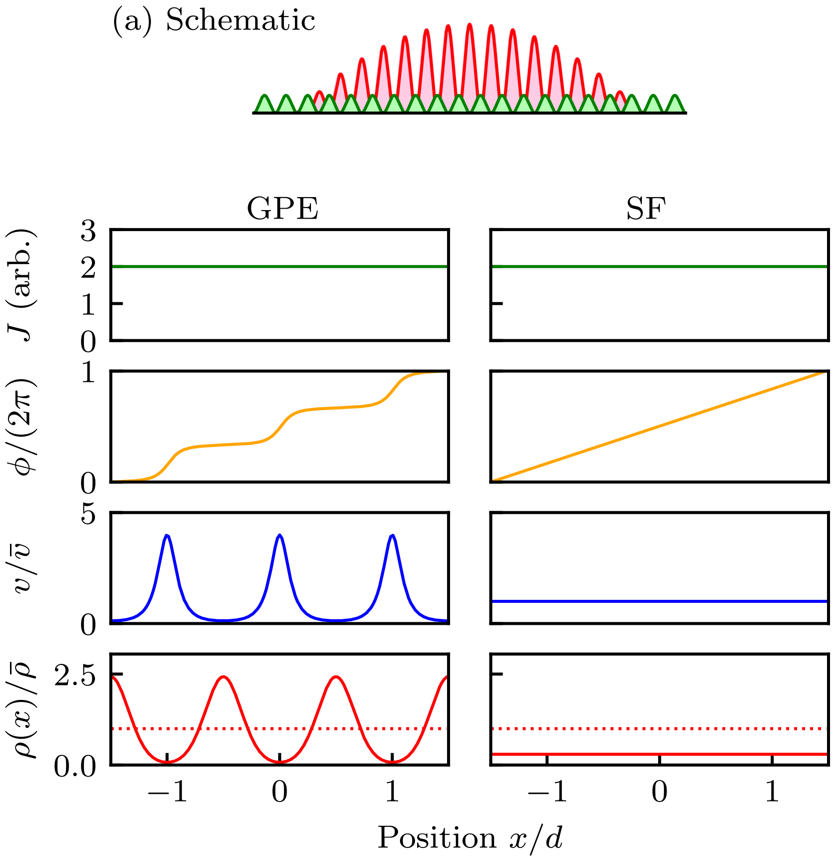
(a) Schematic

Figure 4.1: Concept. (a) The BEC is confined in a harmonic trap superimposed with a 1D optical lattice (along $\mathbf{e}_x$, green), spatially modulating the density (red). The left and right columns indicate the response of the condensate and SF to a force. These plot: current (green), phase (orange), local velocity (blue) and density (red). The red dashed line plots the mean density $\bar{\rho}$.

4.4 Josephson relation and sum rules

Now we switch to the motivation of our experiment. As we have seen, superfluid transport lies in the zero frequency and zero momentum response to the gauge coupling, which should have implications in the low energy excitations of the many-body system. Indeed, this relation can be formulated using linear response again. The superfluid density has an explicit relation to Green function of the many-body Hamiltonian, known as the Josephson sum-rule[43]. Here we derive the sum-rule and relate it to the measurable quantities of the anisotropic sound velocities.

We look at the variation of the condensate wavefunction $\psi(x) = \sqrt{|\psi|}\exp[i\phi(\mathbf{r})]$ due to the external perturbation Hamiltonian $H' = -\int d\mathbf{r}\psi(\mathbf{r})\xi(\mathbf{r})$, where $\xi(\mathbf{r}) = \xi\exp\{\mathbf{i(k\cdot r-\omega t)}\}$. According to linear response theory,

$$\delta\langle\psi(\mathbf{r})\rangle = e^{ik\cdot r-i\omega t}\xi\int_{-\infty}^{\infty} d\omega'\frac{\mathbf{A}(\mathbf{k},\omega')}{\omega+i\eta-\omega'} \tag{4.12}$$

where $A(\boldsymbol{k},\omega)=\int d\mathbf{r}e^{-i\boldsymbol{k}\cdot(\boldsymbol{r}-\boldsymbol{r}')}\int_{-\infty}^{\infty}dte^{i\omega(t-t')}\left\langle\left[\psi(\boldsymbol{r},t),\psi^{\dagger}\left(\boldsymbol{r}',t'\right)\right]\right\rangle$ is the spectral density, and is related to the retarded one-body Green function

$$A(\mathbf{k},\omega)=i\hbar\int d\left(\mathbf{r}-\mathbf{r}'\right)e^{-i\mathbf{k}(\mathbf{r}-\mathbf{r}')}\int_{-\infty}^{\infty}d\left(t-t'\right)e^{i\omega(t-t')}G^{\mathrm{ret}}\left(\mathbf{r},t;\mathbf{r}',t'\right).$$

Similarly, the variation of the current operator $\mathbf{J}(\mathbf{r})=\rho\mathbf{v}$ is

$$\delta\langle\mathbf{J}(r)\rangle = e^{i\mathbf{k}\cdot\mathbf{r}-i\omega t}\xi\int d\omega'\frac{\boldsymbol{\Gamma}\left(\mathbf{k},\omega'\right)}{\omega+i\eta-\omega'} \tag{4.13}$$

with $\Gamma(k,\omega)=\int d\mathbf{r}dte^{-i\omega(t-t')+ik(r-r')}\langle\left[J(r,t),\psi^{\dagger}\left(r',t'\right)\right]\rangle$. In the next we first take $\omega\to 0$ limit, and then take $\mathbf{k}\to 0$.

We want to relate $\delta\langle\mathbf{J}(\mathbf{r})\rangle$ to $\delta\langle\psi(\mathbf{r})\rangle$, as to define the superfluid density. To do that, one observes from the continuity equation $-i\mathbf{k}\cdot\mathbf{J}=\partial_t\rho$ so that

$$\mathbf{J}(\mathbf{r},t)=\int d\mathbf{k}\mathbf{J}(\mathbf{k},t)e^{ik\cdot r}=\int d\mathbf{k}d\mathbf{r}'e^{ik(r-r')}\frac{i\vec{k}}{k^{2}}\partial_t\rho(r',t).$$

Plug it back to equation 4.13, and after some algebra

$$\begin{aligned}\Gamma(\mathbf{k},\omega) &= \int d\mathbf{r}dte^{-i\omega(t-t')+ik(r-r')}\int d\mathbf{k}'d\mathbf{r}''e^{ik'(r-r'')}\frac{i\vec{k'}(-i\omega)}{k'^2}\langle\left[\rho\left(r'',t\right),\psi^\dagger\left(r',t'\right)\right]\rangle \\ &= \int dte^{-i\omega(t-t')}\int d\mathbf{r}''e^{ik(r''-r')}\frac{\mathbf{k}\omega}{k^2}\langle\left[\rho\left(r''t\right),\psi^\dagger\left(r't'\right)\right]\rangle\end{aligned} \tag{4.14}$$

Hence

$$\begin{aligned}\delta\langle\mathbf{J}(\mathbf{r},t)\rangle &= \int d\omega'\frac{\mathbf{\Gamma}\left(k,\omega'\right)}{-\omega'}e^{i\mathbf{k}r}\xi \\ &= -\int d\omega e^{i\mathbf{k}r}\xi\int dte^{-i\omega(t-t')}\int d\mathbf{r}e^{ik\cdot(r-r')}\frac{\vec{k}}{k^2}\langle\left[\rho(r,t),\psi^\dagger\left(r',t'\right)\right]\rangle \\ &= -e^{i\mathbf{k}r}\xi\int d\mathbf{r}e^{i\mathbf{k}\cdot(r-r')}\frac{\vec{k}}{k^2}\left\langle\left[\rho(rt),\psi^\dagger\left(r't\right)\right]\right\rangle \\ &= -e^{ik\cdot r}\xi\frac{k}{k^2}\left\langle\psi^\dagger(r,t)\right\rangle\end{aligned} \tag{4.15}$$

In the last equality we used $\left[\rho(r),\psi^\dagger\left(r'\right)\right] = \left[\psi^\dagger(r)\psi(r),\psi^\dagger\left(r'\right)\right] = \psi^\dagger(r)\delta\left(r-r'\right)$.

For a superfluid system, $\langle\psi(\mathbf{r})\rangle = \psi_0 + \delta\langle\psi(\mathbf{r})\rangle = e^{i\theta(\mathbf{r})}\psi_0$ where we have defined the superfluid phase $\theta(\mathbf{r})$. With the periodic modulation of density introduced by the optical lattice, we take $\psi(\mathbf{r}) \to \bar{\psi}(\mathbf{r}) = a_x a_y a_z\int_{\mathrm{UC}}d\mathbf{r}\psi(\mathbf{r})$.[44] Now we have

$$\begin{aligned}\delta\langle\bar{\mathbf{J}}\rangle &= -e^{i\mathbf{k}\cdot r}\xi\frac{\mathbf{k}}{k^2}\left\langle\bar{\psi}^\dagger\right\rangle \\ \delta\langle\bar{\psi}\rangle &= -e^{i\mathbf{k}\cdot r}\xi\int d\omega\frac{A(k,\omega)}{\omega} \\ \frac{m}{\hbar}\delta\langle\bar{\mathbf{J}}\rangle &= \rho^{sf}\nabla\theta = \rho^{sf}\nabla\frac{\delta\langle\bar{\psi}\rangle}{i\bar{\psi}_0} = \rho^{sf}_{\hat{k}}\mathbf{k}\frac{\delta\langle\bar{\psi}\rangle}{\bar{\psi}_0}\end{aligned}$$

and take $\mathbf{k} \to 0$

$$\rho^{sf}_{\hat{k}} = m\lim_{\mathbf{k}\to 0}\frac{\bar{\psi}_0^*\bar{\psi}_0}{k^2\int_{-\infty}^{+\infty}d\omega\frac{\mathbf{A}(k,\omega)}{\omega}} \tag{4.16}$$

where $\rho^{sf}_{\hat{k}} = \rho^{sf}_{ij}\hat{\mathbf{k}}_j$. For homogeneous weakly interacting Bose gas at $T = 0$, the Bogoliubov theory gives $\mathbf{A}(\mathbf{k},\omega)=\frac{mc}{2k}[\delta(\omega-ck)-\delta(\omega+ck)]$ as $k\to 0$, which leads to $\rho^{sf}_{\hat{k}}=|\psi_0|^2$. For anisotropic systems, the poles of $\mathbf{A}(\mathbf{k},\omega)$ i.e. the sound velocities along different directions will determine the anisotropic superfluid density.

4.5 Anisotropic sound measurement

From this section on we will concentrate on the specific case of a GPE described weakly interacting BEC gas loaded in the optical lattice, and apply our established formalism.

We used $^{87}\mathrm{Rb}$ BECs with $N\approx 2\times 10^5$ atoms in the $|F=1,m_F=1\rangle$ hyperfine ground state. An elliptical $1064\ \mathrm{nm}$ trapping laser traveling along $\mathbf{e}_x$ provided strong vertical confinement with frequency $\omega_z=220$ Hz; the in-plane frequencies, from $\omega_{x,y}=2\pi\times(34,51)$ Hz to $2\pi\times(56,36)$ Hz, were optimized for our different experiments. We created a 1D optical lattice using a retro-reflected $\lambda=532\ \mathrm{nm}$ laser traveling along $\mathbf{e}_x$, giving an $a=266\ \mathrm{nm}$ lattice period, comparable to the $\xi=\mathbf{0.2}\ \mathrm{nm}$ healing length. The optical lattice was linearly ramped on in $\mathbf{100}\ \mathrm{ms}$ to a final depth up to $15\ E_\mathrm{r}$, with single photon recoil energy $E_\mathrm{r}=\hbar^2k_\mathrm{r}^2/(2m)$ and momentum $\hbar k_\mathrm{r}=2\pi\hbar/\lambda$. For Bragg experiments the final state was measured using resonant absorption imaging after a $15\ \mathrm{ms}$ time of flight (TOF); while for collective mode experiments measurements were performed in-situ using partial transfer absorption imaging [45].

The speed of sound for diagonal ρ^{sf}_{ij} can be obtained from $mc_i^2=\kappa^{-1}\rho^{\mathrm{sf}}_{ii}/\rho$ in terms of the compressibility $\kappa=\rho^{-1}\left(\partial\rho/\partial\mu\right)$ and the chemical potential μ. The ratio of the speed of sound along $\mathbf{e}_x$ and $\mathbf{e}_y$

$$\frac{c_x^2}{c_y^2}=\frac{\rho^{\mathrm{sf}}_{xx}}{\rho^{\mathrm{sf}}_{yy}}=\frac{\rho^{\mathrm{sf}}_{xx}}{\rho}, \tag{4.17}$$

provides direct access to the different components of the superfluid density.

We Bragg-scattered the BEC off of a weak sinusoidal potential with wavevector k slowly moving with velocity v by patterning a laser beam with a digital micro-mirror device (DMD [46]). The two complex components of this potential in effect drive two-photon transitions with difference-wavevector $\delta k = 2k$ and angular frequency $\delta\omega = 2kv$. We applied this potential for $\approx 5\text{ms}$; Bragg transitions ensued when the difference energy and momentum were resonant with the BEC's phonon mode. We detected the Bragg-scattered population after TOF.

In Fig. 4.2 are examples of the measured sound velocities by projecting the moving lattice with wavevector ranging from d_{B} from $2\pi/2\ \mu\text{m}^{-1}$ to $2\pi/6\ \mu\text{m}^{-1}$ along and perpendicular to the optical lattice direction $\mathbf{e}_x$ and $\mathbf{e}_y$. The obtained dispersion relation is in a good fit linear to $k = 2\pi/d_{\text{B}}$ which shows the phonon characteristics of the excited modes. Within local density approximation (LDA) and under near isotropy of the harmonic trap along $\mathbf{e}_x$ and $\mathbf{e}_y$, the sound velocities are to a good approximation the slopes of the dispersion curves. With increasing optical lattice depths, the sound velocity in $\mathbf{e}_x$ is largely reduced in accordance to the increase of effective mass m^*. The perpendicular direction $\mathbf{e}_y$ is minimally affected by the optical lattice and shows negligible change of the sound velocity.

As stated in Eq. (4.17), the SF densities are related to the sound velocities. Because there isn't density modulation in $\mathbf{e}_y$ we have assumed that $\rho^{\text{sf}}_{yy} = \rho$ the total density. In Fig. 4.2 the main result of measured SF density along $\mathbf{e}_x$ is shown. Meanwhile, we run the 2D GPE simulation in imaginary time to find the ground state wavefunction in the lattice. We select one unit cell in the center of trap where LDA is satisfied because $d \ll R_{x,y,z}$ where $R_{x,y,z}$ are the Thomas-Fermi radii of the cloud. The Leggett equation of supersolid is then calculated by integrating the density function over the unit cell, which agrees well with the measurement result. In the meanwhile, we

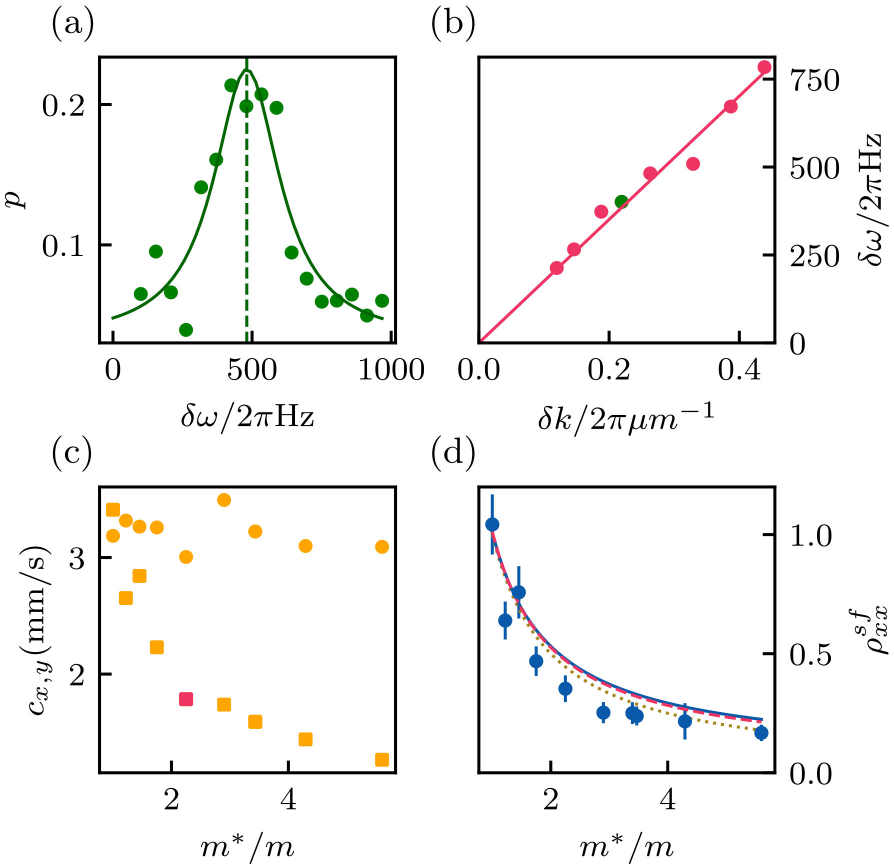

Figure 4.2: Sound velocities measured by Bragg scattering. (c) along $\mathbf{e}_x$ (blue squares) and $\mathbf{e}_y$ (orange dots) by the Bragg scattering. The inset (b) shows an example of the measured dispersion relation at a certain lattice depth U_0. (a)An example of the transferred population fraction with the changing moving speed of the pattern. (d)The measured SF density ρ^{sf}_{xx} compared with the Leggett equation. Both results are also compared with a BdG calculation in a homogeneous gas and an effective mass m/m^* curve. All the simulation is done with real experimental parameters without any fitting.

numerically solved Bogoliubov-de-Gennes (BdG) equations to find the sound velocities and ρ^{sf}_{xx}, which perfectly aligned with the Leggett equation. (Fig. 4.2(d))

4.6 Anisotropic system hydrodynamics

The BEC in an optical lattice that we had in the experiment – made of small 266 nm periods – can be thought of as single particle problem in a periodic potential, which gives rise to the band structure, and then dressed by the mean field interaction. The first part comes from the usual solid state physics treatment, after which we project the Hilbert space to the lowest band, and derive the long wavelength dynamics in terms of the ”effective mass”. Superfluid properties are considered further in this framework by rewriting the problem in GPE.

This section considers the anisotropic system manifested by different effective masses along different directions. Depending on the problem of interest, the effective mass is either a vector or tensor. I will only consider a two dimensional system.

Now I start from the GPE with effective mass tensor

$$i\partial_t\psi = -\frac{\hbar^2}{2}\left(m^{-1}\right)_{ij}\partial_i\partial_j\psi + V\psi + g|\psi|^2\psi$$

By taking conjugate and algebra, we can easily get an equation of the continuity equation form, and the density current

$$j_i = \frac{\hbar}{2i}\left(m^{-1}\right)_{ij}\left(\psi^*\partial_j\psi - \psi\partial_j\psi^*\right)$$

Let $\psi = \sqrt{\rho}e^{i\phi}$, $\rho = |\psi|^2$ and $j_i = \rho v_i$, we know $v_i = \left(m^{-1}\right)_{ij}\partial_j\phi$. This is one of the key results of this section. Plugging this back to the GPE, we get the hydrodynamic equations:

$$\begin{cases} \partial_t\rho + \partial_i j_i = 0 \rightarrow \partial_t\rho + \partial_i\left(\rho\left(m^{-1}\right)_{ij}\partial_j\phi\right) = 0 \\ -\partial_t\phi = \frac{1}{2}\left(m^{-1}\right)_{ij}\partial_i\phi\partial_j\phi + V + g\rho \end{cases}$$

Now let's find the collective modes: make small perturbations about the equilibrium state,

$$\rho \rightarrow R + \delta\rho$$

$$\phi \rightarrow \phi + \delta\phi$$

$$V \rightarrow V + \delta V$$

$$\begin{cases} \partial_t\delta\rho + \left(m^{-1}\right)_{ij}\left[\partial_i\delta\rho\partial_j\phi + \partial_i\rho\partial_j\delta\phi + \delta\rho\partial_i\partial_j\phi + \rho\partial_i\partial_j\delta\phi\right] = 0 \\ -\partial_t\delta\phi = \frac{1}{2}\left(m^{-1}\right)_{ij}\left[\partial_i\phi\partial_j\delta\phi + \partial_i\delta\phi\partial_j\phi\right] + \delta V + g\delta\rho \end{cases}$$

Because of the initial state satisfies $\phi = 0$ and $\rho = \frac{\mu - \frac{1}{2}m\omega_i^2 x_i^2}{g}$,

$$\begin{cases} \partial_t\delta\rho + \left(m^{-1}\right)_{ij}\left[\partial_i\rho\partial_j\delta\phi + \rho\partial_i\partial_j\delta\phi\right] = 0 \\ -\partial_t\delta\phi = \delta V + g\delta\rho \end{cases}$$

Suppose

$$\delta\phi = \delta\phi_{xx}x^2 + \delta\phi_{yy}y^2 + \delta\phi_{xy}xy$$

and $\delta V = 0$, collecting coefficients before all three quadratic terms (I omit the calculation here), the resulting matrix is

$$\begin{pmatrix} \omega^2 - 3\omega_x^2 m\left(m^{-1}\right)_{xx} & -\omega_x^2 m\left(m^{-1}\right)_{yy} & -2m\omega_x^2\left(m^{-1}\right)_{xy} \\ -\left(m^{-1}\right)_{xx} m\omega_y^2 & \omega^2 - 3\omega_y^2 m\left(m^{-1}\right)_{yy} & -2m\omega_y^2\left(m^{-1}\right)_{xy} \\ -2m\omega_y^2\left(m^{-1}\right)_{xy} & -2m\omega_x^2\left(m^{-1}\right)_{xy} & \omega^2 - m\left[\left(m^{-1}\right)_{xx}\omega_x^2 + \left(m^{-1}\right)_{yy}\omega_y^2\right] \end{pmatrix}$$

If $\left(m^{-1}\right)_{xy} = 0$, $\left(m^{-1}\right)_{xx} = \left(m^{-1}\right)_{yy} = m^{*-1}$,

$$\begin{pmatrix} \omega^2 - 3\frac{m}{m^*}\omega_x^2 & -\frac{m}{m^*}\omega_x^2 & 0 \\ -\frac{m}{m^*}\omega_y^2 & \omega^2 - 3\frac{m}{m^*}\omega_y^2 & 0 \\ 0 & 0 & \omega^2 - \frac{m}{m^*}\omega_x^2 - \omega_y^2 \end{pmatrix}$$

The two quadruple mode frequencies are

$$\omega^2 = \frac{3\bar{\omega}^2 \pm \sqrt{9\bar{\omega}^4 - 32\omega_x^2\omega_y^2}}{2}$$

with $\omega_x \to \frac{m}{m^*}\omega_x$, while the scissors mode frequency is $\omega_{sc} = \sqrt{\frac{m}{m^*}\omega_x^2 + \omega_y^2}$.

It can be easily seen from the wavefunction that the scissor mode is decoupled from the other two quadrupole modes. Actually this can be similarly generalized to 3D, where one has three different scissors mode xy, yz, zx. Therefore, although our system is actually 3D, the scissors mode frequency is not changed from the simple 2D result derived here.

4.6.1 Rotational properties

Next I calculate the moment of inertia. In a rotating frame, the (stationary) hydrodynamic equations becomes

$$\begin{cases} \partial_i \left(\rho \left(m^{-1} \right)_{ij} \partial_j \phi \right) - \nabla \cdot \left(\rho \Omega \times r \right) = 0 \\ \frac{1}{2} \left(m^{-1} \right)_{ij} m^{-1} \partial_i \phi \partial_j \phi + \frac{V}{m} + \frac{g\rho}{m} - v \cdot \left(\Omega \times r \right) = 0 \end{cases}$$

Suppose $\phi = \alpha xy$, the second equation is

$$g\rho = x^2 \left(\alpha \Omega - \frac{1}{2} \alpha^2 / m - \frac{1}{2} m \omega_x^2 \right) + y^2 \left(-\alpha \Omega \frac{m^2}{m^*} - \frac{1}{2} \frac{\alpha^2}{m^2} - \frac{1}{2} m \omega_y^2 \right)$$

Plug it to the first equation,

$$\left(\frac{\alpha}{m^*} - \Omega \right) \left(2\alpha \Omega - \frac{\alpha^2}{m} - m \omega_x^2 \right) (-xy) + \left(\frac{\alpha}{m} + \Omega \right) \left(-2\alpha \Omega \frac{m}{m^*} - \frac{\alpha^2}{m^*} - m \omega_y^2 \right) xy = 0.$$

This can be solved in the $\Omega \to 0$ limit

$$\alpha = \Omega \frac{\omega_x^2 - \omega_y^2}{\frac{m}{m^*} \omega_x^2 + \omega_y^2}$$

Hence

$$\langle L_z \rangle = \langle r \times mv \rangle = \alpha \left\langle \frac{m}{m^*} y^2 - x^2 \right\rangle = \frac{\langle x^2 - y^2 \rangle \left\langle \frac{m}{m^*} y^2 - x^2 \right\rangle}{\left\langle \frac{m}{m^*} y^2 + x^2 \right\rangle} \Omega$$

So by definition the moment of inertia is

$$\frac{I}{I_c} = \frac{\langle x^2 - y^2 \rangle \left\langle \frac{m}{m^*} y^2 - x^2 \right\rangle}{\langle x^2 + y^2 \rangle \left\langle \frac{m}{m^*} y^2 + x^2 \right\rangle} \tag{4.18}$$

According to the sum rule

$$(\hbar\omega_{\mathrm{sc}})^2 = \frac{m_1(L_z)}{m_{-1}(L_z)} = \frac{\hbar^2 m \left(\omega_y^2 - \omega_x^2\right) \langle x^2 - y^2 \rangle}{I}$$

it does **not** give the correct scissors mode frequency.

4.6.2 Application to moment of inertia measurement

In the experiment we measured the moment of inertia by imitating the torsion experiment of solid helium. Basically we rotate the anisotropic harmonic trap by a small angle and measure the evolution period. It turns out that full analytic solution of this problem is possible via the effective mass approximation.

We already calculated the moment of inertia in the above section. Now we will relate the scissors mode frequency to it via the dynamical equations. It turns out that in our experiment the rotation of the harmonic trap also changes the torsion spring constant, which we have to calculate below.

One can write the GPE in the hydrodynamic equations form

$$\partial_t J_k + \partial_j T_{jk} + \rho \partial_k \left(\frac{V_{ext}}{m}\right) = 0. \tag{4.19}$$

where

$$T_{jk} = \frac{\hbar^2}{4m}(\partial_j \psi^* \partial_k \psi - \psi^* \partial_j \partial_k \psi + c.c) + \frac{1}{2} g \delta_{jk} |\psi|^4 \tag{4.20}$$

is the stress tensor. We calculate the angular momentum density

$$\Pi_z = -i\frac{\hbar}{2}(\psi^* x \partial_y \psi - \psi x \partial_y \psi^* - \psi^* y \partial_x \psi + \psi y \partial_x \psi^*) = x J_y - y J_x. \tag{4.21}$$

and its time evolution satisfies

$$\partial_t \Pi_z = x \partial_t J_y - y \partial_t J_x = -x \partial_j T_{jy} + y \partial_j T_{jx} - x\rho \partial_y (\frac{V_{ext}}{m}) + y \rho \partial_x (\frac{V_{ext}}{m}). \tag{4.22}$$

Now we assume the lattice is along the e_x and projects to an effective mass m^*. The above equation varies to

$$\partial_t \Pi_z = x \partial_t J_y - y \partial_t J_x = -x \partial_j T_{jy} + y \partial_j T_{jx} - x\rho \partial_y (\frac{V_{ho}}{m^*}) + y \rho \partial_x (\frac{V_{ho}}{m}). \tag{4.23}$$

It is clearly to see now that the stress tensor integrates to zero, so the torsion torque one has derived

$$\tau = \int dx dy \frac{1}{2}(\frac{m}{m^*}\omega_x^2 - \omega_y^2) xy = \frac{1}{2}(\frac{m}{m^*}\omega_x^2 - \omega_y^2)\langle xy \rangle$$

Consider the cloud being rotated by a small angle θ, the $\langle xy \rangle$ moment can be derived in terms of coordinates of the co-rotating frame

$$\langle xy \rangle = \langle (x' \cos\theta - y' \sin\theta)(y' \cos\theta + x' \sin\theta) \rangle = \langle x'^2 - y'^2 \rangle \sin 2\theta$$

The torque is derived as

$$\tau = (\frac{m}{m^*}\omega_x^2 - \omega_y^2)\langle x'^2 - y'^2\rangle\theta \tag{4.24}$$

where $\langle x'^2 - y'^2\rangle$ depends only on the initial Thomas-Fermi distribution of the cloud, as $\theta \to 0$.

4.7 Numerical calculation of the rotational properties

We can verify that the effective mass results are correct when the approximation is valid, by numerical simulation directly from a GPE. But the numerical approach extends to the general including large lattice period case,

First we run a real time simulation of the scissors mode experiment and discuss some qualitative features. As in Fig. 4.3, when there is not optical lattice, the evolution is simple as expected. Here the first 10 ms was used to rotate the trap to impose to the cloud some angular momentum L_z, and then the trap was kept stationary at angle=0. The lattice is always along the e_x axis. We see oscillations of angle and xy moment at the expected scissors mode frequency $\omega_{sc} = \sqrt{\omega_x^2 + \omega_y^2}$. Here we note that the xy moment is proportional to the angle when it is small. The angle of rotation is derived by fitting the density profile to a rotated Gaussian, the same as how we processed the experimental data. Special notation should be paid to the dynamic variables. $L_z = xp_y - yp_x$ oscillates out of phase to the angle. And here we calculate the torque using

$$\tau = -x\rho\partial_y(\frac{V_{ext}}{m}) + y\rho\partial_x(\frac{V_{ext}}{m}).$$

As shown in (d), the torque is again in phase oscillating with the angle, and in fact the ratio between them is the spring constant we are interested in to derive the moment of inertia.

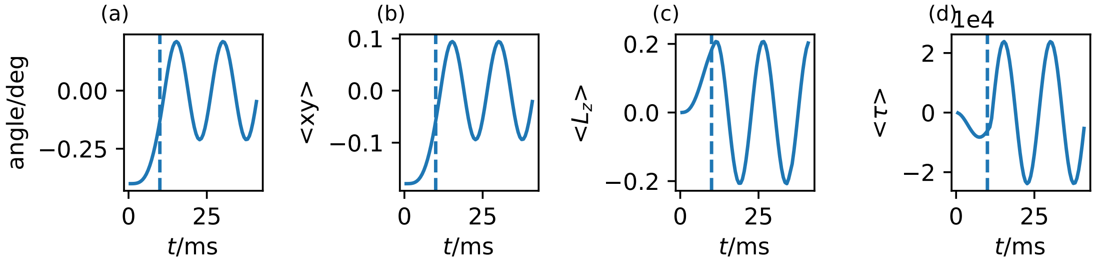

Figure 4.3: Real time evolution of scissor mode when there is not lattice. The units in (b,c,d) are arbitrary.

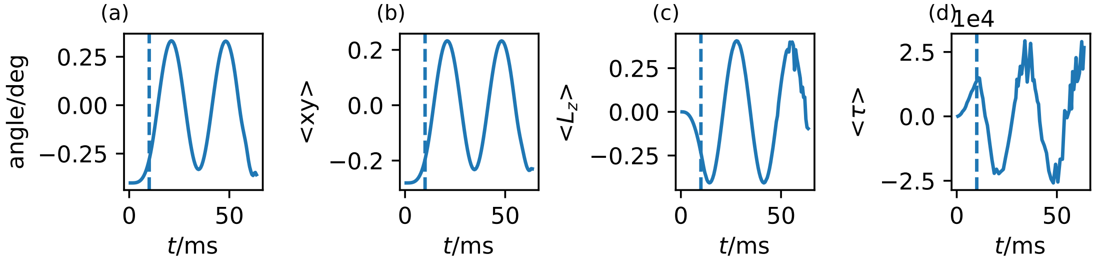

Figure 4.4: Real time evolution of scissor mode when there is optical lattice of period 1 μm and depth $U_0 = 28E_r$.

Now let's apply the optical lattice. For qualitative demonstration we choose a large period lattice of 1 μm and depth $U_0 = 28E_r$. The response to the kick is slightly different, but the angle and xy moment still shows similar features of the cloud following the rotating trap potential and then oscillates about the e_x axis. What is surprising is the in the dynamic variable: one can see that the L_z and τ are both opposite sign compared to the case of $U_0 = 0$! This happens when U_0 is large enough so that the dipole mode frequencies ω_x^d and ω_y^d are inverted. This fact is transparent in the equation 4.24 that we derived in the last section, but here we have a larger period lattice where effective mass description is invalid at all. The inverted sign also suggests that the moment of inertia of the gas goes negative (because the orientation of the cloud does not change)! The inverted I/I_c is also predicted in the equation 4.18.

There is another simulation to show this. We can directly simulate what happens in the

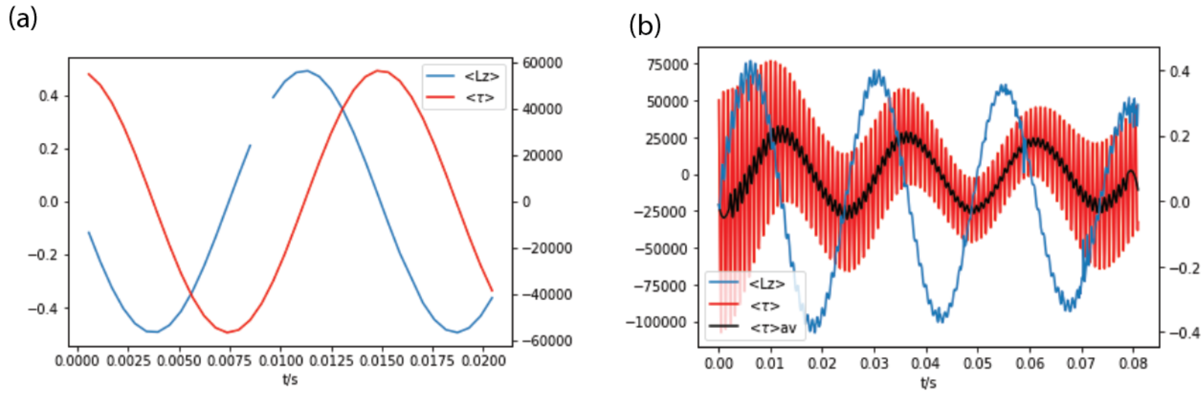

Figure 4.5: Real time simulation when quenching the angle of the harmonic trap. (a) No lattice. (b) 2 μm lattice at 25 E_r.

experiment. We find the ground state of the cloud in the dipole trap that is rotated by 1 deg, and then show the real time evolution after the trap is quenched back to e_x at $t = 0$. The comparison of with or without the lattice is shown in Fig. 4.5. The major difference is that the quench induced significant high frequency oscillations in the dynamical variables like τ and L_z. This is due to that the quench of the trap rotation from 1 deg to 0 excites populations to higher bands, so one expects that the observed micromotion at the frequency of about $> 4E_r/h$. However, after averaging over the micromotion by applying a low pass filter (in (b)), one gets again the negative signs in these variables, consistent with the previous observation.

One might still be skeptical of the negative spring constant and moment of inertia because they are simply counter-intuitive. Below we compare the simulation results to the effective mass hydrodynamics calculation. The results are shown in Fig. 4.6. We see agreement between the GPE simulation and the effective mass analytical result.

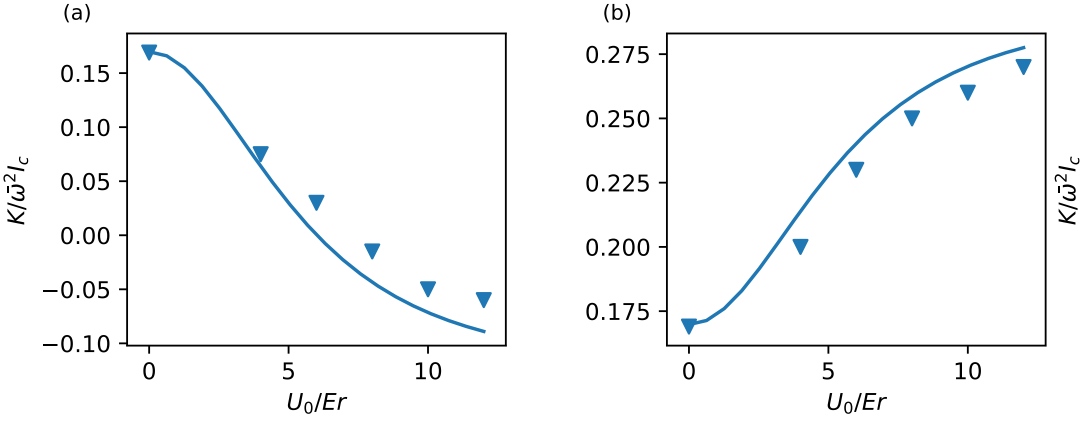

Figure 4.6: Simulated results compared to the effective mass formula in the last section. (a)Harmonic trap $2\pi\times$(56,36)Hz; (b) (36,56)Hz. The triangles are measured from GPE simulations and the curves are calculated from equation 4.24. The numerical simulation in done in a $d = 400$nm period lattice.

4.8 Measurement of moment of inertia

For highly anisotropic traps, the scissors mode describes a fixed density distribution pivoting by a small angle θ about the trap center. In this case we quantify the dynamics in terms of the Lagrangian $L = I\dot{\theta}^2/2 - V(\theta)$, for moment of inertia I and potential energy $V(\theta)$. The ”torsion” spring constant $K = -\theta^{-1}\partial_\theta V$ and the resulting oscillation frequency ω directly gives the moment of inertia $I = K/\omega^2$, which we interpret as resulting from the changing SF density.

In our optical lattice, we use the DMD to pulse an elliptical harmonic potential tilted by $\sim$0.05 to 0.14 from $\mathbf{e}_x$ for $\approx 1\ \mathrm{ms}$, then turn off the pulse and let the BEC evolve in the original trap for variable amount of time. The pulse excites mostly the scissors mode $\delta\rho_{xy}xy$ of the harmonically trapped cloud, which undergoes angular rotation with a period determined by the harmonic trap frequencies as well as the SF densities. To measure the angle, we very briefly address the microwave transition to transfer $\sim 20\%$ of atoms to the $|F = 2, m_F = 2\rangle$ state and pulse the probe light to take an in-situ absorption image. We fit the obtained density profile to a rotated Gaussian distribution to extract the angle. In order to accurately determine the trap frequencies, we also measure the dipole modes in $\mathbf{e}_x$ and $\mathbf{e}_y$ by pulsing magnetic gradient fields.

Fig. 4.7 shows the measurement results of the collective mode frequencies at varied lattice depths, which agrees well with the hydrodynamic theory prediction. These data show ω/ω_0 drops when the lattice is normal to the long-axis of the trap, yielding a major change of the moment of inertia only when the SF moves along the lattice. This is in agreement with our expectation that the non-classical part in the moment of inertia should change when the suitable component of the SF density tensor decreases. To show the effect of the lattice on NCRI, we calculated the torsion spring constant K from a 2D GPE simulation, from which the moment of inertia is derived using $I = K/\omega_{sc}^2$ (Fig. 4.7). The NCRI slowly increases when the lattice is along the long-axis, but surprisingly drops rapidly to negative when it is normal. This is purely quantum behavior, and is interpreted by that the normal fluid attaches to the lattice and the angular momentum is only provided by the current of anisotropic ρ^{sf}, which has either its co- or counter-rotating parts suppressed by the density modulation. (Fig. 4.7) We also note that the superfluid flow J^{sf} no longer satisfies the irrtationality condition because of the anisotropy of ρ^{sf}.

4.9 Emergent normal fluid

There is normal fluid component in our system, as calculated in section 4.3 using the sum-rule. However, there is no obvious dissipation mechanism of a normal fluid current as in the two fluid model of liquid helium. One needs to invent new ways to measure the normal fluid current.

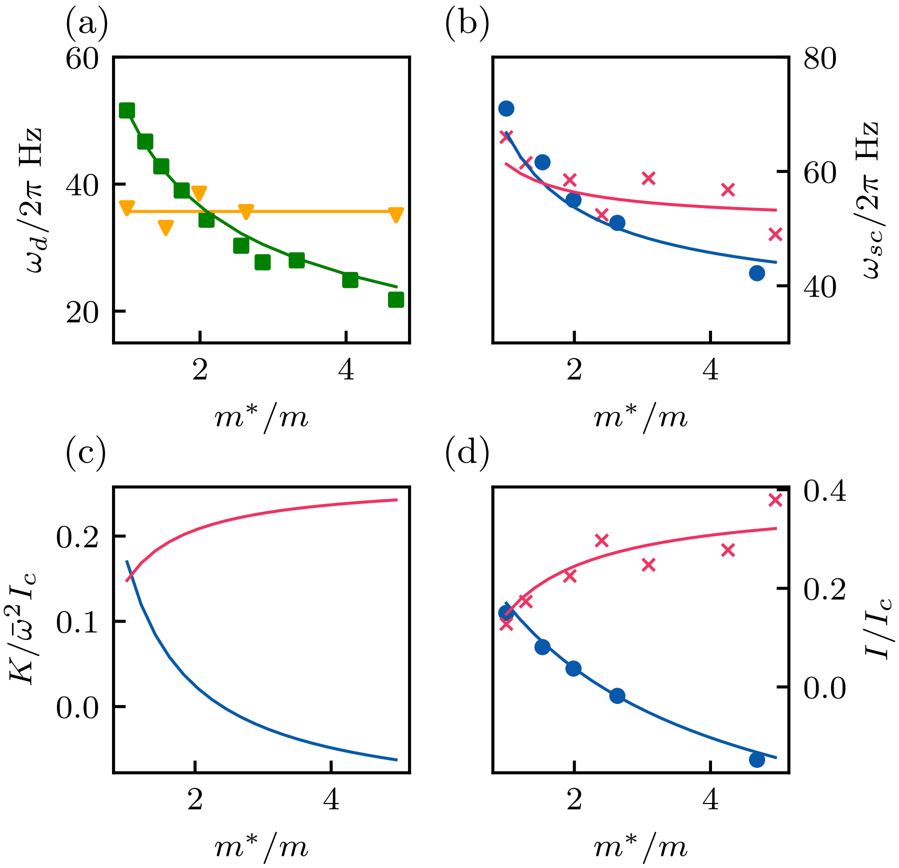

Figure 4.7: The NCRI properties of the trapped BEC gas in a static lattice. (a)The measured dipole mode frequencies, which match the prediction from the calibration of the lattice depth by diffraction experiment. (b)The scissors mode frequency drops with the lattice depth. Theoretical points are obtained by the effective mass hydrodynamics theory in the lowest band. (c)The calculated spring constant from GPE simulated density profile. (d)The inferred NCRI from the scissors mode frequency measurement. In both (b) and (d) the red/black colors stands for two inverted aspect ratios of the trap $2\pi\times$(56,36)Hz and $2\pi\times$(34,51)Hz.

Here we propose several ideas to probe it.

It is naturally found from the sum rule, that the normal fluid responses to a gauge potential coupled to the current operator. In a BEC experiment, one can realize such a potential with the aid of a series of techniques called the artificial gauge field. We make such a Hamiltonian in our experiment, by shining two counterpropagating Raman beams addressing two spinors degree of freedom, introducing a spin-orbit coupling term. By applying a real magnetic field gradient, the Raman detuning is varied in real space, and one can create a spatially varying gauge potential that has nonzero curl. When the Raman coupling is weak enough, the changed effective mass by the Raman coupling itself can be ignored, thus we can focus on the influence by the optical lattice potential.

Let's suppose the gauge potential engineered is of the form $\mathbf{A} = A(y, -x)/r$. When the optical lattice is turned off, the current is entirely diamagnetic and is proportional to the total density. Fig. 4.11 quite clearly displays what to expect when such a gauge field is present with the lattice potential. One would find that a normal fluid current emerges, which is paramagnetic, and proportional to the normal density. This normal current originates from the modulation of the wavefunction by the lattice. Although here our gauge is artificially fixed, the total current being the diamagnetic current plus the emergent normal current is a physical observable, which marks the change of transport property by the lattice.

An analytically simpler example is considering a particle on a ring problem: by wrapping around a 1D stripe of periodic boundary, one gets an azimuthal lattice. Adding the mean field interaction, the problem can again be understood by the GPE. We use potential $V(x, y) = \frac{1}{2}\omega_\perp^2(\sqrt{x^2 + y^2} - R)^2$ for the ring. Now we fix the gauge again $\mathbf{A} = A(y, -x)/R$, where R is the ring radius. (Fig. 4.8) Focusing on the normal part of the current, one can see that the

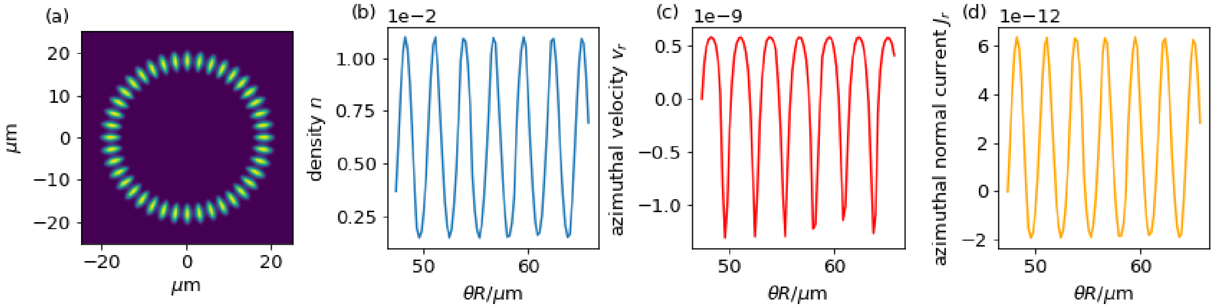

Figure 4.8: The ring trap subjected to a gauge potential. Lattice period $d = 2.85\mu m$ with depth $U_0 = 30E_r$. Plot here are respectively the 2D density, azimuthal density, velocity and current. Y-axes are in arbitrary units.

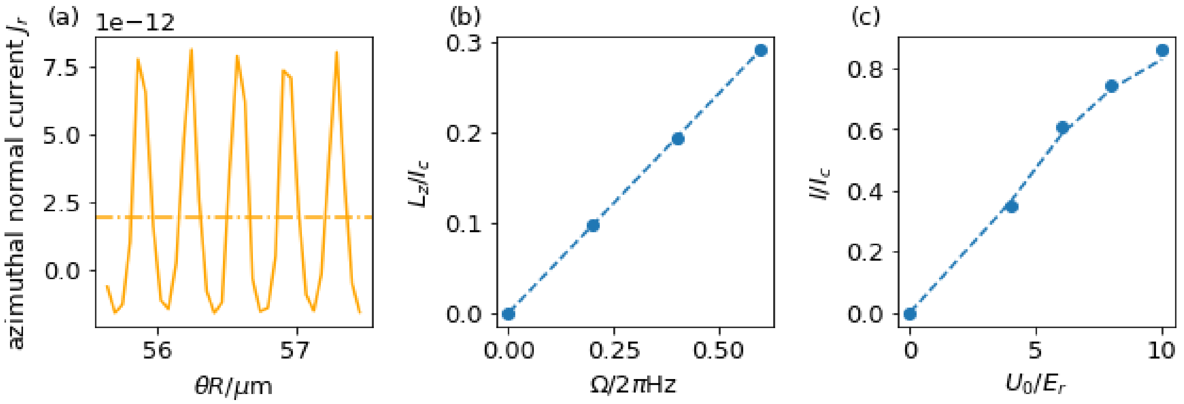

Figure 4.9: Lattice period $d = 0.35\mu m$ on the ring. (a)Normal current and averaged normal current. (b)Integrate normal current to get angular momentum L_z. The result is linear. (c)Calculate the moment of inertia from L_z. The result matches perfectly with the effective mass $1 - m/m^*$ (dashed line) calculated from solving band structure.

azimuthal velocity is strongly modulated over a lattice period – the modulation is in phase with the density modulation, but of a different shape. The normal current being the product of the two, also is modulated, but doesn't average to zero over a unit cell.

For sanity check, we note here that the circumstance is different from when an artificial phase twist (vortex) is applied along ring (Fig. 4.10). There the velocity is never modulated across zero, and the azimuthal total current is a constant, consistent with section 4.3.

Back to the gauge field case, the reason for the modulation of the normal current is that there is another current we haven't counted. The mechanical momentum is $p = -i\partial_\theta\phi - A$.

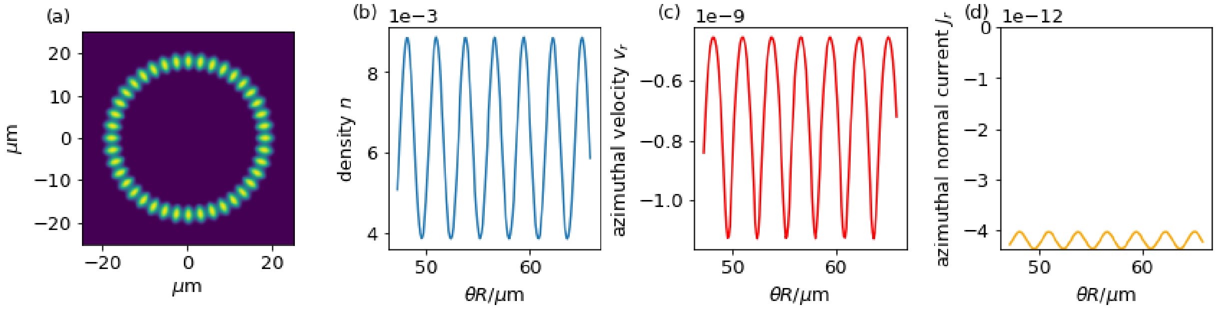

Figure 4.10: The ring trap subjected to a 2π phase twist. Lattice period $d = 2.85\mu m$ with depth $U_0 = 15E_r$. Plot here are respectively the 2D density, azimuthal density, velocity and current. Y-axes are in arbitrary units.

The contribution of the latter term clearly is modulated by the density (because we chose A to be a constant of θ). This is crucial, because otherwise the total current is modulated in space, manifesting non-stationary ground state (a time crystal?) seen from the continuity equation. We verified the fact via real time evolution of the ground state, and did not find varying density or momentum.

We study the quantitative contribution of the normal current (Fig. 4.9) by calculating the angular momentum resulted from the normal current and compare it to the moment of inertia. This time we chose to calculate it in the case of small lattice period for the sake of comparison to analytical result. The found angular momentum increases linearly with the gauge field Ω. And the moment of inertia $I = L_z/\Omega$ is displayed in (c). This compared to the classical $I_c = \langle x^2 + y^2 \rangle$ matches the normal fluid density via the effective mass approximation.

We also studied the problem in the usual harmonic trap, as in our experiment (Fig.4.11). We added a 2D lattice to make e_x and e_y equal weighted, making an isotropic effective mass tensor. The coarse-grained normal current displayed in (a) is clearly reminiscent of perfectly rotating fluid. (b, c) are similar calculation to extract the angular momentum and superfluid density in such as 2D lattice. Furthermore, we applied the result to our experimental setup, where there were 1D lattice and anisotropic trap frequencies. Surprisingly, the moment of inertia doesn't care much about the trap anisotropy in this case.

4.10 Leggett's formula

In the old days Tony Leggett proposed the possibility of the supersolid existence. There he arrived at a limit through very simple arguments. It turned out that the cold quantum gases are ideal systems that closes the gap to his limit. I will briefly review his idea.

Similar to many papers of the same age, this one considers a periodic boundary condition, wrapping the x direction into a ring. Consider the many-body wavefunction on a rotating ring

$$\Psi\left(r_1 r_2 \cdots r_N;\omega\right) = \exp\left\{i\sum_{i=1}^{N}\varphi\left(\overrightarrow{\mathrm{r}}_i;\omega\right)\right\}\Psi_0\left(\overrightarrow{\mathrm{r}_1}\,\overrightarrow{\mathrm{r}_2}\cdots\overrightarrow{\mathrm{r}_\mathrm{N}}\right)$$

where the ansatz has assumed that the phase of the wavefunction is separable into single particle phases and Ψ_0 is real. In the rotating frame the phase satisfies (because of periodic condition in the stationary frame)

$$\varphi(\theta+2\pi) = \varphi(\theta) - 2\pi m R^2\omega/\hbar$$

The energy in this frame is

$$\langle H\rangle_{\text{trial}} = E_0 + \left(\hbar^2/2m\right)\int(\nabla\varphi)^2\rho(\overrightarrow{\mathrm{r}})d\overrightarrow{\mathrm{r}}$$

Now we want to minimize the energy by varying the functional $\psi(x)$. Hence we get the Euler-Lagrange equation

$$\partial_x(\rho\partial_x\phi) = 0.$$

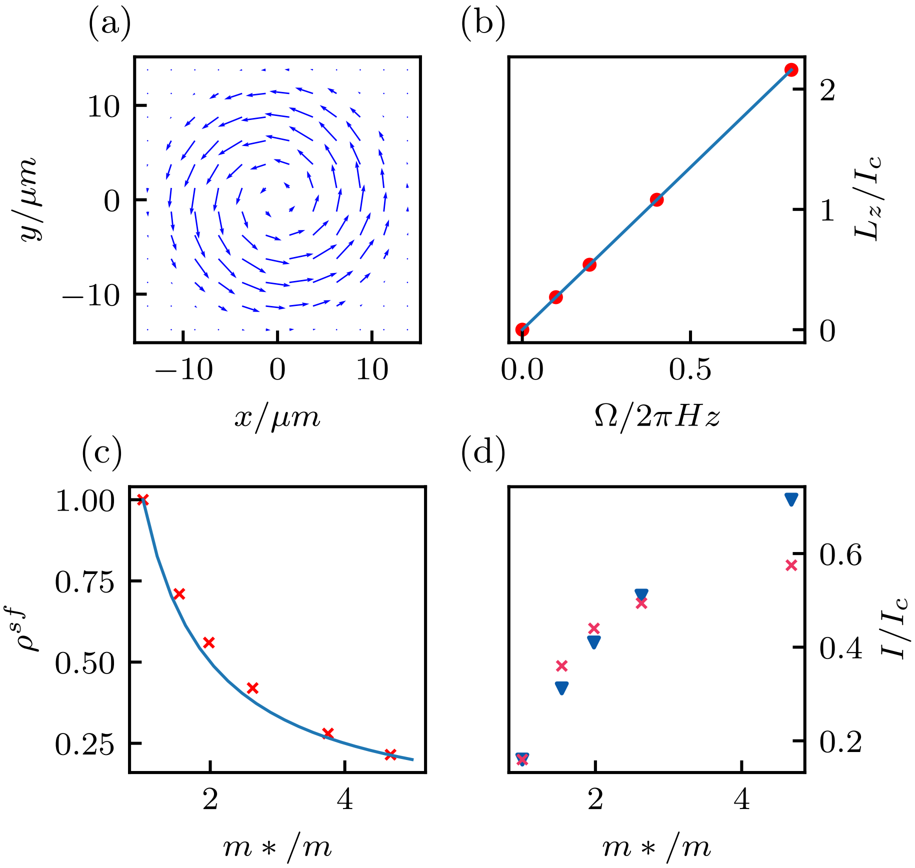

Figure 4.11: The NCRI properties in a rotating lattice. (a)The current after coarse-graining has a rigid-body like distribution in an isotropic trap $2\pi\times$(56,56)Hz and $U_0 = 5E_r$ lattice at d =266nm, and is proportional to the angular velocity Ω. (b)The increase of angular momentum in an isotropic 2D lattice and trap. (c)The SF density is derived from $\rho^{sf} = 1 - I/I_c$. The theory curve is $\rho^{sf} = m/m^*$. (d) The NCRI with a rotating lattice following the trap. Again the red/black colors stands for the two inverted aspect ratios $2\pi\times$(56,36) and $2\pi\times$(36,56)Hz.

With the boundary condition one gets

$$\langle H\rangle_{\text{trial}} = E_0 + \frac{1}{2}NmR^2\omega^2 Q_0$$

with

$$Q_0 \equiv \left(\int_0^1 \frac{dx'}{\int_0^1\int_0^1 \rho'(\vec{r})dy'dz'}\right)^{-1} \leq 1$$

This is the upper limit for the superfluid fraction ρ_s/ρ. For a pure superfluid system there won't be rotational energy associated with any moment of inertia. Leggett argued that a periodic (solid) material must have a superfluid fraction less than 1.

4.11 Spin-orbit coupled superfluid

This section is devoted to the analytical calculation of the rotational velocity field in a spin-orbit coupled gas. The situation is not only analytically simpler but more attractive because such gas is known to have a supersolid phase transition below the critical coupling strength.

The Raman spin orbit coupling Hamiltonian writes

$$H_{sp} = \frac{1}{2m}\left(p_x - \hbar k_0\sigma_z\right)^2 + \frac{1}{2m}p_y^2 + \frac{1}{2m}p_z^2 - \frac{\hbar\Omega}{2}\sigma_x$$

In the BEC we add the interaction term and potential. To derive the hydrodynamic equations, the energy density is calculated at the mean field level

$$\epsilon(\mathbf{r}) = \frac{\hbar^2}{2m}(\nabla\phi)^2 n - \frac{\hbar k_0}{m}\left(\nabla_x\phi\right) s_z + \frac{1}{2}gn^2 + V_{\text{ext}}\, n - \frac{\hbar\Omega}{2}n + \frac{\hbar}{4}\Omega\frac{s_z^2}{n}.$$

And the density current along x is modified by the spin term

$$j_x = \frac{\hbar}{m}\left(n\nabla_x\phi - k_0 s_z\right).$$

We will see that this new term is important and may lead to a different result from the effective mass hydrodynamics.

Now we can get the hydrodynamic equations by varying n, ϕ and s_z respectively

$$\begin{cases} \partial_t n + \frac{\hbar}{m}\nabla\cdot(n\nabla\phi) - \frac{\hbar k_0}{m}\partial_x S_z = 0 \\ \hbar\partial_t\phi = \hbar\Omega/2 - gn - V \\ -\frac{\hbar k_0}{m}\partial_x\phi + \frac{1}{2}\Omega\frac{S_z}{n} = 0 \end{cases}$$

In a rotating frame, we still consider the stationary equations. The first and third equations are modified by ω, while the second equation is unaffected,

$$\nabla\cdot[(\nabla\phi - \omega\times r)n] - k_0 z_x S_z = 0$$

$$-\frac{\hbar k_0}{m}\partial_x\phi + \frac{1}{2}\Omega\frac{S_z}{n} - \omega k_0 y = 0$$

Now we make the anstaz

$$\phi = \alpha xy$$

$$S_z = 2\beta yn$$

with $\vec{v} = \frac{\hbar}{m}n\nabla\phi - \frac{\hbar k_0}{m}S_z\hat{x}$. Equation (2) becomes

$$\frac{\hbar k_o}{m}\alpha = \Omega\beta - \omega k_0$$

hence $\alpha = \frac{\Omega\beta}{k_0} - \omega$. While the first equation generates

$$(\partial_x n) y \left(\alpha + \omega - 2k_0\beta\right) + (\partial_y n)(\alpha - \omega) x = 0$$
$$(\partial_x n) y \left(\frac{\Omega\beta}{k_0} - 2k_0\beta\right) + (\partial_y n) x \left(\frac{\Omega\beta}{k_0} - 2\omega\right) = 0$$

Now plug in the Thomas Fermi n from the middle hydrodynamic equation

$$n = \frac{1}{g}(\mu - V) = \frac{1}{g}\left(\mu - \frac{1}{2}m\omega_x^2 x^2 - \frac{1}{2}m\omega_y^2 y^2\right).$$

One has

$$\omega_x^2 \left(\frac{\Omega}{k_0} - 2k_0\right)\beta + \omega_y^2 \left(\frac{\Omega\beta}{k_0} - 2\omega\right) = 0$$

so

$$\beta = \frac{2\omega\omega_y^2}{\frac{\Omega}{k_0}\left(\omega_x^2 + \omega_y^2\right) - 2k_0\omega_x^2}.$$

Now plug in the result to derive the velocity field,

$$\vec{v} = x\vec{\nabla}\phi - k_0 S_z \hat{x} = \nabla\alpha xy - k_0 2\beta y\hat{x} = \left(y\left(\alpha - 2k_0\beta\right), \alpha x\right)$$
$$\alpha = \frac{\Omega\beta}{k_0} - \omega \to \alpha - 2k_0\beta = \alpha - 2k_0(\alpha + \omega)\frac{k_0}{\Omega} = \alpha\left(1 - \frac{2k_0^2}{\Omega}\right) - \omega\frac{2k_0^2}{\Omega}$$

and

$$\alpha = \omega \cdot \frac{2\omega_y^2\Omega}{\omega_x^2\left(\Omega - 2k_0^2\right) + \omega_y^2\Omega} - \omega = \omega \cdot \frac{\omega_y^2\Omega - \omega_x^2\left(\Omega - 2k_0^2\right)}{\omega_x^2\left(\Omega - 2k_0^2\right) + \omega_y^2\Omega}$$

Now let's look at the isotropic case $\omega_x = \omega_y$. In the anisotropic hydrodynamics approach (int the last section) the moment of inertia vanishes. While here we get

$$\beta = \frac{\omega k_0}{\Omega - k_0^2}$$

and $\alpha = \frac{\Omega\omega}{\Omega - k_0^2} - \omega = \omega \cdot \frac{k_0^2}{\Omega - k_0^2} = k_0\beta$. The velocity is field is

$$\vec{v} = \frac{\omega}{2\Omega - 2k_0^2}\left(-2k_0^2 y, 2k_0^2 x\right)$$

This is just

$$\mathbf{v} = (\omega \times \mathbf{r})\,\frac{\Omega_{cr}}{2\Omega - \Omega_{cr}}$$

where $\Omega_{cr} = 2k_0^2$ is the Raman coupling where the phase transition happens (from the single minimum phase to the plane wave phase). So exactly at the phase transition, the fluid becomes a rigid body.

Next is my result with anisotropy defined (in my notation)

$$1 + \epsilon = \delta = \frac{\omega_y^2}{\omega_x^2}$$

the velocity field is

$$\vec{v} = \left(y\left[\frac{\delta\Omega - (\Omega - 2k_0^2)}{\Omega - 2k_0^2 + \delta\Omega}\frac{\Omega - 2k_0^2}{\Omega} - \frac{2k_0^2}{\Omega}\right], \quad x \cdot \frac{\delta\Omega - (\Omega - 2k_0^2)}{\delta\Omega + \Omega - 2k_0^2}\right)$$

$$\vec{v} = \frac{\omega}{\delta\Omega + (\Omega - 2k_0^2)}\left(\left[\delta\Omega - \left(\Omega - 2k_0^2\right) - 4k_0^2\delta\right]y, \left[\delta\Omega - \left(\Omega - 2k_0^2\right)\right]x\right)$$

Integrating it one gets

$$\frac{L}{L_c} = \frac{A}{(1+\delta)^2}\frac{1}{\delta\Omega + \Omega - 2k_0^2} = \frac{A}{(\epsilon+2)^2\left((\epsilon+2)\Omega - 2k_0^2\right)}$$

where

$$A = (1-\delta)^2\left[\delta\Omega - \left(\Omega - 2k_0^2\right)\right] + (1+\delta)4k_0^2\delta = \epsilon^3\Omega + 2k_0^2\left(3\epsilon^2 + 6\epsilon + 4\right)$$

It's a complicated result, but can be checked to reduce to the isotropic case

$$\frac{L}{L_c} = \frac{8k_0^2}{4\cdot(2\Omega - 2k_0^2)} = \frac{k_0^2}{\Omega - k_0^2}$$

if setting $\epsilon = 0$.

One can compare the result to the last section, and will find that the effective mass gives a different answer this time.

4.12 Conclusion and outlook

Our inability to obtain I/I_c from scissors mode measurements without detailed modeling reinforces similar conclusions in dipolar gases [47]. In both cases the simple argument fails because $\dot{\theta}$ couples to more internal degrees of freedom than L_z alone. In this context Ref. [47] concluded that the scissors mode *does* yield the moment of inertia when 1D density modulations comove with the oscillatory motion: this is consistent with our findings comparing motion in static and rotating lattices. Our GPE simulations indicate that the analytical relations generalize to lattices with period in excess of the healing length.

Although we conclude that a normal fluid exists, it is inseparable from the optical lattice and lacks any internal dynamics of its own, i.e., it is not described by a dynamical equation of motion. Recent calculations for the strongly interacting superfluid $^4\mathrm{He}$ films on materials such as hexagonal boron nitride also predict an anisotropically reduced SF density [48], implying the existence of a pinned normal fluid. In contrast, both the superstripe phase in spin-orbit coupled BECs [49, 50, 51, 52, 53] and supersolid phases of dipolar gases [54, 55, 56], support dynamical density modulations. Leggett's expression applies to both of these systems implying a reduced superfluid density, which in this case could exhibit dynamics, as expected for a system described by a two-fluid model [57, 58].

This leaves open questions regarding nature the normal fluid of spin-orbit coupled systems where an interplay between single-particle physics and interactions govern supersolid-like properties. In addition, ρ^{sf} is expected to be reduced outside of the superstripe phase [52, 53] where the density is uniform (making Leggett's expression inapplicable), but the BEC's spin vector is spatially periodic.

Chapter 5: A Non-Hermitian Quantum Gas

5.1 Open quantum systems

Open quantum systems where the system of interest exchanges particle number, energy or momentum with its environment, have attracted recent interest with both theoretical and experimental efforts. This type of problem is often formulated by the quantum master equation [59] under the Markovian approximation, while a mathematically equivalent method called quantum trajectory, divides the system evolution into a period of non-unitary evolution, followed by a quantum jump. In the equation

$$\dot{\varrho} = -\mathrm{i}[\mathcal{H}, \varrho] + \sum_j \left(L_j \varrho L_j^\dagger - \frac{1}{2}\left\{ \varrho, L_j^\dagger L_j \right\} \right) \equiv -\mathrm{i}\left(H_{\mathrm{nh}}\varrho - \varrho H_{\mathrm{nh}}^\dagger \right) + \sum_j L_j \varrho L_j^\dagger \tag{5.1}$$

the operators L_js are the quantum jump operators, which describe the incoherent process of "wavefunction collapse" due to the dissipation into the environment [60]. In addition, we absorb part of the evolution into the non-Hermitian Hamiltonian

$$H_{nh} = \mathcal{H} - \frac{1}{2}\sum_j L_j^\dagger L_j. \tag{5.2}$$

In fact, the master equation deals with the elements of the density matrix. Generally in a many-particle system, the number of elements in the density matrix scales as n^2, where n is the many-body Hilbert space dimension. (However, we also would like to note that quantum many-body systems are themselves intractable to calculate/simulate for both open and closed systems, because of the scary scaling of n on the single particle Hilbert space dimension L, which is an exponential function $n \sim L^N$. Here N is the number of particles in our physical system.) In a few-body open system with small N, the n^2 scaling becomes important, and it is reasonable to try to find an acceleration on top of it [60].

5.2 Non-Hermitian physics

Sampling is a great way to "bypass" this added complexity, and the quantum trajectory method is one good example of this. (The method is also called quantum Monte Carlo wavefunction [60] in some contexts.) The key spirit is to still describe the system with a "wavefunction" $\psi(t)$ instead of the density matrix $\hat{\rho}(t)$. However, this approximation is only legitimate with a single trajectory and without the procedure of state collapse. To describe the measurements/dissipations, one further introduces the "collapse operators" $\hat{L}_j$, and samples over a probability distribution whether or not to apply the projection L_j. The probabilistic distribution is chosen such that the probability of a quantum jump is determined by the wavefunction evolved to a certain time $\langle\psi| L_j^\dagger L_j |\psi\rangle$. One has to average over the sampled trajectories and look for convergence to the master equation description. This numerical method is fully physics-motivated and proved to be powerful in various AMO subfields.

Beyond the state collapse, the non-Hermitian Hamiltonian is utilized to depict the short-term evolution of an open quantum system before the first quantum jump happens and in between two quantum jumps. In another scenario, it should also serve as a decent approximation when the jump effectively ejects particles out of the ensemble, without perturbing the evolution of the rest. Because the usual and real physical Hamiltonian is Hermitian (according to principles of quantum mechanics [61]), this direction attracts limited attention, mainly from the mathematical and theoretical perspectives. However, the revolution started around 2010 [62], when experimental platforms started to be able to make such non-trivial non-Hermitian Hamiltonian models reality, and people began to search old papers for interesting predictions. The results have been unexpected – the physics in such systems has been beyond imagination – it rapidly expanded and evolved to a new sub-field of physics.

5.3 Previous works on non-Hermitian systems

As is elaborated, non-Hermitian physics is a natural extension when physicists studied the open quantum systems. There has been fruitful progress in exploring this new field [62]. Theoretically, the quantum mechanics of non-Hermitian Hamiltonians is itself exotic. For instance, it doesn't guarantee a real spectrum or a complete and orthonormal set of eigenstates [62, 63]. On the other hand, some symmetry such as the product of parity and time reversal symmetry (PT) together helps recover a real spectrum [64]. Beyond that, many exotic properties of the non-Hermitian bands are predicted in theory, which are related to singularities, chiral transport, and topology [65, 66]. More recently, a new phenomenon regarding the non-reciprocity of the transport in non-Hermitian systems was discovered, and it was given the name the "non-Hermitian skin effect".

Experimentally, however, the progress was mainly about engineering the non-Hermiticity with classical systems and those analogous to non-interacting simple quantum systems. For instance, it is straightforward to engineer the gain and loss within the photonics platforms [65, 67, 68, 69, 70], mechanical resonators [71, 72], and optomechanics systems [73]. Yet, the realization of the real quantum mechanical non-Hermitian physics has remained almost evasive, with only a few examples [74, 75]. It is expected with the more developed control tools with true quantum platforms such as ultracold atoms and molecules, more and more interesting physics can be engineered [76]. The uniqueness of these systems will certainly shed new light on the theoretical community and lead to new understandings.

5.4 Topological physics seen from outside

Topology represents the beauty of geometry since the 19th century. In a modern setting, topology is defined as the property of a geometric manifold, and it is always a global property [77]. From a traditional perspective, topology enters only the fields where geometry becomes important. For example, cosmologists are interested in the topology of spacetime connected to singularities [78]. As another example, some theorists developed mathematical formulation of topological field theories [79].

Things became a bit different around 2000 [80]. It was all of a sudden some theorists found, after the 70th birthday of Bloch's theorem [81], that the Brillouin zone is not that trivial! Strange as it sounds, a locally flat space does not mean completely trivial topology for physicists. The idea is, that despite that the electrons move in the flat space, they still can experience an effective "metric" in some parameter space, such as being homomorphism from the reciprocal space of the Brillouin zone. Such studies began by defining the "metric" or local curvature as a function of the eigenstate wavefunction and its derivative. And due to its analogy to the Anharonov-Bohm (AB) effect in real space, this curvature is named after Berry – the "Berry curvature" [82]. A lot of simple models were revisited, including those with real magnetic field and AB effect, and variants of the 1988 Haldane hexagonal model [83] became the leading trend. It didn't take a long time before experimentalists believed that they could make such systems a reality – by utilizing spin-orbit coupling [81] – as for example proposed for graphene [84] but then turned to the quantum wells due to the stronger coupling strength [85]. This made a new system without external magnetic fields and stimulated people to think about the intrinsic topology of the bands, as mentioned above.

About 10 years later, the "periodic table" of topological bands was completed according to the symmetry class of the single particle fermionic Hamiltonian [86, 87, 88, 89]. These systems are named "symmetry-protected topological phases", as to be told apart from the "real" topological phases that derived from the many-particle correlations. Although they are variants of zero interaction systems, the topology lies in the global topology of functions of a single-band structure. As an example, the spin-orbit coupling allowed the creation of the Z_2 topological class, while keeping the time-reversal symmetry [84, 85].

In order to link to the mainstream of the thesis, I provide two examples of topology. These fall respectively into the category of the **AIII** class in 1D and **A** in 2D. These classes are going to be introduced in Section 5.6.

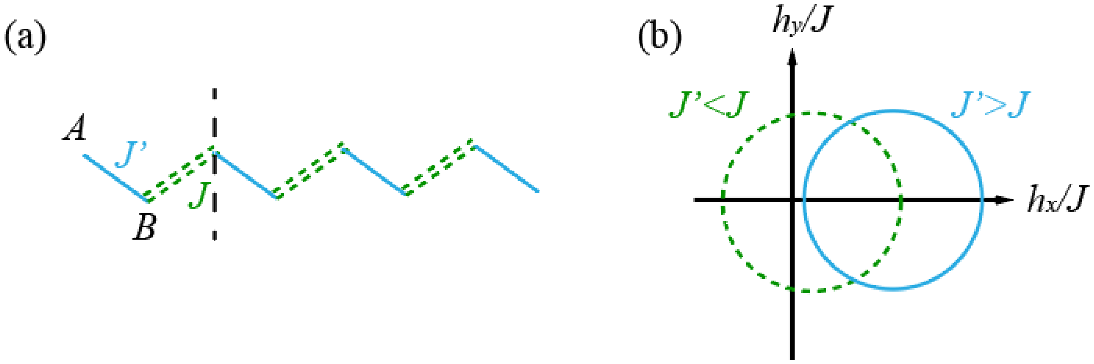

Figure 5.1: Illustration of the SSH model. (a) SSH model is a 1 dimensional chain that is made of two sublattices A and B. The hoppings within and between the A-B unit cells are different and labeled J' and J. (b) The topological winding number defined by the Zak phase counts the number of turns the $\mathbf{h}$ vector winds around the origin, as q goes through the BZ. Figure is reproduced from [4].

5.5 Examples of topological physics in Hermitian systems

5.5.1 Su–Schrieffer–Heeger model: winding number

The Su–Schrieffer–Heeger (SSH) model [4, 90] is a 1D tight binding chain with two sublattices (Fig. 5.1a).

After Fourier transformation to the q space, the Hamiltonian is given by

$$\hat{H}_q = -\begin{pmatrix} 0 & J' + J\mathrm{e}^{-\mathrm{i}qa} \\ J' + J\mathrm{e}^{\mathrm{i}qa} & 0 \end{pmatrix} = -\mathbf{h}(q) \cdot \hat{\sigma} \tag{5.3}$$

where a denotes the distance between the A-B sites. This 2×2 Hamiltonian is summarized in a 2D vector $\mathbf{h}(q)$

$$h_x(q) + \mathrm{i}h_y(q) = J' + J\mathrm{e}^{\mathrm{i}qa} \tag{5.4}$$

which lives in a fictitious space parametrized by the 1D BZ wavevector q. With our definition

$$h_x = J' + J\cos(qa) \text{ and } h_y = J\sin(qa). \tag{5.5}$$

If we plot h_x/J vs h_y/J in the 2D plane (Fig. 5.1), then q parameterizes a circle that can enclose the origin, or not. When $J' > J$, the circle encloses the origin; whereas $J < J'$, it does not. One can define a "Zak phase" [90] in terms of this "property"

$$\phi_{\text{Zak}}^{(-)} \equiv \int_{\boldsymbol{q}_1}^{\boldsymbol{q}_{\mathrm{i}}+\boldsymbol{G}} \mathrm{i}\left\langle u^{(-)} \mid \partial_{\boldsymbol{q}} u^{(-)}\right\rangle \cdot \mathrm{d}\boldsymbol{q} = -\frac{1}{2}\int_{\text{BZ}} \frac{\partial \phi_q}{\partial q}\,\mathrm{d}q \tag{5.6}$$

where $\left|u^{(-)}(\mathbf{q})\right\rangle$ stands for the wavefunction in q space of the lower band and

$$\phi_q = \arg(h_x + ih_y). \tag{5.7}$$

This Zak phase is $-\pi$ when $J' > J$, or zero otherwise. If we want, we can also define a winding number

$$N \equiv -\frac{1}{\pi}\phi_{\text{Zak}}^{(-)} \tag{5.8}$$

such that it is either 0 or 1.

It turns out that this property has an implication when we consider instead an open chain with two open ends. One would find two zero energy "edge states" exponentially localized at each of the boundaries if and only if $N = 1$. These two states are energetically distinct from the other "bulk" states which are separated by a large band gap. This is a known consequence of the "bulk-boundary correspondence".

5.5.2 Quantum Hall system: real gauge field

By applying an external uniform magnetic field perpendicular to the 2D plane, the electrons are subjected to the Lorentz force. In the classical setting, because of the initial velocity they own, their motion forms the “cyclotron orbits”. These orbits prevent the longitudinal transport in the bulk, thereby making the system an insulator. However, when they run into the open boundary of the system, they can skip on the boundary itself, and become orbits of chiral transport, meaning the motion is only along one direction rather than the opposite. These are called “skipping edge orbits”.

It is natural to ask how one can quantize such motion. Indeed, the quantum mechanical problem was solved in early days and gave the quantized integer *Landau levels* which have flat dispersions. Depending on how many levels electrons fill out, the transverse Hall conductance is quantized to the integer filling fraction ν

$$\sigma_e = \frac{e^2}{h}\nu. \tag{5.9}$$

When we put the system on a lattice, this number is related to the *Chern number*, defined with the Berry curvature of the energy band

$$C_n = -\frac{1}{2\pi}\int_{BZ} dk_x dk_y \left(\frac{\partial A_y^{(n)}}{\partial k_x} - \frac{\partial A_x^{(n)}}{\partial k_y} \right) \tag{5.10}$$

where $\mathbf{A}^(n)$ is the Berry connection in the nth band

$$A_j^{(n)}(\mathbf{k}) = i \left\langle u_n(\mathbf{k}) \left| \partial_{k_j} \right| u_n(\mathbf{k}) \right\rangle , \quad \text{for } j = x, y. \tag{5.11}$$

Over a torus (Brillouin zone), the Chern number has to be quantized as an integer. There will also be gapless edge modes (whose number equals the absolute value of the Chern number) if the system is finite-sized. These correspond to the skipping orbits in the classical picture.

5.6 Non-Hermitian topology

This section follows the wisdom summarized in the milestone paper [91], which gives the topological phases classification of non-Hermitian systems in terms of the Altland-Zirnbauer (AZ) classes.

For Hermitian systems, such classification was determined by the systems' symmetry and dimension. In the spirit of the AZ classes, distinct topological phases cannot be continuously deformed into each other under the constraints of an existing energy gap, while respecting the underlying symmetry. Note that it ”secretly” sets a reference energy (Fermi energy) in the energy gap. The classification is listed in Table. 5.1. Here, only the time-reversal symmetry (TRS), particle-hole symmetry (PHS), and sublattice/chiral (SS) symmetry are considered. Other symmetries, according to the group theory, lead to reducible representations of the Hamiltonian (because those symmetries are represented by unitary operators). The **A** class breaks all three symmetries and is the simplest of all. The Chern insulator discussed in the last section is in this class, and under 2D it holds an integer topological invariant, which is just the Chern number. In the meanwhile, the SSH model is in the **AIII** class, which holds an integer winding number.

For the non-Hermitian systems, such “ten-folds way” also existed, as summarized in Table. 5.2. The classification was done by “Hermitianization” – expanding the Hilbert space to construct Hermitian Hamiltonians – in a mathematical way called the “K-theory”. In our current study,

Symmetry class	TRS	PHS	SS	d=0	d=1	d=2
A	0	0	0	$\mathbb{Z}$	0	$\mathbb{Z}$
AIII	0	0	1	0	$\mathbb{Z}$	0
AI	$+$	0	0	$\mathbb{Z}$	0	0
BDI	$+$	$+$	1	$\mathbb{Z}_2$	$\mathbb{Z}$	0
D	0	$+$	0	$\mathbb{Z}_2$	$\mathbb{Z}_2$	$\mathbb{Z}$
DIII	$-$	$+$	1	0	$\mathbb{Z}_2$	$\mathbb{Z}_2$
AII	$-$	0	0	$2\mathbb{Z}$	0	$\mathbb{Z}_2$
CII	$-$	$-$	1	0	$2\mathbb{Z}$	0
C	0	$-$	0	0	0	$2\mathbb{Z}$
CI	$+$	$-$	1	0	0	0

Table 5.1: For Hermitian systems, we have the "ten-folds way" of the AZ classes. It gives the possible topological invariants under different symmetries and dimensions.

AZ class	Classifying space	$d=0$	1	2	3	4	5	6	7
A, DIII, CI	$\mathcal{C}_1$	0	$\mathbb{Z}$	0	$\mathbb{Z}$	0	$\mathbb{Z}$	0	$\mathbb{Z}$
AIII	$\mathcal{C}_1 \times \mathcal{C}_1$	0	$\mathbb{Z} \oplus \mathbb{Z}$	0	$\mathbb{Z} \oplus \mathbb{Z}$	0	$\mathbb{Z} \oplus \mathbb{Z}$	0	$\mathbb{Z} \oplus \mathbb{Z}$
AI, D	$\mathcal{R}_1$	$\mathbb{Z}_2$	$\mathbb{Z}$	0	0	0	$2\mathbb{Z}$	0	$\mathbb{Z}_2$
BDI	$\mathcal{R}_1 \times \mathcal{R}_1$	$\mathbb{Z}_2 \oplus \mathbb{Z}_2$	$\mathbb{Z} \oplus \mathbb{Z}$	0	0	0	$2\mathbb{Z} \oplus 2\mathbb{Z}$	0	$\mathbb{Z}_2 \oplus \mathbb{Z}_2$
AII, C	$\mathcal{R}_5$	0	$2\mathbb{Z}$	0	$\mathbb{Z}_2$	$\mathbb{Z}_2$	$\mathbb{Z}$	0	0
CII	$\mathcal{R}_5 \times \mathcal{R}_5$	0	$2\mathbb{Z} \oplus 2\mathbb{Z}$	0	$\mathbb{Z}_2 \oplus \mathbb{Z}_2$	$\mathbb{Z}_2 \oplus \mathbb{Z}_2$	$\mathbb{Z} \oplus \mathbb{Z}$	0	0

Table 5.2: Non-Hermitian systems can also be categorized into the AZ classes, which are grouped into six. Table reproduced from *Phys. Rev. X* 8, 031079.

we will focus on the simplest **A** class again, in one dimension. The periodic table predicts there exists an integer topological invariant ($\mathbb{Z}$), which we introduce in the next section as the "winding number".

5.7 The Hatano-Nelson (HN) model

Much earlier than the discovery of non-Hermitian topological phases, Hatano and Nelson proposed a lattice model comprised of a simple ingredient of asymmetric hoppings. The non-

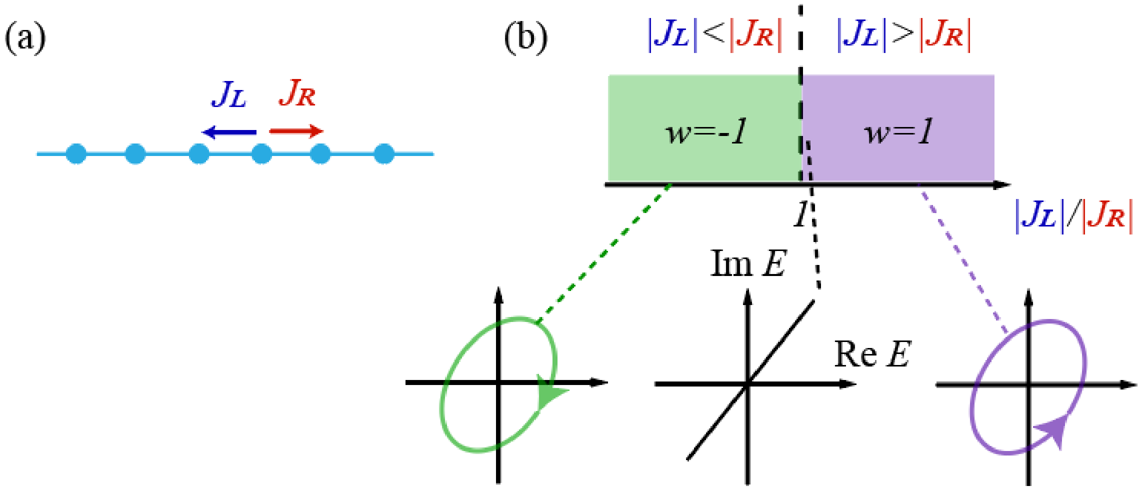

Figure 5.2: Figure reproduced from: Phys. Rev. X 8, 031079. Illustration of the Hatano-Nelson (HN) model. (a) Real space lattice with asymmetric hoppings J_L and J_R. (b) There exists a topological phase transition at $|J_L| = |J_R|$. On the left one has the winding number $w = -1$, and on the right $w = 1$. At the transition point, the system is subjected to a real gauge field and its Hamiltonian spectrum transforms to an arc from a loop.

Hermitian Hamiltonian is presented as following:

$$H = \sum_j -J_R a^\dagger_{j+1} a_j - J_L a^\dagger_j a_{j+1} \tag{5.12}$$

where J_L and J_R are complex tunneling amplitude and in general not equal. This model is depicted in Fig. 5.2a. Intuitively, since the tunneling to the right is larger (smaller) than the tunneling to the left, we expect the wavepacket to accumulate to the right (left) under open boundary condition (OBC). This is indeed the case.

5.7.1 Complex energy spectrum

The simplicity of the tight binding model allows for direct diagonalization both in the periodic and open boundary conditions (PBC and OBC). We first look at the eigen-energies. Because this model has no PT symmetry, the energies are in general complex values.

We first look at the spectrum under PBC. We assume $k \in [-\pi, \pi]$ as the Brillouin zone (BZ), and calculate the $E(k)$. The result is presented in Fig. 5.2. When the parameter $\gamma = |J_L|/|J_R|$ is not equal to unity, the $E(k)$ forms a "loop" as the parameter k runs over the BZ. The loop is counterclockwise if $\gamma > 1$, and is clockwise if $\gamma < 1$. However, when $\gamma = 1$, the spectrum "collapses" to a line (or arc). It turns out that this suggests an important topological invariant, which we define here as w, the "winding number"

$$w = \int_{-\pi}^{\pi} \frac{dk}{2\pi} \partial_k \arg E(k). \tag{5.13}$$

Since we have $\det E(k) \neq 0$ in BZ, this definition is always legit. This winding number can also be written as

$$w = \int_{-\pi}^{\pi} \frac{dk}{2\pi i} \partial_k \ln \det H(k) \tag{5.14}$$

in a more algebraic form. Indeed note that we have secretly chosen a reference "base energy" $E_B = 0$, which is important for the validness of the definition. And more generally,

$$w = \int_{-\pi}^{\pi} \frac{dk}{2\pi i} \partial_k \ln \det[H(k) - E_B] \tag{5.15}$$

is always defined with respect to the base energy.

Thus the winding number $w = 1$ once $\gamma > 1$, and $w < 1$ once $\gamma < 1$. However, when $\gamma = 1$ the winding number becomes ill-defined ($E(k)$ goes past the origin). This is defined as a "topological phase transition" point of the HN model, because w across $\gamma = 1$ is discontinuous and quantized integers, marking two distinct phases.

Following our reference, we would note that the non-Hermitian topological phases are very different from the Hermitian counterparts. In the Hermitian systems, the topological invariant is often defined related to the Berry phase using their eigenstate wavefunctions. As a result, it requires at least two bands to make a non-trivial phase. In contrast here we have only a single band non-Hermitian Hamiltonian, but can define the winding number from its complex spectrum.

5.7.2 Bulk-boundary correspondence

We are familiar with the bulk-boundary correspondence in Hermitian systems. In a quantum Hall (Chern insulator) system, the edge modes (named the skipping orbits) arise because of the non-trivial TKNN or Chern number. But can we expect something similar in the non-Hermitian systems? But it turns out to be not that obvious and controversial for some years.

The first thing to notice is that the energy spectrum is generally a function of the boundary condition type. For the periodic boundary condition or without any boundary (free space), we will recover the complex dispersion as introduced in the above section, and it permits us to define the spectral winding number. However, if what we consider is a finite system with an open boundary, we will find that these eigenenergies change, and the winding number also changes [92, 93]. For the HN model, its spectrum becomes real again with open boundaries, which will be elaborated in the next section.

But to find a potential edge state, we will have to consider a finite system. It turns out that directly solving the finite system predicts the correct eigenstates (as derived in the next section). These states do tend to localize themselves to the edges of the system, and their appearance relates to the winding number we defined in the free space [91, 93].

5.7.3 Exact solutions

In this section, we derive the exact solutions of the Hamiltonian (5.12) under the open boundary condition (OBC), which helps with a comprehensive understanding of the said properties.

The tight-binding Hamiltonian is solved via defining

$$\psi_n = \sqrt{d}\psi(nd)$$

and the system becomes coupled equations

$$E\psi_n = -J_R\psi_{n-1} - J_L\psi_{n+1}. \tag{5.16}$$

The OBC means

$$\psi_0 = \psi_N = 0.$$

To solve this system, we introduce an important parameter $\gamma = \sqrt{J_R/J_L}$ here. We will verify the solutions are (labled by $m \in \mathbb{N}^*$)

$$\psi_n = \sqrt{\frac{N-1}{2}}\gamma^n \sin(k_m nd) \tag{5.17}$$

where $k_m = m\pi/(N-1)d$, with $m = 1, 2, ...$ Now plug it in (5.16):

$$E_m \gamma^n \sin(k_m nd) = -J_R \gamma^{n-1} \sin(k_m(n-1)d) - J_L \gamma^{n+1} \sin(k_m(n+1)d).$$

This is where γ plays its role – it ”re-balances” the asymmetry in J_L and J_R.

$$E_m \sin(k_m nd) = -\sqrt{J_L J_R} 2 \sin(k_m nd) \cos(k_m nd)$$

And we have the eigen-energies

$$E_m = -2\sqrt{J_L J_R} \cos(k_m nd). \tag{5.18}$$

This is an important result because we note that the energies are indeed on the real axis despite the non-Hermitian Hamiltonian, but this is only true under the OBC. Another thing to note is that (5.17) is not the true “edge mode” that goes exponential at the boundary – indeed it is ”quasi-edge modes” we introduced in the last section. All the introduced properties can be verified using this set of solutions.

Now we want to derive the continuum analog of the equation 5.16. To do it, we go back to $\psi_n = \sqrt{d}\psi(x = nd)$. We further introduce ancillary field

$$\phi(x) = \psi(x)\gamma^{-x/d}. \tag{5.19}$$

We can easily find the equation for $\phi(x)$:

$$E\phi(x) = -\sqrt{J_L J_R}(2 + d^2\partial_x^2)\phi(x) \tag{5.20}$$

where we have used

$$\phi(x \pm d) = \phi(x) \pm d\partial_x\phi(x) + \frac{1}{2}d^2\partial_x^2\phi(x).$$

To derive the equation for $\psi(x)$, we just plug it in, and use the rule for higher derivative

$$\partial_x^2(\psi\gamma^{-x/d}) = \partial_x^2\psi\gamma^{-s/d} + \frac{\ln^2\gamma}{d^2}\psi\gamma^{-s/d} - 2\partial_x\psi\frac{\ln\gamma}{d}\gamma^{-s/d}$$

we get

$$E\psi = -\sqrt{J_L J_R}d^2(\partial_x^2 - 2\frac{\ln\gamma}{d}\partial_x + \frac{2 + \ln^2\gamma}{d^2})\psi. \tag{5.21}$$

This equation corresponds to the case with an “imaginary gauge potential”. To see this, we define $A = iq$, where

$$q = \frac{\ln\gamma}{d}.$$

And then

$$(p - A)^2 = p^2 - 2p \cdot A + A^2 = -\partial_x^2 - 2q\partial_x - q^2 \tag{5.22}$$

is the same as that in equation 5.21 but up to constant shift.

5.7.4 Appearance of the imaginary gauge potential

There are a few ways to justify the physical "relevance" of an imaginary vector potential. One way was introduced in the original papers by Hatano and Nelson, by considering the projection of a disordered real gauge field [94]. But recently, people have found it can also be mapped to a curved spacetime. Thus we have a mapping from the non-Hermitian Hamiltonian to an effective metric [95].

This is discovered by introducing a coordinate transformation

$$\frac{y}{y_0} = e^{2qx} \tag{5.23}$$

and one has

$$\partial_x = 2qy\partial_y$$

and

$$\partial_x^2 = 4q^2 y(\partial_y + y\partial_y^2).$$

Plug them in equation (5.21), we have an equation for y

$$E\psi = -\sqrt{J_L J_R} d^2 (4q^2 y^2 \partial_y^2 + \frac{2}{d^2} + q^2)\psi. \tag{5.24}$$

One can then select

$$M = \frac{\hbar^2}{2\sqrt{J_L J_R} d^2} \text{ and } \kappa = 4q^2, \tag{5.25}$$

these are the ”mass” and ”curvature” scalars. Then we arrive at

$$E\psi = -\frac{\hbar^2}{2M}\kappa(y^2\partial_y^2 + \frac{1}{4})\psi. \tag{5.26}$$

This is indeed interpreted as the equation of motion in the curved space.

5.8 Non-Hermitian skin effect

The non-Hermitian skin effect was an unexpected discovery where the topology and non-Hermiticity comes to an interplay, causing directional transport behavior in a system with open boundary conditions. Localized edge states are predicted in such systems, with the number of them scaling as the number of bulk states $N \sim L^d$, in stark contrast with the bulk edge correspondence in Hermitian topological systems, where the number of edge states scales $N \sim L^{d-1}$[91, 96].

So far, most studies of the skin effect focus on the non-interacting lattice models, due to their analytical and numerical simplicity. The non-Hermiticity is often represented by the non-reciprocal tunneling, such as in the Hatano-Nelson (HN) model, which predicts macroscopically accumulated eigenstates at one edge [94, 97]. A non-Bloch band theory was developed to solve such models, and gives insight into a topological winding number that determines the onset of the skin effect [92]. Topological phase transitions were studied theoretically by tuning the chiral symmetry upon closing the band gap. Such predictions were experimentally realized in photonic quantum walks, and recently in an engineered momentum state Raman lattice, where non-reciprocal transport signatures were observed.

However, despite the successful efforts in the lattice models, they are not ideal for developing a more intuitive understanding of the origin of the directional acceleration force. Furthermore, current experimental works were implemented and explained in a non-interacting setting, providing incomplete description of open many-body systems.

Hereby, we study the stationary and dynamic properties of an open spin-orbit coupled Bose-Einstein condensates system. The spin-orbit coupling is induced by Raman lasers crossing at a small angle, and the system is in addition subjected to effective loss of particles via a two-photon type coupling to the electronic excited state. Meanwhile, because the atomic momentum and spin are coupled, this loss translates into a directional force and leads to nonreciprocal transport. We observe the center of mass drift of the BEC in a homogenous box trap, and study its dependence on the loss rate and Raman coupling strength. We find good agreement with the theoretical non-Hermtian model, and further develop numerical simulation with non-Hermitian Gross-Pitaevskii equation (GPE), which focuses on the impact of the interaction. By creating spatially varying potentials, we prepare states that are localized to the box edge, and confirm they are close to the stationary states in later evolution. Thus, we provide the first combined experimental and theoretical research on the skin effect in the continuum, with the presence of many-body interaction.

5.9 Non-Hermitian spin-orbit coupling

In our project, we would like to discover whether a non-Hermitian system with similar properties can be engineered in a distinctly different physical system. Specifically, we will look at a spin-orbit coupled BEC, which is not held in any lattice. Moreover, the atom-atom interaction that renders our BEC a superfluid is present, which makes it an interesting question to ask whether the interaction changes the behavior of the non-Hermitian system.

But to begin with, let us consider a single-particle problem. The non-Hermitian spin-orbit coupled Hamiltonian we intend to engineer is

$$\hat{H}_{\mathrm{SOC}} = \frac{(\hat{p} + 0\sigma_z)^2}{2m} + \frac{\hbar\Omega}{2}\sigma_x + \frac{\hbar\delta}{2}\sigma_z - i\hbar\Gamma\mathcal{P}_{\uparrow} \tag{5.27}$$

with Pauli operators $\sigma_{x,y,z}$, quasi-momentum $\hat{p}$ [98], atomic mass m, Rabi frequency Ω, detuning δ, and spin projection operator $\mathcal{P}_{\uparrow} = \left|\uparrow\right\rangle\left\langle\uparrow\right|$. Without the spin projection operator $\mathcal{P}$, the Hamiltonian is

$$\hat{H}_0 = \frac{(\hat{p} + 0\sigma_z)^2}{2m} + \frac{\hbar\Omega}{2}\sigma_x + \frac{\hbar\delta}{2}\sigma_z. \tag{5.28}$$

This Hamiltonian was briefly discussed in Chapter 4. It is defined on the spin-half Hilbert space made by $\left|\uparrow\right\rangle$ and $\left|\downarrow\right\rangle$. The two spinors are coupled at a coupling strength Ω and a detuning δ. But most importantly, there is a spin-dependent gauge potential $p_0\sigma_z$, which completely changes the behavior of the simple Rabi-coupled model.

We solve the spectrum of the base Hamiltonian at $\delta = 0$ [35], which is shown in Fig. 5.4. Two distinct quantum phases can be seen in the dispersion depending on the strength of the Rabi frequency Ω. The phase transition is at $\hbar\Omega = 4E_0$, where $E_0 = p_0^2/2m$ is the "recoil energy" that is defined from the gauge coupling strength p_0. When $\hbar\Omega < 4E_0$, the dispersion has two degenerate energy minimums, featuring a "double-well" shape in momentum space. Since the atoms are bosons, when we load them into the dressed states, they tend to occupy the lowest energy states at equal probabilities. The ground state profile is plotted in Fig. 5.3 with an external box potential. Experimental studies have shown that there can be another phase

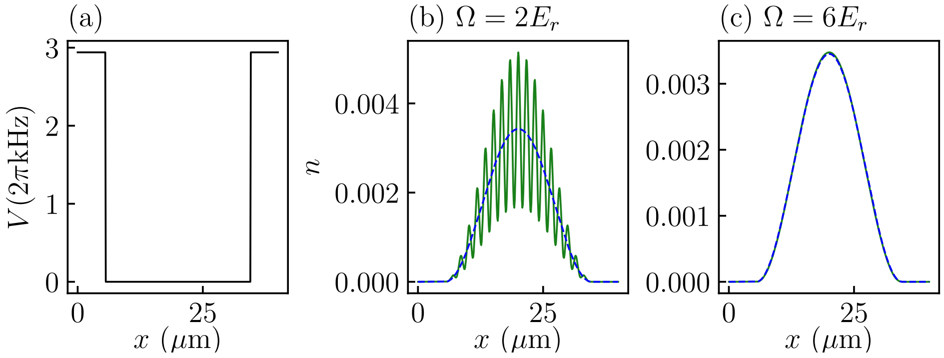

Figure 5.3: The ground state of the spin-orbit coupled Hamiltonian in a box potential. (a) The box potential has a length $L = 30\ \mu$m. (b) In the double minimum phase, the ground state can form a density modulation "stripe" phase (solid); or if there is nonzero detuning ($\delta = E_r$ dashed), it breaks the Z_2 symmetry and falls into the lower minimum. (c) In the single minimum phase, the ground state is always in the single minimum even with δ.

transition at small Ω, below which the atoms are in a coherent superposition of the two energy minimums, and due to interference effect they form "stripes". But above this transition, these two dressed states become "immiscible" and tend to spatially separate from each other, and thus form domains. This process is spontaneous symmetry breaking and was easily observable in the experiments. These two phases exist due to the spin-dependent interactions, and were named the "stripe phase" and the "plane wave" phases. Whereas $\hbar\Omega > 4E_0$, the dispersion transitions from the "double minimums" to a "single minimum". At the bottom of the lower band, the dispersion is near quadratic and gives an effective mass m^*. The bosons will be loaded to this minimum at $p = 0$, and such a phase was given the name "single minimum" phase.

At small but finite δ, the single minimum phase will not change qualitatively but the minimum only shifts from zero momentum. In past works, the "synthetic electric field" and "artificial magnetic field" were engineered by varying the δ in time and space [99, 100]. However, this detuning makes dramatic changes when $\hbar\Omega < 4E_0$. It splits the degeneracy of the two double minimums, and makes bosons condense into the only real ground state.

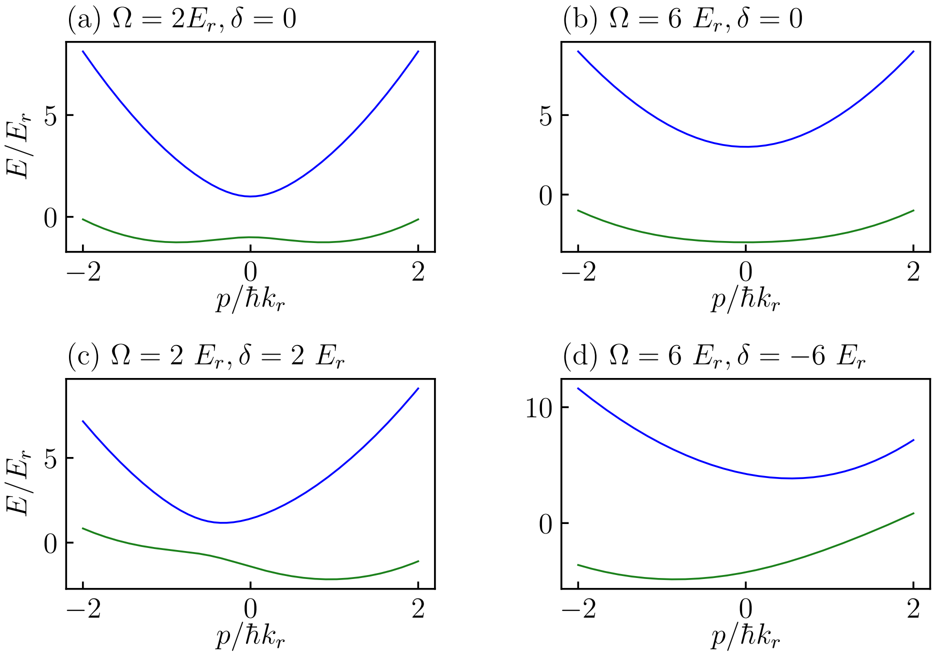

Figure 5.4: Tuning the (Hermitian) spin-orbit coupled Hamiltonian and deriving the dispersion. An upper (blue) band and a lower (green) band emerge because of the coupling Ω. A BEC will always seek the lowest energy ground state in the lower band.

Now we add in the non-Hermitian term $-i\hbar\Gamma\mathcal{P}_\uparrow$. This term is effectively another σ_z term plus an imaginary constant energy because

$$-i\hbar\Gamma\mathcal{P}_\uparrow = -i\frac{\hbar\Gamma}{2} - i\frac{\hbar\Gamma}{2}\sigma_z. \tag{5.29}$$

We note that the imaginary constant is only going to offset the spectrum to the imaginary axis. Hence we can absorb the σ_z term into an “complex detuning”

$$\delta' = \delta - i\Gamma. \tag{5.30}$$

The solution of such a Hamiltonian has richer physics than one thought.

It is generally conceivable that such a non-Hermitian Hamiltonian has a complex spectrum, because the non-Hermiticity no longer requires real eigenvalues. Therefore, we study the real and imaginary parts of the spectrum separately. As shown in Fig. 5.6a and 5.5a, the real part of the spectrum slightly modifies when $\Gamma \ll E_0$ is small, which can be treated using perturbation theory. When one ramps up the Γ, the band gap becomes smaller, and the bands tend to touch each other at $p = 0$. It is noticeable that the dispersion develops a discontinuous $\partial E(p)/\partial_p$ at $p = 0$, and even for the large $\Omega = 6E_r$ case (Fig. 5.5b), the lower band recovers a "double minimum" structure. Finally when $\Gamma = \Omega$, the band gap vanishes and keeps on vanishing for even larger Γ. This marks the appearance of an *exceptional point* at $p = 0$, where two eigen-energies and eigenstates reduce into one, named *coalescence*. This is an important non-Hermitian "phase transition", as it remarks the breaking of the $\mathcal{PT}$ symmetry [101] of the Hamiltonian.

We also look at the imaginary part of the dispersion in Fig. 5.5 and 5.6 (d-f). It is nonzero even with a small Γ, and more importantly, it is asymmetric under parity transformation $\mathbf{p} \to -\mathbf{p}$. This property turns out to be crucial to the physics we study. Above the critical $\Gamma = \Omega$, an energy discontinuity at $p = 0$ is observed which crosses $\mathrm{Im}\, E = 0$.

5.10 Topological band of non-Hermitian SOC

To reveal the topological property of the dispersion, we plot the complex spectrum in the complex 2D plane in Fig. 5.7. The SOC features two bands, where the lower band encloses the origin and the upper band does not. We extend the definition of the winding number in the previous section because the quasi-momentum runs in the free space

$$w = \int_{-\infty}^{\infty} \frac{dk}{2\pi} \partial_k \arg E(k). \tag{5.31}$$

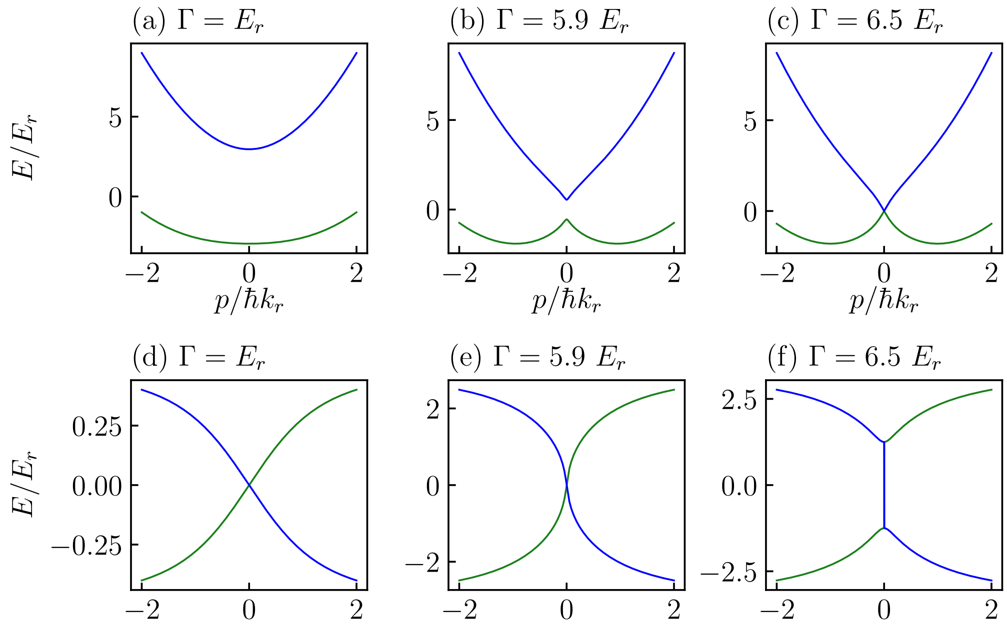

Figure 5.5: Begin with a single minimum phase $\Omega = 6E_r$. Ramp up the spin-dependent non-Hermitian strength Γ. Top row: the real part of the energy dispersion. Blue: upper band; green: lower band. Bottom row: the imaginary part of the energy dispersion. In all the cases, we set $\delta = 0$.

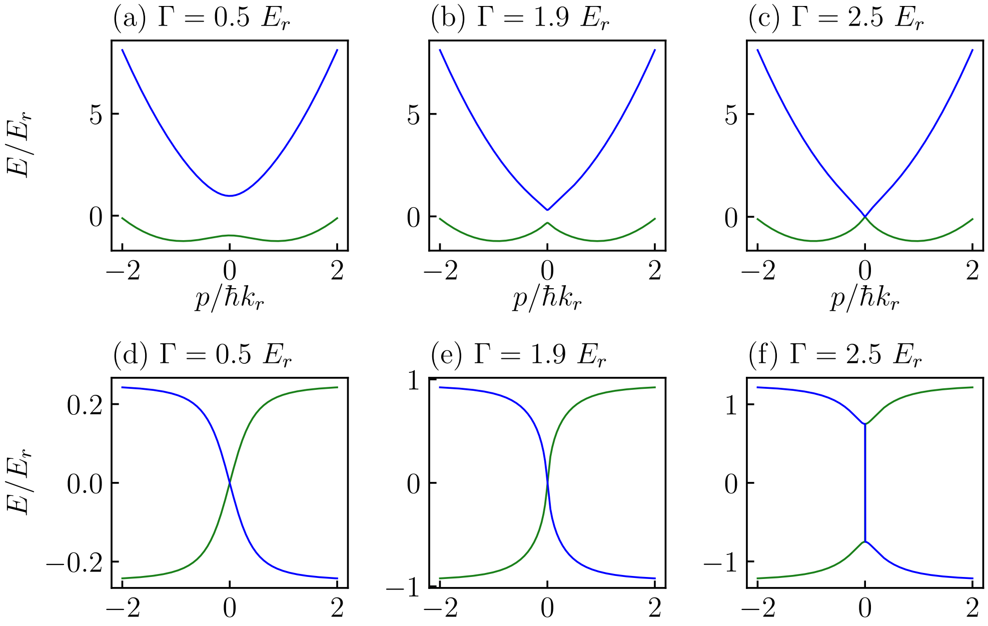

Figure 5.6: Begin with a double minimum phase $\Omega = 2E_r$. Ramp up the spin-dependent non-Hermitian strength Γ. Top row: the real part of the energy dispersion. Blue: upper band; green: lower band. Bottom row: the imaginary part of the energy dispersion. In all the cases, we set $\delta = 0$.

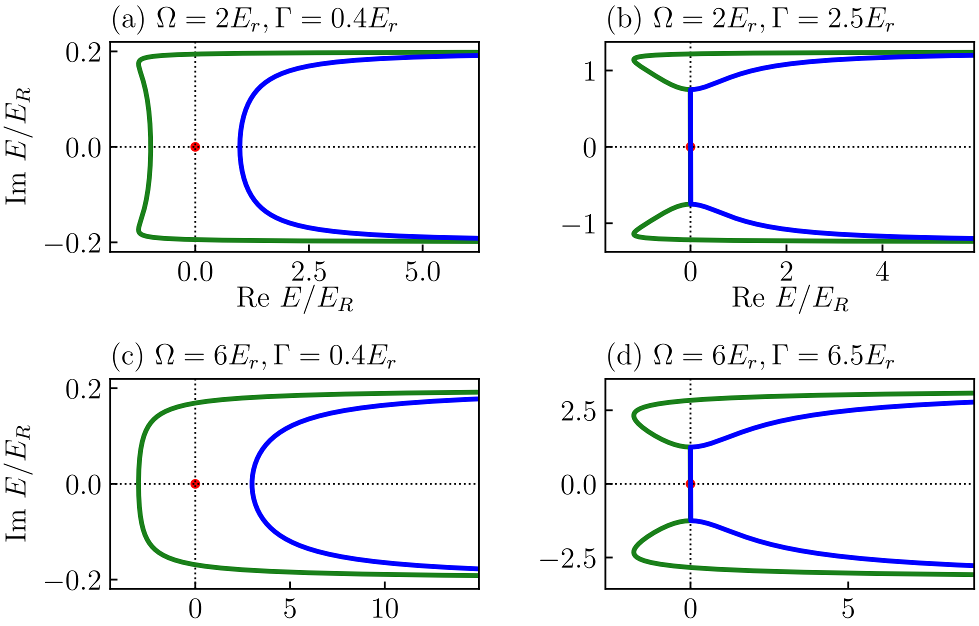

Figure 5.7: The complex dispersion in the complex plane as is parameterized by p. The red reference point is at $E = 0$. The upper (blue) and lower (green) bands are not topologically distinct above and below the double minimum to the single minimum phase transition at $\Omega = 4E_r$. But one could ask if the topology of the dispersion ever changes across the non-Hermitian phase transition at $\Gamma = \Omega$.

It is discovered that the lower band has a finite winding number of $w = \pm 1$ around the origin depending on the sign of Γ, whereas the upper band always has a zero winding number. This property of the bands always holds when one varies the parameters Ω or δ, as well as tuning the quantum phase from the single minimum into the double minimum. It is a topological property of the bands.

We also examine the eigenstates of such a Hamiltonian. We apply an open boundary condition to the system, by turning on a potential that has hard walls. It is noticed that all the eigenstates in the lower band localize themselves to one side of the box. As we flip the sign of Γ, the localization direction reverts. This seems to suggest bulk-boundary correspondence.

Based on the above two observations, it is natural for us to consider the relation between

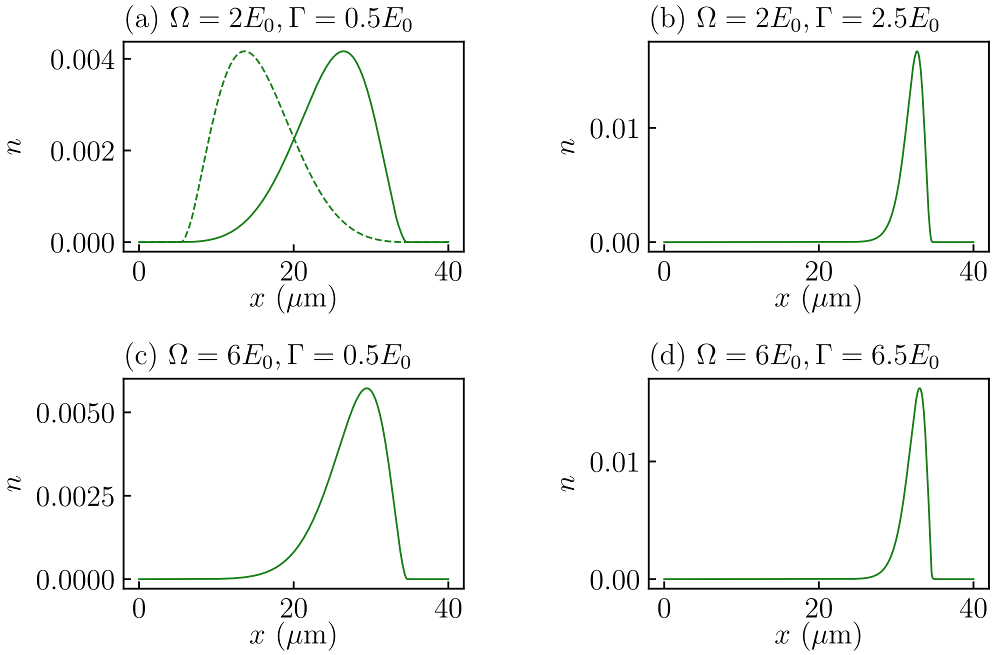

Figure 5.8: Plot the density profile of the particle in the ground state of the non-Hermitian Hamiltonian. In (a) the dashed and solid are for $\Gamma = -0.5$ and $0.5E_0$ respectively. These two cases are symmetric. We observe that the localization property does not seem to change qualitatively across either the SOC phase transition or the non-Hermitian phase transition. The localization "length" – or the center of mass drift $\langle\psi|\, \hat{x}\, |\psi\rangle$ does vary, though.

our Hamiltonian and the Hatano-Nelson model. Both of them have nonzero winding numbers which can be tuned, and both support directional localized eigenstates. Thus, we might be able to engineer an analog to the Hatano-Nelson model.

5.11 Effective single-band Hamiltonian

The usually useful approach to understanding the spin-orbit coupling problem of a BEC is by looking at the Raman-dressed states, which turns out analytically simple. The non-Hermitian term in the problem acts on a single spin, introducing only a trivial spin-dependent loss by its own. However, projecting this loss into the ground band of spin-orbit coupled Hamiltonian yields a momentum-dependent loss and an effective scalar potential. We derive the effective Hamiltonian via this procedure in this section.

The spin-orbit coupling is induced by two Raman lasers, resulting in the effective Hamiltonian in the spin-1/2 subspace:

$$\begin{aligned} H &= \frac{p^2}{2m} + \frac{p_r p}{m}\sigma_z + \frac{\hbar\Omega}{2}\sigma_x \\ &= \frac{(p + p_r\sigma_z)^2}{2m} + \frac{\hbar\Omega}{2}\sigma_x - \frac{p_r^2}{2m} \end{aligned}$$

where $p_r = \hbar k_r$ is the recoil momentum, and p is the canonical momentum. This Hamiltonian is known to have a second order phase transition from the double minimum to single minimum phases at $\Omega = 4\omega_r = 4E_r/\hbar$. The two dressed bands are derived in closed form in both phases:

$$E_\pm = \frac{p^2}{2m} \pm \sqrt{\left(\frac{pp_r}{m}\right)^2 + (\frac{\hbar\Omega}{2})^2}$$

with the eigenstate wavefunctions:

$$\psi_{\pm} = \begin{pmatrix} \sin\phi_{\pm} \\ \\ \cos\phi_{\pm} \end{pmatrix}$$

where

$$\phi_{\pm} = \arctan\left[\pm\sqrt{1+\left(\frac{2k_r p}{m\Omega}\right)^2} - \frac{2k_r p}{m\Omega}\right].$$

We introduce the non-Hermitian term to the Hamiltonian and have

$$H = \frac{(p+p_r\sigma_z)^2}{2m} + \frac{\hbar\Omega}{2}\sigma_x - \frac{p_r^2}{2m} - i\hbar\Gamma\left|\uparrow\right\rangle\!\left\langle\uparrow\right|.$$

The loss is purely on the $|\uparrow\rangle$ spin. We will treat this loss term as a perturbation to the Raman-dressed states, and will derive two models from it: one that approximately expands near $p = 0$, the other accounting for the full $p \in (-\infty, \infty)$. The following treatment is for the single minimum phase when the minimum is at $p = 0$.

5.11.1 Minimal model – imaginary gauge potential

We want to study the dynamics of bosons condensed in the lower band E_- near $p = 0$. In order to make Taylor expansion, we let

$$\lambda = \frac{2k_r p}{m\Omega},$$

and hence

$$\tan\phi_- = -1 - \lambda - \frac{\lambda^2}{2} = -1 - \lambda.$$

Near $p = 0$ the population in the $|\downarrow\rangle$ state is

$$p_\downarrow = \sin^2\phi_- = \frac{(1+\lambda)^2}{1+(1+\lambda)^2} = \frac{1}{2}(1+\lambda) = \frac{1}{2} + \frac{k_r p}{m\Omega} = \frac{1}{2} + \frac{v_r}{\Omega}k$$

where the recoil velocity is $v_r = \hbar k_r/m$.

In the meanwhile, we expand the dispersion relation

$$\begin{aligned} E_- &= \frac{p^2}{2m} - \frac{\hbar\Omega}{2}\sqrt{1+\left(\frac{2k_r p}{m\Omega}\right)^2} \\ &= p^2\left(\frac{1}{2m} - \frac{\hbar k_r^2}{m^2\Omega}\right) - \frac{\hbar\Omega}{2} \end{aligned}$$

from which the effective mass is

$$\frac{m^*}{m} = \frac{1}{1-\frac{4\omega_r}{\Omega}}.$$

Finally this leads to an effective Hamiltonian around $p = 0$:

$$\begin{aligned} H &= \frac{p^2}{2m^*} - i\hbar\Gamma p_\uparrow \\ &= \frac{p^2}{2m^*} - i\hbar\Gamma\left(\frac{1}{2} - \frac{v_r}{\Omega}k\right). \\ &= \frac{p^2}{2m^*} + i\Gamma\frac{v_r}{\Omega}p - i\frac{\hbar\Gamma}{2} \end{aligned}$$

This turns into a "free particle" Hamiltonian with an unusual momentum-dependent loss.

One makes two observations about the Hamiltonian: one it reduces to the reciprocal tunneling in the lattice models. To see that, consider the lattice model

$$H = \sum_j -(t+\gamma)a_{j+1}^\dagger a_j - (t-\gamma)a_j^\dagger a_{j+1}$$

After Fourier transform this becomes

$$\begin{aligned}
H &= -\sum_k \left[(t+\gamma)e^{-ik} + (t-\gamma)e^{ik}\right] a_k^+ a_k \\
&= -\sum_k [2\cos k - i2\gamma \sin k] a_k^+ a_k \\
&= \sum_k \left[-2 + k^2 + i2\gamma k\right] a_k^+ a_k
\end{aligned}$$

where in the last equality we expand near $k = 0$.

5.11.2 Full dispersion $p \in (-\infty, \infty)$

Invert the solution

$$\psi_- = \sin\phi_- \left|\downarrow\right\rangle + \cos\phi_- \left|\uparrow\right\rangle$$

and get

$$\left|\uparrow\right\rangle = \frac{\sin\phi_- \left|\psi_+\right\rangle - \sin\phi_+ \left|\psi_-\right\rangle}{\sin(\phi_- - \phi_+)},$$

so that we can get the full Hamiltonian

$$H = E_+ \left|+\right\rangle\left\langle+\right| + E_- \left|-\right\rangle\left\langle-\right| - i\hbar\Gamma \left|\uparrow\right\rangle\left\langle\uparrow\right|$$

where $\left|+\right\rangle$ and $\left|-\right\rangle$ stand for the upper and lower Raman dressed bands. Plug in the decomposition,

$$\begin{aligned}
H =& E_+ \left|+\right\rangle\left\langle+\right| + E_- \left|-\right\rangle\left\langle-\right| \\
&- \frac{i\hbar\Gamma}{\sin^2(\phi_- - \phi_+)} (\sin^2\phi_- \left|+\right\rangle\left\langle+\right| + \sin^2\phi_+ \left|-\right\rangle\left\langle-\right| \\
&- \sin\phi_- \sin\phi_+ \left|+\right\rangle\left\langle-\right| - \sin\phi_+ \sin\phi_- \left|-\right\rangle\left\langle+\right|).
\end{aligned}$$

To simplify the calculation, let

$$\beta = \frac{\hbar\Gamma}{\sin^2(\phi_- - \phi_+)},\ |+\rangle \rightarrow \frac{|+\rangle}{\sin\phi_-},\ |-\rangle \rightarrow \frac{|-\rangle}{\sin\phi_+}$$

so the Hamiltonian becomes a standard two-band Hamiltonian coupled by $i\beta$,

$$H = \left(\frac{E_+}{\sin^2\phi_-} - i\beta\right)|+\rangle\langle+| + \left(\frac{E_-}{\sin^2\phi_+} - i\beta\right)|-\rangle\langle-|$$
$$+\, i\beta(|+\rangle\langle-| + |-\rangle\langle+|).$$

We solve it in the $\beta \rightarrow 0$ limit

$$E'_- = \frac{E_-}{\sin^2\phi_+} - i\beta - \frac{(i\beta)^2}{\frac{E_+}{\sin^2\phi_-} - \frac{E_-}{\sin^2\phi_+}}$$

and after inverting the variable transformation

$$E'_- = E_- - i\beta\sin^2\phi_+ + \frac{\beta^2\sin^2\phi_+}{\frac{E_+}{\sin^2\phi_-} - \frac{E_-}{\sin^2\phi_+}}.$$

In the single minimum phase,

$$E'_- = E_- - i\hbar\Gamma\left[\frac{\sin\phi_+}{\sin(\phi_- - \phi_+)}\right]^2 + \frac{\sin^2\phi_+}{\sin^4(\phi_- - \phi_+)}\frac{\hbar^2\Gamma^2}{\frac{E_+}{\sin^2\phi_-} - \frac{E_-}{\sin^2\phi_+}}.$$

Let's write it in the Hamiltonian form

$$\begin{aligned}H_- =&\frac{p^2}{2m} - \frac{\hbar\Omega}{2}\sqrt{1+\left(\frac{2k_r p}{m\Omega}\right)^2} - i\hbar\Gamma\left[\frac{\sin\phi_+}{\sin\left(\phi_- - \phi_+\right)}\right]^2 \\ &+ \frac{\sin^2\phi_+}{\sin^4\left(\phi_- - \phi_+\right)}\frac{\hbar^2\Gamma^2}{\frac{E_+}{\sin^2\phi_-} - \frac{E_-}{\sin^2\phi_+}}.\end{aligned} \tag{5.32}$$

5.11.3 Direct diagonalization

In fact, the advantage of the spin-orbit coupling Hamiltonian is that it is analytically simple. In this section we derive the properties of the single particle Hamiltonian (5.60). We rewrite it as

$$\begin{aligned}\hat{H}_{\text{SOC}} =&\frac{(\hat{p}+0\sigma_z)^2}{2m} + \frac{\hbar\Omega}{2}\sigma_x + \frac{\hbar\delta}{2}\sigma_z - i\hbar\Gamma\mathcal{P}_\uparrow \\ =&\frac{(\hat{p}+0\sigma_z)^2}{2m} + \frac{\hbar\Omega}{2}\sigma_x + \frac{\hbar(\delta - i\Gamma)}{2}\sigma_z - \frac{\hbar\Gamma}{2}\mathcal{I}.\end{aligned} \tag{5.33}$$

In the following, we consider the overall loss term as a constant offset.

We can diagnonalize the 2x2 Hamiltonian and derive the eigenenergies

$$\begin{aligned}E_\pm =&\frac{p^2}{2m} \pm \hbar\sqrt{(\frac{\Omega}{2})^2 + (\frac{p_0 p}{m\hbar} + \frac{\delta}{2} - i\frac{\Gamma}{2})^2} \\ =&\frac{p^2}{2m} \pm \hbar\sqrt{(\frac{\Omega}{2})^2 + (\frac{p_0 p}{m\hbar})^2 - i\frac{p_0 p}{m\hbar}\Gamma - (\frac{\Gamma}{2})^2}.\end{aligned} \tag{5.34}$$

We will focus on the lower band for our BEC. To relate to our experiment, we set $\delta = 0$.

In a perturbative treatment, by assuming $\Gamma \ll \Omega, p_0^2/2m$, we can expand

$$\begin{aligned}E_- =&\frac{p^2}{2m} - \hbar\sqrt{(\frac{\Omega}{2})^2 + (\frac{p_0 p}{m\hbar})^2} \\ &+ i\frac{1}{2}\frac{p_0 p}{m\hbar}\Gamma\frac{1}{\sqrt{(\frac{\Omega}{2})^2 + (\frac{p_0 p}{m\hbar})^2}} - \hbar\frac{\Gamma^2}{8}\frac{1}{\sqrt{(\frac{\Omega}{2})^2 + (\frac{p_0 p}{m\hbar})^2}}\end{aligned} \tag{5.35}$$

where the first line

$$E_{-0} = \frac{p^2}{2m} - \hbar\sqrt{(\frac{\Omega}{2})^2 + (\frac{p_0 p}{m\hbar})^2} \tag{5.36}$$

represents the lower band energy without the spin-dependent loss term $\mathcal{P}_\uparrow$.

In our experiment, we load atoms into the "single-minimum" phase of the Hamiltonian, where $\Omega > 2p_0^2/m\hbar$ and allows us to expand near $p = 0$,

$$\begin{aligned} \sqrt{(\frac{\Omega}{2})^2 + (\frac{p_0 p}{m\hbar})^2} &\approx \frac{\Omega}{2}[1 + \frac{1}{2}(\frac{2p_0 p}{m\hbar\Omega})^2] \\ \frac{1}{\sqrt{(\frac{\Omega}{2})^2 + (\frac{p_0 p}{m\hbar})^2}} &\approx \frac{2}{\Omega}[1 - \frac{1}{2}(\frac{2p_0 p}{m\hbar\Omega})^2]. \end{aligned} \tag{5.37}$$

Then we sort out the terms in orders of Γ and p

$$\begin{aligned} E_- =& p^2(\frac{1}{2m} - \frac{p_0^2}{m^2\hbar\Omega} + \frac{1}{2}\frac{\Gamma^2}{\Omega^2}\frac{p_0^2}{m^2\hbar\Omega}) \\ &+ i\frac{p_0\Gamma}{m\Omega}p + 2i\hbar\Gamma(\frac{p_0}{m\hbar\Omega})^3 p^3 \\ &- \frac{\hbar\Omega}{2} - \frac{\hbar\Gamma^2}{4\Omega}. \end{aligned} \tag{5.38}$$

From this result we can see that the non-Hermitian term modifies the effective mass

$$m^* = [\frac{1}{m} - \frac{2p_0^2}{m^2\hbar\Omega} + \frac{p_0^2}{m^2\hbar\Omega}(\frac{\Gamma}{\Omega})^2]^{-1}. \tag{5.39}$$

In addition, we can formulate the imaginary term into an imaginary gauge potential

$$\mathcal{B} = -\frac{p_0\Gamma}{\Omega}\frac{m^*}{m}. \tag{5.40}$$

The exact results of the energy dispersion is plotted and summarized in Fig. 5.5, 5.6, and

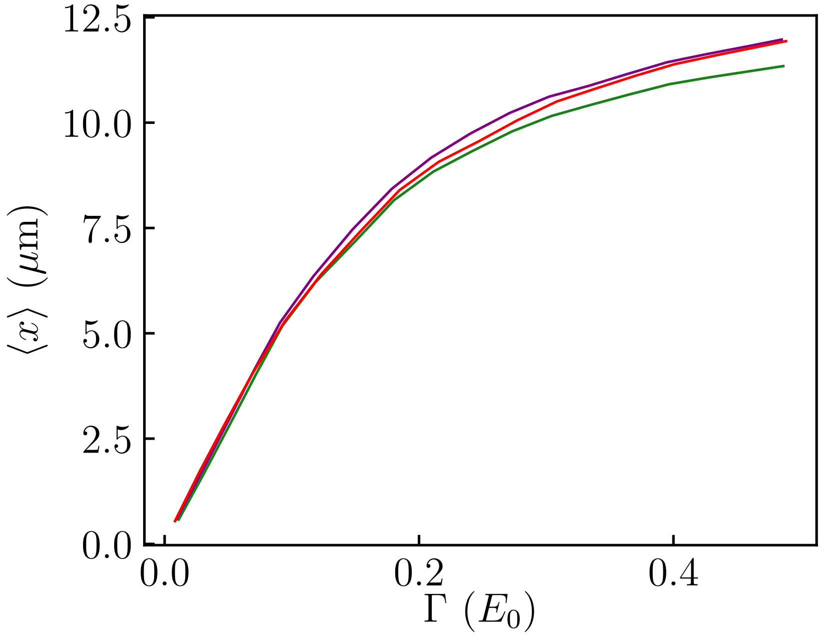

Figure 5.9: Comparison of the three different models on prediction of the ground state. Red: non-Hermitian SOC model; purple: minimal model (effective mass and the imaginary gauge potential); green: projected model (lower band dispersion and the imaginary gauge potential)

5.7. In addition to the spectrum, we can also find the ground state of the Hamiltonian in a flat potential. Examples are displayed in Fig. 5.8.

5.11.4 Prediction of the ground state

We run numeric solvers using the three different Hamiltonians to verify the correctness of the projection and approximation. In Fig. 5.9 we plot the ground state displacement from the center of the box potential, as calculated with the three models. We discover that the imaginary gauge potential works as an excellent approximation for predicting the ground state center of mass drift.

5.12 Quench Dynamics

We know that the non-Hermitian spin-orbit coupled system exhibits the NHSE, which is shown by theoretically finding the ”quasi-edge” modes. But in the following section, we study the time evolution after one suddenly turns on the non-Hermitian term (quench dynamics). This is important because: 1. it is of experimental relevance (our experiment time is limited by the atom loss, typically on the order of 10 ms); and 2. it is itself a valuable question to ask: what unusual dynamics does the non-Hermitian topology bring to system? Does the time evolution relate to the topological invariant? There are already some theoretical studies on the dynamics in a system with NHSE. But they are in different contexts.

We have introduced the simple force model in the last section, which gave us intuition for the source of the acceleration, but it brought us more confusion than understanding. During the development of the model, we were puzzled for a long time by some interesting observations, which I think are better to be elaborate here. We compare the full GPE dynamics simulation with the projected model.

5.12.1 Magnitude of the acceleration

In Fig. 5.10a, we consider a ground state BEC in a box trap. At $t = 0$ we snap on the spin-dependent loss which creates the imaginary gauge potential, and simulate the center of mass evolution of a function of time. According to previous subsection, we know the center of mass would drift. However, in Fig. 5.10b we can consider the same dynamics starting with a non-interacting particle-in-box ground state. We discover that case (b) experience drifts that is much smaller than (a). With case (b), our experimental resolution cannot measure the drift at all – there

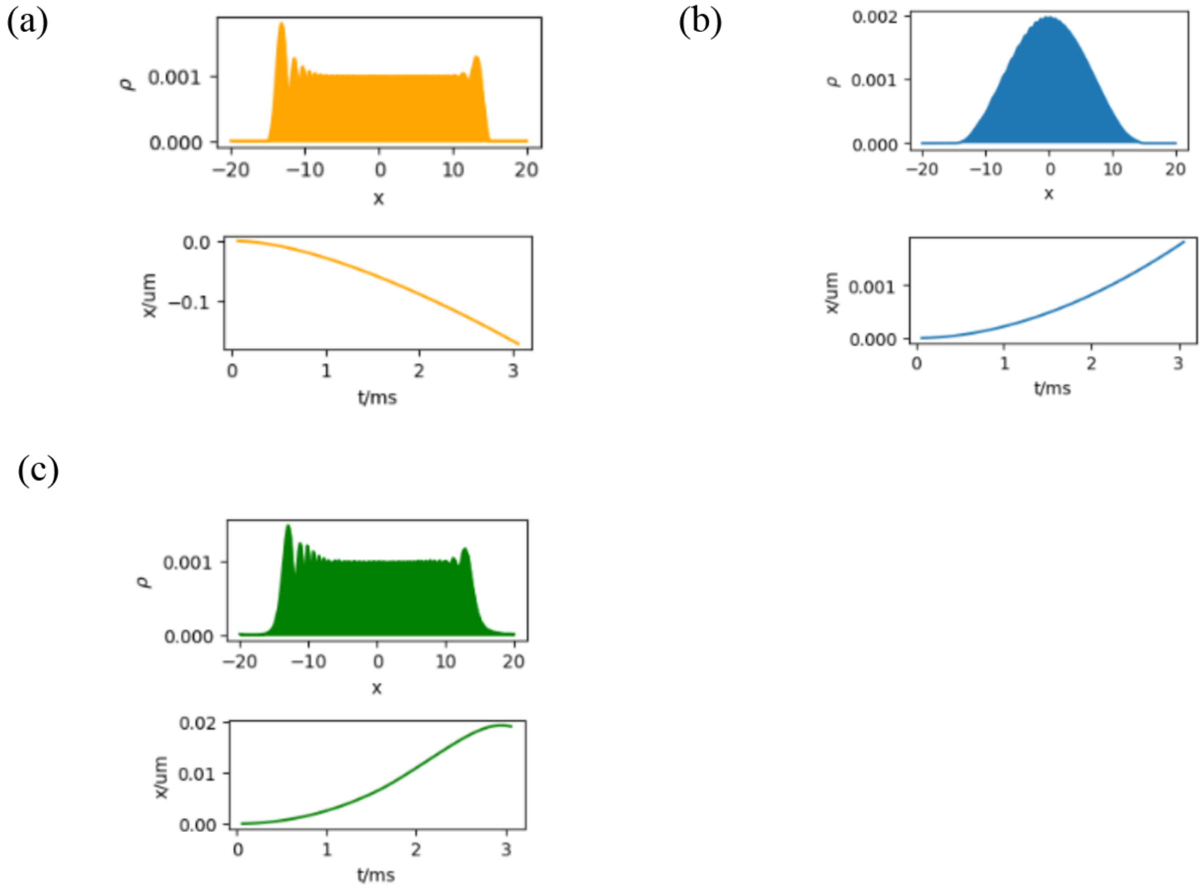

Figure 5.10: Simulated dynamics to illustrate the contribution of the transport. We plot the initial state density profile above, and the $\langle x \rangle$ as a function of time t below. (a) BEC ground state, keep the box trap on. (b) Particle in a box ground state, keep the box trap on. (c) BEC ground state, snap the trap off.

must be some interaction effect.

5.12.2 Direction of the acceleration

In the simulation, we find a strange behavior that the direction of transport is not always the same. We investigated this and the following example is a good illustration. We consider the cases beginning with the GPE ground state (a,c). What is different in case (c) is that the box trap is snapped off at $t = 0$. We notice that the atoms experience an opposite acceleration to case (a) where the trap is kept. We intend to resolve these puzzles by building a mathematical model for the non-Hermitian evolution in real space.

5.12.3 Dynamics model

We noticed that the imaginary term is indeed a "gauge field". Thus, the canonical momentum might be different from the mechanical momentum from our experience with the real gauge field. Is there a simple way to understand it?

We are considering the time evolution under the Hamiltonian

$$H = H_1 + iH_2 = \frac{p^2}{2m^*} + V(x) + i\beta p \tag{5.41}$$

with or without the external trap potential (box or harmonic). We would like to study the quantum mechanics by ignoring the mean field interaction. The evolution follows

$$\begin{cases} i\partial_t \left|\psi\right\rangle = (H_1 + iH_2) \left|\psi\right\rangle \\ i\partial_t \left\langle\psi\right| = \left\langle\psi\right| (H_1 - iH_2) \end{cases} . \tag{5.42}$$

Following the spirit of Heisenberg,

$$\begin{aligned} i\partial_t \langle\psi|\,\hat{O}\,|\psi\rangle &= -\langle\psi|\,(H_1 - iH_2)O\,|\psi\rangle + \langle\psi|\,O(H_1 + iH_2)\,|\psi\rangle \\ &= -\langle[H_1, \hat{O}]\rangle + i\langle\{H_2, \hat{O}\}\rangle \end{aligned} \tag{5.43}$$

This looks simple but we overlooked the fact that state vector $|\psi\rangle$ is not normalized to unity because of the non-Hermitian Hamiltonian.

$$\langle\psi|\psi\rangle = \langle\psi(0)|\, e^{iH_1t+H_2t} e^{-iH_1t+H_2t}\,|\psi(0)\rangle \tag{5.44}$$

So our real physical observable is

$$\partial_t \frac{\langle\psi|\,\hat{O}\,|\psi\rangle}{\langle\psi|\psi\rangle} = -\frac{\langle O\rangle}{\langle\psi|\psi\rangle^2}\partial_t \langle\psi|\psi\rangle + \frac{\partial_t\langle O\rangle}{\langle\psi|\psi\rangle} \tag{5.45}$$

As a special case, we first plug in $\hat{O} = \mathbb{I}$ to equation 5.43

$$\partial_t \langle\psi|\psi\rangle = \langle\psi|\,2H_2\,|\psi\rangle = 2\beta\,\langle\psi|\,p\,|\psi\rangle$$

We introduce the equation of motion of the physical observable

$$\partial_t\langle\langle\hat{O}\rangle\rangle = -\langle\langle\hat{O}\rangle\rangle\frac{\partial_t \langle\psi|\psi\rangle}{\langle\psi|\psi\rangle} + i\langle\langle[\hat{H}_1, \hat{O}]\rangle\rangle + \langle\langle\{\hat{H}_2, \hat{O}\}\rangle\rangle \tag{5.46}$$

where we define

$$\langle\langle\hat{O}\rangle\rangle = \frac{\langle\hat{O}\rangle}{\langle\psi|\psi\rangle} \tag{5.47}$$

as the renormalized physical observable which is what we measure in the experiment.

Thus, the equation for $\hat{O} = x$ is

$$\partial_t \langle\langle x \rangle\rangle = \frac{\langle\langle p \rangle\rangle}{m^*} + \beta\Big(\langle\langle \{p, x\} \rangle\rangle - 2\langle\langle x \rangle\rangle \langle\langle p \rangle\rangle \Big). \tag{5.48}$$

And the equation for p is:

$$\partial_t \langle\langle p \rangle\rangle = i\langle\langle [V, p] \rangle\rangle + 2\beta\Big(\langle\langle p^2 \rangle\rangle - \langle\langle p \rangle\rangle^2 \Big). \tag{5.49}$$

There are two unusual terms. In the p equation, the second term is an "acceleration" proportional to the variance of the canonical momentum p. On the other hand, the x equation has also a second term proportional to the "covariance" in the phase space. In the coordinate basis, the $\{p, x\}$ term is

$$\langle \psi | \{p, x\} | \psi \rangle = \int dx \frac{\hbar}{i} x (\psi^* \partial_x \psi - \psi \partial_x \psi^*).$$

and is sometimes responsible for the opposite physical momentum to the canonical momentum.

We note that

$$\langle \{p, x\} \rangle - 2\langle x \rangle \langle p \rangle = \langle \{x - \langle x \rangle, p - \langle p \rangle\} \rangle \tag{5.50}$$

and

$$\begin{aligned} \{p, x\} =& i\hbar\{(a^\dagger + a), (a^\dagger - a)\} \\ =& 2i\hbar(a^\dagger a^\dagger - aa) \end{aligned} \tag{5.51}$$

5.12.4 Example: Gaussian wave packet evolution

As a concrete example, hereby we consider the time evolution of a Gaussian wave packet at $t = 0$

$$\psi(x, t = 0) = e^{-\frac{x^2}{2\sigma^2}}$$

that evolves under the Hamiltonian

$$H = \frac{p^2}{2m} + i\beta p.$$

The Fourier component is

$$\tilde{\psi}(p) = \int dx e^{ipx} e^{-\frac{x^2}{2\sigma^2}} = C e^{-\frac{\sigma^2}{2}p^2}$$

The wavepacket at t is

$$\psi(x, t) = e^{-iHt}\psi(x, t = 0) = e^{-iHt} \int dp e^{-\frac{\sigma^2}{2}p^2} e^{ipx}$$

Plug in

$$\begin{aligned} \psi(x, t) &= \int dp e^{-i\frac{p^2}{2m}t} e^{-\frac{\sigma^2}{2}p^2 + \beta p t} e^{ipx} \\ &= \int dp e^{-\frac{p^2}{2}\left(\frac{it}{m} + \sigma^2\right)} e^{p(\beta t + ix)} \\ &= \exp\left\{-\frac{1}{2}\frac{(x - i\beta t)^2}{\sigma^2 + \frac{it}{m}}\right\}. \end{aligned}$$

Expand the exponent into the real and imaginary parts:

$$\psi(x,t) = e^{-\frac{1}{2}\frac{\left(x^2-\beta^2t^2\right)\sigma^2-\frac{2\beta t^2}{m}x}{\sigma^4-\frac{t^2}{m^2}}} e^{\frac{i}{2}\frac{2\beta t\sigma^2 x+\frac{t}{m}\left(x^2-\beta^2t^2\right)}{\sigma^4-\frac{t^2}{m^2}}}.$$

The Gaussian center drifts

$$\langle x(t)\rangle = \frac{\hbar\beta t^2}{m^*\sigma^2}.$$

This means the wavepacket has a constant acceleration

$$a = \hbar\beta/m^*\sigma^2.$$

On the other hand, we can use our equations of motion in the last section. To do that, we need to compute a bunch of Gaussian integrals. And we will use old notations of $\langle O\rangle$ rather than O because we normalize the wavefunctions first, and then compute the expectation values.

First we normalize the wavefunction:

$$\psi(x,t=0) = \frac{e^{-\frac{x^2}{2\sigma^2}}}{\sqrt[4]{\pi}\sqrt{\sigma}}.$$

And that of time t becomes

$$\psi(x,t) = \frac{\sqrt{m\sigma}\exp\left(-\frac{\beta^2t^2}{2\sigma^2}-\frac{m(x-i\beta t)^2}{2m\sigma^2+2it}\right)}{\sqrt[4]{\pi}\sqrt[4]{m^2\sigma^4+t^2}}.$$

We verify that canonical momentum

$$\begin{aligned}\langle\psi|\, p\, |\psi\rangle &= -i\int dx\ \psi^*\partial_x\psi \\ &= \frac{\beta t}{\sigma^2}\end{aligned} \tag{5.52}$$

and position

$$\begin{aligned}\langle\psi|\, x\, |\psi\rangle &= -i\int dx\ \psi^* x\psi \\ &= \frac{\beta t^2}{m\sigma^2}.\end{aligned} \tag{5.53}$$

We noted that the results match what we directly derived from the form of the wavefunctions.

The second moments are

$$\begin{aligned}\langle\psi|\, \{p,x\}\, |\psi\rangle &= \int dx \frac{\hbar}{i} x(\psi^*\partial_x\psi - \psi\partial_x\psi^*) \\ &= \frac{t\,(\sigma^2+2\beta^2t^2)}{m\sigma^4}\end{aligned} \tag{5.54}$$

and

$$\begin{aligned}\langle\psi|\, p^2\, |\psi\rangle &= -\int dx \psi^*\partial_x^2\psi \\ &= \frac{\sigma^2+2\beta^2t^2}{2\sigma^4}.\end{aligned} \tag{5.55}$$

Now we can verify the equations 5.48 and 5.49. For equation 5.48,

$$\textbf{LHS} = \frac{2\hbar\beta t}{m\sigma^2} \tag{5.56}$$

while

$$\begin{aligned}\textbf{RHS} =& \frac{\beta t}{m\sigma^2} + \beta\Big(\frac{t\,(\sigma^2+2\beta^2t^2)}{m\sigma^4} - 2\frac{\beta t^2}{m\sigma^2}\frac{\beta t}{\sigma^2}\Big) \\ =& \frac{2\beta t}{m\sigma^2}.\end{aligned} \tag{5.57}$$

For equation 5.49,

$$\textbf{LHS} = \frac{\beta}{\sigma^2} \tag{5.58}$$

and

$$\begin{aligned}\textbf{RHS} =& 2\beta\Big(\frac{\sigma^2 + 2\beta^2 t^2}{2\sigma^4} - (\frac{\beta t}{\sigma^2})^2\Big)\\ =& \frac{\beta}{\sigma^2}.\end{aligned} \tag{5.59}$$

Therefore, we confirmed that the equations of motion are correct.

5.13 Experimental observations

The base experimental system we make is a spin-orbit coupled quantum gas in the single minimum phase. As shown in Fig. 5.11(b) a pair of lasers Raman-coupled two internal states $|\downarrow\rangle$ and $|\uparrow\rangle$ with strength Ω, recoil momentum 0 [35] and recoil energy $E_0 = p_0^2/(2m)$; an additional microwave field drove transitions between $|\uparrow\rangle$ and a lossy subspace. This realized a two-band non-Hermitian SOC model with Hamiltonian

$$\hat{H}_{\text{SOC}} = \frac{(\hat{p} + 0\sigma_z)^2}{2m} + \frac{\hbar\Omega}{2}\sigma_x + \frac{\hbar\delta}{2}\sigma_z - i\hbar\Gamma\mathcal{P}_\uparrow \tag{5.60}$$

with Pauli operators $\sigma_{x,y,z}$, quasi-momentum $\hat{p}$ [98], atomic mass m, detuning δ, and spin projection operator $\mathcal{P}_\uparrow = |\uparrow\rangle\langle\uparrow|$.

We make an adiabatic approximation in which dynamics are projected into the lowest band and focus on the large Raman coupling ($\Omega > 4E_0$) "single minimum" limit [102], where the Hermitian contribution to $\hat{H}_{\text{SOC}}$ has low-energy dynamics well described by an effective mass m^* [103]. The ground state, a plane-wave at $p = 0$, consists of an equal superposition of

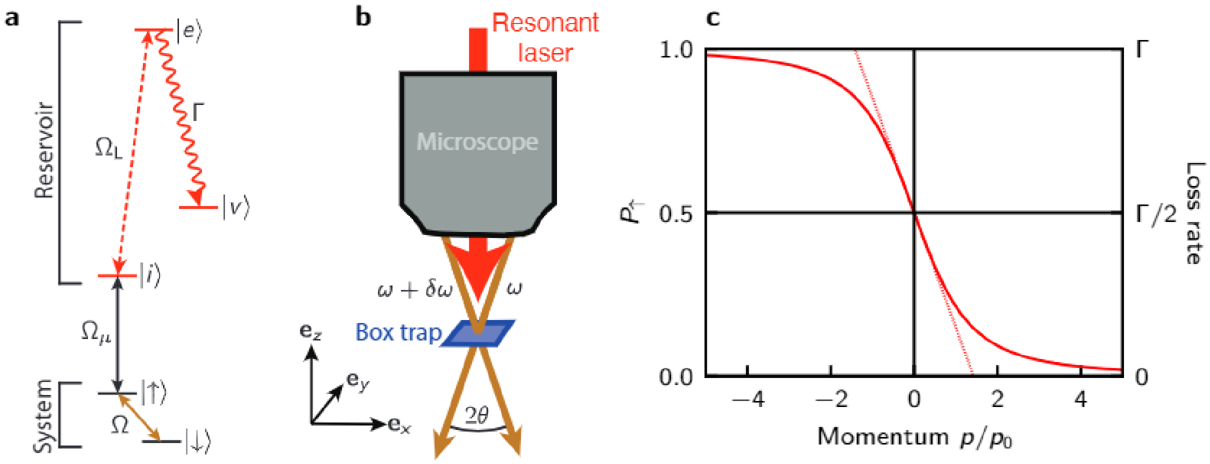

Figure 5.11: (b) A homogeneous BEC was confined in the e_x-e_y plane, and Raman-dressed by a pair of laser beams project through a high-resolution microscope objective. Depletion from the $|\uparrow\rangle$ spin was engineered through continuous illumination of a resonant laser (to D_2 line) and microwave field. (a) The effective internal level diagram. The Raman lasers were used to engineer SOC. (c) At $\hbar\Omega > 4E_R$, the single minimum state had spin decomposition linear to p near $p = 0$.

and ; for eigenstates with $p \ll \sqrt{2m\hbar\Omega}$ the occupation probabilities are proportional to p with $P_{\uparrow,\downarrow}(p) = [1 \mp 2p_0 p/(m\hbar\Omega)]/2$ (Fig. 5.11c). In this case the non-Hermitian contribution to Eq. (5.60) becomes $-i\hbar\Gamma P_\uparrow(\hat{p})$, leading to an imaginary gauge field

$$\mathcal{B} = -p_0 \frac{\Gamma}{\Omega} \frac{m^*}{m} \tag{5.61}$$

along with an overall loss rate $\Gamma/2$. These expressions are suitable for our experimental configuration.

5.13.1 Setup

We initialized nearly pure ^{87}Rb BECs with N_0 atoms confined in an optical dipole trap (ODT) in the space spanned by $|f = 1, m_F = 0\rangle$ and $|f = 1, m_f = 1\rangle$ that served as our spin states $|\uparrow\rangle$ and $|\downarrow\rangle$, respectively. Our experiments were performed with a bias magnetic field $B_0\mathbf{e}_y$

that provided a sufficient quadratic contribution to the Zeeman shift for us to resonantly couple $|\uparrow\rangle$ and $|\downarrow\rangle$ whilst being far off resonance to $|f=1, m_F=-1\rangle$. We induced spin-orbit with strength $0=(2\pi\hbar/\lambda_R)\times\sin(\theta_R)$ by Raman-coupling $|\uparrow\rangle$ and $|\downarrow\rangle$ with a pair of $\lambda_R = 790.12\ \mathrm{nm}$ laser beams intersecting with half-angle $\theta_R = 16.5$ degrees (see Fig. 5.11a). The spin-dependent loss in Eq. (5.60) was created by simultaneously microwave coupling $|\uparrow\rangle$ (with Rabi frequency Ω_μ) to an intermediate state $|i\rangle = |f=2, m_F=0\rangle$ while expelling atoms with a laser resonant between $|i\rangle$ and $|f'=3, m_F'=0\rangle$, aligned along $\mathbf{e}_z$ with intensity I giving an optical Rabi frequency $\Omega_{\mathrm{L}}/\Gamma = \sqrt{I/(2I_{\mathrm{sat}})}$ in terms of the natural line-width Γ and saturation intensity $\mathrm{I}_{\mathrm{sat}}$. As we describe below, the loss experienced by $|\uparrow\rangle$ was controlled either by changing Ω_{L} or Ω_μ.

5.13.2 Quantum Zeno effect

The behavior of open quantum systems—described by the Master equation—can be approximated by non-Hermitian Hamiltonians for times up to the first so-called quantum jump, in our case at about twice the $26\ \mathrm{ns}$ lifetime of $^{87}\mathrm{Rb}$'s $5P_{3/2}$ excited state. The leads to a question: how can a non-Hermitian a picture remain valid for our $\approx 10\ \mathrm{ms}$ evolution times?

We experimentally explore this question using a simplified setup replacing Raman $|\uparrow\rangle \leftrightarrow |\downarrow\rangle$ coupling with RF [1]. Beginning with a BEC, we suddenly applied a combination of optical, microwave, and RF fields for a duration t, and monitored the time-evolving populations $N_\uparrow$, $N_\downarrow$, and N_i. In what follows we contrast two simplified coupling schemes [Fig. 5.12(a)] to describe this combination of fields: in the first "closed" scheme, spontaneous decay from an electronic excited state $|e\rangle$ returns population to $|i\rangle$, and in the second "open" scheme, decay from $|e\rangle$ populates an otherwise inert vegetable state $|v\rangle$. The open models captures the additional physics

---

[1] For these data set the bias field to $B_0 = 10\ \mathrm{G}$.

that the momentum imparted during a spontaneous decay suffices to eject an atom from our shallow ODT, never to return.

Figure 5.12(b) shows the resulting evolution without RF coupling for a range of optical Rabi frequencies $\Omega_{\rm L}$. The time evolution transitions from damped Rabi oscillations between and $|i\rangle$ (small $\Omega_{\rm L}$) to exponential decay of (large $\Omega_{\rm L}$). The inset plots both τ and the product $\omega\tau$ obtained from a simple oscillatory decay model $\exp(-t/\tau)\cos^2(\omega t/2)$ fit to the data as well as both the closed and open models. The quantum Zeno effect (QZE) describes the exponential decay regime, with $\omega\tau \gg 1$, in which the $|{\uparrow}\rangle$ lifetime increases with $\Omega_{\rm L}$. The curves plot fits to the closed (grey) and open (red) models to these data respectively, showing that only the open model correctly describes the experimental dynamics. Together these then resolve the question: the "open" dynamics assures that no observed atoms have experienced a quantum jump, making the non-Hermitian description valid for all times. Furthermore the QZE partly decouples the $|{\uparrow},{\downarrow}\rangle$ subspace, and makes the remaining non-Hermitian contribution to the dynamics easily tunable.

The evolution in Fig. 5.13 with RF coupling further confirms this picture. The solid curves plot the predicted non-Hermitian evolution computed with no free parameters using the decay rates measured in (b) and the separately measured RF Rabi frequency. These cases are specific examples of a more general scenario, where a subspace $|G\rangle$ undergoing otherwise Hamiltonian evolution is weakly coupled to a subspace $|E\rangle$ (with typical strength Ω_{GE}) that decays into to an uncoupled subspace $|V\rangle$ (with typical rate γ). When $|\Omega_{GE}| \ll \gamma$ the above description applies, leading to long-time non-Hermitian evolution in $|G\rangle$ with QZE suppressed loss rates.

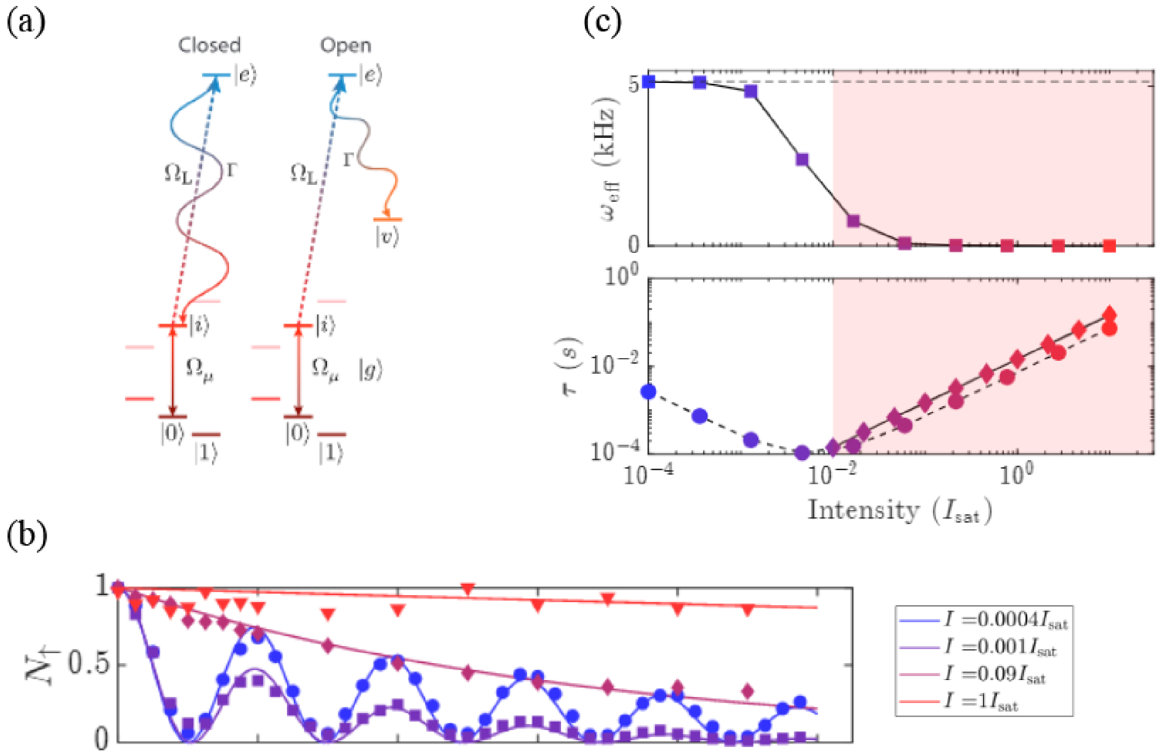

Figure 5.12: (a) Complete level diagram for engineering the effective loss Γ. Our experiment corresponds to the "open" case, where the decayed atoms are expelled out of the system. (b, c) Γ is a decreasing function of resonant laser power in the QZE regime. At $I \gg I_{sat}$, the loss rate increased again due to off-resonant scattering from the $f = 1$ states. However, before that the dependence of oscillation frequency and damping rate on the loss rate is complicated.

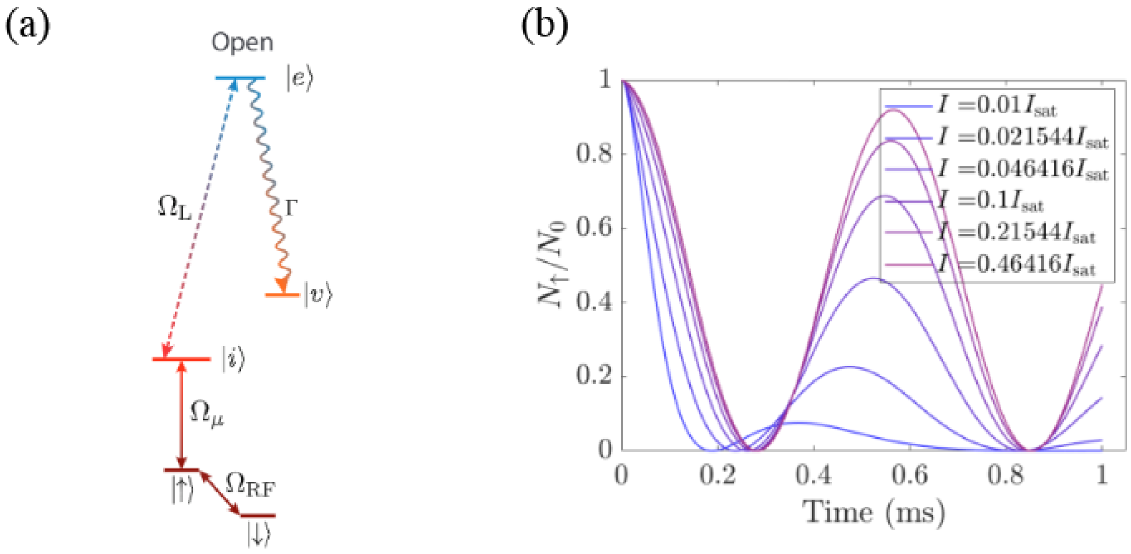

Figure 5.13: Simulation data for the case with the RF/Raman coupling between the and shown in (a). As one increases the dissipation strength to enter the QZE regime, the oscillations (b) become more coherent.

5.13.3 Raman experiment

We observed these effects using an $N_0 \approx 5 \times 10^4$ atom BEC confined in the $\mathbf{e}_x$-$\mathbf{e}_y$ plane by a $30\ \mu\mathrm{m}$ square box potential with walls formed by a blue-detuned optical field ($\lambda = 635\ \mathrm{nm}$), and harmonically confined along $\mathbf{e}_z$ with $\omega_z/(2\pi) \approx 220\ \mathrm{Hz}$. The bias field $B_0 \approx 10\ \mathrm{G}$ was selected so that the initially $|\downarrow\rangle$ polarized BEC was detuned by $\delta = 10.0(5)E_R$ from Raman resonance. We adiabatically transferred the BEC to the $\Gamma = 0$ SOC ground state (i.e., with $p = 0$ and in the lowest SOC band) by first ramping the intensity of Raman beams from zero to $\hbar\Omega_R = 5.7(1)E_R$ in $150\ \mathrm{ms}$ and then ramping detuning δ to zero in $150\ \mathrm{ms}$. The system was then rendered non-Hermitian by abruptly applying the microwave and optical couplings at $t = 0$.

The Raman coupling parameters were chosen to maximize the observable impact of $\mathcal{B}$.

Firstly, we selected a $\Omega_R \gtrsim 4E_0$ Raman coupling strength: large enough for the ground SOC band to be nominally harmonic with effective mass $m^* \gtrsim m$, yet small enough to minimize spontaneous emission driven heating. Recalling that $E_0 \propto p_0^2$, the remaining contributions to $\mathcal{B}$ in Eq. (5.61) are inversely proportional to p_0 and therefore a decreasing function of intersection angle θ_R. Our final choice of $\theta = 16.5$ degrees yields an easily observable signal while still maintaining a wide range of momenta for which Eq. (5.61) is valid.

5.13.4 Non-reciprocal transport

After preparing the BEC in the SOC ground state, we simultaneously applied the microwave and optical fields and allowed the system evolve a time t up to $9\ \mathrm{ms}$. Using the high NA microscope pictured in Fig. 5.11(a), we separately measured the final $|\uparrow\rangle$ and $|\downarrow\rangle$ density distributions in-situ using partial transfer absorption imaging [104]. Fig. 5.14 plots the time evolution of the center of mass position that initially evolves linearly in time. We fit the short-time dynamics up to $\sim$10 ms to a constant acceleration a, and plotted it as a function of varying Γ.

The dynamics of a BEC are affected by its mean-field interaction and hence are expected to be described by the Gross-Pitaevskii equation (GPE) $i\partial_t\psi(\mathbf{x}) = (\hat{H} + g|\psi(\mathbf{x})|^2\mathcal{I})\psi(\mathbf{x})$, g being the contact interaction strength. We first computed the ground state of a BEC under spin-orbit coupling using the time-splitting pseudo-spectral method. Then, by introducing non-Hermiticity, we simulated the real-time GPE evolution of the Hamiltonian (5.60). Quantitative agreement was found between the predicted and measured transport and acceleration (Fig. 5.14a, b). Furthermore, we confirmed that the dynamics fully happened in the lower band of (5.60), so they were well approximated with m^* and the imaginary gauge potential $\mathcal{B}$ (Fig. 5.14b).

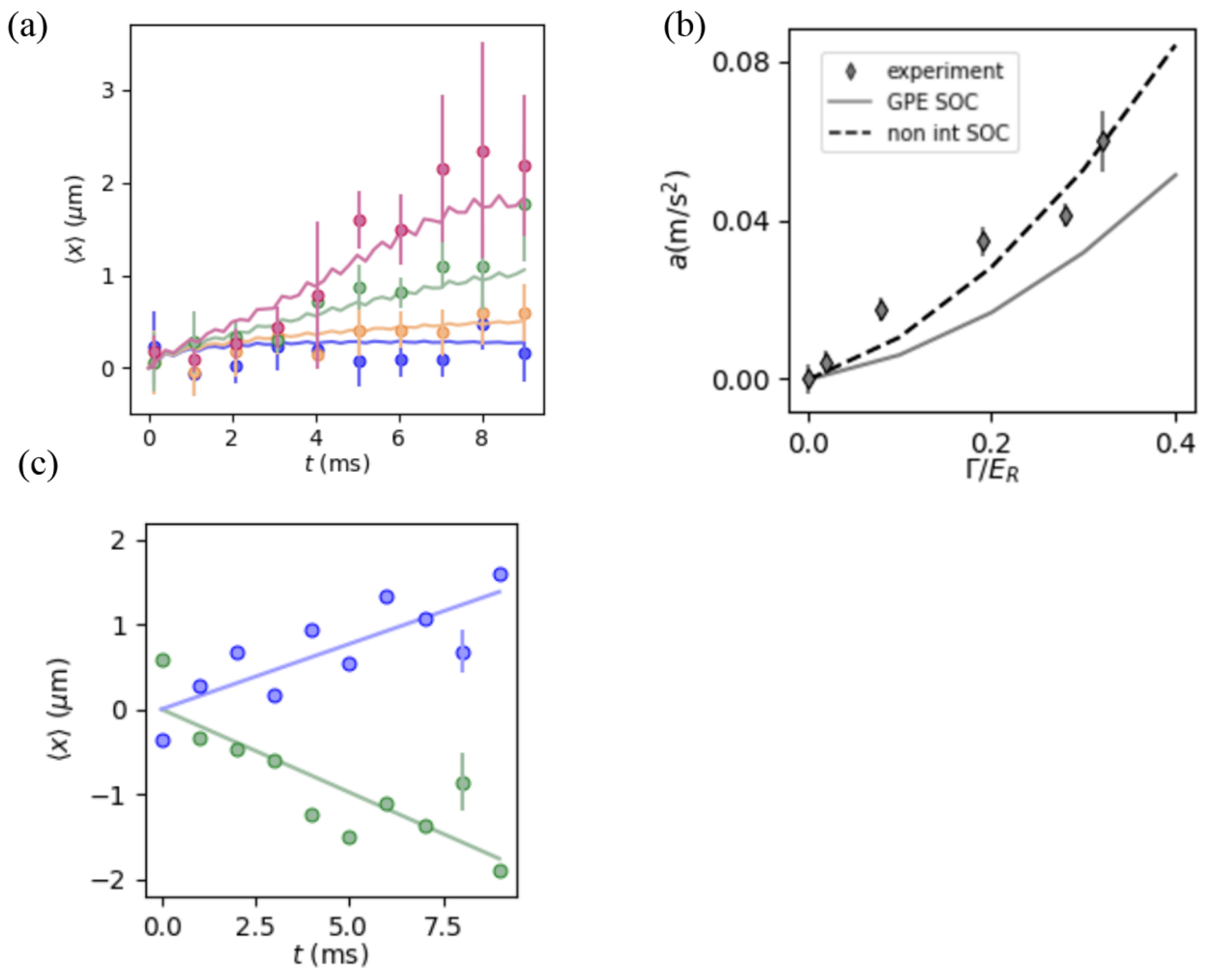

Figure 5.14: (a) Center of mass time evolution. Each point reflects the average of about 10 measurements and the uncertainties are the standard error of the mean. Solid curves are the result of GPE simulations. The colors mark Γ with blue: 0.02, orange: 0.08, green: 0.19, pink: $0.32E_0$. Inset: comparison of loss in $|\uparrow\rangle$ (blue) versus $|\downarrow\rangle$ (green). (b) The acceleration as function of Γ. Comparing experimental data with error bars from fitting (diamond), GPE simulation (solid line), and single particle simulation (dashed line). (c) The transport direction could be inverted by changing the depleted spin state. This effectively switched the sign of the imaginary gauge potential.

We calculated the force induced by the imaginary gauge field, with both a GPE ground state and a single particle ground state in the same box trap potential. We found that the initial acceleration for the single particle ground state is an order of magnitude smaller. The transport is greatly enhanced by the large $\langle p^2 \rangle$ in the initial state canonical momentum distribution.

5.13.5 Non-Hermitian skin effect

The Non-Hermitian skin effect predicts that for a system with nonzero winding number, there will be corresponding eigenstates that localize at the system boundary. We intend to prepare such states. For Hermitian topological systems, preparing the edge states in a real spatial dimension is difficult (but doable! See the exciting works in [105, 106]). It is because for Hermitian systems the number of edge modes is of order L^{d-1}, but there are many more bulk modes L^d. It requires clever and careful engineering to not let the initial wavefunction overlap much with those bulk modes. For our (lowest order) non-Hermitian systems, this is no longer the case. And we can easily prepare these modes using our DMD.

We commanded and ramped up an asymmetric potential in $\mathbf{e}_x$ which pushes the BEC to one side of the box, and measured the center of mass $\langle x \rangle(0)$ in this state. At $t = 0$, we snap off this potential and snap on the spin-dependent loss. We discovered that the dynamics is a function of the loss rate Γ, and we could tune it such that $\langle x \rangle(t)$ is a constant of time. We changed the initial potential for preparing different $\langle x \rangle(0)$, and measured the Γ which made it a stationary state. The result is summarized in Fig. 5.15. We further ran two simulations: the non-interacting solution found by exact diagonalization overestimated the $\langle x \rangle$ drift; but a non-Hermitian GPE simulation recovered our experimental data.

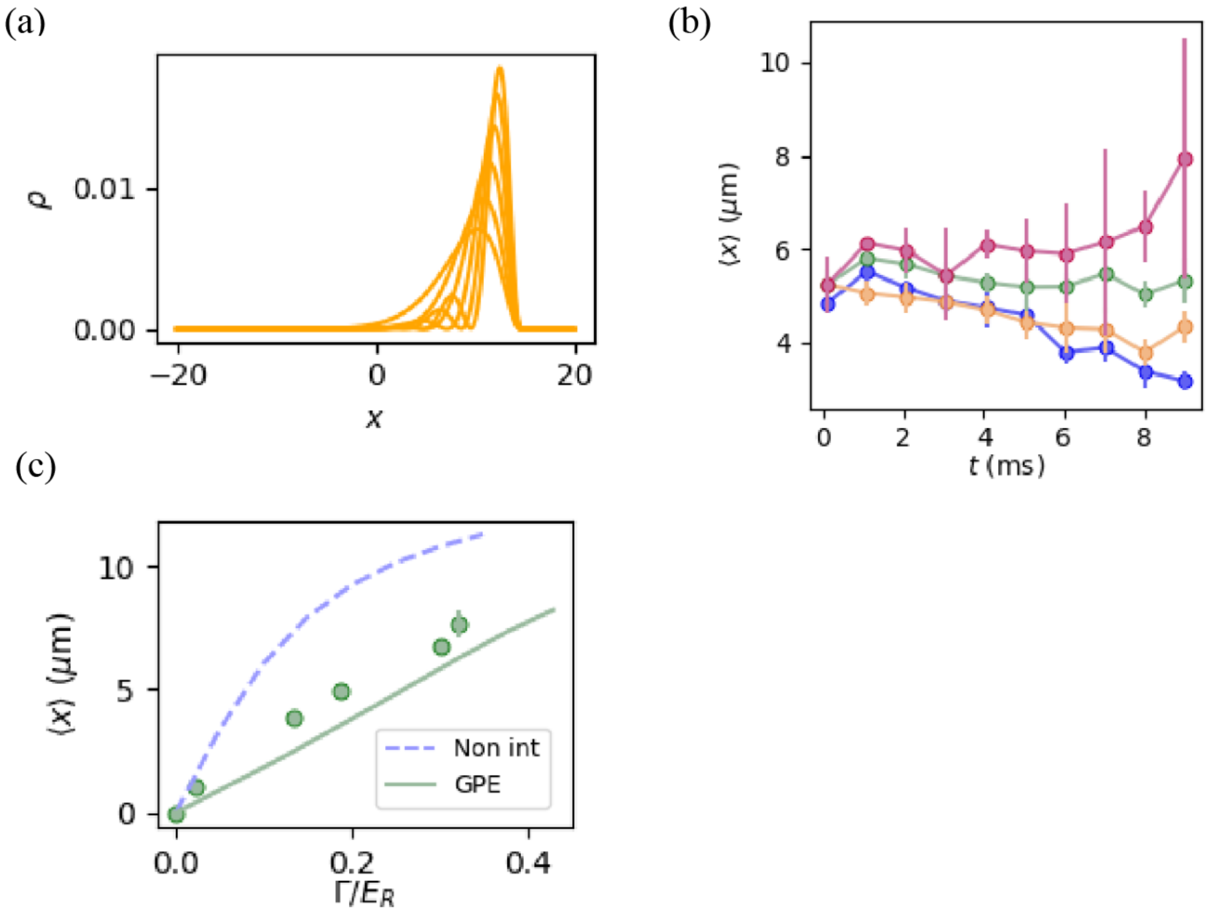

Figure 5.15: (a) Bulk edge correspondence: wavefunctions of low-lying single-particle eigenstates for the non-Hermitian Hamiltonian. (b) We were able to prepare an edge state that was invariant under time evolution. (c) Dependence of edge state displacement on the loss rate Γ.

5.13.6 Impact of interaction

In contrast to the previous non-Hermitian works in photonics, our BECs are intrinsically interacting systems, and the impact of the interaction strength g can be summarized as the following. First, the observation would not be possible if we use a non-interacting cloud (or even thermal cloud), due to the smallness of the "force" that drives the non-reciprocal transport. We took advantage of the momentum extent up to the inverse healing length in the BECs, which magnified the force by more than ten times.

Secondly, during the course of the transport, the atomic density dropped due to the loss term with 1/e lifetime of milliseconds, which quickly rendered the dynamics effectively described by the non-interacting equations.

Thirdly, however, as we prepared the edge states as the initial states, their initial dynamics was still impacted by the interaction. Our experimental data are more aligned with the GPE simulations rather than the single-particle stationary states.

5.14 Hydrodynamics picture

As an aside, we derive the equations of motion for the density n and velocity v in the hydrodynamics picture. We have hoped this can provide some insights with or without atomic interaction. From the Schrodinger equation

$$i\hbar\partial_t\psi = \left[-\frac{\hbar^2}{2m^*}\frac{\partial^2}{\partial x^2} - \frac{B\hbar}{m^*}\frac{\partial}{\partial x} + V_{ext}\right]\psi \tag{5.62}$$

and its complex conjugate

$$-i\hbar\partial_t\psi^* = \left[-\frac{\hbar^2}{2m^*}\frac{\partial^2}{\partial x^2} - \frac{B\hbar}{m^*}\frac{\partial}{\partial x} + V_{ext}\right]\psi^*, \tag{5.63}$$

we obtain

$$i\hbar\partial_t(\psi^*\psi) = -\frac{\hbar^2}{2m^*}\partial_x\left[\psi^*\partial_x\psi - \psi\partial_x\psi^*\right] \tag{5.64}$$

$$-\frac{B\hbar}{m^*}\left[\psi^*\partial_x\psi - \psi\partial_x\psi^*\right]. \tag{5.65}$$

Then apply the hydrodynamics mapping $\psi = \sqrt{n}e^{i\phi}$, and $v = \frac{\hbar}{m^*}\partial_x\phi$, then we obtain the new continuity equation

$$\partial_t n = -\partial_x(nv) - 2\frac{B}{\hbar}nv. \tag{5.66}$$

The term with B describes the lossy process and it is quite interesting to be proportional to the current $j = nv$. Now I will derive the Eq. (5.48) in the main text from Eq.5.66.

$$\langle x\rangle = \frac{\int dx\, nx}{\int dx\, n}. \tag{5.67}$$

$$\partial_t\langle x\rangle = \frac{\int dx\, x\partial_t n}{\int dx\, n} - \frac{\int dx\, \partial_t n}{\int dx\, n}\frac{\int dx\, nx}{\int dx\, n} \tag{5.68}$$

$$= \frac{\int dx\, x\left[-\partial_x(nv) - \frac{2B}{\hbar}nv\right]}{\int dx\, n} - \frac{\int dx\, \frac{-2B}{\hbar}nv}{\int dx\, n}\langle x\rangle \tag{5.69}$$

$$= \frac{\int dx\, nv}{\int dx\, n} - \frac{\int dx\, \frac{2B}{\hbar}nxv}{\int dx\, n} + \frac{2B}{\hbar}\langle x\rangle\langle v\rangle \tag{5.70}$$

$$= \langle v\rangle - \frac{2B}{\hbar}\left(\langle xv\rangle - \langle x\rangle\langle v\rangle\right) \tag{5.71}$$

This is exactly Eq. 5.48 under the transformation $v = p/m^*$, and $2\langle xv\rangle = \langle\{\hat{x}, \hat{p}/m^*\}\rangle$.

So if we understand the lossy term in Eq.5.66 we understand the Eq.5. It is not surprising that the lossy term should be proportional to n and the v comes from the $iB\hat{p}$ in the Hamiltonian. (I think I am rephrasing Eq.(17).)

The equation of motion for v can be obtained from the real part of the Schrodinger equation with $\partial_t\phi$, i.e.,

$$\partial_t v = -\partial_x\left[-\frac{\hbar^2}{2m^*\sqrt{n}}\frac{\partial^2}{\partial x^2}\sqrt{n} - \frac{B\hbar}{m^*\sqrt{n}}\partial_x\sqrt{n}\right] - \partial_x(\frac{v^2}{2}) - \partial_x V_{ext} \tag{5.72}$$

Similarly, we can derive Eq. (5.49) from that. The term with B is another pressure term $P_B = -\frac{B\hbar}{m^*\sqrt{n}}\partial_x\sqrt{n}$, and it is very interesting that it gives the initial acceleration originating from the inhomogeneity of the density. For example, in the box trap, this pressure term is nonzero only around the boundary, and at $P_B(x = -L/2) < 0$, $P_B(x = +L/2) > 0$, which pushes the atoms to the left edge.

5.15 Outlook

We developed a non-Hermitian tool in ultracold atoms that was able to engineer the topological effects, observed by measuring the atomic transport. There are indeed many directions that can be pursued using this tool. Here is an incomplete list.

First, one can study the non-Hermitian skin effect in the interplay with other interesting physics. For instance, Anderson transition or even many-body localization have been observed in ultracold atoms as another localization mechanism [107, 108, 109, 110]. However, it localizes the atoms to wavepackets scattered in the trap due to disorder, but not to the boundaries. One would expect that the non-Hermitian effect is going to compete with the random localization, and there exists a predicted phase transition. In our setup, it is straightforward to use our DMD$_2$ to project the disordered potentials.

Second, higher-order non-Hermitian skin effects were predicted in theory [111]. In these models, the number of edge states can be of order L^{d-1} or less, similar to Hermitian systems. It can be derived that such effects are to be engineered with 2D spin-orbit coupling [112], but still following a similar recipe to our work to introduce the spin-dependent loss.

Thirdly, the general non-Hermitian tool is new and useful to ultracold research, as is elaborated in the following.

5.15.1 The non-Hermitian tool

For example, we can ask how continuous measurement transforms many-body systems? While strong measurement directly projects states or creates entanglement, weak continuous measurement can often be modeled through non-Hermitian Hamiltonian, as well as back-acted fluctuations due to the fluctuation-dissipation theorem. The local measurement can be induced by our developed tools, by shining the Raman beam on our DMD, which creates local atom losses.

The novelty lies in the interplay of non-Hermitian terms with atomic interaction, which is only recently considered in theory studies. I'll list two examples. For a bulk quantum gas like in our experiment, we can introduce an atomic drain at the center of the box. This will induce a velocity field that flows inwards, and can be rigorously mapped to a *Schwarzschild metric* for acoustic phonons in the system [113]. If the local speed of sound is slower than the velocity inflow, the phonons cannot get out and the drain turns into a classic blackhole. This blackhole allows studies of analog gravitational physics such as gravitational lensing (Fig. 5.16a), the Hawking radiation, etc [114]. It is also predicted that such a blackhole would emit solitons rings [113].

For another example, consider a Bose-Hubbard ladder (made by an optical lattice) subjected to local losses [115]. It is predicted to support interesting nonlinear solutions such as unusual localization, solitons and breathers (e.g. Fig.5.16b). There are also recent works that research on the interacting topological system subjected to non-Hermitian terms [116, 117]. Such studies will in general be informative to broaden new fields in applied math and physics.

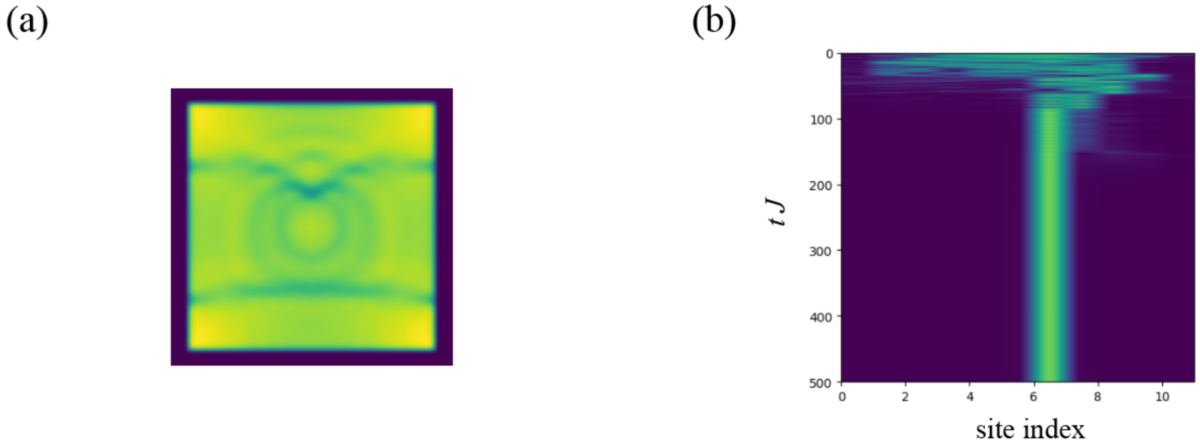

Figure 5.16: Simulations for proposals of non-Hermitian projects. (a) The phonon wavepacket passes through the analog blackhole and is focused due to “gravitational lensing”. (b) A Hubbard chain subjected to non-Hermitian loss term at the edges. The atoms localize to a single site at the center of the chain.

Bibliography

[1] Farzan Jazaeri, Arnout Beckers, Armin Tajalli, and Jean-Michel Sallese. A review on quantum computing: From qubits to front-end electronics and cryogenic mosfet physics. In *2019 MIXDES-26th International Conference" Mixed Design of Integrated Circuits and Systems"*, pages 15–25. IEEE, 2019.

[2] James E Lidsey, Andrew R Liddle, Edward W Kolb, Edmund J Copeland, Tiago Barreiro, and Mark Abney. Reconstructing the inflaton potential—an overview. *Reviews of Modern Physics*, 69(2):373, 1997.

[3] JH Huckans, IB Spielman, B Laburthe Tolra, WD Phillips, and JV Porto. Quantum and classical dynamics of a bose-einstein condensate in a large-period optical lattice. *Physical Review A*, 80(4):043609, 2009.

[4] NR Cooper, J Dalibard, and IB Spielman. Topological bands for ultracold atoms. *Reviews of modern physics*, 91(1):015005, 2019.

[5] Richard P Feynman et al. Simulating physics with computers. *Int. j. Theor. phys*, 21(6/7), 1982.

[6] Immanuel Bloch, Jean Dalibard, and Wilhelm Zwerger. Many-body physics with ultracold gases. *Reviews of modern physics*, 80(3):885, 2008.

[7] Peter T Brown, Debayan Mitra, Elmer Guardado-Sanchez, Reza Nourafkan, Alexis Reymbaut, Charles-David Hébert, Simon Bergeron, A-MS Tremblay, Jure Kokalj, David A Huse, et al. Bad metallic transport in a cold atom fermi-hubbard system. *Science*, 363(6425):379–382, 2019.

[8] J Ignacio Cirac, Paolo Maraner, and Jiannis K Pachos. Cold atom simulation of interacting relativistic quantum field theories. *Physical review letters*, 105(19):190403, 2010.

[9] Erez Zohar, J Ignacio Cirac, and Benni Reznik. Quantum simulations of lattice gauge theories using ultracold atoms in optical lattices. *Reports on Progress in Physics*, 79(1):014401, 2015.

[10] Celia Viermann, Marius Sparn, Nikolas Liebster, Maurus Hans, Elinor Kath, Álvaro Parra-López, Mireia Tolosa-Simeón, Natalia Sánchez-Kuntz, Tobias Haas, Helmut Strobel, et al. Quantum field simulator for dynamics in curved spacetime. *nature*, 611(7935):260–264, 2022.

[11] Simon J Devitt, William J Munro, and Kae Nemoto. Quantum error correction for beginners. *Reports on Progress in Physics*, 76(7):076001, 2013.

[12] Nathanan Tantivasadakarn, Ryan Thorngren, Ashvin Vishwanath, and Ruben Verresen. Long-range entanglement from measuring symmetry-protected topological phases. *arXiv preprint arXiv:2112.01519*, 2021.

[13] Hans J Briegel, David E Browne, Wolfgang Dür, Robert Raussendorf, and Maarten Van den Nest. Measurement-based quantum computation. *Nature Physics*, 5(1):19–26, 2009.

[14] Claude Cohen-Tannoudji and David Guéry-Odelin. Advances in atomic physics: an overview. 2011.

[15] Christopher J Foot. *Atomic physics*, volume 7. OUP Oxford, 2004.

[16] Daniel A Steck. Rubidium 87 d line data. 2001.

[17] J.R. Johansson, P.D. Nation, and Franco Nori. Qutip 2: A python framework for the dynamics of open quantum systems. *Computer Physics Communications*, 184(4):1234–1240, 2013.

[18] J Robert Johansson, Paul D Nation, and Franco Nori. Qutip: An open-source python framework for the dynamics of open quantum systems. *Computer Physics Communications*, 183(8):1760–1772, 2012.

[19] Misha Lukin. Lecture notes for modern atomic and optical physics ii, 2016.

[20] Paul D Lett, William D Phillips, SL Rolston, Carol E Tanner, RN Watts, and CI Westbrook. Optical molasses. *JOSA B*, 6(11):2084–2107, 1989.

[21] Rudolf Grimm, Matthias Weidemüller, and Yurii B Ovchinnikov. Optical dipole traps for neutral atoms. In *Advances in atomic, molecular, and optical physics*, volume 42, pages 95–170. Elsevier, 2000.

[22] JF Barry, DJ McCarron, EB Norrgard, MH Steinecker, and D DeMille. Magneto-optical trapping of a diatomic molecule. *Nature*, 512(7514):286–289, 2014.

[23] Markus Greiner, Immanuel Bloch, Theodor W Hänsch, and Tilman Esslinger. Magnetic transport of trapped cold atoms over a large distance. *Physical Review A*, 63(3):031401, 2001.

[24] Daniel A Steck. Quantum and atom optics. 2007.

[25] Franco Dalfovo, Stefano Giorgini, Lev P Pitaevskii, and Sandro Stringari. Theory of bose-einstein condensation in trapped gases. *Reviews of modern physics*, 71(3):463, 1999.

[26] Wolfgang Ketterle, Dallin S Durfee, and DM Stamper-Kurn. Making, probing and understanding bose-einstein condensates. *arXiv preprint cond-mat/9904034*, 1999.

[27] Eugene P Gross. Structure of a quantized vortex in boson systems. *Il Nuovo Cimento (1955-1965)*, 20(3):454–477, 1961.

[28] Lev P Pitaevskii. Vortex lines in an imperfect bose gas. *Sov. Phys. JETP*, 13(2):451–454, 1961.

[29] László Erdős, Benjamin Schlein, and Horng-Tzer Yau. Rigorous derivation of the gross-pitaevskii equation. *Physical review letters*, 98(4):040404, 2007.

[30] Christopher J Pethick and Henrik Smith. *Bose–Einstein condensation in dilute gases*. Cambridge university press, 2008.

[31] David H Sharp. An overview of rayleigh-taylor instability. *Physica D: Nonlinear Phenomena*, 12(1-3):3–18, 1984.

[32] Carlos Barcelo, Stefano Liberati, and Matt Visser. Analogue gravity. *Living reviews in relativity*, 14:1–159, 2011.

[33] Uwe R Fischer and Ralf Schützhold. Quantum simulation of cosmic inflation in two-component bose-einstein condensates. *Physical Review A*, 70(6):063615, 2004.

[34] Giovanni I Martone, Yun Li, and Sandro Stringari. Approach for making visible and stable stripes in a spin-orbit-coupled bose-einstein superfluid. *Physical Review A*, 90(4):041604, 2014.

[35] Y-J Lin, K Jiménez-García, and Ian B Spielman. Spin–orbit-coupled bose–einstein condensates. *Nature*, 471(7336):83–86, 2011.

[36] Abigail Reiko Perry. *An apparatus for light-less artificial gauge fields and new imaging techniques*. PhD thesis, 2015.

[37] Francisco Salces Carcoba. Microscopy of elongated superfluids. 2020.

[38] Chen-Lung Hung, Xibo Zhang, Li-Chung Ha, Shih-Kuang Tung, Nathan Gemelke, and Cheng Chin. Extracting density–density correlations from in situ images of atomic quantum gases. *New Journal of Physics*, 13(7):075019, 2011.

[39] Andika Putra, Daniel L Campbell, Ryan M Price, Subhadeep De, and IB Spielman. Optimally focused cold atom systems obtained using density-density correlations. *Review of Scientific Instruments*, 85(1), 2014.

[40] Anthony J Leggett. Can a solid be" superfluid"? *Physical Review Letters*, 25(22):1543, 1970.

[41] L Tanzi, JG Maloberti, G Biagioni, A Fioretti, C Gabbanini, and G Modugno. Evidence of superfluidity in a dipolar supersolid from nonclassical rotational inertia. *Science*, 371(6534):1162–1165, 2021.

[42] Matthew A Norcia, Claudia Politi, Lauritz Klaus, Elena Poli, Maximilian Sohmen, Manfred J Mark, Russell N Bisset, Luis Santos, and Francesca Ferlaino. Two-dimensional supersolidity in a dipolar quantum gas. *Nature*, 596(7872):357–361, 2021.

[43] Roger Corthan Clark and Graham Holbrook Derrick. *Mathematical Methods in Solid State and Superfluid Theory: Scottish Universities' Summer School*. Springer, 2013.

[44] Cord A Müller. Josephson relation for disordered superfluids. *Physical Review A*, 91(2):023602, 2015.

[45] Anand Ramanathan, Sérgio R Muniz, Kevin C Wright, Russell P Anderson, William D. Phillips, Kristian Helmerson, and Gretchen K Campbell. Partial-transfer absorption imaging: A versatile technique for optimal imaging of ultracold gases. *Review of Scientific Instruments*, 83(8):083119–083119–9, 2012.

[46] Li-Chung Ha, Logan W Clark, Colin V Parker, Brandon M Anderson, and Cheng Chin. Roton-maxon excitation spectrum of bose condensates in a shaken optical lattice. *Physical review letters*, 114(5):055301, 2015.

[47] S. M. Roccuzzo, A. Recati, and S. Stringari. Moment of inertia and dynamical rotational response of a supersolid dipolar gas. *Phys. Rev. A*, 105:023316, Feb 2022.

[48] Saverio Moroni, Francesco Ancilotto, Pier Luigi Silvestrelli, and Luciano Reatto. Localization versus inhomogeneous superfluidity: Submonolayer ^{4}He on fluorographene, hexagonal boron nitride, and graphene. *Phys. Rev. B*, 103:174514, May 2021.

[49] Y. J. Lin, K. Jiménez-García, and I. B. Spielman. Spin-orbit-coupled Bose-Einstein condensates. *Nature*, 471(7336):83–86, 3 2011.

[50] Jun-Ru Li, Jeongwon Lee, Wujie Huang, Sean Burchesky, Boris Shteynas, Furkan Çağrı Top, Alan O. Jamison, and Wolfgang Ketterle. A stripe phase with supersolid properties in spin–orbit-coupled bose–einstein condensates. *Nature*, 543(7643):91–94, 3 2017.

[51] Yun Li, Giovanni I. Martone, Lev P. Pitaevskii, and Sandro Stringari. Superstripes and the excitation spectrum of a spin-orbit-coupled bose-einstein condensate. *Phys. Rev. Lett.*, 110:235302, June 2013.

[52] Yi-Cai Zhang, Zeng-Qiang Yu, Tai Kai Ng, Shizhong Zhang, Lev Pitaevskii, and Sandro Stringari. Superfluid density of a spin-orbit-coupled bose gas. *Physical Review A*, 94(3):033635, 2016.

[53] Giovanni Italo Martone and Sandro Stringari. Supersolid phase of a spin-orbit-coupled Bose-Einstein condensate: A perturbation approach. *SciPost Phys.*, 11:92, 2021.

[54] L. Tanzi, E. Lucioni, F. Famà, J. Catani, A. Fioretti, C. Gabbanini, R. N. Bisset, L. Santos, and G. Modugno. Observation of a dipolar quantum gas with metastable supersolid properties. *Phys. Rev. Lett.*, 122:130405, Apr 2019.

[55] Fabian Böttcher, Jan-Niklas Schmidt, Matthias Wenzel, Jens Hertkorn, Mingyang Guo, Tim Langen, and Tilman Pfau. Transient supersolid properties in an array of dipolar quantum droplets. *Phys. Rev. X*, 9:011051, Mar 2019.

[56] L. Chomaz, D. Petter, P. Ilzhöfer, G. Natale, A. Trautmann, C. Politi, G. Durastante, R. M. W. van Bijnen, A. Patscheider, M. Sohmen, M. J. Mark, and F. Ferlaino. Long-lived and transient supersolid behaviors in dipolar quantum gases. *Phys. Rev. X*, 9:021012, Apr 2019.

[57] D Guéry-Odelin and S Stringari. Scissors mode and superfluidity of a trapped bose-einstein condensed gas. *Physical review letters*, 83(22):4452, 1999.

[58] O. M. Maragò, S. A. Hopkins, J. Arlt, E. Hodby, G. Hechenblaikner, and C. J. Foot. Observation of the scissors mode and evidence for superfluidity of a trapped bose-einstein condensed gas. *Phys. Rev. Lett.*, 84(10):2056–2059, March 2000.

[59] Claude Cohen-Tannoudji, Jacques Dupont-Roc, and Gilbert Grynberg. *Atom-photon interactions: basic processes and applications*. John Wiley & Sons, 1998.

[60] Klaus Mølmer, Yvan Castin, and Jean Dalibard. Monte carlo wave-function method in quantum optics. *JOSA B*, 10(3):524–538, 1993.

[61] Paul Adrien Maurice Dirac. *The principles of quantum mechanics*. Number 27. Oxford university press, 1981.

[62] Yuto Ashida, Zongping Gong, and Masahito Ueda. Non-hermitian physics. *Advances in Physics*, 69(3):249–435, 2020.

[63] Carl M Bender. Making sense of non-hermitian hamiltonians. *Reports on Progress in Physics*, 70(6):947, 2007.

[64] Ramy El-Ganainy, Konstantinos G Makris, Mercedeh Khajavikhan, Ziad H Musslimani, Stefan Rotter, and Demetrios N Christodoulides. Non-hermitian physics and pt symmetry. *Nature Physics*, 14(1):11–19, 2018.

[65] Mohammad-Ali Miri and Andrea Alu. Exceptional points in optics and photonics. *Science*, 363(6422):eaar7709, 2019.

[66] Michel Fruchart, Ryo Hanai, Peter B Littlewood, and Vincenzo Vitelli. Non-reciprocal phase transitions. *Nature*, 592(7854):363–369, 2021.

[67] Konstantinos G Makris, R El-Ganainy, DN Christodoulides, and Ziad H Musslimani. Beam dynamics in p t symmetric optical lattices. *Physical Review Letters*, 100(10):103904, 2008.

[68] Hengyun Zhou, Chao Peng, Yoseob Yoon, Chia Wei Hsu, Keith A Nelson, Liang Fu, John D Joannopoulos, Marin Soljačić, and Bo Zhen. Observation of bulk fermi arc and polarization half charge from paired exceptional points. *Science*, 359(6379):1009–1012, 2018.

[69] Lei Xiao, Tianshu Deng, Kunkun Wang, Gaoyan Zhu, Zhong Wang, Wei Yi, and Peng Xue. Non-hermitian bulk–boundary correspondence in quantum dynamics. *Nature Physics*, 16(7):761–766, 2020.

[70] L Xiao, X Zhan, ZH Bian, KK Wang, X Zhang, XP Wang, J Li, K Mochizuki, D Kim, N Kawakami, et al. Observation of topological edge states in parity–time-symmetric quantum walks. *Nature Physics*, 13(11):1117–1123, 2017.

[71] Ananya Ghatak, Martin Brandenbourger, Jasper Van Wezel, and Corentin Coulais. Observation of non-hermitian topology and its bulk–edge correspondence in an active mechanical metamaterial. *Proceedings of the National Academy of Sciences*, 117(47):29561–29568, 2020.

[72] Javier Del Pino, Jesse J Slim, and Ewold Verhagen. Non-hermitian chiral phononics through optomechanically induced squeezing. *Nature*, 606(7912):82–87, 2022.

[73] Yogesh SS Patil, Judith Höller, Parker A Henry, Chitres Guria, Yiming Zhang, Luyao Jiang, Nenad Kralj, Nicholas Read, and Jack GE Harris. Measuring the knot of non-hermitian degeneracies and non-commuting braids. *Nature*, 607(7918):271–275, 2022.

[74] Qian Liang, Dizhou Xie, Zhaoli Dong, Haowei Li, Hang Li, Bryce Gadway, Wei Yi, and Bo Yan. Dynamic signatures of non-hermitian skin effect and topology in ultracold atoms. *Physical review letters*, 129(7):070401, 2022.

[75] Jiaming Li, Andrew K Harter, Ji Liu, Leonardo de Melo, Yogesh N Joglekar, and Le Luo. Observation of parity-time symmetry breaking transitions in a dissipative floquet system of ultracold atoms. *Nature communications*, 10(1):855, 2019.

[76] Linhu Li, Ching Hua Lee, and Jiangbin Gong. Topological switch for non-hermitian skin effect in cold-atom systems with loss. *Physical review letters*, 124(25):250402, 2020.

[77] James Munkres. Topology james munkres second edition.

[78] Marc Lachieze-Rey and Jean-Pierre Luminet. Cosmic topology. *Physics Reports*, 254(3):135–214, 1995.

[79] Danny Birmingham, Matthias Blau, Mark Rakowski, and George Thompson. Topological field theory. *Physics Reports*, 209(4-5):129–340, 1991.

[80] M Zahid Hasan and Charles L Kane. Colloquium: topological insulators. *Reviews of modern physics*, 82(4):3045, 2010.

[81] Charles Kittel and Paul McEuen. *Introduction to solid state physics*. John Wiley & Sons, 2018.

[82] Di Xiao, Ming-Che Chang, and Qian Niu. Berry phase effects on electronic properties. *Reviews of modern physics*, 82(3):1959, 2010.

[83] F Duncan M Haldane. Model for a quantum hall effect without landau levels: Condensed-matter realization of the" parity anomaly". *Physical review letters*, 61(18):2015, 1988.

[84] Charles L Kane and Eugene J Mele. Quantum spin hall effect in graphene. *Physical review letters*, 95(22):226801, 2005.

[85] B Andrei Bernevig, Taylor L Hughes, and Shou-Cheng Zhang. Quantum spin hall effect and topological phase transition in hgte quantum wells. *science*, 314(5806):1757–1761, 2006.

[86] Alexander Altland and Martin R Zirnbauer. Nonstandard symmetry classes in mesoscopic normal-superconducting hybrid structures. *Physical Review B*, 55(2):1142, 1997.

[87] Shinsei Ryu, Andreas P Schnyder, Akira Furusaki, and Andreas WW Ludwig. Topological insulators and superconductors: tenfold way and dimensional hierarchy. *New Journal of Physics*, 12(6):065010, 2010.

[88] Alexei Kitaev. Periodic table for topological insulators and superconductors. In *AIP conference proceedings*, volume 1134, pages 22–30. American Institute of Physics, 2009.

[89] Robert-Jan Slager, Andrej Mesaros, Vladimir Juričić, and Jan Zaanen. The space group classification of topological band-insulators. *Nature Physics*, 9(2):98–102, 2013.

[90] J Zak. Berry's phase for energy bands in solids. *Physical review letters*, 62(23):2747, 1989.

[91] Zongping Gong, Yuto Ashida, Kohei Kawabata, Kazuaki Takasan, Sho Higashikawa, and Masahito Ueda. Topological phases of non-hermitian systems. *Physical Review X*, 8(3):031079, 2018.

[92] Shunyu Yao and Zhong Wang. Edge states and topological invariants of non-hermitian systems. *Physical review letters*, 121(8):086803, 2018.

[93] Nobuyuki Okuma, Kohei Kawabata, Ken Shiozaki, and Masatoshi Sato. Topological origin of non-hermitian skin effects. *Physical review letters*, 124(8):086801, 2020.

[94] Naomichi Hatano and David R Nelson. Localization transitions in non-hermitian quantum mechanics. *Physical review letters*, 77(3):570, 1996.

[95] Chenwei Lv, Ren Zhang, Zhengzheng Zhai, and Qi Zhou. Curving the space by non-hermiticity. *Nature Communications*, 13(1):2184, 2022.

[96] Emil J Bergholtz, Jan Carl Budich, and Flore K Kunst. Exceptional topology of non-hermitian systems. *Reviews of Modern Physics*, 93(1):015005, 2021.

[97] Naomichi Hatano and David R Nelson. Vortex pinning and non-hermitian quantum mechanics. *Physical Review B*, 56(14):8651, 1997.

[98] Y-J Lin, Robert L Compton, Abigail R Perry, William D Phillips, James V Porto, and Ian B Spielman. Bose-einstein condensate in a uniform light-induced vector potential. *Physical Review Letters*, 102(13):130401, 2009.

[99] Y-J Lin, Rob L Compton, Karina Jiménez-García, James V Porto, and Ian B Spielman. Synthetic magnetic fields for ultracold neutral atoms. *Nature*, 462(7273):628–632, 2009.

[100] Yu-Ju Lin, Robert L Compton, Karina Jimenez-Garcia, William D Phillips, James V Porto, and Ian B Spielman. A synthetic electric force acting on neutral atoms. *Nature Physics*, 7(7):531–534, 2011.

[101] Zejian Ren, Dong Liu, Entong Zhao, Chengdong He, Ka Kwan Pak, Jensen Li, and Gyu-Boong Jo. Chiral control of quantum states in non-hermitian spin–orbit-coupled fermions. *Nature Physics*, 18(4):385–389, 2022.

[102] Yun Li, Lev P. Pitaevskii, and Sandro Stringari. Quantum tricriticality and phase transitions in spin-orbit coupled bose-einstein condensates. *Phys. Rev. Lett.*, 108:225301, May 2012.

[103] Y-J. Lin, R. L. Compton, K Jimenez-Garcia, W. D. Phillips, J. V. Porto, and I. B. Spielman. A synthetic electric force acting on neutral atoms. *Nature Physics*, 7(7):531–534, March 2011.

[104] Erin Marshall Seroka, Ana Valdés Curiel, Dimitrios Trypogeorgos, Nathan Lundblad, and Ian B Spielman. Repeated measurements with minimally destructive partial-transfer absorption imaging. *Optics Express*, 27(25):36611–36624, 2019.

[105] Ruixiao Yao, Sungjae Chi, Biswaroop Mukherjee, Airlia Shaffer, Martin Zwierlein, and Richard J Fletcher. Observation of chiral edge transport in a rapidly-rotating quantum gas. *arXiv preprint arXiv:2304.10468*, 2023.

[106] Christoph Braun, Raphaël Saint-Jalm, Alexander Hesse, Johannes Arceri, Immanuel Bloch, and Monika Aidelsburger. Real-space detection and manipulation of topological edge modes with ultracold atoms. *arXiv preprint arXiv:2304.01980*, 2023.

[107] Laurent Sanchez-Palencia, David Clément, Pierre Lugan, Philippe Bouyer, Georgy V Shlyapnikov, and Alain Aspect. Anderson localization of expanding bose-einstein condensates in random potentials. *Physical Review Letters*, 98(21):210401, 2007.

[108] SS Kondov, WR McGehee, JJ Zirbel, and B DeMarco. Three-dimensional anderson localization of ultracold matter. *Science*, 334(6052):66–68, 2011.

[109] Donald H White, Thomas A Haase, Dylan J Brown, Maarten D Hoogerland, Mojdeh S Najafabadi, John L Helm, Christopher Gies, Daniel Schumayer, and David AW Hutchinson. Observation of two-dimensional anderson localisation of ultracold atoms. *Nature communications*, 11(1):4942, 2020.

[110] Jae-yoon Choi, Sebastian Hild, Johannes Zeiher, Peter Schauß, Antonio Rubio-Abadal, Tarik Yefsah, Vedika Khemani, David A Huse, Immanuel Bloch, and Christian Gross. Exploring the many-body localization transition in two dimensions. *Science*, 352(6293):1547–1552, 2016.

[111] Kohei Kawabata, Masatoshi Sato, and Ken Shiozaki. Higher-order non-hermitian skin effect. *Physical Review B*, 102(20):205118, 2020.

[112] Lianghui Huang, Zengming Meng, Pengjun Wang, Peng Peng, Shao-Liang Zhang, Liangchao Chen, Donghao Li, Qi Zhou, and Jing Zhang. Experimental realization of two-dimensional synthetic spin–orbit coupling in ultracold fermi gases. *Nature Physics*, 12(6):540–544, 2016.

[113] Dries Sels and Eugene Demler. Thermal radiation and dissipative phase transition in a bec with local loss. *Annals of Physics*, 412:168021, 2020.

[114] S Giovanazzi. Hawking radiation in sonic black holes. *Physical review letters*, 94(6):061302, 2005.

[115] Giovanni Barontini, R Labouvie, F Stubenrauch, A Vogler, V Guarrera, and H Ott. Controlling the dynamics of an open many-body quantum system with localized dissipation. *Physical review letters*, 110(3):035302, 2013.

[116] Shu Hamanaka and Kohei Kawabata. Multifractality of many-body non-hermitian skin effect. *arXiv preprint arXiv:2401.08304*, 2024.

[117] Faisal Alsallom, Loïc Herviou, Oleg V Yazyev, and Marta Brzezińska. Fate of the non-hermitian skin effect in many-body fermionic systems. *Physical Review Research*, 4(3):033122, 2022.